UNIVERSITAT POLITÈCNICA DE VALÈNCIA

Departamento de Máquinas y Motores Térmicos

DOCTORAL THESIS:

Measurement, Simulation, and 1D-Modeling of Turbocharger Radial Turbines at Design and Extreme Off-Design Conditions

---

Presented by: LUKAS BENJAMIN INHESTERN
Supervised by: DR. JOSÉ RAMÓN SERRANO CRUZ

in fulfillment of the requisites for the degree of

Doctor of Philosophy

Valencia, March 2019

PhD. Thesis

Measurement, Simulation, and 1D-Modeling of Turbocharger Radial Turbines at Design and Extreme Off-Design Conditions

AUTHORS

Presented by: LUKAS BENJAMIN INHESTERN
Supervised by: PROF. DR. JOSÉ RAMÓN SERRANO CRUZ

DEFENSE COMMITTEE

Chairman: PROF. DR. JOSÉ GALINDO LUCAS
Secretary: PROF. DR. MARÍA DE LOS REYES GARCÍA CONTRERAS
Member: PROF. DR. MIHAI MIHAESCU

DISSERTATION READERS

PROF. DR. MIHAI MIHAESCU
PROF. DR. COLIN DOUGLAS COPELAND
PROF. DR. OCTAVIO ARMAS VERGEL

Submitted: December 2018
Presented: March 2019

Measurement, Simulation, and 1D-Modeling of Turbocharger Radial Turbines at Design and Extreme Off-Design Conditions

Lukas Benjamin Inhestern

Abstract

To achieve an optimal matching between the turbocharger and internal combustion engine over a wide range of the engine operation map, their complex interaction is commonly analyzed by means of transient one-dimensional modeling. The pulsating flow of the engine exhaust gases causes high variations of turbine inlet mass flow, total pressure, and total temperature. This pushes the turbocharger turbine operation towards extreme off-design conditions. Hence, wide turbine operation maps are required as input for the one-dimensional models. The measurement of turbine maps is typically restricted by compressor choke and surge. At the same time, only minor geometrical changes are required to maintain the important thermal characteristics of the turbocharger.

In this thesis the turbocharger compressor was converted into a centrifugal turbine to assist the axis rotation when the turbine produces or even consumes low power. For enhancing the power output from the compressor wheel, an IGV was placed upstream of the compressor inlet. To reduce the effort for adiabatizing, a simple correlation only dependent on fluid temperature measurements was developed. Further test monitoring strategies were documented that can assist the measurement of off-design conditions.

With the obtained off-design data a CFD setup for the achievement of convergent results in extreme off-design conditions was validated. To reduce the problem of high swirl angles in the turbine outlet when operating with low mass flows, the outlet duct was extended and a tapered duct had to be attached just before the domain outlet. By means of the well validated CFD results, three-dimensional flow effects were analyzed. Operating in high off-design conditions the outlet swirl and thus, the static pressure gradient was so high that the flow collapses and a reverse flow develops. This reverse flow reenters the rotor and mixes again with the main flow. On one hand this effect produces pressure losses and locally negative torque at the hub. However, on the other hand the reentering flow increases the mass flow locally and restricts the flow section close to the hub. Hence, blade loading and local torque production are increased close to the shroud. Although a clear change in the stage loading vs. flow coefficient plot was noticed as soon as the reverse flow occurs, no clear impact on the efficiency can be seen. Further analysis of tip leakage flow over a wide range showed the importance of friction driven flow and incidence induced leakage flow in off-design condition. In general, greater tip leakage losses were observed as further the turbine operates away from the design point. Furthermore, it was stated that a commonly used correlation for the characterization of tip leakage flow is not capable of reproducing either qualitative trends nor quantities when the tip gap height or the operating point is varied.

Finally, the observed effects were modeled in one-dimensional form. A tip leakage loss model that is capable of reproducing the found trends and shows good extrapolation capability was developed. Results were validated

using three-dimensional CFD data. As a result, it was possible to develop a novel method for tip leakage flow characterization, which can model tip leakage flow momentum and velocities for varying tip gap heights in design and off-design conditions. Following, a complete one-dimensional extrapolation model for adiabatic turbine efficiency maps was developed. Taking advantage of the newly developed tip leakage model and other findings from the CFD campaign, good extrapolation quality in terms of speed, blade-to-jet speed ratio and VGT opening was achieved. High accuracy of the results was stated by the comparison with the initially measured wide range data.

Resumen

Para lograr una correspondencia óptima entre el turbocompresor y el motor de combustión interna en un amplio rango del mapa de operación del motor, su compleja interacción se analiza comúnmente por medio de modelos transitorios unidimensionales. El flujo pulsante de los gases de escape del motor causa altas variaciones de caudal, presión total y temperatura total en la entrada de la turbina. Esto lleva a la turbina del turbocompresor hacia condiciones extremadamente fuera de diseño. Por lo tanto, se requieren amplios mapas de operación de turbina como entrada para estos modelos unidimensionales. La medida de los mapas de turbinas suele estar restringida por el choque y el bombeo del compresor. Al mismo tiempo, solo se desean cambios geométricos menores para mantener las importantes características térmicas del turbocompresor.

En esta tesis, el compresor del turbocompresor se convirtió en una turbina centrífuga para ayudar a la rotación del eje cuando la turbina produce o incluso consume baja potencia. Para aumentar la potencia de salida de la rueda del compresor, se colocó una IGV aguas arriba de la entrada del compresor. Para reducir el esfuerzo de adiabatización de la significativa transferencia de calor interna en estas condiciones de operación, se desarrolló una correlación simple que solo depende de las medidas de temperatura de fluidos. Se documentaron otras estrategias para la monitorización de ensayos que pueden ayudar a medir en condiciones fuera del diseño.

Con los datos obtenidos fuera del diseño, se validó una configuración de CFD para el logro de resultados convergentes en condiciones extremadamente fuera del diseño. Para reducir la problemática de los elevados ángulos de flujo en la salida de la turbina, cuando se opera con bajos caudales másicos, el conducto de salida se extendió y se tuvo que colocar un conducto cónico justo antes de la salida del dominio. Por medio de los resultados de CFD bien validados, se analizaron los efectos tridimensionales del flujo. Operando en condiciones fuera del diseño, el remolino de salida, y por lo tanto, el gradiente de presión estática es tan alto que el flujo colapsa y se produce un flujo reverso. Esta reversión del flujo regresa al interior del rotor y se mezcla nuevamente con el flujo principal. Por un lado, este efecto produce pérdidas de presión y un par localmente negativo en el rodete. Por otro lado, el flujo revertido aumenta localmente el flujo de masa y restringe la sección de flujo cerca de la carcasa. Por lo tanto, la carga del alabe y la producción de torsión local aumentan cerca del espacio por encima del alabe. Aunque se notó un cambio claro en la gráfica de la carga de la etapa en función del coeficiente de flujo tan pronto como ocurre el flujo reverso, no se puede notar un impacto claro en la eficiencia. El análisis adicional del flujo de fuga de la punta en un amplio rango mostró la importancia del flujo impulsado por fricción y el flujo de fuga inducido por incidencia en una condición fuera del diseño. En general, se observó que las pérdidas por fugas en la punta se volvieron más importantes a medida que la turbina opera lejos del punto de diseño. Además, se indicó que una correlación

comúnmente utilizada para la caracterización del flujo de fuga de la punta no es capaz de reproducir tendencias ni cantidades cualitativas cuando se varió la altura del espacio de la punta o el punto de operación.

Finalmente, los efectos observados fueron modelados unidimensionalmente. Se desarrolló un modelo de pérdida de fugas en la punta que es capaz de reproducir las tendencias encontradas y muestra una buena capacidad de extrapolación. Los resultados fueron validados con los datos tridimensionales de CFD. A continuación, fue posible desarrollar un método novedoso para la caracterización del flujo de fuga de la punta, que puede modelar el momento y las velocidades del flujo de fuga de la punta para diferentes alturas de separación de la punta en condiciones de diseño y fuera del diseño. Siguiendo con lo anterior, se desarrolló un modelo de extrapolación unidimensional completo para mapas de eficiencia de turbinas adiabáticas. Aprovechando el modelo de fuga de puntas recientemente desarrollado y otros hallazgos de la campaña CFD, se logró una buena calidad de extrapolación en términos de velocidad, relación cinemática de BSR y apertura de VGT. La alta calidad de los resultados se estableció mediante la comparación con el amplio rango de datos medidos en primer lugar.

Resum

Per aconseguir una correspondència òptima entre el turbocompressor i el motor de combustió interna en una amplia zona del mapa d'operació del motor, la seva complexa interacció s'analitza comunament per mitjà de models transitoris unidimensionals. El flux polsant dels gasos d'escapament del motor causa altes variacions de cabal, pressió total i temperatura total a l'entrada de la turbina. Això porta a la turbina del turbocompressor cap a condicions extremadament fora de disseny. Per tant, es requereixen amplis mapes d'operació de turbina com a entrada per a aquests models unidimensionals. La mesura dels mapes de turbines sol estar restringida pel choke i el surge del compressor. Alhora, només es volen canvis geomètrics menors per mantenir les importants característiques tèrmiques del turbocompressor.

En aquesta tesi, el compressor del turbocompressor va esdevenir una turbina centrífuga per ajudar a la rotació de l'eix quan la turbina produeix o fins i tot consumeix baixa potència. Per augmentar la potència de sortida de la roda del compressor, es va col·locar una IGV aigües amunt de l'entrada del compressor. Per reduir l'esforç de adiabatización de la significativa transferència de calor interna en aquestes condicions d'operació, es va desenvolupar una correlació simple que només depèn de les mesures de temperatura del fluids. Es van documentar altres estratègies per a la monitorització d'experimentacions que poden ajudar a mesurar en condicions fora del disseny.

Amb les dades obtingudes fora del disseny, es va validar una configuració de CFD per a l'assoliment de resultats convergents en condicions extremadament fora del disseny. Per reduir la problemàtica dels elevats angles de flux a la sortida de la turbina, quan s'opera amb baixos cabals màssics, el conducte de sortida es va estendre i es va haver de posar un conducte cònic just abans de la sortida del domini. Per mitjà dels resultats de CFD ben validats, es van analitzar els efectes tridimensionals del flux. Operant en condicions fora del disseny, el remolí de sortida, i per tant, el gradient de pressió estàtica és tan alt que el flux col·lapsa i es produeix un flux revers. Aquesta reversió del flux torna a l'interior del rotor i es barreja novament amb el flux principal. D'una banda, aquest efecte produeix pèrdues de pressió i un parell localment negatiu en el rodet. D'altra banda, el flux revertit augmenta localment el flux de massa i restringeix la secció de flux prop del carcassa. Per tant, la càrrega del alabi i la producció de torsió local augmenten prop de l'espai per sobre damunt del alabi. Encara que es va notar un canvi clar en la gràfica de la càrrega de l'etapa en funció del coeficient de flux quan succeeix el flux revers, no es pot notar un impacte clar en l'eficiència. L'anàlisi addicional del flux de fugida de la punta en un ampli rang va mostrar la importància del flux impulsat per fricció i el flux de fugida induït per incidència en una condició fora del disseny. En general, es va observar que les pèrdues per fuites a la punta es van tornar més importants quan la turbina opera lluny del punt de disseny. A més, es va indicar que una correlació comunament utilitzada per a la

caracterització del flux de fugida de la punta no és capaç de reproduir tendències ni quantitats qualitatives quan es va variar l'altura de l'espai de la punta o el punt d'operació.

Finalment, els efectes observats van ser modelats unidimensionalment. Es va desenvolupar un model de pèrdua de fuites a la punta que és capaç de reproduir les tendències trobades i mostra una bona capacitat d'extrapolació. Els resultats van ser validats amb les dades tridimensionals de CFD. A continuació, va ser possible desenvolupar un mètode innovador per a la caracterització del flux de fugida de la punta, que pot modelar el moment i les velocitats del flux de fugida de la punta per diferents alçades de separació de la punta en condicions de disseny i fora de l' disseny. Seguint amb l'anterior, es va desenvolupar un model d'extrapolació unidimensional complet per a mapes d'eficiència de turbines adiabàtiques. Fent ús del model de fugida de puntes recentment desenvolupat i altres troballes de la campanya CFD, es va aconseguir una bona qualitat de extrapolació en termes de velocitat, relació cinemàtica de BSR i obertura de VGT. L'alta qualitat dels resultats es va establir mitjançant la comparació amb la gran quantitat de dades mesurades en primer lloc.

List of Publications

The following publications form the basis of this thesis:

- **J. R. Serrano, A. Tiseira, L. M. García-Cuevas, L. B. Inhestern, H. Tartoussi**. "Radial Turbine Performance Measurement Under Extreme Off-Design Conditions". In: *Energy* 125 (2017), pp. 72-84. [1]
- **J. R. Serrano, L. M. García-Cuevas, L. B. Inhestern, H. Mai, A. Rinaldi**. "Methodology to Evaluate Turbocharger Turbine Performance at High Blade to Jet Speed Ratio Under Quasi Adiabatic Conditions". In: *ASME Turbo Expo 2017, Charlotte NC, USA*. [2]
- **J. R. Serrano, A. Gil, R. Navarro, L. B. Inhestern**. "Extremely Low Mass Flow at High Blade to Jet Speed Ratio in Variable Geometry Radial Turbines and its Influence on the Flow Pattern: A CFD Analysis". In: *ASME Turbo Expo 2017, Charlotte NC, USA*. [3]
- **J. R. Serrano, R. Navarro, L. M. García-Cuevas, L. B. Inhestern**. "Turbocharger Turbine Rotor Tip Leakage Loss and Mass Flow Model Valid up to Extreme Off-Design Conditions with High Blade to Jet Speed Ratio". In: *Energy* 147 (2018), pp. 1299-1310. [4]
- **J. R. Serrano, L. M. García-Cuevas, L. B. Inhestern, S. Guilain, H. Tartoussi**. "Analysis of Unsteady Energy Fluxes in a Turbocharger by Using a Holistic Model Extrapolating Standard Lookup Tables in Full Engine Operating Map". In: *ASME Turbo Expo 2018, Oslo, Norway*. [5]
- **J. R. Serrano, R. Navarro, L. M. García-Cuevas, L. B. Inhestern**. "Method for Non-Dimensional Tip Leakage Flow Characterization in Radial Turbines". In: *ASME Turbo Expo 2018, Oslo, Norway*. [6]
- **J. R. Serrano, F. J. Arnau Martinez, L. M. García-Cuevas, L. B. Inhestern**. "An Innovative Losses Model for Efficiency Map Fitting of Vaneless and Variable Vaned Radial Turbines Extrapolating Towards Extreme Off-Design Conditions". In: *Energy*. Under 2nd revision. [7]
- **J. R. Serrano, R. Navarro, L. M. García-Cuevas, L. B. Inhestern**. "Contribution to Tip Leakage Loss Modeling in Radial Turbines Based on 3D Flow Analysis and 1D Characterization". In: *Heat and Fluid Flow*. Under 2nd revision. [8]
- **L. B. Inhestern, J. Braun, G. Paniagua, J. R. Serrano**. "Design, Optimization, and Analysis of Supersonic Radial Turbines". In: *ASME Turbo Expo 2019, Phoenix AZ, USA*. Accepted for conference and journal publication. [9]

Other Publications

The author of this thesis was also involved in the work of the following article. Work including this publication contributed significantly to the understanding of the heat transfer coupled with complex aerodynamic processes.

- **Z. Liu, L. B. Inhestern, J. Braun, G. Paniagua**. "Unsteady Heat Transfer Assessment of Supersonic Turbines Downstream of a Rotating Detonation Combustor". In: *ASME Turbo Expo 2019, Phoenix AZ, USA*. Accepted for conference publication. [10]

Division of work between authors

The publications [1, 2, 3, 4, 5, 6, 7, 8] have been done in collaboration with other researchers, being the author signatures in order of seniority. First experimental measurements in [1] were executed by L. M. García-Cuevas and the respondent. Following experiments, presented in [2], were realized in collaboration between J. R. Serrano, H. Mai, and A. Rinaldi. The respondent performed numerical campaign, experimental and numerical results post-processing and developed the models presented in these publications. Discussions of results and methodologies were done in collaboration with his supervisor, Dr. José Ramón Serrano Cruz, as well as with the co-authors.

The publications [9, 10] have been done in collaboration with the listed coauthors, being the author signatures in order of contributions. Discussions of results and methodologies were done with the coauthors.

Acknowledgements

It is impossible to properly express all my thanks to the people that contributed directly or indirectly to the writing of this document during the last four years in just a few words. Although it is hard to do this section justice, I will try my best.

My greatest thanks goes to Prof. José Ramón Serrano for his trust, his endless support, and for giving me freedom while guiding me through the last few years. I feel very lucky indeed to have been given the chance to work with him and to receive such great mentoring.

I also need to be thankful to all of my office mates that I have had the pleasure to meet, who I have learned to love and who have become friends for life. I will always remember the immediate and very warm welcome I received over some super chilled beers. Inside and outside of the university I received more support than I could have ever imagined. As well as introducing me to the marvelous Spanish culture I also got taught countless things by people from all over the world.

To all of the friends I have made in the Club de Bádminton San Fernando, thank you for making Valencia feel like home to me and trying to keep me in shape. I say 'trying' because this thesis is the reason why I had to miss so many training sessions.

I cannot be happier that I came to this place and now, reading back through what I am writing it confirms to me that it was one of the best decisions I have made in my life.

I also have to thank all of my friends back home for their patience and loyalty. I am proud to say that it still always feels the same when we get together even when we haven't seen each other for a while.

Finally, I want to express my thanks to my dear brother and my parents, who never got tired to motivate, to assist and to visit me.

"Im Kampf zwischen dir und der Welt,
sekundiere der Welt"
Franz Kafka. 1917-1918.

Contents

List of Figures

List of Tables

Nomenclature

Abbreviations

TE	Trailing Edge
DC	Diameter Correction
ER	Expansion Ratio
ICS	Independent Cooling System
ILS	Independent Lubrication System
BSR	Blade Speed Ratio
CAE	Computer-aided engineering
CFD	Computational Fluid Dynamics
DES	Detached Eddy Simulation
DNS	Direct Numerical SImulation
EGR	Exhaust Gas Recirculation
GDICI	Gasoline Direct Injection Compression Ignition
IGV	Inlet Guide Vane
LES	Large Eddy Simulation
MAE	Mean Average Error
NSE	Navier Stokes Equations
PS	Pressure Side
RANS	Reynolds Averaged Navier Stokes
RDE	Real Driving Emissions
RMSE	Root Mean Square Error
SS	Suction Side
TC	Turbocharger
URANS	Unsteady Reynolds Averaged Navier Stokes
VGT	Variable Geometry Turbocharger
WLTP	Worldwide harmonized Light vehicles Test Procedure

Greek Letters

α	angle in absolute reference frame
β	angle in relative reference frame
ϵ	tip gap height
η	efficiency
γ	blade surface angle, heat capacity ratio

Δ	difference
μ	dynamic viscosity
ω	angular velocity
∂	differential
ϕ	flow coefficient
π	corresponding pressure ratio
ψ	stage loading coefficient
ρ	density
σ	blade speed ratio
τ	engine torque
ε	error

Latin Letters

$\dot{m}$	mass flow
$\dot{Q}$	heat flow
$\dot{W}$	power
dr	radial integrator
A	area
a	fitting constant
b	fitting constant in the exponent
c	velocity in absolute reference frame
C_d	discharge coefficient
c_p	isobaric specific heat capacity
D	diameter
f	substitution value
g	substitution value
g_θ	gravity vector component
h	specific enthalpy
K	fitting constant
l	length
M	momentum
N	rotational speed
P	coordinates point
p	pressure
R	specific gas constant
r	radius
$R_{sub.}$	momentum ratio non-dimensional number
Re	reynolds number
s	specific entropy, standard deviation
$sh.$	shroud
T	temperature
$T\#$	turbine number
u	uncertainty
w	velocity in relative reference frame
Y	loss coefficient
y^+	non-dimensional wall distance
z	blade number

Symbols and Numbers

$'$	section at pivot angle in stator row
$+$	pressure driven tip leakage flow
$-$	friction and incidence driven tip leakage flow
0	turbine inlet section
1	stator passage inlet section
2	stator passage outlet section
3	rotor inlet section
4	rotor outlet section
5	turbine outlet section
$\overline{}$	averaged value
$\perp$	perpendicular flow component

Subscripts

θ	circumferential component
a.	adiabatic condition
ax.	axial component
bl.	blade
CFD	CFD data
comp.	compressor
d.	diabatic condition
eff.	effective
Exp.	experimental value
filt.	filtered
fl.	fluid
geom.	geometry
inc.	incidence
in	inlet section
mech.	mechanical condition
Mod.	model value
m	meridional component
NS	based on Navier Stokes equation
nut	nut
opt.	optimum
out	outlet section
pas.	passage
PS	pressure side
red.	reduced numbers
rot.	rotor
sh.	shroud
SS	suction side
stat.	stator
surf.	surface
s	isentropic condition
tip	value at rotor tip
ts	total to static condition
ts	total-to-static
turb.	turbine

t	total or stagnation condition
Vless	vaneless space
x	x-coordinate
y	y-coordinate
z	axial coordinate

CHAPTER 1

Introduction

Contents

1.1 Background

Turbochargers are taking a bigger role in the worldwide automotive market as a part of downsizing and downspeeding technique. This success is causing the replacement of natural aspired engines by turbocharged ones. Thus, OEMs can offer low marks of fuel consumption in homologation cycles mainly by the reduction of mechanical losses at very low load. This has been achieved due to several factors: the higher average torque at which engines operate; the use of variable valve timing and also, thanks to cooling the boosted air charge, by reducing heat losses in the combustion chamber. With new up-coming CO_2 regulations, so called EU6d [11] and EU7, legislators put more pressure to obtain fuel consumption benefit and depollution efficiency in all driving conditions. WLTP cycle and RDE homologations will play an important role to push forward new technologies. For instance, to reduce fuel consumption, OEMs are studying GDICI like concepts in petrol engines with high rates of EGR and variable valve actuation for Atkinson/Miller cycle combined with higher volumetric compression ratio [12]. To avoid a efficiency drop of catalysts in low load, pre-turbo aftertreatment can be used Luján et al. [13]. Most of these features will have huge impact on the turbocharger behavior. In the meantime, the automotive industry requests more and more efficient processes to design new engines. As regulation and market requests can change rapidly, time to market is a key indicator that leads to change the usual way of developing engines. To shorten the development time, CAE is surely an important tool and especially we need to assess components that have a long duration process such as turbochargers. In a recent past, calculations were done to pre-select 2-3 turbochargers in full load. The final choice was done by tests in every condition. Nowadays, the choice should be done numerically, in every condition (full load, part load, transients, altitude, ...). In traffic conditions, where engines change their speed frequently their mean air consumption changes additionally to the pulsating flow that can be found at the turbocharger turbine inlet. Further complexity is added by acceleration and deceleration of the turbocharger axis [14]. To improve the operating condition according to the mean mass flow, turbochargers with variable guide vanes can be used. However, the turbine still has to operate at extreme off-design conditions up to very high BSRs, very low mass flow, and close zero power outputs due to the transient pulses of the cylinder exhaust gas [15, 16].

Currently engine manufacturers rely during the engine development on fast one-dimensional models like the one by Jensen et al. [17] or commercial programs like GT-Power. These models take advantage of transient one-dimensional sub-models to calculate the dynamics of the flow. Transient turbocharger models for transient computations were presented in [18], [19], and [20] and require complete wide maps as input data.

1.2 Motivation

As highlighted before, pulsating flow plays an important role in turbocharger turbines and makes its optimum design challenging. While the turbine is designed for one-design point, its real working condition is most of the time in off-design. Due to the pulsating flow the instantaneous efficiency underlies huge fluctuations. In Figure 1.1 the standard deviation with:

$$s = \sqrt{\frac{\sum_{i=1}^{N} \left(\eta_{\text{turb.,i}} - \bar{\eta}_{\text{turb.}}\right)^2}{N-1}} \tag{1.1}$$

has been shown to highlight engine map regions where the turbocharger and turbine efficiency pulses are of high magnitude. Here a turbocharged Diesel

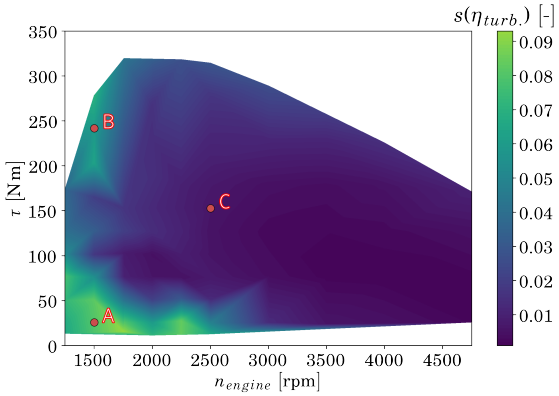

Figure 1.1: Standard deviation of turbine efficiency.

engine with 4 cylinders was simulated using GT-Power coupled with a CMT-Turbocharger model [5]. While the standard deviation is rather small at high engine speeds, logically it increases towards lower engine rpms. Surprisingly, efficiency fluctuations start to increase towards regions of higher engine torque between 1250 and 1750 engine rpm after passing zones of less deviation.

Following, three turbine pulsating flows at different steady engine running conditions are analyzed. First, one running point at 1500 engine rpm, low engine torque, low turbocharger efficiency and low pulse amplitude (A in Figure 1.1). Next, one point at 1500 engine rpm with high efficiency fluctuation (B in Figure 1.1) and finally the point of highest turbocharger efficiency (C in Figure 1.1). Turbine efficiency has been defined considering thermodynamic conditions downstream turbine volute (upstream turbine stator). As the turbine volute is not considered in the adiabatic efficiency definition, the typical thick loops caused by mass accumulation in the volute relative big volume cannot

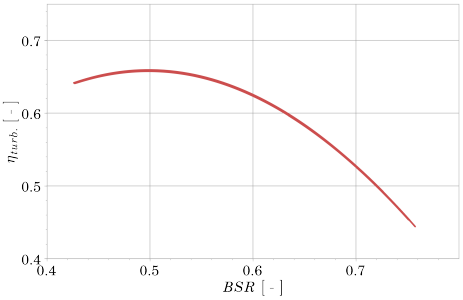

(a) Running point A in Figure 1.1.

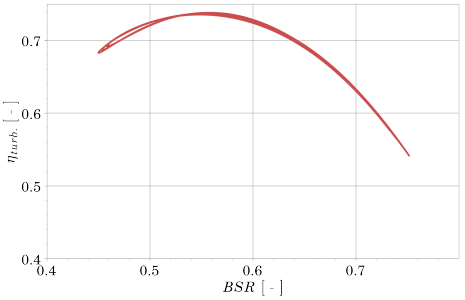

(b) Running point B in Figure 1.1.

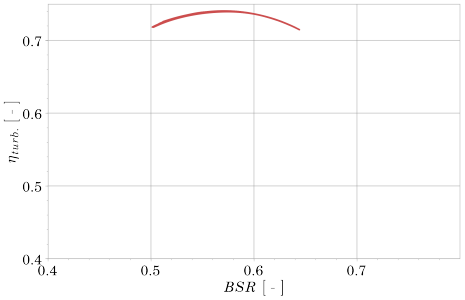

(c) Running point C in Figure 1.1.

Figure 1.2: Efficiency pulses vs. BSR.

be seen in Figure 1.2. As it can be seen in Figure 1.2 (a) efficiency fluctuates between 46 to 66 % over a wide range of BSR when the engine mass flow and rotational speed are low. Here, the turning point of the curve is relatively close to its highest efficiency point. Looking at running point B in Figure 1.2 (b) with higher mass flow it can be seen that the fluctuation is still high, but the efficiency reaches a higher maximum and is operating longer around the highest adiabatic turbine efficiency of 73 %. The chosen running point at highest mean turbocharger efficiency in the engine map, shows much lower fluctuations in BSR and efficiencies due to the higher engine speed. Although peak efficiency in point B is similar to point C, the average value is much higher in C due to lower instantaneous efficiency fluctuations. Efficiency variations, that can be seen in Figure 1.2 (c) are below 3 % and the turbine is working the whole time around its highest efficiency point of the current speed.

Since the turbine power is of main interest and not only depends on the turbine efficiency but also on mass flow, inlet temperature and pressure pulses, it has been shown against the adiabatic turbine efficiency in Figure 1.3 (a) for

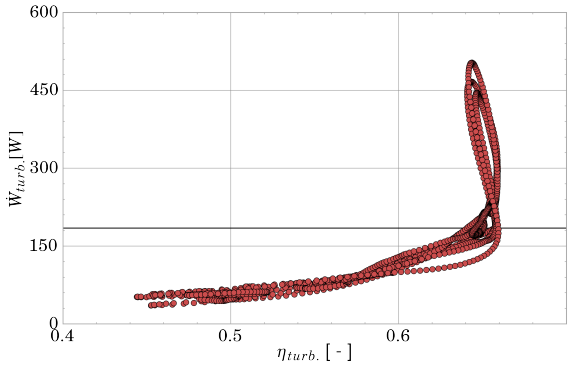

(a) Turbine power vs. turbine efficiency.

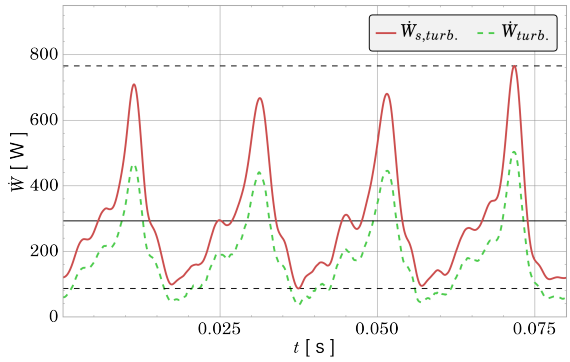

(b) Isentropic turbine power (red) & turbine power (green) vs. time.

Figure 1.3: Pulses over one cycle in engine running point A of Figure 1.1.

running point A (The mean value of the turbine power is shown by a horizontal line). Here, it can be seen that the curve has two main characteristics. In the peak of the pulse the turbine operates with highest efficiency and produces the highest turbine power. During the peak, the curve moves upwards in vertical direction. As second characteristic, a relatively horizontal part of the curve can be identified. While the efficiency experiences its biggest change, the turbine power changes less than in the first characterized part peak power. This highlights the main importance of pressure, mass flow, and temperature pulses for turbine power. Since the isentropic turbine power $\dot{W}_{\mathrm{s,turb.}}$ with:

$$\dot{W}_{\mathrm{s,turb.}} = \dot{m}_{\mathrm{turb.}} \cdot c_p \cdot T_{\mathrm{t,in}} \cdot \left[1 - \left(\frac{1}{\pi_{\mathrm{turb.}}} \right)^{\frac{\gamma-1}{\gamma}} \right] \tag{1.2}$$

combines all mentioned pulses of gas numbers it has been shown against the time in Figure 1.3 (b). For this running point A the peaks of each pulse are reached by a sudden increase of $\dot{W}_{\mathrm{s,turb.}}$ and maintains only over a short time. This is the reason why the averaged turbine power $\dot{W}_{\mathrm{turb.}}$ in Figure 1.3 (a) is low compared to the mean value of minimum and maximum, although the adiabatic efficiency is higher during the peak of the pulse. This indicates, that an efficiency optimization for peak isentropic power condition is not the best procedure.

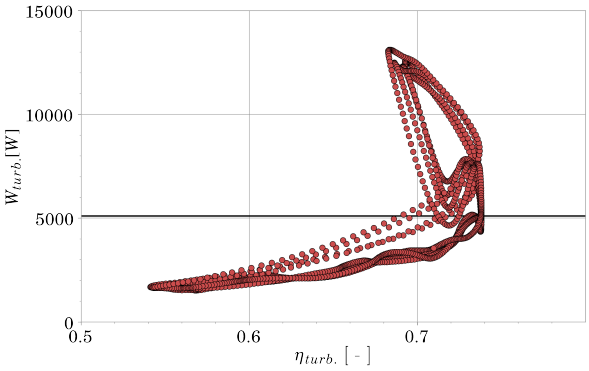

(a) Turbine power vs. turbine efficiency.

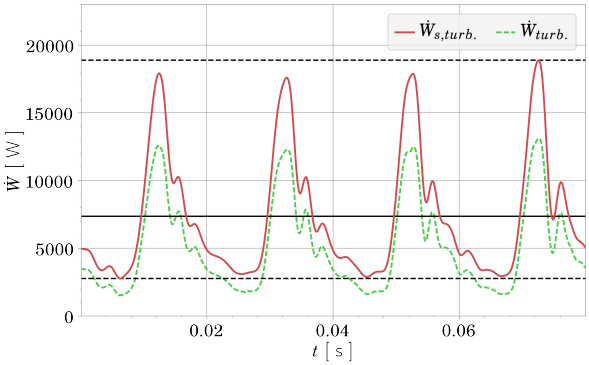

(b) Isentropic turbine power (red) & turbine power (green) vs. time.

Figure 1.4: Pulses over one cycle in engine running point B of Figure 1.1.

Also, in running point B, shown in Figure 1.4, are the aforementioned regions of vertical and horizontal movement of $\dot{W}_{\mathrm{turb.}}$ visible. This confirms that the main impact on turbine power is the isentropic turbine power. Further, the mean value is again relatively close to the horizontal zone. Thus, more

isentropic energy has been converted into mechanical power over the time while the efficiency is not at its maximum value. Also, in this running point the peak times of isentropic turbine power is short, as it can be seen in Figure 1.4 (b). This shows again the importance of low isentropic power zones for potential turbine design in common engine running conditions.

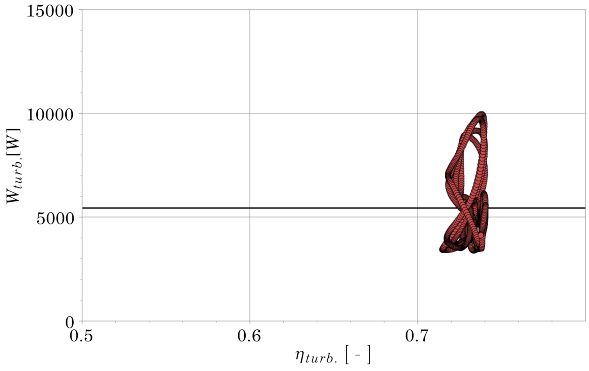

(a) Turbine power vs. turbine efficiency.

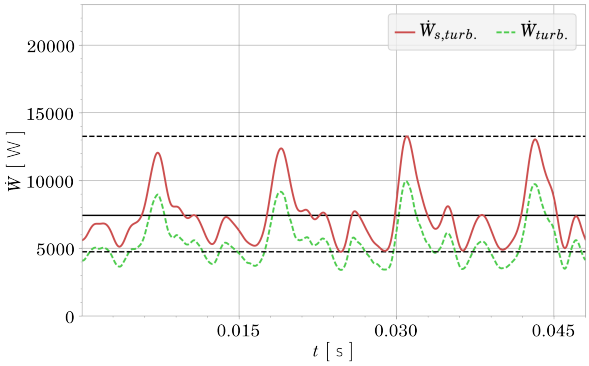

(b) Isentropic turbine power (red) & turbine power (green) vs. time.

Figure 1.5: Pulses over one cycle in engine running point C of Figure 1.1.

Since the turbine efficiency does not vary so much in point C, the horizontal zone cannot be identified in Figure 1.5 (b). However, the mean turbine power is close to the lower region of the curve. The reason for that is again the short peak time, which is even more distinctive in this running point, as it can be seen in Figure 1.5. Comparing Figure 1.4 and Figure 1.5 can be seen how in spite point B has both higher peak power and isentropic power the average efficiency and

average power are lower than in point C. Again, this highlights the importance of efficiency optimization out of peak power conditions.

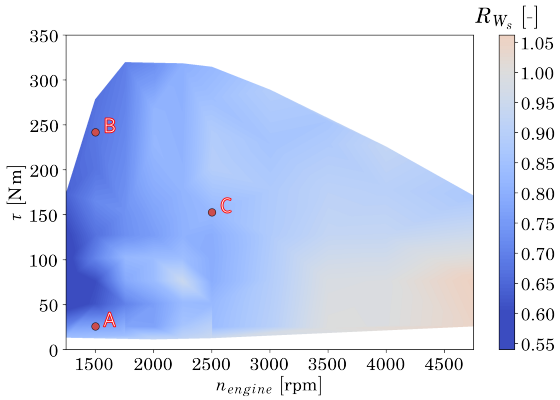

Figure 1.6: Isentropic power ratio according to Equation 1.3.

To evaluate the importance of isentropic energy in valley and peak on its mean value for each simulated running point the following number has been formulated:

$$R_{\dot{W}_s} = \frac{\text{avg.}(\dot{W}_{\text{s,turb.}})_{\text{cycle}}}{\frac{min(\dot{W}_{\text{s,turb.}}) + max(\dot{W}_{\text{s,turb.}})}{2}}. \tag{1.3}$$

For values higher than 1 the main isentropic power is considered to be in the peak of the pulse, while values lower than 1 indicate decreasing importance of the isentropic energy during a pulse peak. As it can be seen in Figure 1.6 the impact of peak isentropic energy is low for the biggest parts of the engine map. Thus, energy rich pulses only last for a short time and pulse valleys gain importance. Especially at lower speeds the ratio $R_{\dot{W}_s}$ decreases, since peaks are relatively high but only for a short time. In a region from 50 N m up to 150 N m and an engine speed up to 1750 rpm the number $R_{\dot{W}_s}$ shows values well below 0.6. This can indicate that big parts of the energy is below peak pulse power, what can be considered as off-design conditions. Again, this is highlighting the big importance of pulse valleys when extracting efficiently the energy from the engine exhaust gases. $R_{\dot{W}_s}$ values in the range of 0.6 to 0.7 can be detected in low end torque area (below 1750 rpm and between 200 N m and 300 N m) this is fundamental area for engine acceleration. Here, turbocharger efficiency increments at off-design conditions will have a substantial contribution for increasing engine efficiency and reducing turbocharger lag during tip in accelerations. Furthermore, the precise prediction of the off-design efficiency becomes necessary for the engine design process.

1.3 Objectives

The main objective of this thesis is to supply turbocharger radial turbine performance data in extreme off-design conditions and to improve the aerodynamic understanding in this condition. In the end, it will be possible to achieve this objective by experimental measurements, CFD simulations, and by applying a novel efficiency extrapolation model on narrow maps. It is intended to develop easy and industrial applicable procedures. Furthermore, an overall picture of extreme off-design aerodynamics will be drawn.

1.4 Methodology

As Figure 1.7 shows, the work of this thesis can be separated into three main parts: The experimental campaign, the numerical analysis of three-dimensional flow, and the one-dimensional modeling of tip leakage losses and the overall turbine performance. The achievement of experimental data in a wide range is

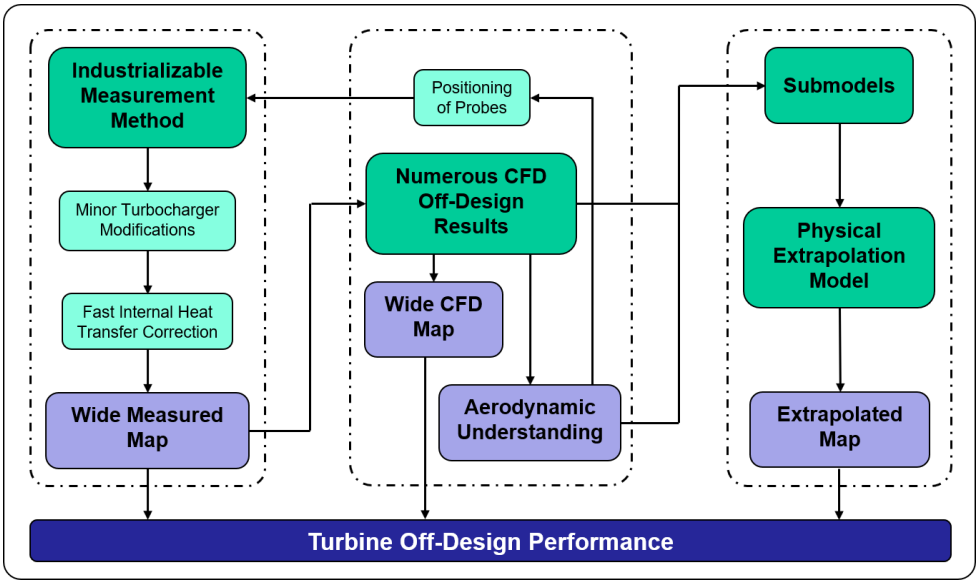

Figure 1.7: Methodology and thesis structure.

fundamental for the data validation of obtained CFD results and model extrapolation results. Thus, the development of an industrial applicable measurement procedure for extreme off-design points is developed first. Two experiments were performed to achieve this goal: one experiment in a CMT turbocharger test bench in Valencia to develop the general procedure and a second at CRITT M2A in Villebon sur Yvette, France using a test facility of KRATZER AUTOMATION

to prove repetitiveness and to develop easy to use and suited monitoring strategies. In line with this, a simple to use model for the correction of internal heat transfer was developed.

Following, the knowledge of the internal flow pattern and secondary flow effects in these running conditions was supplied with validated CFD data from the first experiments. A high number of CFD simulations with steady boundary conditions (in RANS and URANS) was performed by means of the commercial CFD solver STAR-CCM+ from Siemens. The won 3D flow data helped to design and validate aerodynamic submodels and to characterize tip leakage flow with a high level of detail.

Finally, the newly designed sub-model for tip leakage flow and knowledge of the secondary flow field allows to design a robust one-dimensional efficiency extrapolation model with a low number of coefficients. The model was developed and programmed using the commercial MATLAB code by MathWorks.

CHAPTER 2

State of the Art

Contents

2.1 Turbine Performance Data

The performance characteristics of a turbine are typically documented by means of a mass flow map and an efficiency map. To guarantee a characterization which is mostly independent from the aerodynamic boundary conditions during the experiment as temperature and pressure, reduced numbers are used. These reduced numbers as reduced massflow or reduced speed result from Mach similitude in meridional or circumferential direction respectively. For the reduced massflow follows:

$$\dot{m}_{\text{red.}} = \frac{\dot{m}\sqrt{T_{\text{t,0}}}}{p_{\text{t,0}}} \tag{2.1}$$

and for the reduced speed:

$$N_{\text{red.}} = \frac{N}{\sqrt{T_{\text{t,0}}}}. \tag{2.2}$$

Thus, it is assumed that these adiabatic performance maps are the same when they are measured under same reduced conditions when measured under adiabatic or quasi-adiabatic conditions. The efficiency is mostly defined as the work done by the fluid, devided by the flow potential in an isentropic nozzle. Since the flow potential is defined by the total-to-static pressure ratio as:

$$\pi_{\text{turb.}} = \frac{p_{\text{t,0}}}{p_{\text{s,out}}} \tag{2.3}$$

the calculated efficiency is called total-to-static efficiency with (in steady flow):

$$\eta_{\text{ts}} = \frac{\dot{W}}{\dot{W}_{\text{s}}} = \frac{T_{\text{t,0}} - T_{\text{t,out}}}{T_{\text{t,0}}\left(1 - \left(\frac{1}{\pi_{\text{turb.}}}\right)^{\left(\frac{\gamma-1}{\gamma}\right)}\right)} \tag{2.4}$$

The efficiency is typically plotted against either the total-to-static pressure ratio or the blade-to-jet-speed ratio (BSR), which is the ratio of the blade tip speed and the isentropic velocity of an nozzle with:

$$\sigma_{\text{turb.}} = \frac{\omega r_{\text{in}}}{\sqrt{2\bar{c}_{\text{p}} T_{\text{t,0}}\left(1 - \left(\frac{1}{\pi_{\text{turb.}}}\right)^{\left(\frac{\gamma-1}{\gamma}\right)}\right)}} \tag{2.5}$$

Typically maps are obtained with several measurements at one constant reduced speed to achieve the characteristic of one "speedline". This is done for different speedlines to cover different possible operating conditions. For VGT turbines these kind of maps are measured for several rack positions, since the turbine performance characteristic changes drastically when the stator angle changes.

2.2 Radial Turbine Aerodynamics

The adiabatic efficiency and the mass flow are the result of complex aero-thermodynamics. The aerodynamics of radial turbines are governed by loss generating vortex structures.

In the case of a radial VGT turbine similar secondary flow structures to the ones in axial turbines where identified in the stator passage by Simpson et al. [21] and Marsen and Moreau [22]. Thus, horseshoe vortex, passage vortex, tip leakage vortex, and a vane wake are dominating the flow field. Additionally, Simpson et al. [21] identified two counter rotating vortexes, which have their origin in the stator upstream geometry. Results by Marsen and Moreau [22] show a high acceleration from low flow velocities in the volute to very high velocities in the stator throat due to the radial design. This high velocities also increase friction losses. All these flow phenomena contribute to the losses of turbines. Furthermore, mainly vane tip leakage vortex and vane wake cause rotor-stator interaction, which is responsible for noise generation in radial turbines [22]. For one design point it has been stated that vaneless radial turbines can even have a favorable performance [21]. However, the flexibility of VGT turbines to expand the operative range of the turbine is highly desired for varying engine running conditions.

Baines [23] concluded the overall flow effects in the rotor wheel. The main difference between radial inflow turbines and axial turbines occurs in the inflow section of the wheel due to acting Coriolis forces with $-2(wx\omega)$. Thus, when the fluid is flowing inwards a force in counter direction to the wheel rotation acts on the flow. This force in combination with the pressure gradient between pressure side and suction side can cause flow separations and shifts the optimum incidence angle towards high negative values in the range of -20 to $-40°$. Due to the radial to axial change of the meridional flow direction, an additional vortex appears, which moves fluid along the pressure side from hub to shroud. It was reported that this vortex increases its strength with reducing inlet-to-exit tip radius ratio. Following, this vortex is expected to be of high importance in small turbocharger turbines.

According to Marson and Moreau [22] and Baines [23] the outlet region is dominated by passage vortex and the tip leakage vortex as they can be found in axial turbines as well. Murugan et al. [24] focused on the analysis of the outlet section on the turbine passage. A region of high losses close to the shroud was identified. This region has its origin in tip leakage flow and mixing of the tip leakage vortex with the blade wake. It was reported that the impact of this characteristic loss region increases operating more and more in off-design.

Due to the increasing research effort in the measurement of extended turbine maps and in the extrapolation towards low mass flow regions of turbine maps, these zones become also aerodynamically interesting. While extreme off-design

conditions, where the radial turbine works at low BSR and under very high positive incidence, have been analyzed by Walkingshaw et al. [25], common investigations of radial turbines working at high BSR like the one by Sauret and Gu [26] do not cover conditions where turbines produce close to zero or negative power output. Hence, the flow field is widely undiscovered in these conditions.

2.3 Measurements in Off-Design Condition

Traditionally turbocharger turbine maps are measured under stationary flow conditions [27]. Due to the energy equilibrium of turbine power, compressor power, bearing losses and heat losses, the compressor power consumption has to be low for measurements at very low turbine power outputs, which can cause compressor surge. At the same time the turbine experiences a limitation due to the highest possible compressor braking power, which is affected by compressor choking. Thus, measured turbocharger turbine maps are naturally restricted to a narrow range of BSRs. This drives the issue that turbocharger maps given by suppliers are measured in conditions quite far from those we have in a wide range and transient engine operation.

In past publications by Romagnoli et al. [28], De Bellis et al. [29] and Smiljanovski et al. [30] the potential of an electrical brake instead of a compressor wheel, like depicted by Figure 2.1, as a power consuming part is pointed out. With the use of a brake, the consumed power can be reduced down to zero. At

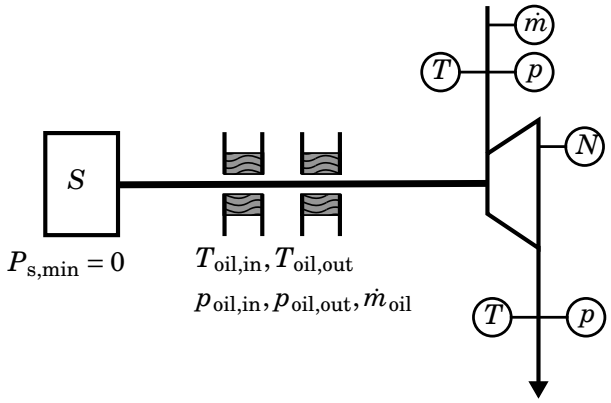

Figure 2.1: Sketch of a turbocharger with electrical brake [30].

this specific running point the turbine still produces power to overcome the bearing losses. Thereby, this method for achieving low turbine efficiencies is

restricted to the zero mechanical efficiency point; where the turbine, especially at high speed, produces power outputs much bigger than zero. Reversible brakes could be used for pushing the limit to even lower measurable turbine power, even though this procedure is just eligible for lower rotational speed due to arising balancing issues as shown by Deligant et al. [31], when increasing the rotational speed. An electrically assisted turbocharger has successfully been tested with extremely low and even negative mass flows by Terdich [32] also for higher speeds. For the testing of common turbochargers a modification towards

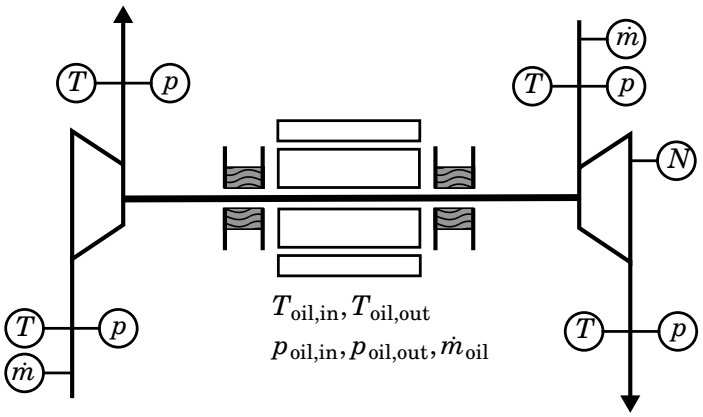

Figure 2.2: Sketch of a electrical assisted turbocharger.

an electrically assisted assembly is not feasible, as the thermal characterization changes and the effort is remarkable. Salameh et al. [33] have force fed the compressor wheel with high pressurized air in the outlet to run the compressor as a turbine, supporting the turbocharger shaft with power to maintain the rotational speed when the turbine generates low power. In a next step, to realize tests at low turbine power, the compressor wheel was replaced with an especially designed turbine wheel as shown in Figure 2.3 and blew pressurized air at the compressor outlet in the opposite flow direction [33]. Also, by means of this method up to negative mass flows in the turbine were measurable. Also the procedure by Salameh et al. [33] requires high and expensive modifications on the turbocharger. Therefore, this testing method is not suitable for industrial applications.

Instead of using low mass flows on the compressor side, the compressor could be fed by pressurized high mass flow rates in traditional flow direction making the compressor working at pressure ratios lower than one. When the mass flow can be increased enough, the compressor is able to act as a centrifugal turbine and to produce the necessary power to overcome the bearing losses. Hence,

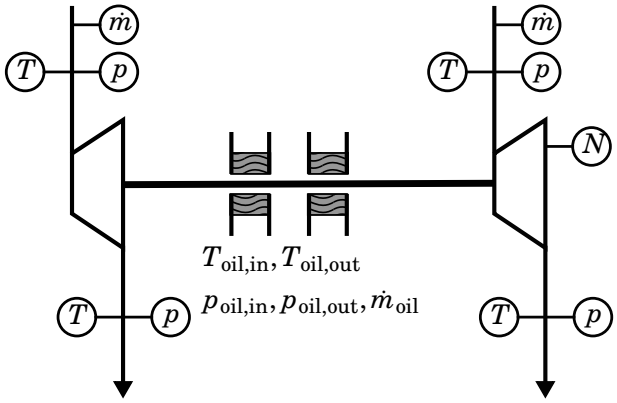

Figure 2.3: Sketch of a turbocharger, where the compressor wheel is replaced by a turbine wheel.

measurements at zero turbine power output and thus, at zero efficiency might be achievable.

Measurements of radial compressors at pressure ratios lower than one can rarely be found in the literature. Pucher [34] fed the turbocharger by means of an additional compressor upstream of the turbo compressor to expand the achievable mass flow range of the turbo compressor. Leufén and Eriksson [35] were able to measure non-modified radial compressors at pressure ratios lower than one with a similar test bench by supplying a compressor inlet pressure of up to two bar for low rotational speeds. Since the compressor consumes higher mass flows when reaching pressure ratios lower than one with increasing speed, the power of the pressurizing facility is the limiting factor. Also, at very high speeds the choking mass flow will be reached before arriving to the map region of gas expansion. Wallace et al. [36] and Najjar and Akeel [37] showed that the compressor map can be expanded significantly by introducing a swirl component in the compressor inlet, what can result in later choking of the compressor wheel in the zone of compression ratios higher than one. Furthermore, Müller et al. [38] have used a circumferential loading by introducing a swirled inlet flow at the blade tip to allow the compressor to run as a centrifugal turbine. However, it requires significant changes of the casing geometry.

Additionally, it is difficult to compare maps from different suppliers because they consider different boundary conditions, which can affects the internal and external heat transfer. Like shown by Serrano et al. [39, 40] and Schinnerl et al. [41] heat fluxes influence in particular the efficiency of small sized geometries. Furthermore, even when measuring under quasi-adiabatic conditions internal

heat transfer must be considered when the turbine power output is low or close to zero [42]. Hence, these have to be computed additionally after or during the experiment to supply reliable data. This can be done as shown by Sirakov and Casey [43], Zimmermann et al. [44], or Serrano et al. [45]. By means of gained thermal measurements heat flux models can be considered to transform regular turbine maps into the needed adiabatic maps. A method to obtain the complex system of internal heat fluxes, which occurs in turbocharger geometries, during experiments has been proposed by Serrano et al. [39, 46]. The model is graphically illustrated in Figure 2.4.

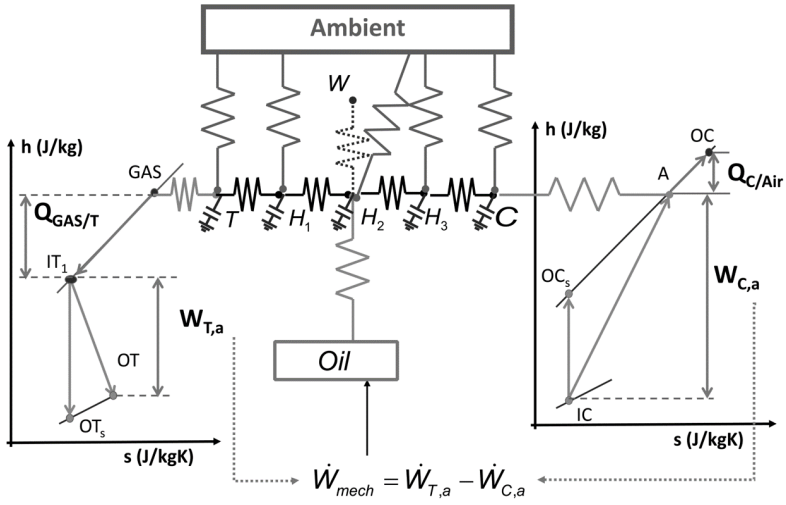

Figure 2.4: Lumped heat transfer model [45].

Each node of T, H_1, H_2, H_3, and C represents a measured metal temperature. 15 thermocouples have been placed in these five different planes of the turbocharger. The internal conductances can be obtained in a different testing campaign or general correlations can be used. The external heat flow has been computed by measuring the temperature of the thermal insulation skin at the turbocharger and inlet and outlet ducts, as well as the ambient temperature and air speed. By means of these measurements, the measured gas temperatures, oil temperatures, ambient temperature, the heat transfer to the shown connections can be estimated. Following the diabatic efficiency can be corrected to obtain the adiabatic efficiency. The mass flow can be considered to be not affected by heat transfer.

2.4 1D Radial Turbine Modeling

Since measurement methods for extended maps have not reached an industrial applicability, extrapolation models have to be used to obtain data in unmeasured regions (high BSR/ high speeds) of the map and can be used to verify measured data in running conditions with high measurement uncertainty (high BSR/ low speeds). In the recent past a lot of effort has been done to model the turbocharger performance with mathematical models and to extrapolate the turbocharger maps mainly in terms of high BSRs. These models can appear in a form of empirical models, semi-empirical models, or physically based mean line models. While empirical models try to correlate the efficiency and reduced mass flow directly with correlations, semi-empirical models break the efficiency down to global physical numbers, which are then correlated. Following, mean line models classify different sections of the turbine to calculate flow angles and define losses by means of sub-models to finally be able to calculate the needed gas number for the efficiency calculation.

When the efficiency is plotted against the BSR, the efficiency curves for iso-speedlines look alike parabolic curves. Hence, models that correlate the efficiency with simple parabolic curves dependent on the BSR are commonly found in the industry [47]. Eriksson [48] formulates this relationship with a simple empirical model:

$$\eta_{ts} = \eta_{ts,max}\left(1 - a(\sigma - \sigma_{max})^2\right) \tag{2.6}$$

where a is a fitting coefficient. However, this model can only be applied for single speedlines. Thus, a extrapolation or model interpolation between different speeds is not possible. Furthermore, it can only be taken advantage of the data of one speedline for the model fitting, which reduces the model reliability.

Other models like the one by Orkisz and Stawarz [49] solve this problem and include an additional link with the reduced speed:

$$\eta_{ts} = a_0 + a_1 N_{red.} + a_2 N_{red.}^2 + a_3 N_{red.}\pi_{turb.} + a_4 \pi_{turb.} + a_5 \pi_{turb.}^2. \tag{2.7}$$

The addition of various trends can increase the number of data that can be fitted but also bears the risk of overestimating trends, which are not important far away from the fitted data and increases the number of fitting coefficients.

Following Fang and Xu [50] propose a model, which takes advantage of physical relations combined with empirical trends:

$$\eta_{ts} = a_0 + \frac{\ln \pi_{turb.}}{\pi_{turb.}^{\frac{\gamma-1}{\gamma}} - 1}\left(a_1 + a_2\sigma + a_3\sigma^2\right) \tag{2.8}$$

By doing this the number of coefficients was reduced and the fitting quality of the data was improved. Thus enhancing physical relations seem to be a good way to improve model reliability and stiffness.

Semi-empirical models like the one by Martins et al. [51] or by Serrano et al. [52] start with the formulation of the efficiency taking advantage of Euler´s turbomachinery equation:

$$\eta_{\mathrm{ts}} = \frac{\omega\left(R_1 c_{\theta,1} - R_2 c_{\theta,2}\right)}{c_{\mathrm{p}} T_{\mathrm{t},0}\left(1 - \left(\frac{1}{\pi_{\mathrm{turb.}}}\right)^{\left(\frac{\gamma-1}{\gamma}\right)}\right)}. \tag{2.9}$$

Apart from further physical modeling of the rotor inlet velocity and outlet velocity Serrano et al. [52] achieved a fitting in good quality by introducing a correction factor for the rotor inlet velocity:

$$z = -(a_0 N_{\mathrm{red.}} + a_1)\sigma + a_2 N_{\mathrm{red.}} + a_3 VGT + a_4 VGT^2 + a_5 \tag{2.10}$$

This model is able to fit the entire efficiency maps of several VGT positions with one set of coefficients. Hence, it increases significantly the amount of data that can be used to characterize the turbine performance. A high degree of modeled physics adds further reliability in the extrapolated data of this semi-empirical model.

To increase the reliability even more mean line models might be needed. In numerous works the gas numbers in turbine inlet and outlet were calculated by following the flow path and simplifying the complex three dimensional flow to one-dimensional flow [53, 54, 28, 29, 55]. In those models each section as volute, stator, vane less space, rotor, and outlet are individually modeled and several pressure or enthalpy loss models are used. This way the path trough the one-dimensional T-s diagram can be followed as it is shown in Figure 2.5. Typically, some of the used loss models own fitting parameters which grant the ability to fit the model towards experimental measurements. It is worth highlighting that as more physical sub-models are included the number of fitting coefficients usually rises. Also, the amount of needed geometrical details increases.

In the past, a high number of sub-models for radial turbines has been published. One of the most commonly used one is e.g. the passage loss model, which sums up the aforementioned loss phenomena in the rotor passage in a simple correlation depending on the kinetic energy in passage inlet and outlet [57]:

$$\Delta h_{\mathrm{pass,loss}} = K \frac{\left[\cos\left(i - \beta_{\mathrm{opt,in}}\right) w_{\mathrm{in}}\right]^2 + w_{\mathrm{out}}^2}{2} \tag{2.11}$$

An overview and evaluation of various other loss models is given by Suhrmann et al. [58] and Meroni et al. [59].

Concluding, to reproduce the physics of a turbine by means of a simple one dimensional model as much data as available should be used for the model fitting. In the case of a VGT, data of each VGT position can add valuable

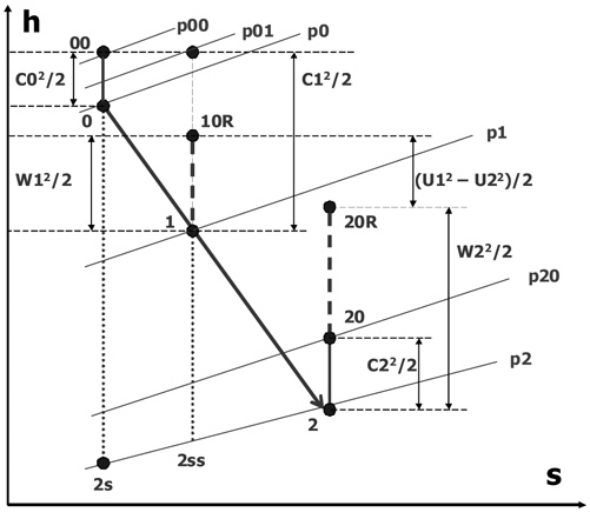

Figure 2.5: Total enthalpy change and losses in a turbine [56].

information. To fit the physical behavior of the turbine, all data should be used for the fitting with one set of parameters, although the geometry is changing. Thus, taking advantage of the available data of different VGT positions allows to fit the physics of the rotor aerodynamic in a broader range. However, the losses in the stator passage and the vaneless space have to be able to reproduce the physical trends of these systems.

One risk in one-dimensional modeling and the fitting of model parameters is the overestimation of rather small and unimportant aerodynamic effects. Thus, adding increasing numbers of submodels with including fitting parameters simplifies the curve fit of the given data but also might misjudge the extrapolated zones of the map. Hence, an equilibrium of the degree of detail and simplicity is from high importance. Furthermore, a growing number of fitting coefficients requires an increasing number of data points. Hence, it should be tried to reach low numbers of variable parameters.

Due to the small geometry of passenger car engine turbocharger, the heat transfer affects significantly the efficiency of the turbine and compressor. Therefore, the required models have to take heat flux into account or the maps have to be adiabatized before extrapolating the maps. By using the aforementioned procedures maps can be adiabatized so that a simply adiabatic turbine model can be used for map extrapolation.

2.5 1D Tip Leakage Modeling

Physical one-dimensional extrapolation models often rely on sub-models to estimate losses like passage or tip leakage losses.

For axial turbines it can be assumed, that tip leakage losses are responsible for one third of the aerodynamic losses [60]. However, Wallace [61] mentioned that typical radial turbomachinery tip losses are by one third smaller than for axial machines of similar size. Reason for this could be the compensation effect of shroud friction and blade loading, which is naturally high in the axial tip gap in the inducer section of radial turbines [62]. Even though the tip leakage losses are one of the main loss sources in radial turbines.

Due to the typically small size of turbocharger radial turbines, they have rather high blade tip gap to blade tip radius ratios. Also the radial inducer section and thus the axial tip gap is barely existing in current turbocharger turbine designs. All this makes especially the turbocharger turbine efficiency prone to tip leakage losses as confirmed by Kammeyer et al. [63]. Hence, the modeling of the losses and a detailed knowledge of the main physical effects are of high interest for one-dimensional modeling and turbine design. Due to the aforementioned off-design operation of the turbine, models valid over a wide range of operating conditions, from low pressure ratios to high pressure ratios and from low rotational speed to high rotational speed, are in demand. Several one-dimensional submodels predicting tip leakage losses have been published yet.

In general it can be assumed that the flow passing through the tip gap does no work and is proportional to the ratio of tip gap height and passage height. In the 1960s a simple correlation for modeling the tip leakage losses of radial turbines was commonly used:

$$Y = K \frac{\Delta r}{r_{\text{tip}} - r_{\text{hub}}}. \tag{2.12}$$

In the literature values for K vary in a wide range from 0.1 mentioned by Krylov and Spunde [64] up to 0.3 and even 1 [65].

Later in 1976, Glassman [66] proposed a slightly refined variation of this sub-model for tip leakage losses.

$$Y = \frac{\Delta r_{\text{out}}}{D_{\text{out}}} \frac{2}{1 - \frac{r_{\text{hub,out}}}{r_{\text{tip,out}}}} \tag{2.13}$$

As it can be seen in Equation 2.13, the loss correlation is still a strict formulation dependent on geometrical parameters.

It can be observed that authors like Yaras and Sjolander [67] modeled the tip clearance flow in axial turbines depending on the in orthogonal direction

passing leakage kinetic energy.

$$Y = K \frac{l_{\text{tip}} \cdot \int 0.5 \cdot \rho \cdot w_{\perp,\text{tip}} \cdot w_{\perp,\text{tip}}^2 \, \mathrm{d}r}{\dot{m}_{\text{turb.}} \cdot \Delta h_0} \tag{2.14}$$

Equation 2.14 for the tip loss coefficient Y is widely used in the literature to correlate the relative tip velocity w with produced losses. The unknown velocities are modeled by assuming discharged flow along the pressure gradient between pressure side and suction side according to Bernoulli:

$$w_{\perp,\text{tip}} = \sqrt{\frac{2\Delta p_{(\text{PS,SS})}}{\rho}} \tag{2.15}$$

This way the operating condition of one particular running point is considered.

Similarly, Spraker [68] related the tip leakage losses of radial turbines with the clearance mass flow fraction and the kinetic energy passing through the gap:

$$Y = \frac{1}{2} \frac{\dot{m}_c}{\dot{m}} U_{\text{out}}^2, \tag{2.16}$$

while the tip leakage flow velocity was here assumed to be equal to the rotational speed and the leakage mass flow was estimated as:

$$\dot{m}_c = K \frac{1}{2} \rho U \epsilon_{\text{r}} L N_{\text{r}}. \tag{2.17}$$

Here K was experimentally evaluated as 1.5. Following, Baines [53, 69] took advantage of the observation by Dambach et al. [62] separating the tip leakage flow in different zones to refine this correlation. The model was fitted with three discharge coefficients for the different zones towards experimental data:

$$\begin{aligned} Y &= \frac{U_4^3 Z_{\text{r}}}{8\pi} \left(K_{\text{x}} \epsilon_{\text{x}} C_{\text{x}} + K_{\text{r}} \epsilon_{\text{r}} C_{\text{r}} + K_{\text{xr}} \sqrt{\epsilon_{\text{x}} \epsilon_{\text{r}} C_{\text{x}} C_{\text{r}}} \right) \\ \text{with:} \quad C_{\text{x}} &= \frac{1 - (r_{5\text{t}}/r_4)}{C_{\text{m4}} b_4} \quad \text{and} \quad C_{\text{r}} = \left(\frac{r_{5\text{t}}}{r_4} \right) \frac{z - b_4}{C_{\text{m5}} \bar{r}_5 b_5} \end{aligned} \tag{2.18}$$

The discharge coefficients were estimated to $K_{\text{x}} = 0.4$, $K_{\text{r}} = 0.75$, $K_{\text{xr}} = -0.3$. Although this model is one of the most advanced models for radial tip leakage losses and commonly used in turbocharger extrapolation models and mean line modeling, it only considers geometric details and rotational speed. Hence, conditions in off design might not be modeled in the right way. Furthermore, modeled physical effects are orientated to rather traditional radial turbines with big size and with significant axial tip clearance.

Also empirical approximations that have been introduced by Wallace [61] and later generalized and suited for turbocharger turbines by Kammeyer et al.

[63, 70] to:

$$\Delta\eta_{\mathrm{TC}} = 40.216\frac{[mm]}{D_{\mathrm{in}}^{0.56}}\left[1.65\left(\frac{N}{N_{\mathrm{des.}}}\right) - 0.65\left(\frac{N}{N_{\mathrm{des.}}}\right)^2\right] \tag{2.19}$$

are mainly dependent on geometrical details and the rotational speed and thus, mainly suited for close to design operation.

Dambach et. al [62] states that the tip leakage flow can mainly be characterized with the mass and momentum passing through the tip gap. Dambach et. al [62, 71, 72] also highlighted the importance of pressure driven tip leakage flow and friction driven tip leakage flow, which is oriented in opposing direction. He also showed experimentally that the ratio of chordwise positive and negative momentum behaves qualitatively as the specific tip loss coefficient shown in Equation 2.14 over the chord length [62]. Thus, it has been recommended to formulate the momentum ratio of both leakage flows for characterizing the tip flow as:

$$R = \frac{M_{\mathrm{tip},+}}{M_{\mathrm{tip},-}} = \frac{\Delta p_{(\mathrm{PS,SS})}}{\rho\omega^2 r_{\mathrm{sh.}}^2 \cos\gamma^2}. \tag{2.20}$$

Here, the only needed fluid number is the surface pressure difference between SS and PS close to the wall, which makes this number easy to use. However, this rather simple correlation does not own geometrical information, so that important tendencies might be unresolved. The consistent modeling of the reciprocal effect of opposing flow patterns in the tip region over wide range of speeds and blade loadings can be challenging.

The dragged tip leakage flow should not be neglected in the radial turbine observation. At off-design conditions with low mass flow and low blade loading the dragged flow through the tip clearance is expected to play an even bigger role as pointed out by Deng et al. [73]. This role could be more extended by the typically high turbocharger rotational speeds. Thus, the tip loss model can be considered as very important to achieve good extrapolation results towards off-design conditions.

2.6 CFD Modeling in Small Radial Turbomachinery

To analyze the three dimensional flow in small radial turbomachinery, CFD modeling can be a useful tool. CFD models mainly consist of the Navier Stokes Equations (NSE), which are solved in discretized volume segments of the simulated domain. The discretization of the domain is done by meshing strategies. Usually it can be distinguished between structured and unstructured meshing. To obtain high numerical stability and accurate prediction of the flow meshed cells should be aligned to the flow. Mendonça et al. [74] states high solution quality for turbomachinery applications when unstructured meshes are used.

Furthermore, the cell density influences the degree of detail that can be resolved but at the same time the computational costs. If no turbulence model is used, the cells need to be of the dimension of the Kolmogorov length scale, where the turbulent vortexes dissipate. This CFD approach is called Direct Numerical Simulations (DNS) and has extremely high computational costs. The computational costs can be reduced by modeling the turbulence on different levels. Large Eddy Simulations (LES) [75] require meshes that resolve the bigger turbulent vortexes. Smaller turbulent structures are modeled. To be able to use even coarser meshes, the entire turbulence spectrum can be modeled. Therefore, the NSE are time averaged over the turbulent timescale. Turbulent variations from the averaged value are called Reynolds stresses and can be modeled. Calculations with this set of equations can be found as Unsteady Reynolds Averaged Navier Stokes (URANS) simulations in the literature. The turbulence closure is often achieved by two-equation models, which can widely be found in industry and investigation. The most important two-equation models can be named as $k-\epsilon$ model [76], modeling the turbulent kinetic energy k and the turbulent dissipation rate ϵ, and the $k-\omega$ model [77, 78], also modeling the turbulent kinetic energy transport and the specific dissipation rate ω. While the $k-\epsilon$ model is known for having a good accuracy in the far field, the $k-\omega$ model shows high accuracy close to the wall regions. Hence, Menter [79] proposed his Shear Stress Transport (SST) model blending the $k-\epsilon$ and the $k-\omega$ model between both regions. This model has become the most used model in radial turbomachinery and is widely validated to reproduce the flow turbulence in good quality [80, 21]. Also the hybrid technique of Detached Eddy Simulations (DES) finds increasingly application to analyze the aerothermodynamics considering heat transfer under transient conditions [81] or aeroacoustics [82]. In this approach URANS models are used in the boundary layer region and LES in the free stream zones.

The adequate solution of the boundary layer is a key factor to resolve the secondary flow development and separation phenomena in turbomachinery. Although strategies exist, where simply one logarithmic function is assumed for the dimensionless flow velocity close to the wall in one cell, in turbomachinery it is typically chosen to resolve the gradients in the boundary layer with a higher cell resolution. Due to the high gradients in the boundary layer a high number of cells is needed to be resolved. It is recommended that the first cell at the wall should be thinner than the viscous sublayer. Normally this is the case when the dimensionless wall distance y^+ has low values in the range of one. The thickness of the next cells is continuously increased until the free stream is reached. These kind of discretizations can be called Low-Reynolds mesh. Menter [83] recommends y^+-values below 2 to achieve accurate results in combination with the SST turbulence model.

To reduce the computational effort even more, the time derivative can be neglected if a steady problem needs to be analyzed. In turbomachinery problems boundaries between moving and stationary parts of the domain often exist. Here, the choice between steady and unsteady simulations also influences the treatment of the interface between both parts. In steady simulations it can often be seen that a multi reference frame approach, where the variables are averaged circumferentially, is used. However, this method does not resolve rotor stator interactions, which are important to resolve acoustics and transient aerodynamics. Palfreyman and Martinez-Botaz [84] mentioned that this simplification can influence the results sensitively in turbocharger applications. Lam et al. [85] states the use of a sliding mesh approach in URANS simulations is needed to reproduce the detailed behavior of stator rotor passage interaction. With this approach the rotor mesh rotates each time step for a fraction of the rotation. By other authors [21] a time discretization of 20 timesteps per rotor-staror passing is recommended. Over the interface the transport equations are solved over the neighbored cells.

The simulated domain is often connected to longer outlet and inlet ducts to allow the development of boundary layer and turbulence variables as it has been done by Galindo et al. [15]. However, also short ducts in the inlet and outlet of the analyzed domain can be found in the literature [16]. In the simulation of subsonic radial turbomachinery, the definition of total temperature and total pressure in the inlet and of static pressure in the outlet provide good numerical stability [21].

CHAPTER 3

Wide Range Turbine Map Measurement

Contents

3.1 Introduction

In this chapter the development of an experimental procedure to obtain measurement at extreme off-design condition is described. Special focus has been put on avoiding geometrical modifications on the turbocharger geometry to maintain the thermal characterization. To minimize heat transfer, tests have been executed under quasi-adiabatic conditions.

First, a theoretical explanation is given about how the compressor wheel is used as a centrifugal turbine. Then, an experimental procedure to supply measurement data at extreme turbine off-design conditions is presented. Furthermore, experimental methodology repetitiveness is proven. Finally, a method for a simple correction of internal heat transfer and testing monitoring has been developed. Gained results supply needed data for validating extrapolation models or CFD simulations in a broad range.

3.2 Theoretical Background

This section presents the measurement limitations of common test benches and discusses the potential of non-modified configuration to extend the measurement range.

3.2.1 Turbine Testing Principle

The main problem when trying to measure turbocharger turbine performance in a wide range of operating conditions is the lack of a suitable braking capacity of the remaining turbocharger parts. For high power, the mechanical losses due to friction can be risen by using a high viscosity oil or the compressor can be forced to consume more power by rising the total pressure at its inlet and operating with high mass flow rates. For low power, a low viscosity oil can be used and the compressor can be operated near its surge line with low density at its inlet. Even when doing this, the measurable range in the turbine map for a given reduced speed remains small [86].

Another possibility is to force-feed the turbocharger compressor, without modifications of the shaft or of the rotor and thus, avoiding the shaft balancing issues. Moreover, it can be feasible to measure the full range of turbine operating conditions, which can be found in normal automotive driving cycles.

According to Figure 3.1, high turbine power outputs (A-B) are measurable by running the compressor in the range of B' to B within the normal range of compressor power consumption and, thus providing braking power. By force-feeding the compressor, points beyond B' are achievable. In addition the compressor can be even made to work as a centrifugal turbine, producing enough power to drive the turbocharger shaft.

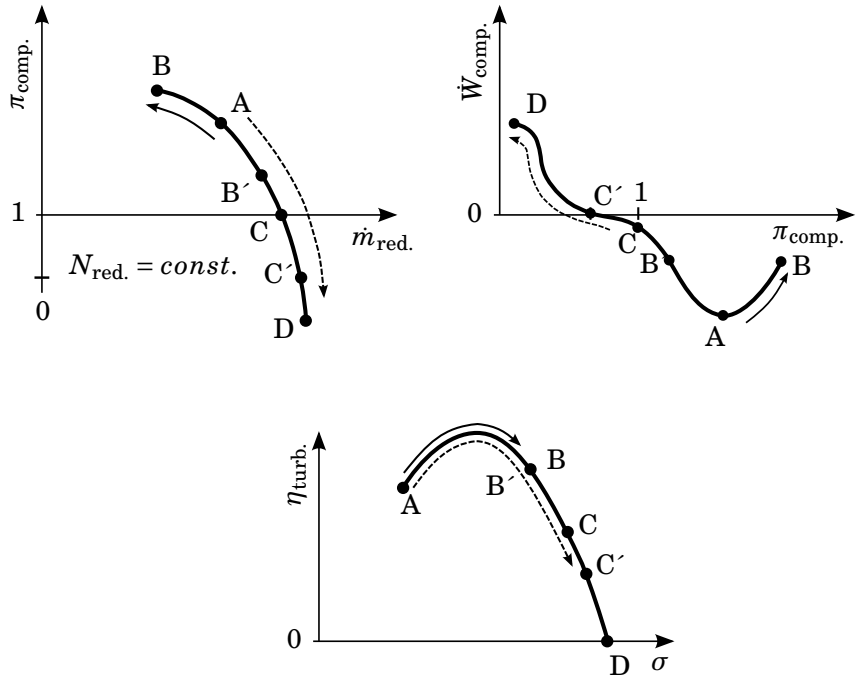

Figure 3.1: Relation between compressor and turbine running condition.

For doing so, the compressor pressure ratio has to become lower than one (Point C) to operate in the range of C' ($\eta_{turb.,mech.} = 0$) and D, where the compressor produces a net power output ($\dot{W}_{comp.} > 0$). When running at high speeds the compressor may start to choke at pressure ratios bigger than one. Then, the needed reduced mass flow for gaining power output is not obtainable and the zero efficiency point D of the turbine is hard to reach at these speeds.

3.2.2 Potential in Common Configurations

Euler's turbomachinery equation has been used for computing the power output of a compressor rotor:

$$\dot{W}_{comp.} = \dot{m}_{comp.} \cdot \omega \cdot \left(\bar{r}_{in} \cdot c_{\theta,in} - r_{out} \cdot c_{\theta,out} \right). \tag{3.1}$$

Where $\dot{W}_{comp.}$ is the compressor power output, $\dot{m}_{comp.}$ is the compressor mass flow rate, ω is the rotor angle velocity, $\bar{R}_{in}$ is the mean radius at the rotor inlet, R_{out} is the radius at the rotor outlet and $c_{\theta,in}$ and $c_{\theta,out}$ are the tangential speeds in an inertial reference frame fixed in the center of the rotor at its inlet and at its outlet (Figure 3.2).

In common cases with axial flow inlet $c_{\theta,\text{in}}$ is negligible and $c_{\theta,\text{out}}$ is bigger than 0, leading to a power consumption (negative power output) as Figure 3.2 (a) shows. If the compressor flow rate is high enough and the rotational speed is low the tangential speed at the rotor outlet in the relative reference frame can be high enough to produce a negative tangential speed component in the inertial reference frame $c_{\theta,\text{out}}$ as Figure 3.2 (b) illustrates. According to Equation 3.1 this results in positive power outputs. This can be achieved by force-feeding the

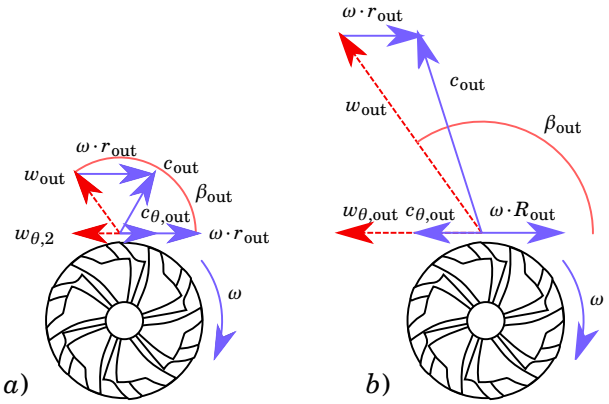

Figure 3.2: (a):Velocity triangle at normal operating condition; (b):velocity triangle with high flow rate

compressor with pressurized air and high mass flows at its inlet, making it to operate at lower than one pressure ratios. In these conditions, the turbine might be measured with very low power outputs and at a given turbocharger speed, as the compressor provides part of the power consumed in mechanical losses. In some cases, the compressor might provide even more power than the mechanical losses, and the turbine can be measured at the zone of very low pressure ratios, where it consumes mechanical power instead of producing it.

A simple model can be used to estimate the trends of limitations faced during the experimental campaign and was also used to show the potential of several setups, which were installed step by step into the test bench. Objective of the model is to deliver the unknown parameter $c_{\theta,\text{out}}$ of Euler's turbomachinery Equation 3.1, calculating the relative outlet velocity by means of the rothalpy conservation equation, rearranged as:

$$w_{\text{out}} = \sqrt{2 \cdot c_{\text{p}} \cdot T_{\text{t,in}} \cdot \left[1 - \left(\frac{p_{\text{t,in}} - \Delta p_{\text{t}}}{p_{\text{out}}}\right)^{\frac{1-\gamma}{\gamma}}\right] - \omega^2 \cdot \left(\bar{r}_{\text{in}}^2 - r_{\text{out}}^2\right)}. \tag{3.2}$$

Here Δp_{t} is the sum of the NASA loss models for incidence and passage losses by [57]. When the critical pressure ratio is reached, the NASA shock model is

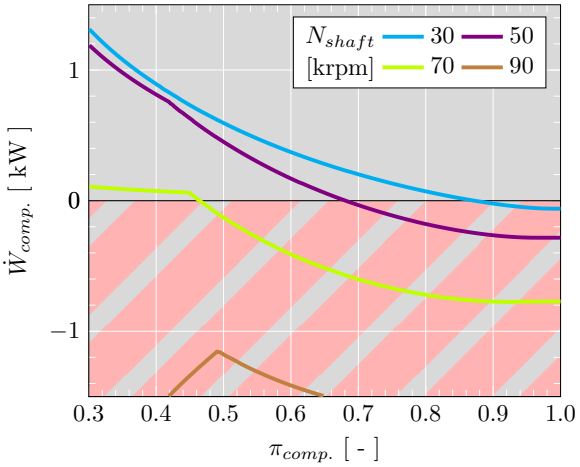

Figure 3.3: Compressor model results of compressor power output with 50 °C inlet air temperature

used. Assuming that the flow exits the passage with the blade angle β_{out} defined like in Figure 3.2 and thus, not considering deviation or estimating a slip factor, the velocity component $c_{\theta,\text{out}}$ can be calculated as:

$$c_{\theta,\text{out}} = w_{\text{out}} \cdot \cos\beta_{\text{out}} + \omega \cdot r_{\text{out}}. \tag{3.3}$$

Results of the calculation of the compressor power with low inlet temperature of 50 °C are presented in Figure 3.3. The expected maximum measurable rotational speed where the compressor operates as a centrifugal turbine is rather low and the needed pressure ratio rather low ($\pi \ll 1$). When the blade tip tangential speed rises, the flow speed at the rotor outlet has to rise to produce a negative tangential absolute speed component, as Equation 3.3 shows. Since the available compressor inlet pressure is usually restricted by the maximum power of the air supplying units, just very low speeds are measurable with such an unmodified test configuration. Additionally compressor choking could take place before a sufficient net compressor power output is noticeable and no further velocities may be reached.

3.3 Development of Methodology & Measurement of VGT Turbine

Experimental results of a complete compressor map measurement, where the compressor was not configured but force-fed to reach very low pressure ratios are presented. Procedures for realising the needed compressor power production

and thereby obtainable results on the turbine side at very low turbine efficiencies are presented in the following.

3.3.1 Experimental method

This section contains the description of the experimental test facility used for the development of the measurement procedure. The gas stand setup and its control will be introduced; then the turbocharger installation is described.

3.3.1.1 Gas stand setup

The scheme of the final gas stand arrangement is shown in Figure 3.4. A truck engine is used as a gas generator for the turbine. Its crankshaft is connected to a reversible asynchronous motor, that can brake and power the engine, so the temperature at the inlet of the turbine can be controlled by the amount of fuel injected regardless of the rotational speed of the engine. The engine discharges towards a plenum (a) that is connected to the turbine and to the exhaust line, being the latter connection controlled by means of two automatic valves (1). When the flow rate through the turbine has to be set lower than the engine flow rate, this plenum valves can be opened to divert a part of the flow and reduce the turbine pressure ratio.

The reversible asynchronous motor has two heads: one end is connected to the engine crankshaft, and the other one is connected to a gearbox that drives an auxiliary screw compressor. This compressor is used for boosting the engine and as a gas generator for the turbocharger compressor. By controlling the rotational speed of the engine (and, thus, the speed of the screw compressor) the pressure and temperature at the engine intake and the turbocharger compressor inlet can be regulated. In combination with discharge valves in the engine intake line (2) and the turbocharger compressor inlet line (3) the loading can be adjusted for both lines independently. To manipulate the back pressure of the turbocharger compressor two electrical valves (4) are installed in parallel.

For obtaining the needed turbine measurements the turbine has initially been operating at moderate mass flow like in point B of Figure 3.1. At this conditions the valves (1) are in mid-position, the valves (2) and (3) are completely opened whereas the compressor outlet valves (4) are predominantly closed. First, the turbine mass flow has been increased by means of closing the turbine valves (1). In order to maintain the rotational speed the compressor back pressure has been reduced by opening the compressor valves (4) until the braking power has been sufficiently increased. This procedure can be continued until the maximum braking power is obtained, corresponding to point A in Figure 3.1. Following, the turbine valves (1) have been opened slowly again to measure at low turbine mass flows beyond running point B' in Figure 3.1. At

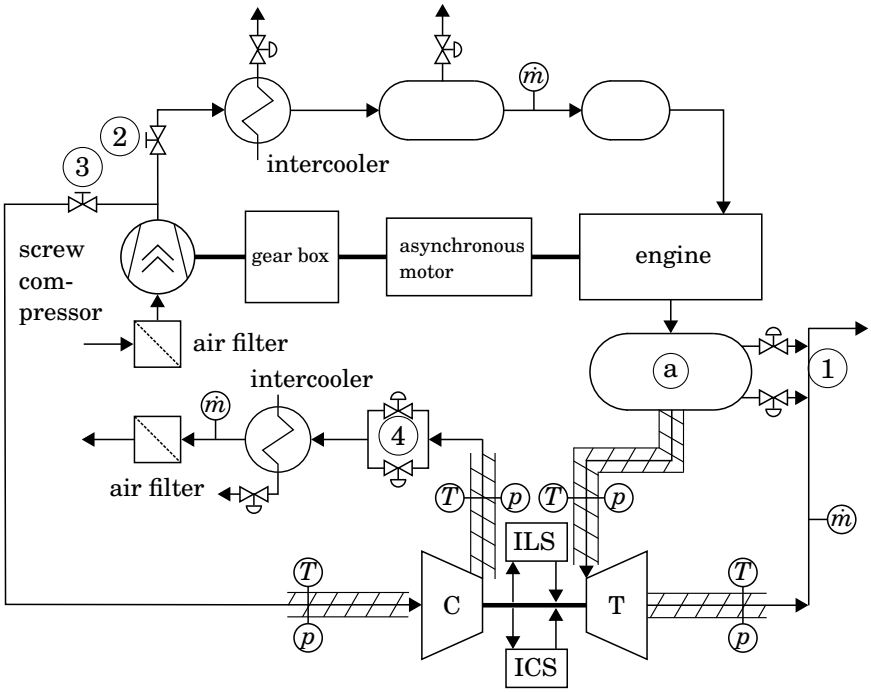

Figure 3.4: Gas stand scheme.

low turbine mass flow the turbo compressor running condition is driven towards even lower compression ratios via a stepwise closing of valve (2) and simultaneous opening of valve (3). When the turbine runs with very low mass flow, at running points where the compressor has to supply supporting power (beyond C' in Figure 3.1), the rotational speed of the screw compressor can be risen and valves (4) can be further opened. Thus, it has been possible to force-feed the compressor additionally.

The mass flow rate is measured at the outlet of the compressor and at the outlet of the turbine, as well as at the engine inlet. The engine also counts with a fuel flow rate sensor and a blow-by flow sensor, so the composition of the gases passing through the turbine can be computed. Also, the turbine flow rate can be measured redundantly when the engine exhaust plenum valves (1) are totally closed. The mass flow rate at the compressor outlet and engine inlet is measured with hot-wire flow meters, while the turbine outlet sensor is a differential pressure, V-cone shaped flow meter [87].

The pressure and temperature probes are six diameters away of the inlet and outlet of compressor and turbine. In each of this measurement planes there are two piezoresistive transducers for pressure measurements. On the compressor

side the temperatures have been measured by two K-type thermocouples, on the turbine side by four.

An independent lubrication system is used. This way, the pressure and temperature of the lubrication oil of the turbocharger can be set for each experiment. The oil flow rate is measured with a Coriolis flow meter, its pressure with piezoresistive transducers and its temperature at the turbocharger inlet and outlet with thermocouples. The accuracy of the measurement media used in the experiment are listed in Table 3.1.

Variable	Sensor type	Accuracy
Gas pressure	Piezoresistive	± 1250 Pa
Gas and metal temperature	K-type thermocouple	± 2.2 K
Gas mass flow	V-cone	± 0.5 %
Oil pressure	Piezoresistive	± 2500 Pa
Oil temperature	RTD	± 0.15 K
Oil mass flow	Coriolis	± 0.1 %

Table 3.1: Accuracies of measurement sensors.

3.3.1.2 Turbocharger setup

An automotive turbocharger has been measured during the experimental campaign. It has a variable geometry turbine, is equipped with a water cooling system and normally operates in 2 L diesel engines.

During the experimental campaign, the internal and external heat flows were kept as low as possible, so that the water cooling system was disconnected. The turbocharger as well as its inlet and outlet ducts were also thermally insulated. The flow temperature at the turbine inlet was kept close to the lubrication temperature, minimizing the internal heat transfer. Even after taking these measures, the flow evolution differs from the fully adiabatic one. Low turbine power is affected by residual heat fluxes, which would normally be considered as negligible as the turbine power output is of higher magnitude. Effectively, the power output can be obtained by measuring the enthalpy leap in the turbine:

$$\dot{m}_{\text{turb.}} \cdot \bar{c}_{\text{p}} \cdot \left(T_{\text{t,in}} - T_{\text{t,out}}\right) = \dot{W}_{\text{turb.}} + \dot{Q}_{\text{turb.}} \tag{3.4}$$

Where $\dot{m}_{\text{turb.}}$ is the turbine flow rate, $\bar{c}_{\text{p}}$ is the average isobaric specific heat capacity of the evolution inside the turbine, $T_{\text{t,in}}$ is the turbine inlet total temperature, $T_{\text{t,out}}$ is the turbine outlet total temperature, $\dot{W}_{\text{turb.}}$ is the turbine power output and $\dot{Q}_{\text{turb.}}$ is the heat transfer to the oil and to the turbine casing. When the absolute value of the last term is much smaller than the former,

which is a normal condition during the almost adiabatic measurements (with $\dot{Q}_{\text{turb.}} < 0$), the turbine power output is easily approximated with a high degree of precision from the enthalpy leap. However, at very high BSRs, the power output is low enough to be comparable to the residual heat flow, so that it has to be additionally corrected as described in section 2.3. The internal conductances have been obtained in a different testing campaign for this turbocharger. During the turbine tests the measurements of the turbocharger casing temperatures have been monitored. After changing the turbine and compressor running conditions, the measurements has been taken as soon as the temperatures are stabilized.

Four rack positions have been set for the variable geometry turbine stator during the experiments: 10 %, 30 %, 60 % and 80 % of displacement. Whereby 0 % marks the closest stator position and 100 % the widest stator opening. At each, 6 different reduced rotational speeds have been measured: 1710, 2830, 3890, 4890, 5830 and 6715 rpm/$K^{0.5}$. Extremely high blade speed ratios have been measured for the first four reduced speeds, which are equivalent to a physical speed range from 45 to 130 krpm when operating at a common turbine inlet temperature of around 700 K, and from 56 to 160 krpm at around 1100 K. This is a common range for the diesel engine exhaust gas temperature upstream of the turbine.

3.3.1.3 Procedure Check List

1. Prepare test bench; Set oil temperature; Adjust VGT position.
2. Set valves in starting position.
3. Start the installation preferably with high mass flow to achieve fast thermal stabilization. (30 to 60 min)
4. Change valve positioning according to the aforementioned description to modify the operating point.
5. Wait for thermal stabilization. (5 to 10 min)
6. Take measurements.
7. Continue with 4. until the desired points are measured or until one of the below mentioned limitations are reached.

3.3.2 Compressor Measurements Without Modification

Since the regime of the compressor plays a significant role for the obtainable turbine measurements the compressor map results are shown in Figure 3.5(a) first.

Aside of the traditional compressor map also the specific enthalpy change is plotted in Figure 3.5(b). Thus, the potential of running the turbine with the positive

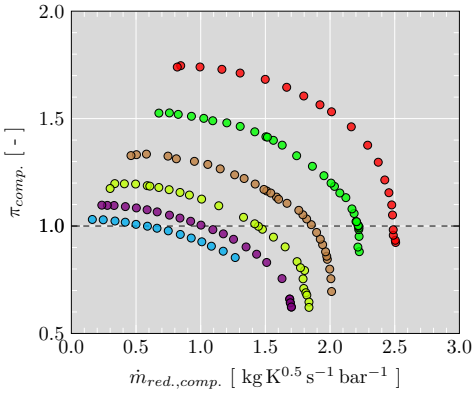

(a) Compressor map without modification

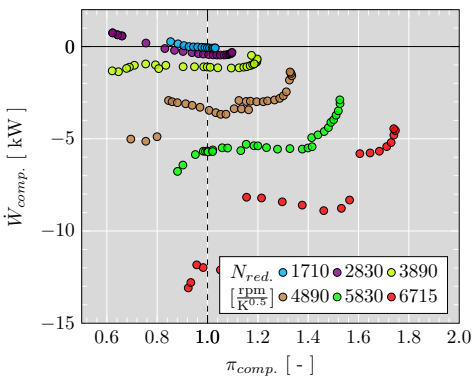

(b) $\dot{W}_{comp.}$ without modification

Figure 3.5: Compressor maps in unmodified configuration

power output of the compressor can be seen as relatively small. For the two lowest reduced speeds positive power outputs are achievable: for 1710 krpm from moderately low compression ratios less than 0.91; for 2830 krpm the compression ratio has to pass even below 0.83. However, these positive power outputs are rather low. At 3890 krpm and higher speeds no net positive compressor power output has been achieved. Hence, some turbine measurements below the mechanical turbine efficiency are feasible by means of simply force-feeding the compressor, though the number of points is low. To expand the limiting number of measurable points some modifications have to be made, like presented in the following sections.

3.3.3 Enhanced Testing Methodology and Results

Anticipating the experience of the performed measurements it can be said, that the need of high compressor mass flows and operating at compression ratios lower than one has several inherent limitations for common test benches and common compressors, which have been overcome during the performed measurements. Thereby, three different setups have been used on the compressor side to obtain as much turbine measurements at high BSRs as possible. These arrangements for high BSR measurements have kept identical for speedlines over changing VGT openings.

3.3.3.1 Inlet Guide Vane

Examining the Equation 3.1 shows that the possible control of the inlet velocity has been unused yet. Thus, the aforementioned limitation can be extended by rotating the flow at the rotor inlet. Indeed, by using a properly sized IGV device, the absolute tangential speed $c_{\theta,\text{in}}$ can be risen to non-negligible values like shown in Figure 3.6, thus contributing to the compressor net positive power output. Thereby, the necessary power output can be obtained at lower

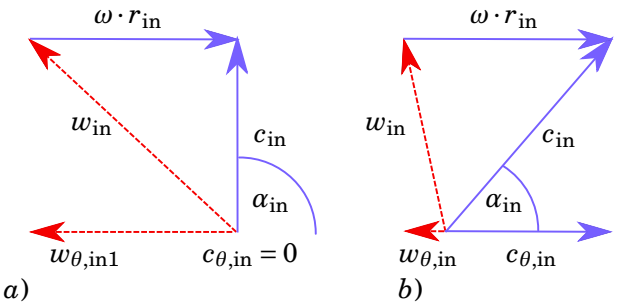

Figure 3.6: (a): Velocity triangle at normal operating condition; (b): velocity triangle with inlet swirl.

reduced mass flows. In Figure 3.7 the modeled net compressor power output can be noticed at lower pressure ratios and at higher speeds than in Figure 3.3 without swirl component. Furthermore, the rotor choking limit itself could be pushed towards higher reduced mass flows since the relative inlet Mach number decreases [37].

The assembled IGV is shown in Figure 3.8. It has been positioned 55 mm upstream of the compressor inlet. The IGV has five arc shaped blades, which are slightly twisted in circumferential direction, with 1 mm thickness and a reduced blade-width at the trailing edge to decrease the trailing edge wake effects. These blades are extruded from a rotated NACA0012 profile [88], which acts as a hub. In addition, the IGV blade angle is optimized by the use of CFD simulations to guarantee an average flow angle between 45° and 55°, according to the definition in Figure 3.6, and a low pressure drop across the full operating range.

3.3.3.1.1 Compressor Side During all measurements at very low turbine mass flow rates, the IGV has been used to guide the inlet flow of the compressor. When measuring at normal operating conditions, it is not necessary to support the turbine with power gained by the compressor and the swirl at low compressor mass flow would result in high incidence angle [36]. Thus, the IGV was detached

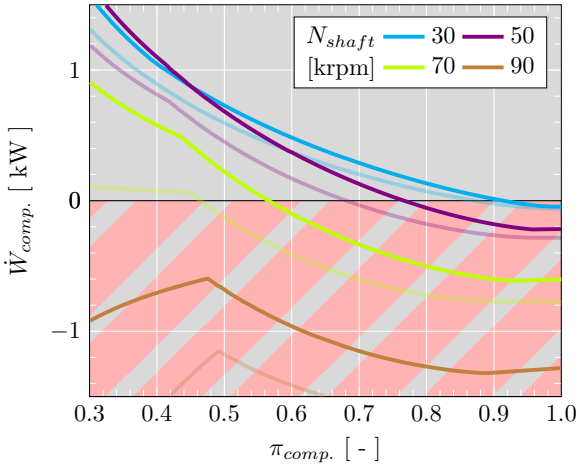

Figure 3.7: Compressor model results with 50 °C inlet temperature and imposed swirl component $c_{\theta,\text{in}}$ (α_{in} = 50°); compared with results of Figure 3.3 (light color lines).

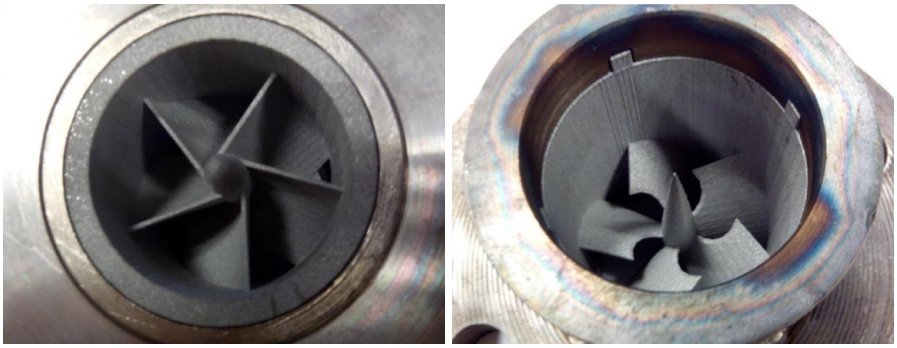

(a) Inlet view. (b) Outlet view.

Figure 3.8: IGV upstream of the compressor.

to avoid compressor surge during the measurements at normal turbine operating conditions of lower BSRs and high turbine efficiencies.

By means of the IGV the compressor power output can be risen high enough, so that the turbine efficiency map at low turbine efficiencies has been measurable between the reduced rotational speeds 1710 to 3890 rpm/K$^{0.5}$. The characteristic compressor lines measured, while using the IGV at the inlet, are shown in Figure 3.9. The IGV has realized the generation of positive compressor power at a rotational speed of 3890 rpm/K$^{0.5}$, which has not been possible before (Figure 3.9(b)). However, the flow starts to choke at lower reduced mass flows

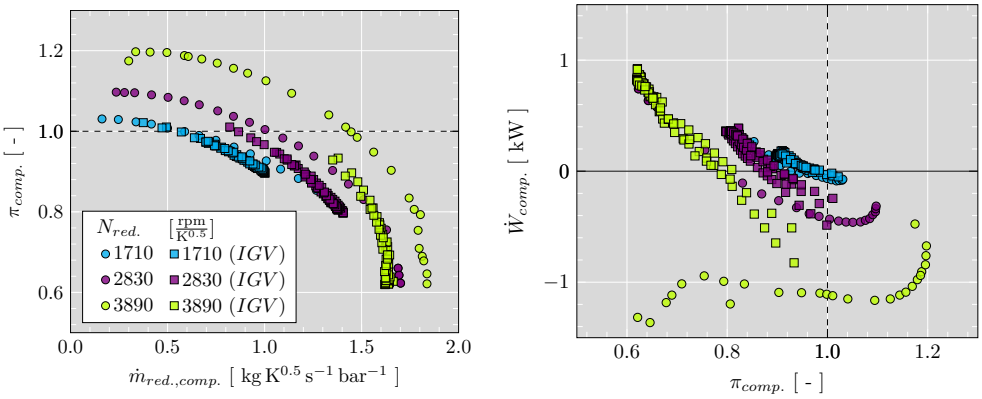

(a) Compressor map with and without IGV in the inlet.

(b) $\dot{W}_{\text{comp.}}$ with and without IGV in the inlet.

Figure 3.9: Compressor maps with IGV in comparison with the results of the unmodified configuration.

than without IGV (Figure 3.9(a)). When the compressor mass flow has been risen, choking inside of the compressor volute and diffuser has taken place, before a sufficient power can be obtained to achieve measurements at higher rotational speed. Thus, no further reduced speedlines at very low turbine mass flow have been measured with this method.

3.3.3.1.2 Turbine Side The obtained measurements are executed in high resolutions to guarantee a high reliability of the gained data. The measurement results achieved on the turbine side; together with turbine model results of the models described in the work of Serrano et al. [52] and Payri et al. [89]; are shown in Figure 3.10.

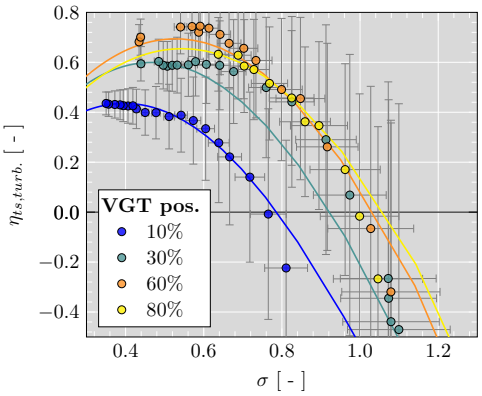

(a) Efficiency at 1710 rpm/K$^{0.5}$.

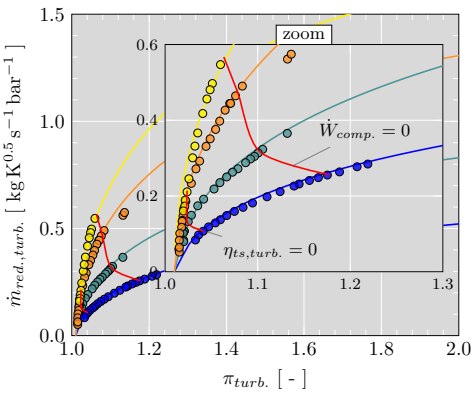

(b) $\dot{m}_{\text{red.}}$ at 1710 rpm/K$^{0.5}$.

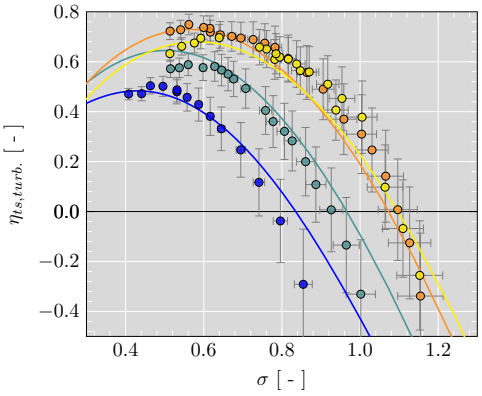

(c) Efficiency at 2830 rpm/K$^{0.5}$

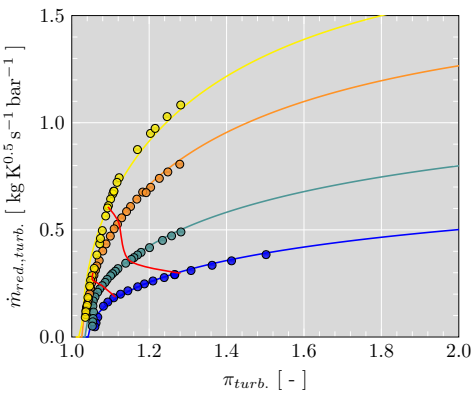

(d) $\dot{m}_{\text{red.}}$ at 2830 rpm/K$^{0.5}$.

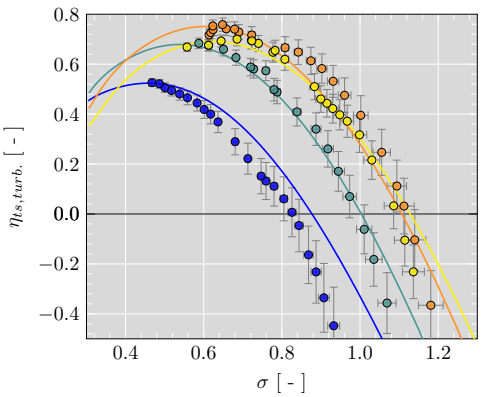

(e) Efficiency at 3890 rpm/K$^{0.5}$.

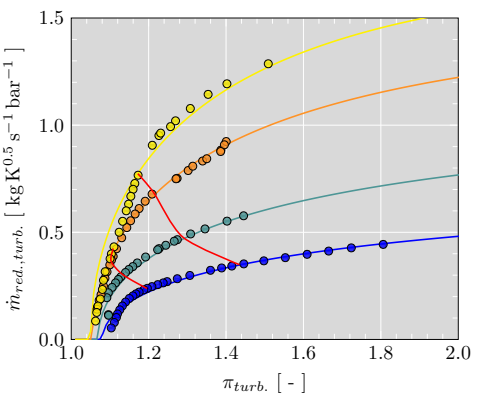

(f) $\dot{m}_{\text{red.}}$ at 3890 rpm/K$^{0.5}$.

Figure 3.10: Turbine maps with IGV.

The model is fitted with five points of each speedline in normal operating range with high turbine power (lower BSR) and predicts the efficiency and mass

flow for higher BSRs. Thus,the model lines can be understood as a guide for achieved results from the experiment. In Figure 3.10 ((a), (b) , (c)) efficiencies are shown down to −50 % and a BSR up to 1,2, even when further points with much lower efficiency have been measured.

In the mass flow maps, shown in Figure 3.10 ((b), (d) , (f)), it can be seen that it has been possible to measure at very low turbine mass flow for each particular speed. Measurement discontinuities at higher mass flow in the maps of Figure 3.10(c) - Figure 3.10(f) for 80 % VGT opening are caused by the detachment of the IGV. Furthermore, lines of zero compressor work and zero efficiency are added here. The line of zero compressor work visualizes the improvement of the measurement range regarding obtainable measurements with current state of the art methods [30]. A remarkable improvement has been gained for all speedlines by means of the presented procedure. The line of zero efficiency marks the region, where the turbine work starts to be negative. Here the turbine wheel consumes power from the shaft since the aerodynamic losses are from dominant behaviour and effect a contrary momentum/torque.

In the mass flow measurements a sudden change of the curvature in regions of negative efficiencies is conspicuous. This distinction appears strongly at 30 % VGT opening and grows with reduced speed as it is highlighted by Figure 3.11. It is worth highlighting, that during the mass flow measurements in this particular region unusual fluctuations have been recognized. Similar behaviour of the mass flow curves can be observed in the experimental data by Terdich [32] for 30 % VGT opening at very low mass flow.

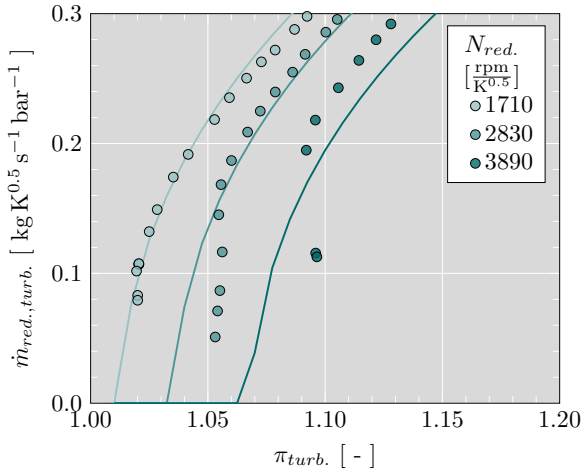

Figure 3.11: Conspicious behaviour of very low mass flow.

Such a behaviour could be affected by small fluctuations of the VGT blades, caused by a drop of stator blade loading, loose blade positioning caused by production. Furthermore the flow could start to fluctuate before changing the direction entirely, when reducing the pressure ratio even more. A change of the flow direction has been observed by Terdich [32] at expansion ratios close to one.

Due to the low magnitude of power outputs and pressure ratios, which are measured in the extreme off-design condition, high uncertainties can occur. With common precision of k-type thermocouples of 2.2 K and the precision of 2500 Pa of the pressure probes, like shown in Table 3.1, along with the aforementioned conditions and at the same time not negligible heat fluxes the uncertainties in efficiency are naturally high. Hence, the inaccuracies are growing towards lower rotational speed and towards decreasing efficiency. Nevertheless a high repeatability has been stated for the efficiency and the trends match the extrapolation results. A comparison with further data is not possible since this turbocharger has not been measured by authors like Terdich [32] and Salameh et al. [33] that propose different procedures for measuring at high BSRs. The uncertainties for the mass flow are rather low for the full measurement range.

3.3.3.2 Milled Volute

After decreasing the compressor pressure ratio by means of the IGV it has been noticed, that the reduced mass flow is limited again as shown in Figure 3.9. This time by volute and diffuser choking, since the compressor volute requires tangential rotor outlet flow with an opposite orientation (Figure 3.2), which results in high mixing and pressure losses in the volute. Furthermore, the compressor area ratios are not designed for gas expansions.

(a) Top view.

(b) Side view.

Figure 3.12: Milled compressor casing.

Hence, this limitation can be overcome by milling the compressor casing, maintaining its inlet pipe but removing material from the outlet diffuser and volute, so that the rotor expands towards the ambient as it can be seen in Figure 3.12.

3.3.3.2.1 Compressor Side To reach the following required reduced speed a compression ratio close to 0.5 is required while expanding to the ambient pressure. Thus, using the milled compressor volute, the gas does not pass neither the mass flow meter nor the temperature and pressure probes downstream the compressor. Hence, none compressor map can be obtained for this experiments. When it has been tried to reach even higher rotational speeds during the expansion to the ambient pressure, the lubrication film has broken down. At this condition a huge amount of oil is sucked and blown to the surrounding and metal to metal contact occurs, which can result in the destruction of the turbocharger. This denotes a limitation of obtaining zero efficiency measurements of the turbine driven by the compressor for the test facility in the current setup of Figure 3.4.

3.3.3.2.2 Turbine Side Via using the milled compressor volute the reduced speed of 4890 rpm/K$^{0.5}$ has additionally been measured. The results are shown in Figure 3.13. Due to the blown compressor exhaust the experimental condition inside of the test bench has changed to higher outer air velocities and thus higher convective heat fluxes. Hence, the measurements at particular operating points have been repeated to prove the repeatability of those and a high repeatability has been stated.

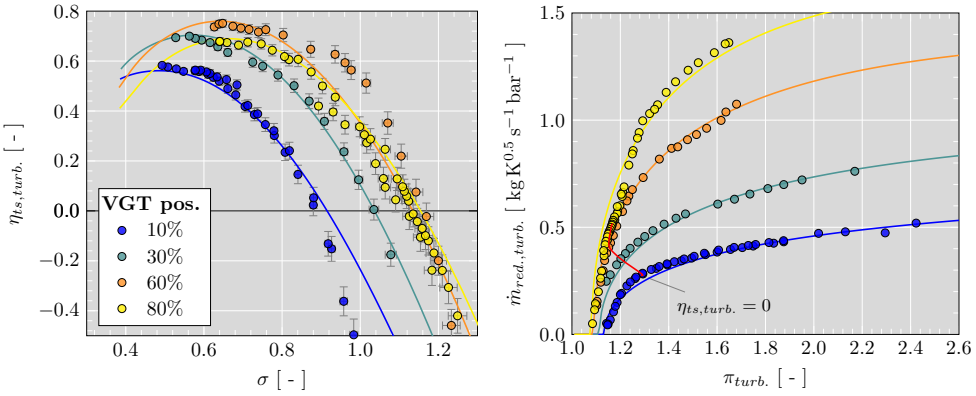

(a) Efficiency at 4890 rpm/K$^{0.5}$

(b) $\dot{m}_{\text{red.}}$ at 4890 rpm/K$^{0.5}$

Figure 3.13: Turbine maps with milled compressor casing

It is worth highlighting that especially for the VGT opening of 80 % a strong agreement between experimental and calculated (extrapolated) efficiency has been obtained with the model described in [89].

3.3.3.3 Without Compressor Wheel

To gain beneficial results for the two remaining speeds 5830 rpm/$K^{0.5}$ and 6715 rpm/$K^{0.5}$, the point close to zero mechanical efficiency has been measured ($\dot{W}_{comp.} = 0$). For this purpose the power output/input of the compressor has to become zero wherefore the compressor wheel and its casing have been detached. Due to balancing issues a metal cylinder has been replaced.

Figure 3.14: Metal cylinder which replaces the compressor wheel

Hence, the turbine has had to produce the power to overcome the friction losses in the bearings and also the friction losses of the metal cylinder with the surrounding air.

3.3.3.3.1 Turbine Side For the two higher rotational speeds the normal operating range has been measured by means of the original compressor volute. Additionally, the points of zero mechanical efficiency have been measured with the aforementioned assembly. The obtained results are presented in Figure 3.15(a) - Figure 3.15(d).

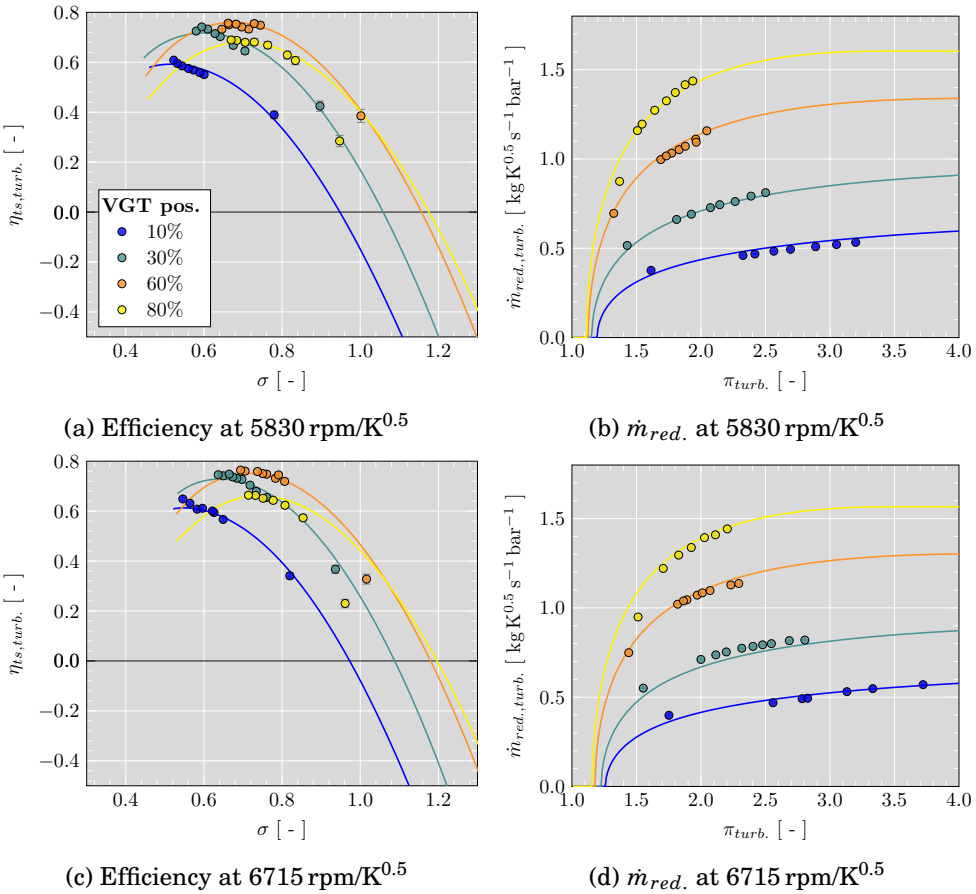

(a) Efficiency at 5830 rpm/K$^{0.5}$

(b) $\dot{m}_{red.}$ at 5830 rpm/K$^{0.5}$

(c) Efficiency at 6715 rpm/K$^{0.5}$

(d) $\dot{m}_{red.}$ at 6715 rpm/K$^{0.5}$

Figure 3.15: Turbine maps; points of lowest mass flow are obtained with cylinder on compressor side

In the case of the measurements for 80 % VGT opening the points measured with zero compressor power show very bad agreement with extrapolated trends for the reduced speeds 5830 rpm/K$^{0.5}$ and 6715 rpm/K$^{0.5}$ (Figure 3.15). It is expected to have an error in the measurement according to VGT position or turbospeed since they are the only points with such a level of disagreement and the uncertainty is low at these reduced speeds.

3.3.4 Uncertainty Analysis

The uncertainties for the BSR and the efficiency are calculated as it is proposed in [90]:

$$u_c^2 = \sum_{i=1}^{n} \left\{ \frac{1}{2} \left(f\left[x_1, ..., x_i + u(x_i), ..., x_n\right] - f\left[x_1, ..., x_i - u(x_i), ..., x_n\right] \right) \right\}^2 . \tag{3.5}$$

High inherent inaccuracies occur when measuring at low turbine power with low pressure ratio and are naturally increasing towards higher BSRs and towards lower reduced speeds like visible in Figure 3.16.

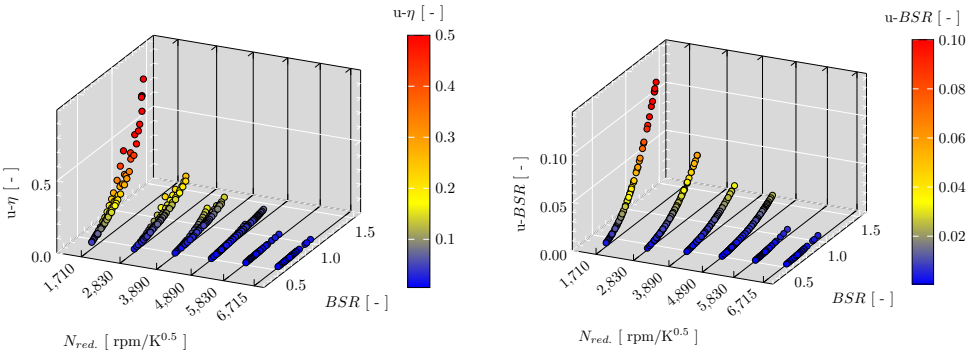

(a) Possible $\eta_{\text{turb.}}$-error

(b) Possible BSR-error

Figure 3.16: Measurement uncertainties

Consequently, measuring at higher rotational speeds for obtaining extreme off-design results allows to obtain a more trustworthy dataset. Thus, it is from interest to improve the measurement method and to allow measurements at higher speeds. The obtained mass flow maps in this thesis are less influenced by the heat transfer, as observed by Serrano et al. [39], and thus, its measurement accuracies. Since these uncertainties are not worth mentioning they are not presented.

For an improvement of the measurement quality at the running points of extreme off-design and low reduced speeds advanced measurement methods like presented by Baar et al. [91] would be of high interest.

3.4 Repetitiveness, Extension to Non-Adiabatic Condition & Measurement of Vaneless Turbine

In this section the repetitiveness of the presented measurement method will be demonstrated to allow following steps for industrializing the procedure.

Therefore, the second experimental facility is presented first. Following, it has been shown how useful data for measurement monitoring can be obtained from the pure performance data. To reduce the complexity of the correction of internal heat transfer an easy to use heat transfer correlation, which only depends on fluid variables, is presented.

3.4.1 Experimental Method

The experimental method applied in a second commercial turbocharger test-bench is explained in this section.

3.4.1.1 Experimental Facility

All the experimental results presented in this section have been obtained by tests at CRITTM2A at its testing facility which is equipped with five test benches manufactured by KRATZER AUTOMATION. The test rig is a continuous flow apparatus particularly suitable for performing investigations on exhaust turbochargers. It is characterized by the availability of two independent supply lines for compressor and turbine. The turbocharger turbine is fed with compressed air at defined temperature while the compressor can operate at a controlled pressure level. Compressor back pressure is controlled by an appropriate back pressure regulating system. The flow rate measurement can vary from $0.01\,\mathrm{kg\,s^{-1}}$ to $0.25\,\mathrm{kg\,s^{-1}}$. The turbine hot gas temperature is obtained by heat supplied by an electrical heater. A lubrication rig is used to ensure the correct operation of the bearings. Three temperature probes type Pt100 are inserted in the fluid vane both at compressor inlet and outlet. Three thermocouples type K are inserted at the turbine interfaces. Standard pressure sensors are placed at the interfaces on a stabilization ring which physically averages three pressure tappings on the wall of the flow. Air humidity, test cell air conditions and turbocharger speed are acquired with commercial sensors. Figure 3.17 shows the principal points where the measurements used for the thermodynamic calculations and gives a rough overview of the fluid flow in the test object.

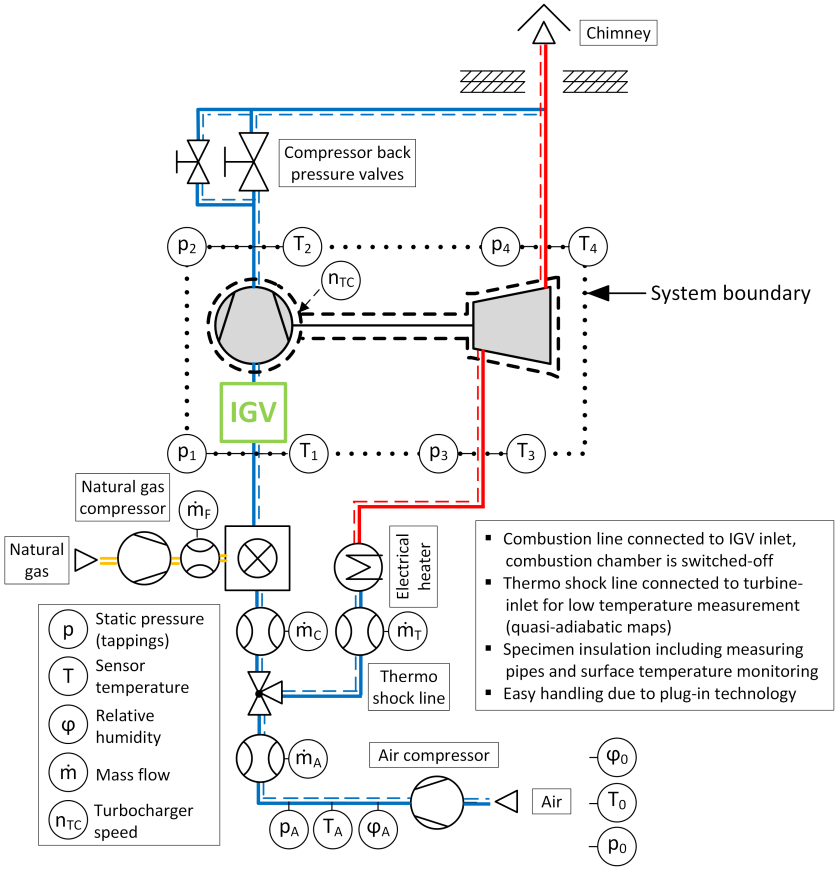

Figure 3.17: Sketch of turbocharger test bench using an IGV.

3.4.1.2 IGV Design

An IGV with five arc shaped blades and a rotated NACA profile as a hub, similar to the IGV that was manufactured in section 3.3, has been designed for the used test bench. The blade trailing edges are directed into the rotating direction of the compressor. In the experiment the flow comes from a wide duct and is guided though a sleeve to a smaller diameter duct for connecting the turbo-compressor inlet. It has been decided to design an IGV for the bigger diameter to ensure the applicability for other turbocharger geometries and to reduce pressure losses that could rise a lot with a smaller IGV diameter when operating at necessary high mass flows. The final IGV has been simulated by means of three dimensional CFD for the observed compressor inlet geometry of this test setup. The redirection of the flow can be seen in Figure 3.18.

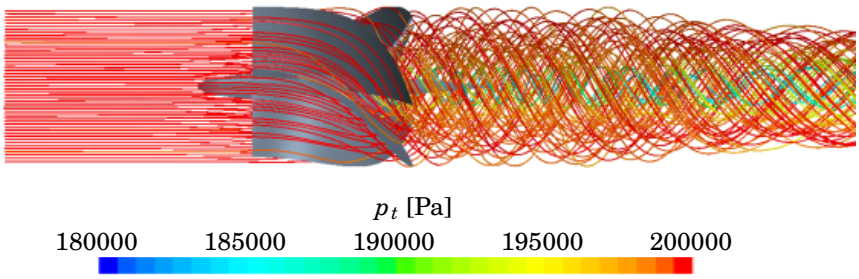

Figure 3.18: Swirl introduction by designed IGV at 2.2 $\mathrm{kg\,K^{0.5}\,s^{-1}\,bar^{-1}}$.

Simulations have been executed at flow parameters of 0.9 $\mathrm{kg\,K^{0.5}\,s^{-1}\,bar^{-1}}$ and at 2.2 $\mathrm{kg\,K^{0.5}\,s^{-1}\,bar^{-1}}$. Pressure losses of only 1441 Pa and 3724 Pa and average angles of 47.6° and 47.3° have been predicted respectively. The IGV has been 3D printed with aluminum alloy.

3.4.1.3 IGV Integration

The integration of the IGV device requires a slightly adjusted turbocharger installation. As the compressor side needs to be force fed, the IGV is connected to the compressor inlet on the one hand and on the other hand it must be connected to the combustion chamber outlet. This one is switched off in order to provide only fresh air under pressure. The IGV mounted upstream of the compressor in the test bench setup is shown in Figure 3.17 and a picture of the detail in Figure 3.19.

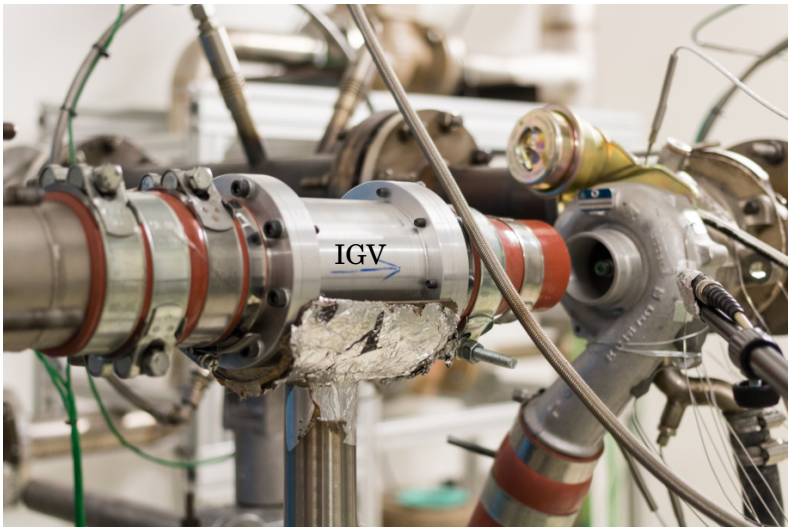

Figure 3.19: IGV integration in turbocharger test bench.

The focus of the experimental campaign is set on measurements at operating conditions where the turbine produces/consumes low amounts of power. Operating around the zero efficiency points, heat transfer plays an important role for the results. Thus, the entire turbocharger has been externally insulated up to the measurement sections in the inlet and outlet ducts. For analyzing remaining heat transfer, the turbocharger casing is equipped with temperature sensors according to Serrano et al. [46]. The internal and external heat transfer can be computed by means of the obtained wall temperatures using the model described in [39]. The IGV tests are performed in quasi-adiabatic conditions. The particular working conditions means running the test with turbine inlet temperature equal to the mean lubrication oil temperature between oil inlet and oil outlet. Under these conditions, it is clear that the turbine temperature of testing cannot exceed the maximum oil temperature and turbine heat losses are kept low. Furthermore, a constant oil inlet temperature has been interesting for the thermal analysis. During the tests the very small changes of the turbine inlet temperature have had negligible effect on the constant reduced speed.

3.4.2 Results & Post-processing

A vaneless turbocharger turbine, which serves as a reference turbine for KRATZER AUTOMATION, has been tested in the experiment. The tests have been executed at three reduced iso-speeds with three different oil temperatures each.

3.4.2.1 Measurement Results and Adiabatization

As in the former experiments minor internal heat transfer effects had to be considered and results were adiabatized with the same model. For this turbocharger generally correlated heat transfer coefficients were assumed. The

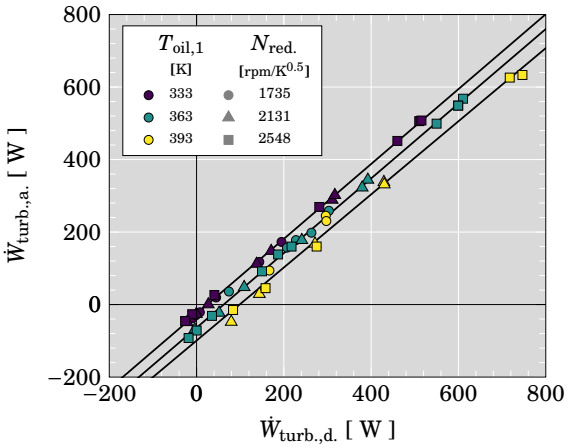

Figure 3.20: Adiabatization of measured turbine power.

diabatic power is formulated with the experimental temperature measurements as:

$$\dot{W}_d = \dot{m} \cdot c_p \cdot \left(T_{t,in} - T_{t,out}\right). \tag{3.6}$$

Figure 3.20 shows how the higher the oil temperature is, the higher the difference between adiabatic and diabatic power is. The differences are negligibly dependent on the speed and very constant for each oil temperature. It also shows that the zero diabatic turbine power is very close to the zero adiabatic one for the 333 K case, as it corresponds to totally adiabatic tests.

Also Zimmermann et al. [44] identified a rather constant heat transfer rate with turbocharger speed when the diabatic turbine power was plotted against the isentropic compressor power. Since the compressor power increases towards positive values by being force fed, the data has another physical basis than in [44] and the same trends cannot be identified by the same procedure. Instead, the diabatic turbine power has been plotted against the isentropic turbine power in Figure 3.21.

Due to the quasi adiabatic testing the required heat transfer correction is rather low for all cases on the turbine side. Figure 3.21(a) shows that the diabatic powers are also here quite parallel for constant oil temperature especially at high turbine power. The adiabatic turbine power (calculated with model sketched in Figure 2.4) coincides in one line at high powers, as Figure 3.21(b) shows. The

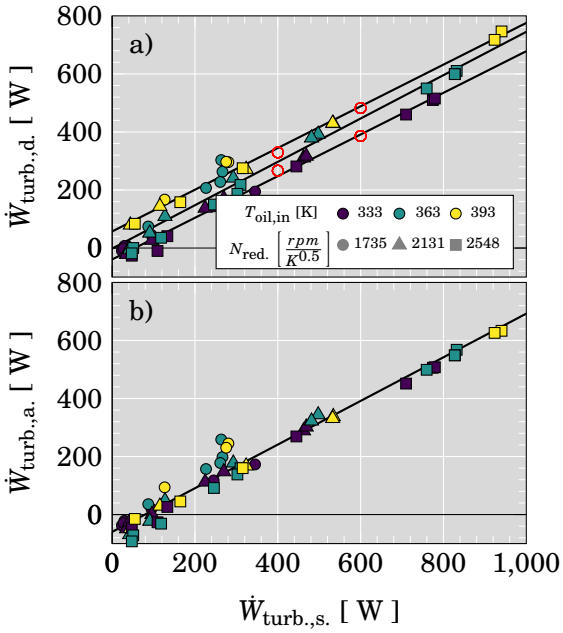

Figure 3.21: Adiabatization of measured turbine power vs. isentropic power.

considered amount of heat transfer clearly depends on the oil temperature and thus on the temperature level at the turbine inlet in quasi adiabatic conditions.

Figure 3.21(b) shows that whatever the oil temperature is there is only one relation between isentropic and adiabatic turbine power. This is coherent since the relation is reflecting the adiabatic efficiency and this is indeed independent of oil temperature. Furthermore, Figure 3.21(b) shows that adiabatic efficiency is quite independent of turbine speed for the tested range as it will be shown in Figure 3.23.

In the reduced mass flow map, shown in Figure 3.22, it can be seen that it has been possible to measure at very low turbine mass flow for each particular speed. A remarkable improvement has been gained for all speedlines by means of the presented procedure.

In Figure 3.23 the measured and adiabatic efficiencies are shown. Calculating the turbine efficiency curves with the diabatic power results in very divers shapes for each measurement with a different oil inlet temperature as it can be seen in Figure 3.23(a), Figure 3.23(c), and Figure 3.23(e). The same calculation with the adiabatized data leads to consistent results for all measurements with different oil temperatures. It is worth highlighting that the differences between diabatic and adiabatic efficiencies are big considering the rather small amount of heat transfer that has been produced. This shows the high necessity of using

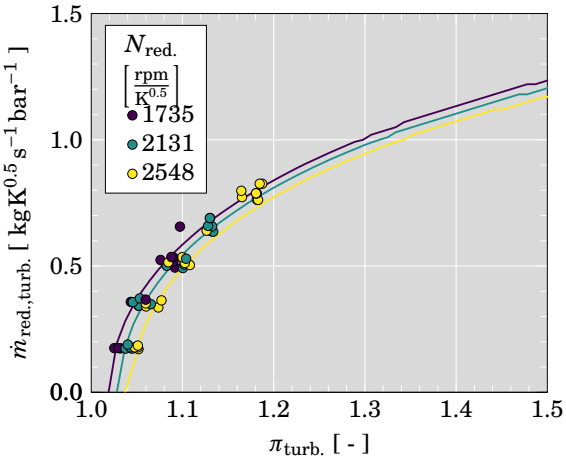

Figure 3.22: Turbine mass flow map.

an adequate heat transfer model when measuring at running points where the turbine power is low even when the tests have been executed at close to adiabatic conditions. Apparently, the measured efficiency differs more from the adiabatic results when the lubrication oil temperature is higher. At tests with 333 K the diabatic efficiency looks similar to the adiabatized efficiency and own similar trends. Furthermore, the high consistency within the adiabatic efficiency results of the two highest reduced speeds shows that the quality of the used heat transfer model is good enough. This is consistent to the adiabatic power results shown in Figure 3.21. In addition the turbine extrapolating model proposed by Serrano et al. [52] has been fitted with the experimental points of the two highest speedlines and the lowest speed (1735 rpm/$\text{K}^{0.5}$) has been extrapolated by this model. Thus, the model lines can be understood as a guide for achieved results at lower speed. The line of zero efficiency marks the region, where the turbine work starts to be negative. Here the turbine wheel consumes power from the shaft since the aerodynamic losses are dominant and effect a contrary momentum/torque as it will be shown in subsection 4.5.1.

Due to the low magnitude of power outputs (Equation 3.6) and pressure ratios, which are measured in the extreme off-design condition, high uncertainties can occur as it can be seen in Figure 3.23. Measurement errors have been considered according to Equation 3.5 leading to the presented uncertainties in Figure 3.23. With common precision of k-type thermocouples of 1.5 K and the precision of 0.1 % of the pressure probes, along with the aforementioned conditions and at the same time not negligible heat fluxes the uncertainties in efficiency are naturally high. Hence, the uncertainty is growing towards lower rotational speed and towards decreasing efficiency (i.e.: increasing BSR)

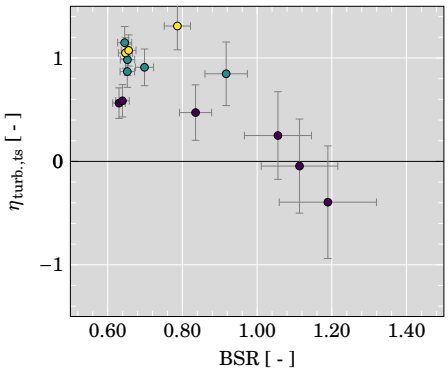

(a) Diabatic efficiency at 1735 rpm/K$^{0.5}$.

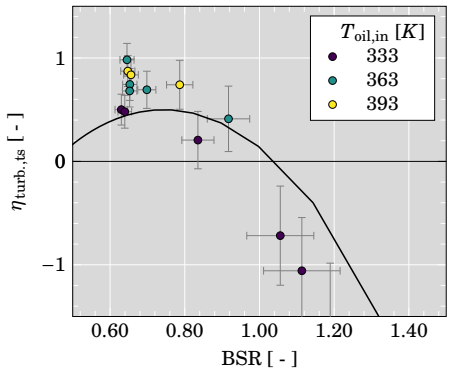

(b) Adiabatic efficiency at 1735 rpm/K$^{0.5}$.

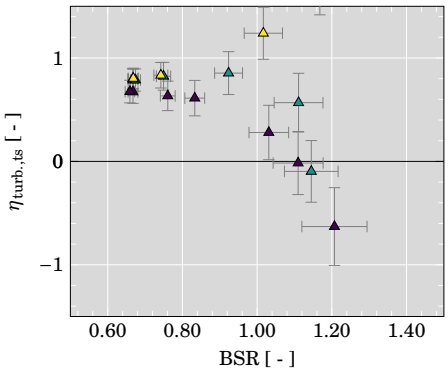

(c) Diabatic efficiency at 2131 rpm/K$^{0.5}$.

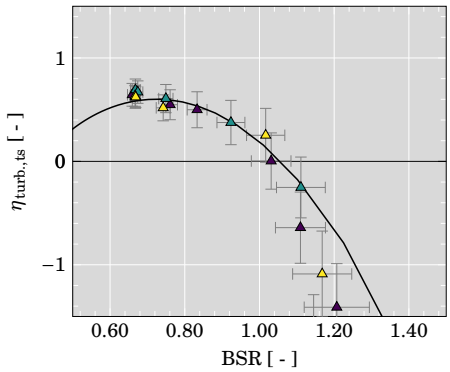

(d) Adiabatic efficiency at 2131 rpm/K$^{0.5}$.

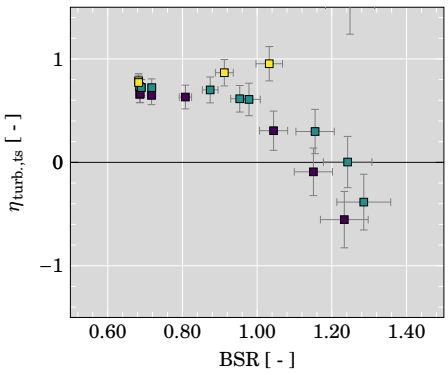

(e) Diabatic efficiency at 2548 rpm/K$^{0.5}$.

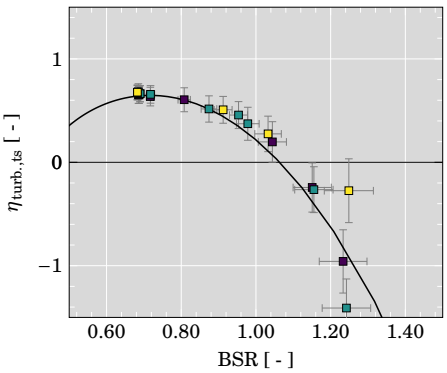

(f) Adiabatic efficiency at 2548 rpm/K$^{0.5}$.

Figure 3.23: Diabatic (left) and adiabatic (right) turbine efficiency.

as shown in Figure 3.23(b), Figure 3.23(d), and Figure 3.23(f). Nevertheless a high repeatability has been stated for the efficiency. The uncertainties for the mass flow are rather low for the full measurement range.

It can be stated that the negligible influence of the oil temperature in the adiabatic efficiency. Also Figure 3.23 shows that adiabatic efficiency depends more on BSR than on reduced speed for the tested speed range. It is worth highlighting that even negative efficiencies have been measured but with higher uncertainties.

3.4.3 Analysis & Testing Monitoring

Possible analysis with the available data demonstrated and important monitorig parameters that should be observed during the experiment are highlighted in this section.

3.4.3.1 Potential & Limitations

Since the potential of the presented procedure mainly depends on the power supply of the compressor, this discussion has been focused on the compressor. The diabatic power for the compressor will be calculated using Equation 3.6, being negative power when compressor consumes mechanical power. During all measurements, the IGV has been used to guide the inlet flow of the compressor. Again, the adiabatized data have to be taken into account. On the compressor side the thermal correction done by the heat transfer model shows similar characteristics to the turbine adiabatization as it can be seen in Figure 3.24. For keeping the same reference the reduced turbine speed is used for identification in Figure 3.24 plot.

In Figure 3.24, the adiabatization shows a power increment with respect to the diabatic compressor power. Since the focus of the test has been on the turbine side and the turbine has been kept under quasi adiabatic conditions, the amount of heat transfer on the compressor side is bigger. Figure 3.24 shows that zero compressor adiabatic power is now further from zero compressor diabatic one for all three oil temperatures. The difference is minimal for the lowest oil temperature.

In analogy to the turbine side the compressor power has also been plotted against its isentropic power in Figure 3.25. Comparing Figure 3.25(a) and Figure 3.21(a), the compressor diabatic power does not show the clear trend as the turbine, since the compressor efficiency seems to depend more on the reduced speed at tested range. Effectively, when the heat transfer model eliminates heat transfer effects and adiabatic compressor power is obtained (Figure 3.21(b)) the effect of turbo speed on adiabatic efficiency is clearly observed. Figure 3.21(b) shows how the relation of adiabatic and isentropic compressor power is clearly

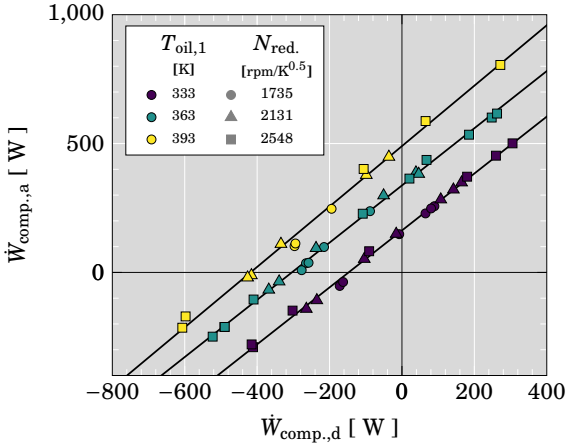

Figure 3.24: Adiabatization of measured compressor power.

independent of heat transfer ($T_{oil,in}$) but highly dependent on the speed over the tested range.

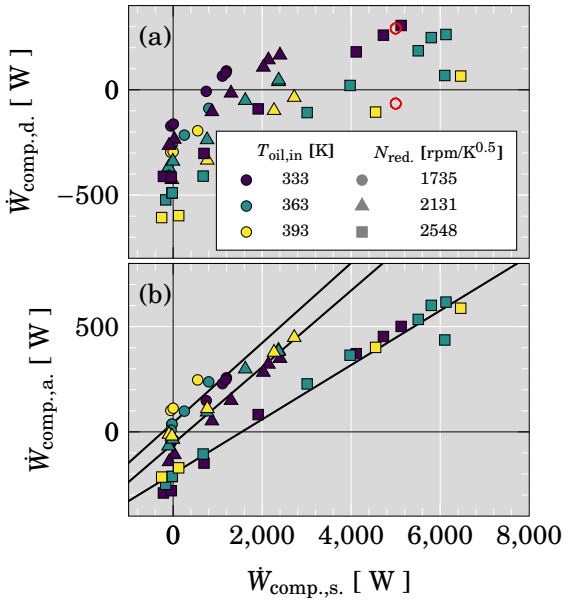

Figure 3.25: Adiabatization of measured compressor power vs. isentropic power.

Due to the IGV it has been possible to supply compressor power to the shaft at all measured speeds, like shown in Figure 3.24. Figure 3.26 shows adiabatic

compressor power vs. adiabatic turbine power. First, the turbine produces power while the compressor consumes power from the shaft like in normal running conditions (coordinate quadrant IV.). Then, a transition phase starts in quadrant I when the compressor starts to supply additional power to the shaft. By means

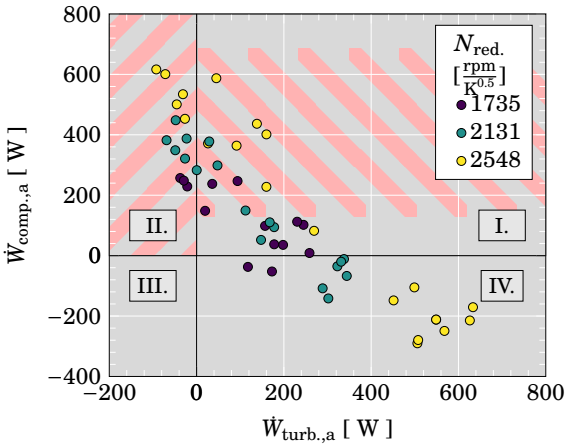

Figure 3.26: Adiabatic turbine power vs. adiabatic compressor power.

of the additional power the turbine power has been reduced even beyond zero (quadrant II.) while maintaining the reduced turbine speed. Thus, the turbine efficiency map has been measurable up to very low and negative efficiencies at speeds up to 2548 rpm/K$^{0.5}$. Under hot conditions, like 600 °C that can be found in passanger cars this would lead to a rotational speed of 75 291 rpm. The measured compressor map, with mounted IGV, can be seen in Figure 3.27 for the three measured turbine reduced speeds. For the majority of the measured points the compressor is working under a compression ratio lower than one. The limiting factor of this procedure in the executed test has been the pressure that can be supplied to the inlet of the compressor. It can be seen that the compressor is not working in choke. Thus, the potential of the used procedure can be fully exploited when using higher compressor inlet pressure. By doing so, results at higher reduced rotational speed, where the compressor needs to supply more power to overcome the increasing friction losses, can be achieved. The test bench used for obtaining here presented results was capable of supplying 0.25 kg s^{-1} at CRITTM2A. So further speeds can easily be achieved by using a gas stand with bigger flow.

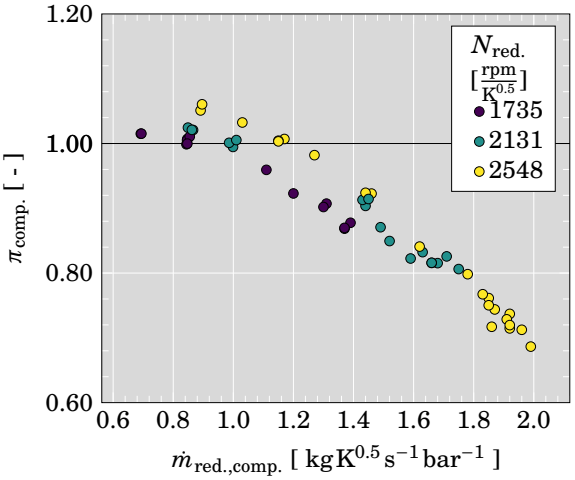

Figure 3.27: Compressor map with IGV.

3.4.3.2 Friction Loss Analysis

Relying on the adiabatized data, friction losses can easily be calculated by the turbocharger power equilibrium as shown in Equation 3.7 and attending to the power definition of Equation 3.6.

$$\dot{W}_{\text{fric.}} = -\dot{W}_{\text{turb.,a}} - \dot{W}_{\text{comp.,a}} \tag{3.7}$$

Thus, the plot of the adiabatic compressor power against the adiabatic turbine power can be used for interpreting the friction. Figure 3.28 shows just the results of the lowest T_{oil}, since the measurements had to be corrected less by the heat transfer model. At each axis crossing of one line the turbine or compressor power is zero. The friction power is consequently equal to the remaining power. Figure 3.28 shows how the axis are crossed at different values for all measured speedlines. The y-axis is crossed at higher values than the x-axis for all three speeds. This means that the friction losses not only depend on shaft speed and oil temperature, which should indicate an additional dependency on the axial loading of the turbocharger bearing and even occurring metal-to-metal contact. In order to check this, a simple approximation of the axial loading can be made:

$$\begin{aligned} F_{\text{axial}} = &\frac{p_{\text{comp.,in}} + p_{\text{comp.,out}}}{2} \cdot \left(\frac{D_{\text{comp.,out}}}{2}\right)^2 \cdot \pi - \\ &- \frac{p_{\text{turb.,in}} + p_{\text{turb.,out}}}{2} \cdot \left(\frac{D_{\text{turb.,in}}}{2}\right)^2 \cdot \pi. \end{aligned} \tag{3.8}$$

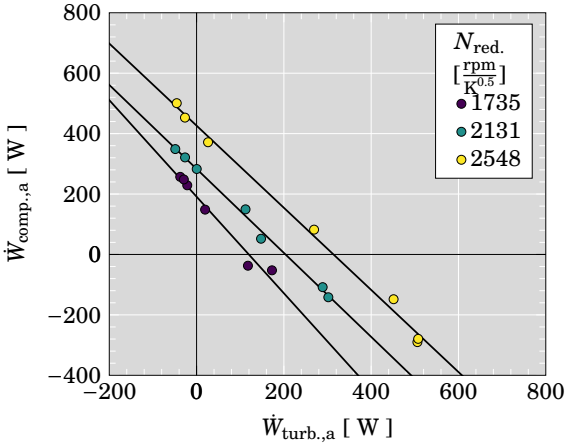

Figure 3.28: Adiabatized compressor power vs. adiabatized turbine power for $T_{\text{oil}} = 333$ K.

Figure 3.29 shows that friction losses rise continuously with the proposed axial force estimation from Equation 3.8. In Figure 3.30 the disassembled axial

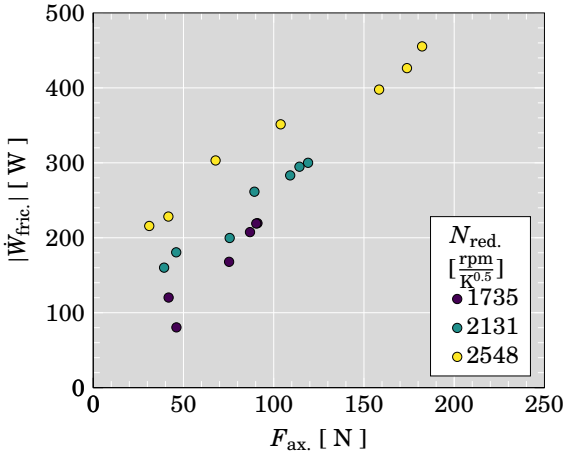

Figure 3.29: $|\dot{W}_{\text{fric.}}|$ vs. axial loading for $T_{\text{oil}} = 333$ K.

bearing (right bearing) is shown in comparison with a brand new axial bearing (left bearing). Metal removal is noticeable on both sides of the axial bearing. Especially on the compressor side metal has been removed due to compressor pushing when force feeding. This observation is coherent with results shown in Figure 3.28 and Figure 3.29.

(a) Compressor side.

(b) Turbine side.

Figure 3.30: New axial bearing (left) and used axial bearing (right).

This could lead to problems when higher rotational speed measurements are desired. By force feeding the compressor with higher pressure fully axial bearing damage could be effected. Furthermore, the turbine blades could be moved towards the shroud surface due to the axial forces. This can result in blade destruction when the turbine blade contacts the shroud or results in a change of the tip clearance and thus, in a different turbine performance.

3.4.3.3 Method for Fast Heat Transfer Correction

It has been found out that Equation 3.9 fits the experimental turbine diabatic power ($\dot{W}_{\text{turb.,d}}$) and the calculated adiabatic turbine power ($\dot{W}_{\text{turb.,a}}$) with a very high R^2 equal to 0.9963, $a_{\text{turb.}}$ equal to 1.009, and $c_{\text{turb.}}$ equal to -1.398.

$$\dot{W}_{\text{turb.,a}} = a_{\text{turb.}} \cdot \dot{W}_{\text{turb.,d.}} + c_{\text{turb.}} \cdot \left(T_{\text{oil,out}} - T_{\text{comp,out}}\right) \tag{3.9}$$

The temperature $T_{\mathrm{oil,out}}$ represents a temperature similar to the wall temperature and $T_{\mathrm{comp,out}}$ represents a heat transfer relevant value of the compressor, which is the mayor heat sink in the described experiment. Thus, $c_{\mathrm{turb.}}$ describes a fraction of the heat flux going through this heat sink and assigns it to the turbine heat loss. Accordingly, the corresponding value $c_{\mathrm{comp.}}$ (see Equation 3.11) for the compressor can be understood as a heat transfer coefficient. The coefficient a considers changes of the heat transfer at different running points. Since a is almost equal to 1 this dependency is rather low, confirming the aforementioned results with rather constant heat transfer.

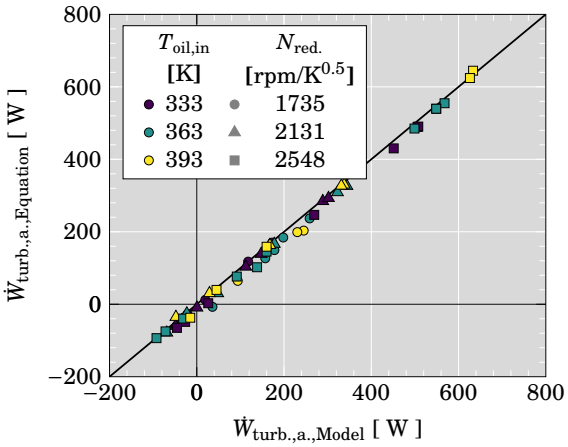

Figure 3.31: Adiabatic turbine power from Equation 3.9 vs. adiabatic turbine power by the model from Figure 2.4, $c_{\mathrm{turb.}} = -1.6\,\mathrm{W\,K^{-1}}$.

The adiabatic data presented in Figure 3.21(b) and Figure 3.25(b) have been generated by the heat transfer model shown in Figure 2.4. They demonstrate that two or more diabatic powers measured at different oil temperatures ($T_{\mathrm{oil,in}}$) and at the same isentropic turbine power share the same adiabatic power for the same speed. However, the amount of heat transfer has been quite independent of rotational speed. Thus, Equation 3.9 can be substituted for two measurement points to obtain the unknown coefficients ($a_{\mathrm{turb.}}$ and $c_{\mathrm{turb.}}$) that are assumed to be constant for the entire map since the previous fitting has been very good:

$$\begin{aligned}\Big[\ \dot{W}_{\mathrm{turb.,a}} &= a_{\mathrm{turb.}} \cdot \dot{W}_{\mathrm{turb.,d.,1}} + c_{\mathrm{turb.}} \cdot \left(T_{\mathrm{oil,out,1}} - T_{\mathrm{comp.,out,1}}\right) \\ &= a_{\mathrm{turb.}} \cdot \dot{W}_{\mathrm{turb.,d.,2}} + c_{\mathrm{turb.}} \cdot \cdot \left(T_{\mathrm{oil,out,2}} - T_{\mathrm{comp.,out,2}}\right)\Big]_{\substack{N_{\mathrm{red.}}=const. \\ \dot{W}_{\mathrm{s}}=const.}} \cdot\end{aligned} \tag{3.10}$$

Trying to solve $a_{\mathrm{turb.}}$ and $c_{\mathrm{turb.}}$ by means of two sets of measurements at constant isentropic turbine powers results into an inconsistent system of equations. Assuming $a_{\mathrm{turb.}} = 1$ only two measurement points at constant isentropic turbine

power, would be enough to estimate the coefficient $c_{\text{turb.}}$ for the whole map. It is expected that the value varies with different turbochargers due to a different geometry. The measurements should be taken at rather high isentropic turbine power to reduce temperature uncertainties. For test purposes, this has been executed by interpolated values of $\dot{W}_{\text{turb.,d.}}$, $T_{\text{oil,out}}$, and $T_{\text{comp.,out}}$ (red circles in Figure 3.21(a)). With an estimated $c_{\text{turb.}}$ and Equation 3.9 very similar results to the rather complex heat transfer model have been obtained as it can be seen in Figure 3.31.

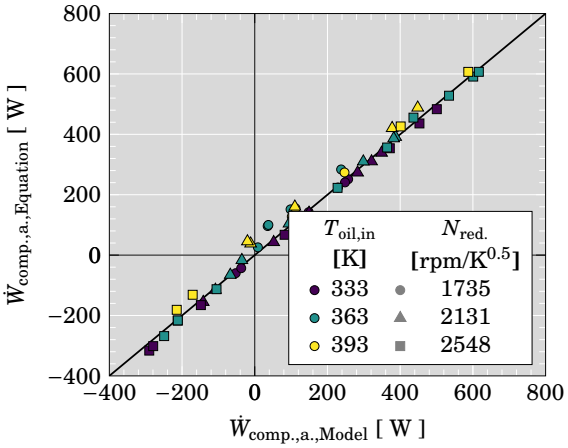

Figure 3.32: Adiabatic compressor power from Equation 3.11 vs. adiabatic compressor power by the model from Figure 2.4, $c_{\text{comp.}} = 5.8\,\text{W}\,\text{K}^{-1}$.

The adiabatization of the compressor depends again mainly on the oil temperature and the adiabatic power coincides also for the compressor in one line for each speed and can be fitted with the correlation:

$$\dot{W}_{\text{comp.,a.}} = a_{\text{comp.}} \cdot \dot{W}_{\text{comp.,d.}} + c_{\text{comp.}} \cdot \left(T_{\text{oil,out}} - T_{\text{comp,out}}\right). \tag{3.11}$$

Performing the parameter fitting the following coefficients have been found: $a_{\text{comp.}} = 1.018$ and $c_{\text{comp.}} = 7.022\,\text{W}\,\text{K}^{-1}$ with a R^2 coefficient of 0.9938. Thus, also for the compressor side a fast adiabatization by means of the same strategy has been succeeded. Interpolated measurement results (red circles in Figure 3.25(a)) lead to almost the same adiabatic power like estimated by the model as it can be seen in Figure 3.32.

Of course, more measurement points at constant isentropic power will increase the accuracy. The advantage of this procedure is that only a very low number of measurements is necessary to characterize the heat transfer and no measurements of wall temperatures are needed. Thus, it can be applied before

the turbine mapping starts and friction losses can be calculated during the test. Furthermore, the quality of the adiabatic measurement can be estimated at early testing stages.

3.5 Conclusions

1. In section 3.3, a systematic procedure for measuring radial turbine performance at extreme high blade speed ratios and almost zero mass flow has been developed.

2. In the experiments, the turbocharger compressor acts not only as a braking unit but also as a power supplier for the turbine. To run the compressor as a centrifugal turbine several limitations like e.g. rotor choking and volute choking have had to be overcome due to modifications of the initial assembly.

3. An IGV has been introduced into the inlet duct of the compressor to produce a inlet momentum and to take advantage of Euler's turbomachinery equation for assisting and powering the turbocharger shaft. A comparison with a unmodified compressor has clarified the benefit of using inlet swirl for the conversion of the compressor into a centrifugal turbine. By means of this assembly turbine efficiencies much lower than zero percent, where the turbine even consumes power, have been measurable for three moderate reduced rotational speeds at almost adiabatic conditions. Since the compressor has worked close to choke when powering the turbocharger shaft, no higher speed has been measurable.

4. By milling the compressor volute the air has been able to expand to the ambient pressure and thus, the compressor has been able to produce enough power to turn the turbocharger shaft at higher speed. At even higher speed the lubrication film has collapsed due to the low pressure at the compressor side. Consequently, four complete speedlines have been measured by means of the presented approaches. In normal hot conditions these result in the full range of turbocharger speeds, that is usually found during urban driving. Thus, valuable data for model development and evaluation have been obtained.

5. For even higher speeds the compressor wheel has been replaced by a balanced cylinder. With this kind of assembly it has been possible to obtain the point of zero mechanical efficiency in a simple way and to gain additional data for very high speeds.

6. The uncertainties, which play an important role at low efficiency measurements, have been observed. The possible errors have a very high

magnitude for low rotational speeds. Even though, a high repeatability has been stated for the tests.

7. In section 3.4, the industrial applicability of the developed turbine measurement procedure at high blade to jet speed ratios has been stated. Measurements up to negative turbine efficiencies have been able to be obtained with a second turbocharger at 75 291 rpm (at engine like operating condition) and it is possible to measure at even higher speeds.

8. Analysis of different lubrication oil temperature levels have shown the impact of internal heat transfer even at quasi adiabatic measurements with low temperatures. Hence, the use of heat transfer models or corrections to process the measured turbine power is needed as the results have shown.

9. Using higher inlet pressure on the compressor side can allow measurements at higher rotational speeds.

10. To omit axial bearing destruction the turbine inlet can be fed by pressurized air, while throttling the turbine outlet with a back pressure valve.

11. A simple and novel method for heat transfer estimation at quasi adiabatic turbine measurements, that only needs the measurement of few running points (4 to 8), has been described and proposed here as an alternative to more complex heat transfer determination. Results are in agreement with more complex model outputs.

12. Influence of axial loading in friction losses can be assessed by playing with both turbine throttling and compressor inlet pressure. Also friction losses could then be studied with this procedure.

CHAPTER 4

Turbine CFD Simulation in a Wide Range

Contents

4.1 Introduction

This section of the thesis presents the first extended aerodynamic analysis in the available literature of adiabatic numerical simulations with very low mass flow where the turbine works under extreme off-design conditions. The results will help to improve the experimental instrumentation and form a first step for developing new advanced loss models and design one-dimensional extrapolation models towards high BSRs.

For the analysis, experimental points obtained in section 3.3 and adiabatized by the model described by Serrano et al. [45] serve the basis for the validation of the performed CFD simulations in the range from high up to low mass flow rates.

First, the CFD method is presented and validated. Following, overall passage flow phenomena at low mass flow are characterized. Finally, tip leakage flow, which turned out to have high importance for the extrapolation quality of one-dimensional models, has been analyzed in a wide range of possible operating conditions.

4.2 Geometry & CFD Model

For the analysis and validation, the same radial turbocharger turbine geometry has been used, that has been measured in a wide range from optimum efficiency points over off-design conditions up to very low mass flow and negative turbine power in section 3.3. The blade rows of the simulated turbine are shown in Figure 4.1 and important turbine dimensions are listed in Table 4.1. The rotor and stator tip clearances have also been considered in the analysis.

Apart from the stator and rotor, the volute and outlet volume have been simulated (see Figure 4.4) plus the corresponding ducts as shown in Figure 4.2. The computational domain covers a 200 mm long inlet duct, which is equal to 6 inlet duct diameters.

Due to the high swirl that can occur at low mass flow downstream the rotor wheel, a high radial pressure gradient can develop in the outlet duct. To overcome back flow in the outlet plane and related convergence problems, the outlet duct has been chosen to be rather long. The outlet duct measures 9 outlet duct diameters. Thus, the flow can mix more out before reaching the boundary. Since the duct would have to be much longer to obtain a sufficient mixing of the flow, a tapered duct has been added at the outlet (blue part in Figure 4.2). This way the flow accelerates close to the outlet reducing the swirl angle and radial pressure gradient. This approach turned out to be very effective in overcoming convergence issues due to the outlet swirling flow. Furthermore,

Stator	
Blade number	11
Nozzle vane hight	8 mm
Blade angle α (VGT opening)	72.95°(30 %),62.95°(60 %),
(α according to Fig. 4.1 (b))	53.45°(80 %)
Chord length	18.95 mm
Tip clearance	0.2 mm
Rotor	
Blade number	9
Inlet radius $r_{\text{tip,in}}$	20.05 mm
Outlet radius $r_{\text{tip,out}}$	19 mm
Outlet blade angle γ_{out}	59°
Inlet tip clearance ϵ_{in}	0.36 mm
Outlet tip clearance ϵ_{out}	0.4 mm
Axial tip clearance	13 mm
length ($l_{\text{tip,ax.}}$)	
Leading edge thickness $\Delta\theta$	0.0195 rad

Table 4.1: Turbine specifications.

it can be assumed that the influence of this geometry change on the upstream rotor flow is negligible due to the extended outlet duct length.

For the CFD calculations the commercial software STAR-CCM+ 10.02.012 [92] has been used and its segregated solver has been chosen. To model turbulence the RANS k-ω SST model has been taken. An inlet turbulence intensity of 4 % has been set. Due to the main focus of this thesis on low mass flows and thus, low Mach numbers a pressure based solver has been used [92]. Since the pressure based solver has also been evaluated as accurate for high Mach numbers according to [92], all simulations have been executed with this method to preserve consistency in the results.

Since the analysis is focused on the aerodynamic behavior and the validation comparing adiabatized turbine maps, the domain walls are set to be adiabatic. Furthermore, non-slip boundary condition has been activated to compute the wall friction. Experimental total temperature in combination with the experimental total pressure have been set as inlet boundary condition and the static pressure has been imposed at the outlet boundary.

For the validation of steady simulations the rotational domain has been connected to the stationary domain by means of a mixing plane. The unsteady simulations have been performed with a second order implicit unsteady solution of the time under the sliding mesh approach, where the time step size has been chosen so that a rotation of two degrees is resolved, being in the order of

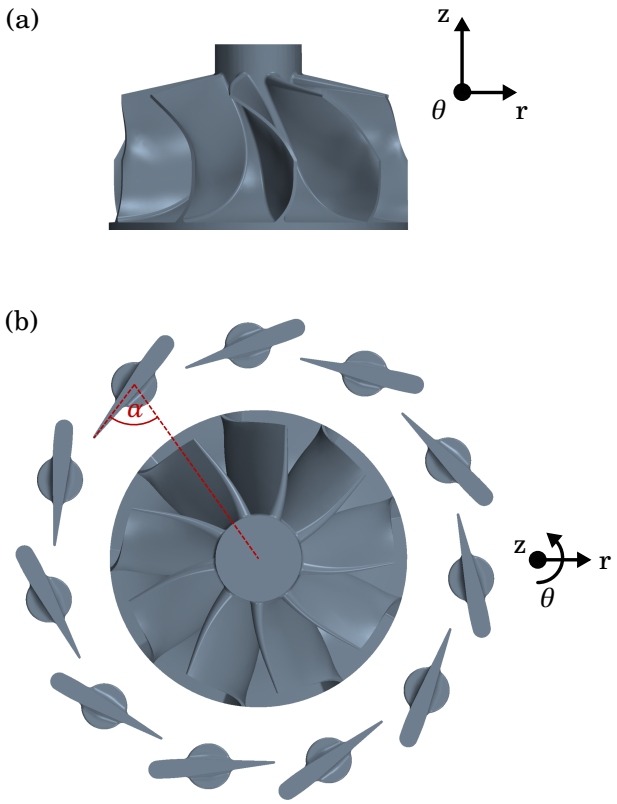

Figure 4.1: Rotor geometry: a) side view; b) top view with variable stator blade geometry.

magnitude of other authors [21]. With eight inner iteration steps a high degree of convergence has been obtained for all simulated cases. A second order implicit unsteady solution of the time has been used.

4.3 Meshing & Mesh Convergence

The inner volume of volute, stator, rotor, and outlet has been discretized by means of a unstructured polyhedral mesh [74]. In the inlet and outlet duct an extruded mesh has been used as it can be seen in Figure 4.4. The boundary layer has been meshed with prism layers aiming a low Reynolds mesh. To find a reasonable number of cells a mesh convergence analysis has been executed. This analysis has been performed with steady flow simulations. The mixing of jet wake regions has been avoided by using the frozen rotor approach so that

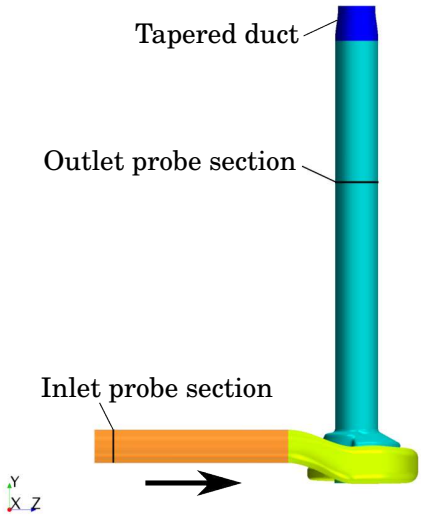

Figure 4.2: Domain with extended outlet and tapered duct.

also reliable results for the unsteady simulations with a sliding mesh approach have been able to obtain under justifiable time effort.

Since the below described validation and further simulations have been performed with different variable guide vane positions, flow conditions can differ essentially in stator and rotor at higher mass flows. Thus, the mesh analysis has been performed for a high and a low stator blade opening in parallel to find a mesh density that can cover all cases. As reduced speed, which is compared in the following section with experimental data, 3890 rpm/K$^{0.5}$ has been chosen. The volute and duct mesh has been kept constant with a medium core resolution and an average y^+ value of around 2. For all meshes the experimental point with the highest measured mass flow of each, opened and closed VGT position, has been simulated. Furthermore, boundary and core mesh have been varied independently in the rotor and the stator. Three different core mesh densities and four boundary layer meshes (A-D, from fine to coarse) have been combined. Thus, 24 meshes have built the basis for the meshing analysis with two VGT positions.

Figure 4.3(a) and Figure 4.3(b) show the relative variation of the mass flow and power corresponding to the mesh with the highest boundary layer and core mesh resolution. While the mass flow is less dependent on the boundary layer resolution for opened VGT positioning, the mass flow changes significantly with closed VGTs and higher y^+ values in stator and rotor. Furthermore, the turbine power experiences changes of higher order when the boundary meshes C and

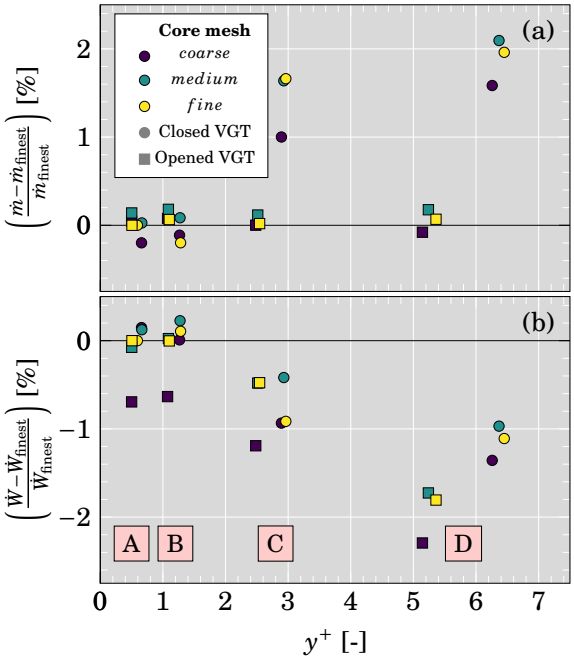

Figure 4.3: Mesh convergence in turbine mass flow and turbine power for closed and opened VGT.

D are used. Even with fine boundary layer meshing A and B the power varies a lot when they are combined with a coarse core mesh. Thus, a medium core mesh with the second finest boundary layer meshing B has been chosen for the following analysis. After running first simulations at low pressure ratios the mesh has been modified at certain positions. The final mesh, as it can be seen in Figure 4.4, has 4.15 million cells in the whole domain with 12 prism layers at the wall boundary.

4.4 CFD Results vs. Experimental Data

Experimental results have been obtained by means of quasi adiabatic measurements in section 3.3. Remaining internal and external heat flows have been corrected with the heat transfer model that is described by Serrano et al. [45]. This way, an adiabatic map was experimentally obtained and has been used as the basis for validating the CFD results. Hence, simulations with adiabatic walls can be validated with a reduced uncertainty due to heat transfer. The measurements at high BSRs have been obtained as described in section 3.3 for the here simulated turbine. The extended map measurements were performed

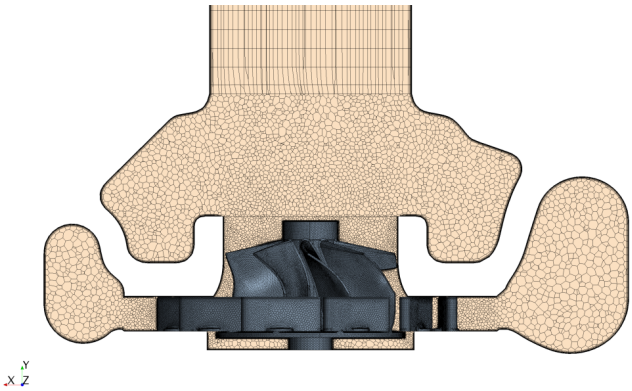

(a) Side view.

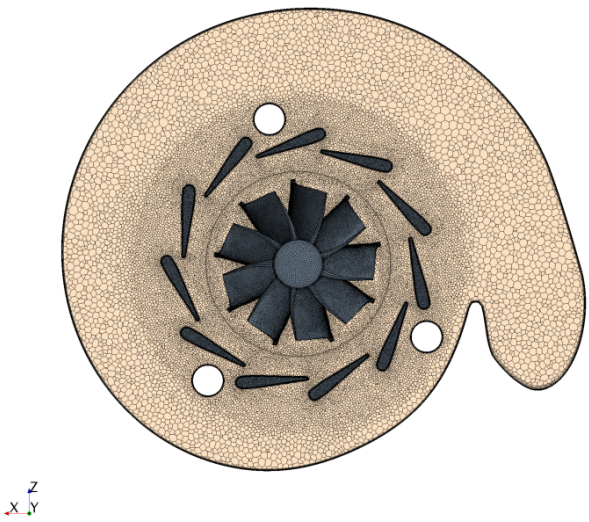

(b) Top view.

Figure 4.4: Final mesh.

at four reduced speeds. The third reduced speed 3890 rpm/K$^{0.5}$ has been selected for the validation of CFD results due to their high reliability in the experimental and adiabatic results (Figure 4.5 shows very small uncertainties in the measurements). Apart from that, a further speedline at rather high reduced speed of 6715 rpm/K$^{0.5}$ has been simulated for 30 % VGT opening.

The experimental VGT position was measured by a displacement sensor connected with the blade moving mechanism and a linear correlation has been assumed between VGT angle and determined displacement. However, the measured displacement is not fully reliable and just serves as a guidance for the initial position. Following, the stator blades have been moved in 0.5° steps at the running point of highest pressure ratio until the simulated mass flow matches the experimental one as good as possible for each of the analyzed VGT openings 30 %, 60 %, and 80 %. Anticipating the simulation results at low mass flow it can be said that the flow owns high tangential velocity components in the turbine outlet and thus, also in the measurement plane. The high tangential velocity component results in a high radial pressure gradient in the measurement section due to the radial equilibrium [93]:

$$\frac{\partial p}{\partial r} = \rho \frac{c_\theta^2}{r}. \tag{4.1}$$

Thus, especially at low pressure ratios it is important to take pressure probes at the same location as it was measured in the experiment. Accordingly, the pressure probes in the outlet measurement section, which is shown in Figure 4.2, have been taken as circumferential average of the wall pressure.

4.4.1 Steady Flow Results

By means of RANS simulations it has been possible to obtain convergent results up to total to static pressure ratios around 1.1 as it can be seen in Figure 4.5. At lower mass flow/pressure ratio no stationary flow has been obtained. However, it has been possible to simulate stationary cases where the turbine even consumes power, visible in Figure 4.5 (b), (d), (f).

The experimental reduced mass flow curves, shown in Figure 4.5 (a), (c), (e), have been reproduced in a good quality for 30 % and 60 % VGT positioning up to low mass flows. With 80 % VGT opening the simulation points follow well the experimental behavior until the experimental curve changes its curvature. Since even the one dimensional model prediction, with the models described by Serrano et al. [52], shows better agreement with the CFD results it is probable that the VGT position has slightly changed in the experiment due to the imperfect fixing of the stator blade moving mechanism.

Since the stator angle has been adjusted until the mass flow has matched the point with the highest pressure ratio, an inherent simulation error might

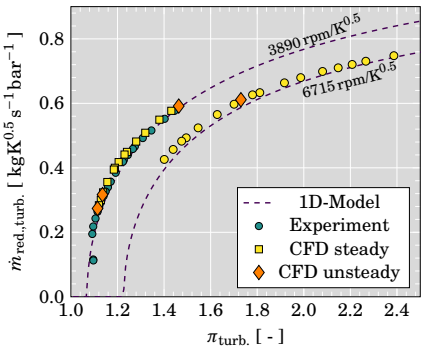

(a) $\dot{m}_{\text{red.}}$ at 30 % VGT opening.

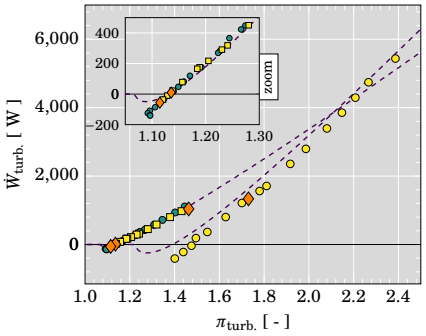

(b) $\dot{W}_{\text{turb.}}$ at 30 % VGT opening.

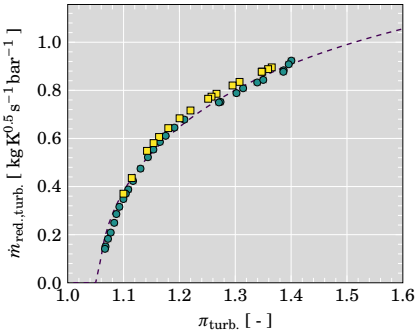

(c) $\dot{m}_{\text{red.}}$ at 60 % VGT opening.

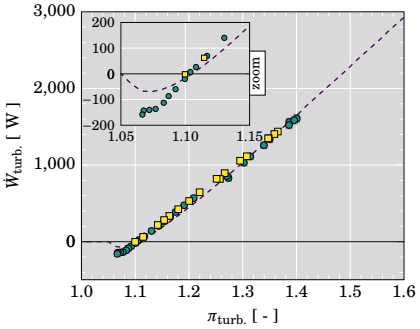

(d) $\dot{W}_{\text{turb.}}$ at 60 % VGT opening.

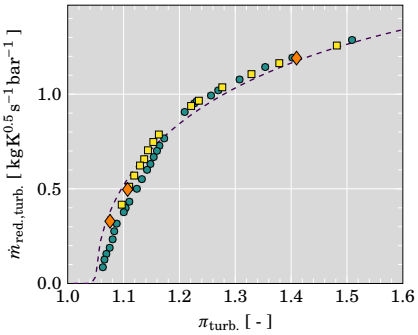

(e) $\dot{m}_{\text{red.}}$ at 80 % VGT opening.

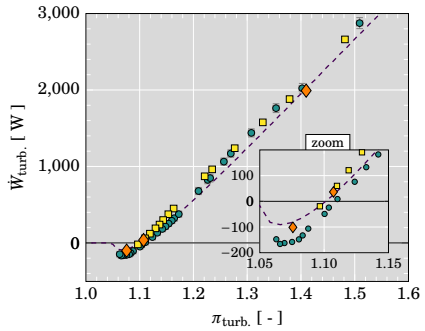

(f) $\dot{W}_{\text{turb.}}$ at 80 % VGT opening.

Figure 4.5: Reduced mass flow and turbine power at 3890 rpm/$K^{0.5}$ and 6715 rpm/$K^{0.5}$ (in (a) & (b)).

have been transfered into the VGT positioning. However, the qualitative shape of the mass flow curves allows the assumption that the geometry is accurate enough. Here, the power has been evaluated due to the high measurement errors that appear in the estimation of the efficiency at operation points of interest as demonstrated in subsection 3.3.4 [94]. The CFD results show also very good agreement in terms of power prediction for low mass flows at 30 %, for the entire range at 60 %, and for high mass flows at 80 % VGT opening. At low mass flows and 80 % VGT opening the calculated turbine power has not been reproduced in a good quality by means of CFD. This could also be caused by the possible change of experimental stator positioning at this VGT opening.

Also for the high reduced speed of 6715 rpm/$K^{0.5}$ and at 30 % VGT opening, results with negative power have been obtained. At this speed such extreme off-design conditions occur at rather high mass flow as it can be observed in Figure 3.10(b).

4.4.2 Unsteady Flow Results

Beside of the high number of stationary RANS results, URANS simulations have been performed for the closest and for the openest simulated VGT positionings 30 % and 80 % of the set of experimental data that has been used for validation purposes.

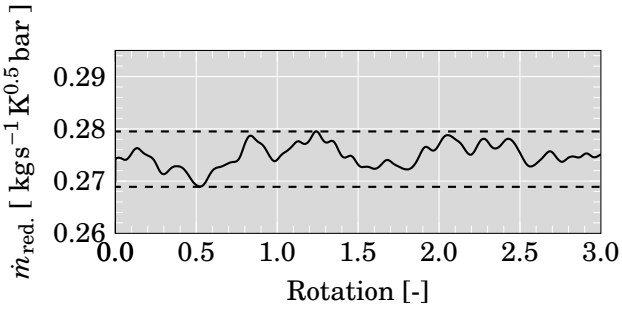

Figure 4.6: Mass flow for 30 % VGT opening; lowest simulated mass flow.

In Figure 4.5 also transient simulations, where the results have been time-averaged over three entire turbine rotor rotations, are shown. It can be seen that also the URANS simulation results match with the experiments in a good quality.

However, the unsteady simulation results at the low simulated mass flow for 30 % and 80 % VGT opening show fluctuating mass flow, as it can be seen in Figure 4.6 and Figure 4.7 for the cases at the lowest simulated mass flow rates. Mass flow fluctuations with a peak-to-peak amplitude of 3.9 % can be

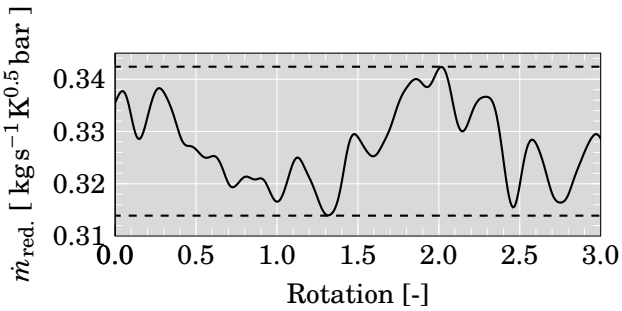

Figure 4.7: Mass flow for 80 % VGT opening; lowest simulated mass flow.

measured in the observed period of three wheel rotations for the case of 30 % VGT opening around the average simulated mass flow can be observed for the case with 30 % VGT opening. The case of 80 % VGT opening produces a higher fluctuation peak-to-peak magnitude of 8.7 % in the shown period.

4.4.3 Outlet Swirl Influence on Pressure & Efficiency Interpretation

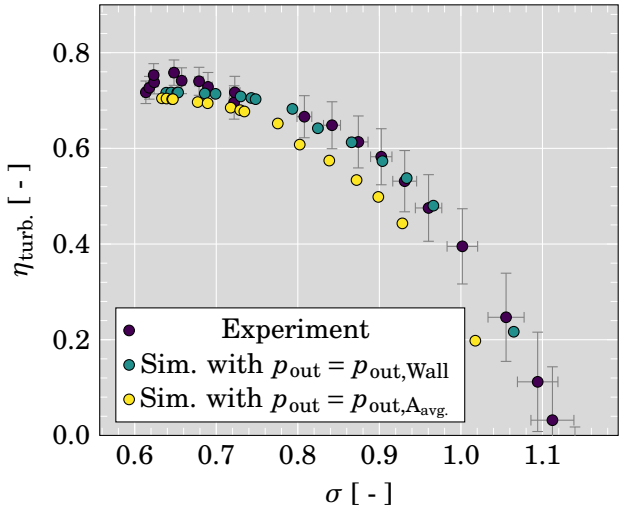

Figure 4.8: Variation of efficiency results at 60 % VGT opening.

Furthermore, it has been observed that the radial pressure distribution can lead to misleading results in upcoming measurement procedures of extended

map testing. In typical measurements the pressure sensors are located near the duct wall. Thus, a higher pressure is measured close to the wall than the physically more relevant area average in the measured cross section. Since the swirl and pressure gradient rises with reducing mass flow, the discrepancy between both values becomes bigger. Hence, the efficiency at high and very high BSR can be overestimated against the real physical potential.

In Figure 4.8 the efficiency of the steady simulation results of 60 % VGT opening are demonstrated since they show good agreement between experimental and simulation efficiency when the turbine outlet pressure is taken as the wall pressure in the outlet section. Just by changing the calculation from using the wall pressure probes to using the area average in the measurement cross section, the results at high BSR can be significantly be influenced. The efficiency can drop up to 15 percentage points at already low efficiencies. Since the outlet swirl will be even higher when the rotor turns faster, the highlighted difference will be even higher when the turbine is measured at higher rotational speeds.

4.4.4 Conclusions

1. A tapered duct far away from the rotor outlet made it possible to achieve convergent results up to a pressure ratio close to 1.1, where the flow owns high swirl components. Reducing the pressure ratio even more no stationary flow has been able to stabilize.

2. A comparison of experimental data with RANS and URANS CFD simulations has shown good agreement of reduced mass flow and turbine power prediction. Hence, the qualitative reliability of the flow analysis has been stated.

3. It has been shown that the typical measurement of static pressure close to the wall can cause an overestimation of the real turbine efficiency, when the turbine is tested with low mass flow. Thus, it is recommended to measure at further radial locations.

4.5 3D Flow in Extreme Off-design Condition

To identify zones of interest at off-design conditions the flow is analyzed in the rotor outlet (close to the TE like in [24]), which is also an important control section for one-dimensional modeling. The local total enthalpy change over the rotor is divided by the specific work:

$$\Delta h_{\mathrm{t,RC}} = \frac{\bar{h}_{\mathrm{t,rot,in}} - h_{\mathrm{t}}}{\bar{h}_{\mathrm{t,rot,in}} - \bar{h}_{\mathrm{t,rot,out}}}. \tag{4.2}$$

Since, the total enthalpy in the rotor inlet is predominantly homogeneous, the value of $\Delta h_{\mathrm{t,RC}}$ gives a good impression of the local specific work extraction in different regions.

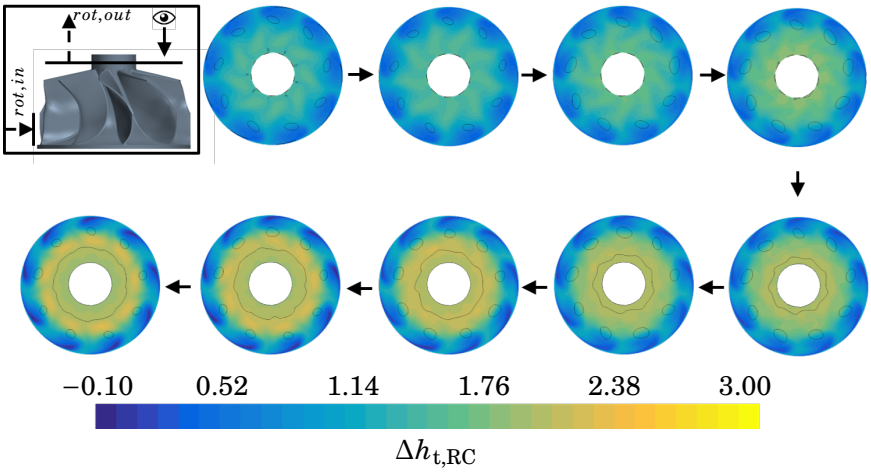

Figure 4.9: Relative total enthalpy change at plane in the rotor outlet over with 30 % VGT opening; lines: $v_{\mathrm{ax.}} = 0$.

In Figure 4.9 the change of $\Delta h_{\mathrm{t,RC}}$ over the simulated speedline with 30 % VGT from high massflow towards low massflow opening is displayed. Close to design condition 9 zones of low relative total enthalpy extraction (close to zero) can be identified close to the shroud. These zones are related with the tip leakage flow and tip leakage flow mixing with rotor wake [24] and state that work is not extracted by flow passing through the gap. Small zones of reverse flow are caused by passage flow vortexes. With reducing massflow three main changes can be highlighted:

1. The specific work extraction is increasingly nonuniform.
2. A zone of reverse flow develops and grows towards low mass flow.
3. Minimum values in tip leakage flow are reducing meaning higher impact in off-design conditions, which confirms the observation by Murugan et al. [24].

Hence, the focus of the flow analysis is put on the tip leakage flow and passage flow with reverse flow characteristic in the following section.

4.5.1 Off-Design Passage Flow Characterization

To deepen the aerodynamic understanding of the flow at extreme off-design conditions, typical one-dimensional numbers and the fluid field have been analyzed. First, further flow analysis and characteristics at low mass flow are given. Second, the arise of mass flow fluctuations has been explained. Finally, the results are discussed and certain aspects are highlighted and concluded.

4.5.1.1 Steady Flow Analysis

In Figure 4.10 the stage loading coefficient has been plotted against the flow coefficient for the whole simulated range of steady simulations. Since the stage loading coefficient is often simplified for conditions where the tangential outlet flow component is negligible as it has been shown by [95] and this simplification is not valid for the observed extreme off-design conditions, the following equation has been used:

$$\psi = \frac{\Delta h_\mathrm{t}}{U_\mathrm{in}^2} = \frac{c_{\theta,\mathrm{in}}}{U_\mathrm{in}} - \frac{\overline{r}_\mathrm{out}}{r_\mathrm{in}} \cdot \frac{c_{\theta,\mathrm{out}}}{U_\mathrm{in}}. \tag{4.3}$$

Here c_in has been calculated as the mass flow average in the inlet of the rotational domain and c_out as the mass flow average in the outlet of the rotor domain. The flow coefficient has been calculated as:

$$\phi = \frac{c_\mathrm{ax.,out}}{U_\mathrm{in}}. \tag{4.4}$$

In Figure 4.10 a sudden change in the slope of the data can be found when the stage loading coefficient is low and the flow coefficient around 0.3. This effect seems to be more distinctive with closing VGT position. Analyzing the flow field in the turbine outlet, a reduction of the axial velocity close to the turbine hub can be noted. In results with even further reduced mass flow, negative axial velocities in this region have been found. The arise of this effect could cause a reduction of the flow coefficient and thus, the change of the slope. It is worth highlighting, that although both simulated speeds at 30 % VGT positioning generate very different power and differ significantly in rotational speed, the moment of occurring reverse flow can be found at very close positions in the representation in Figure 4.10. According to Equation 4.3 this means that the specific enthalpy drop is rather high when the reverse flow arises at high speed. Here, this results in high efficiencies while the back flow is occurring at higher speed. For the case at 6715 rpm/$\mathrm{K}^{0.5}$ reduced speed 42 % efficiency with a power output of 1212.9 W has been calculated for the running point after the distinct change of the slope and occurring back flow.

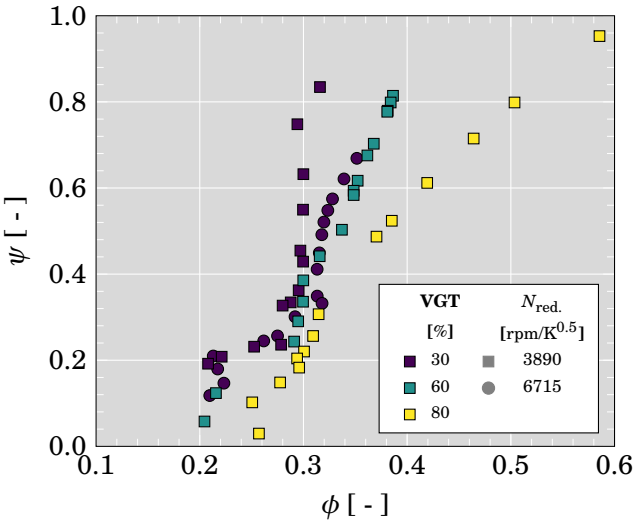

Figure 4.10: Stage loading coefficient vs. flow coefficient at 3890 rpm/K$^{0.5}$ and 6715 rpm/K$^{0.5}$.

4.5.1.2 Unsteady Flow Analysis

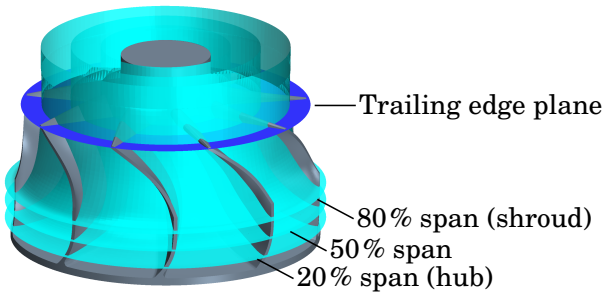

Figure 4.11: Considered planes for result plotting.

In unsteady results, as well as in steady results a back flow into the rotor wheel has been observed. Here, only the flow field results of the unsteady CFD simulations at the lowest achieved mass flows at 30 % and 80 % VGT opening and at 3890 rpm/K$^{0.5}$ are presented. With 80 % opening the current total to static pressure ratio is 1.076, the reduced mass flow 0.329 kgK$^{0.5}$bar^{-1}. The results for 30 % are shown when the turbine operates under a total to static

pressure ratio of 1.114 and a reduced mass flow of 0.274 $\mathrm{kg\,K^{0.5}\,bar^{-1}}$. As it can be seen in Figure 4.11 the following instantaneous results have been presented in the rotor outlet section and at constant span surfaces, according to Drela and Youngren [96].

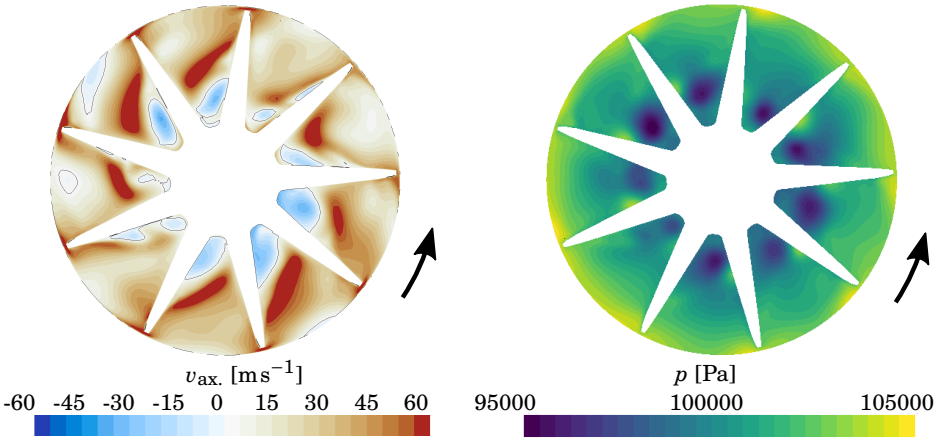

(a) Axial velocity. (b) Static pressure.

Figure 4.12: Trailing edge plane for 80 % VGT opening at 3890 $\mathrm{rpm/K^{0.5}}$; lowest simulated mass flow.

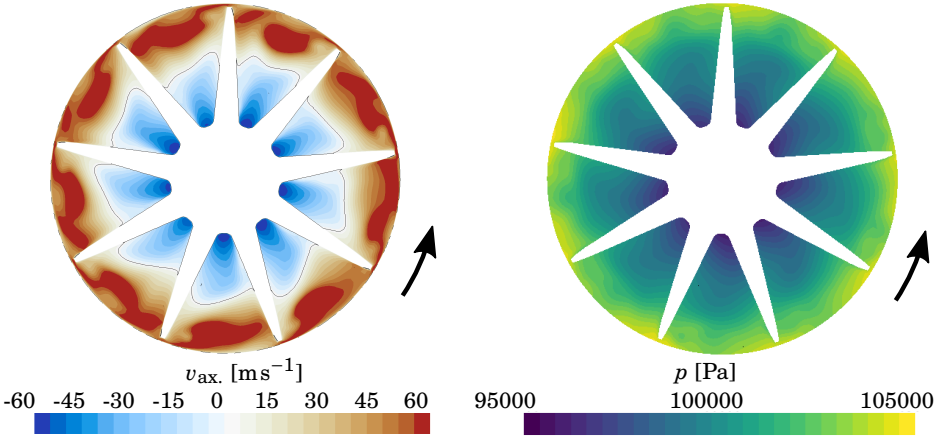

(a) Axial velocity. (b) Static pressure.

Figure 4.13: Trailing edge plane for 30 % VGT opening at 3890 $\mathrm{rpm/K^{0.5}}$; lowest simulated mass flow.

Looking at the axial velocity component $c_{ax.}$ shown in Figure 4.12(a) and in Figure 4.13(a), regions of reverse flow close to the rotor hub can be recognized for both VGT positions. The solution for 80 % VGT opening (Figure 4.12(a)), that resolves slightly higher mass flow has smaller zones of back flow. This back flow consists of 6 % of the net mass flow in the considered plane. Furthermore, the shape is not evenly developed in all rotor passages, so that the flow shape is not stable and highly transient as it can be seen in Figure 4.7.

In Figure 4.13(a) the back flow characteristic has a similar dispersion in all rotor passages. The reverse flow is outspread up to the middle of the passage in spanwise direction. 38.4 % of the net mass flow is passing the plane at the trailing edge in reverse direction. At the same time, the back flow effects a restriction of the fluid following the conventional flow direction. This results in higher axial velocities close to the shroud. Even when the flow seems to be completely developed it has fluctuating mass flow as it has been shown before in Figure 4.6.

The presented pressure profiles in Figure 4.12(b) and Figure 4.13(b) show continuously rising pressure with increasing radius according to Equation 4.1. However, the 80 % VGT case shows higher gradients close to the hub where reverse flow has been found, while the pressure field of the 30 % VGT case looks smoother. Thus, radial flow might be initiated where the high gradients occur.

In Figure 4.14 and Figure 4.15 the blade-to-blade views at constant span that have been introduced by Figure 4.11 are presented. By high friction loss levels in the turbine outlet vortex the reverse flow vortex turns in contra rotating direction inside the rotational reference frame and enters through the wheel outlet back into the turbine rotor passage at 20 % span. Thus the reverse flow is directed towards the rotor suction side. Since the back flow is not stable in the passages in 20 % span at 80 % VGT opening many different flow shapes like cross flow from the suction side (SS) towards the pressure side (PS) or reverse flow separations at the trailing edge can be observed. In most of the passages in Figure 4.14 (20 % span) and in all passages visible in Figure 4.15 (20 % span) the back flow reaches the rotor region of radial inflow. There the back flow collides with the rotor inflow, which is rolled up as a vortex due to the high negative incidence in the calculated running conditions. At 50 % span, the mixing of both contrary flows takes place. Even when in Figure 4.14 (50 % span) the downstream flow already dominates, high disturbance of the flow with high velocity gradients at around 50 % chord length can be recognized. For the case shown in Figure 4.15 (50 % span) the direction of the flow close to the rotor trailing edge is still predominantly upstream orientated. It is worth highlighting, that the rather slow core flow in Figure 4.14 (50 % span) is downstream directed while the flow close to the blade walls keeps its reverse direction in most of the passages. Finally, at 80 % span the flow in conservative flow direction dominates.

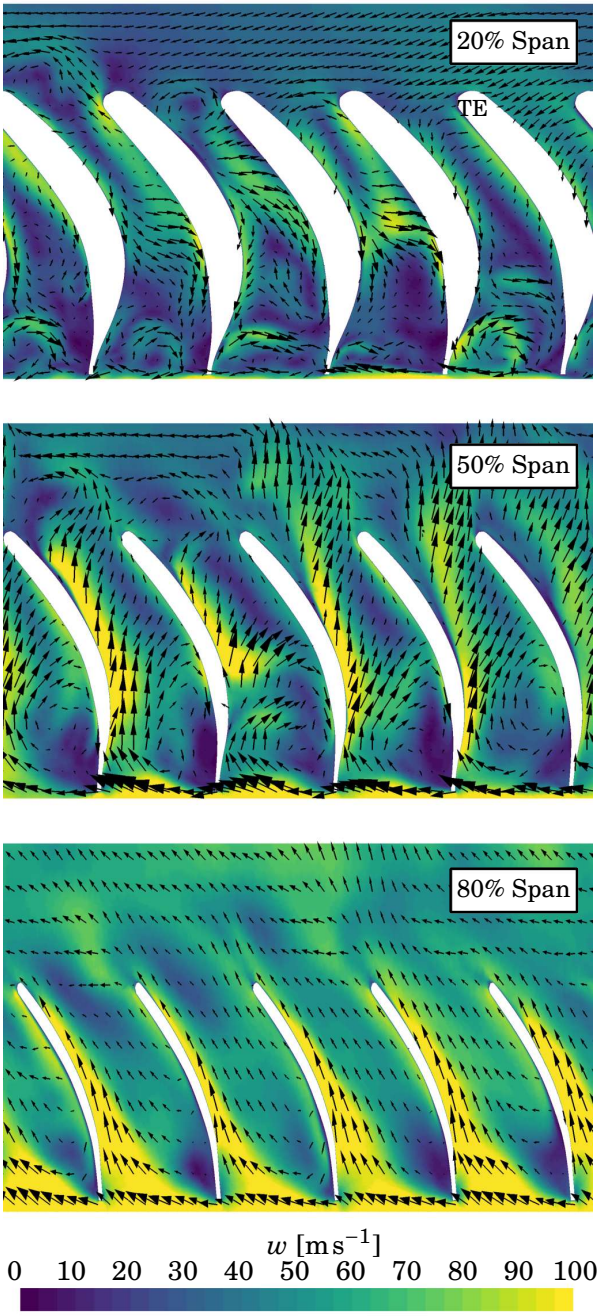

Figure 4.14: 80 % VGT opening at 3890 rpm/K$^{0.5}$ over 5 rotor passages; lowest simulated mass flow; velocity in rotational frame (w).

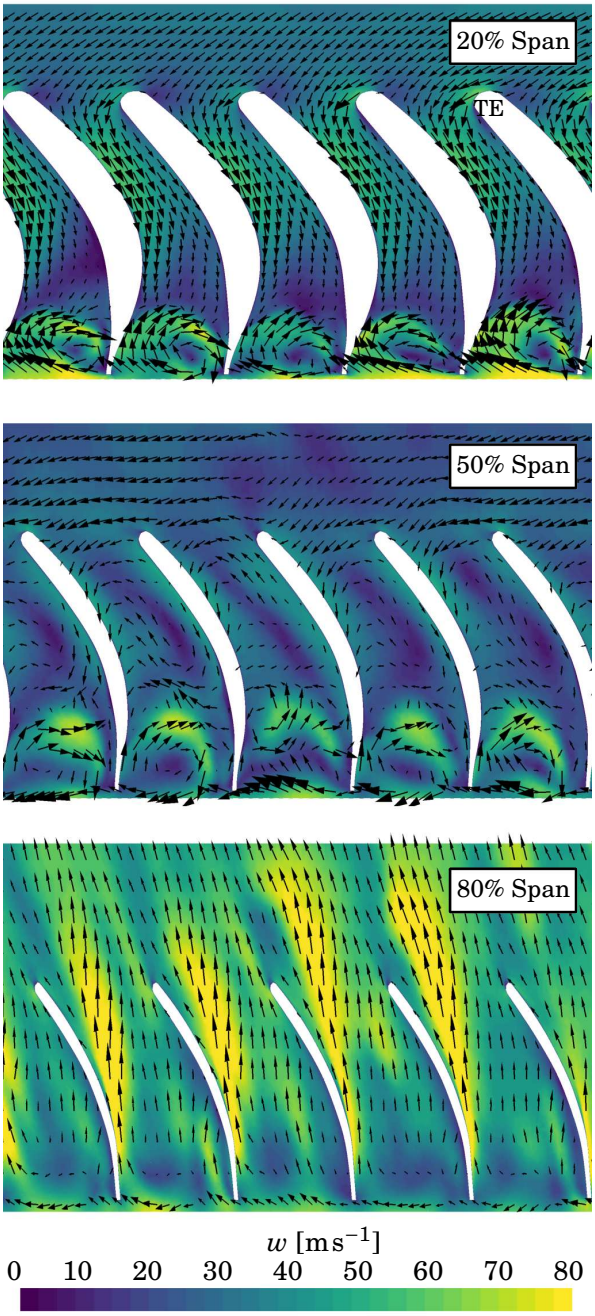

Figure 4.15: 30 % VGT opening at 3890 rpm/K$^{0.5}$ over 5 rotor passages; lowest simulated mass flow; velocity in rotational frame (w).

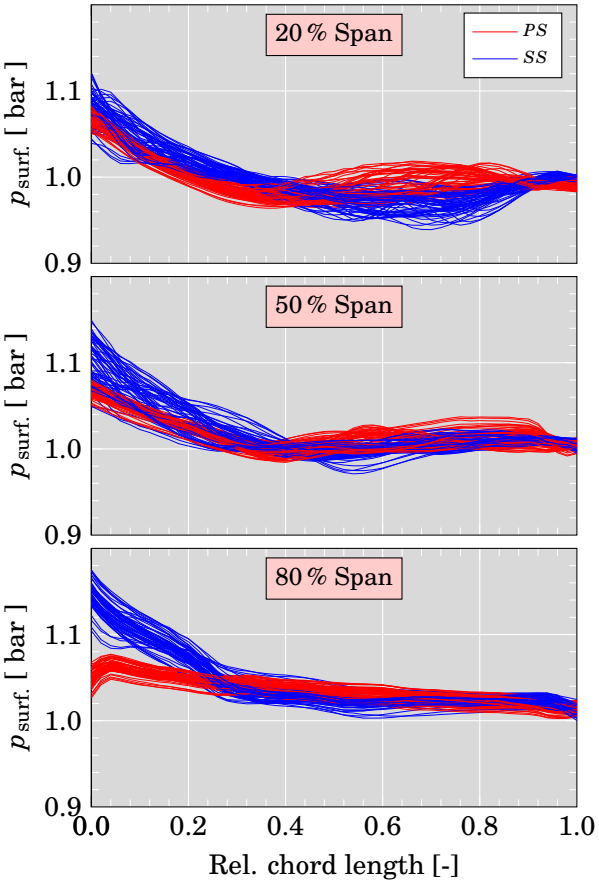

Figure 4.16: Pressure profiles for 80 % VGT opening; lowest simulated mass flow.

For analyzing the transient behavior of the reverse flow and the occurrence of mass flow fluctuations, that have been highlighted in Figure 4.6 and Figure 4.7, despite constant boundary conditions, transient surface pressure profiles are shown in Figure 4.16 and in Figure 4.17. In general, the influence of the extremely high incidence can be observed in both cases, which also introduces instability on the flow field. Apparently, the incidence for the case of 80 % VGT opening is more distinct. Also worth highlighting is the switch of SS and PS (due to the incidence of the backflow), which could provoke the aforementioned cross flow. For the case of 30 % VGT opening the SS and PS are switched over the entire chord length at almost every time step at 20 % and 50 % span, where also the back flow has been identified. In Figure 4.17 at 20 % span an unstable flow separation on the PS can be observed at 0.2 rel. chord length, where the reverse flow faces increasing adverse pressure gradients. As it can be seen in Figure 4.17

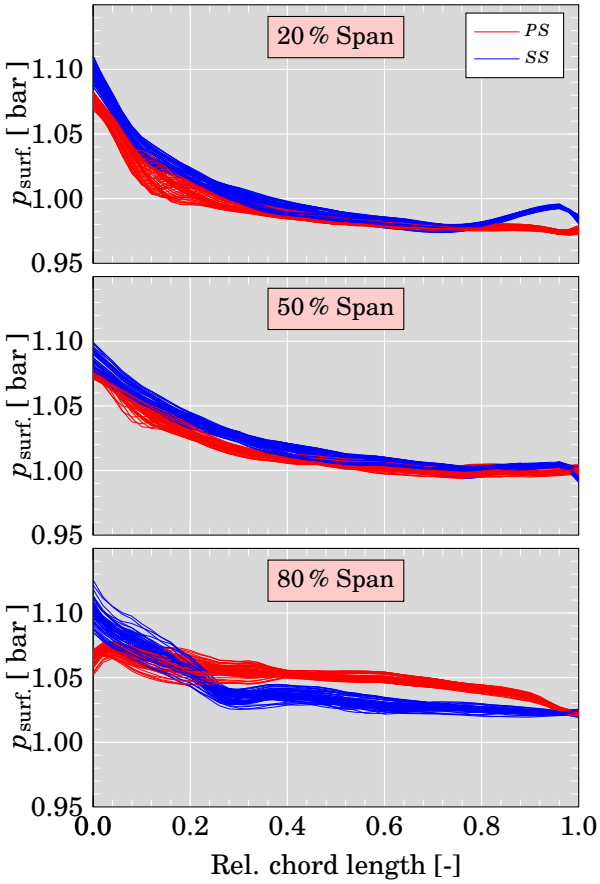

Figure 4.17: Pressure profiles for 30 % VGT opening; lowest simulated mass flow.

at 50 % and at 80 % span, the mentioned fluctuation introduces instability in these spans. Thus, the mass flow of the back flow mixes time dependent with the main flow, which can result in observed mass flow fluctuations of this case. In the case of 80 % VGT opening (Figure 4.16) highly transient behavior can be observed at lower spans directly after the revers flow enters in the passage. Possibly the aforementioned high pressure gradients (Figure 4.12(b)) cause radial flow and higher mixing with the main flow between 0.4 and 0.9 rel. chord length.

Resulting from surface pressure profiles the spanwise loading has been presented in Figure 4.18 and in Figure 4.19. The spanwise loading is mainly negative, which concurs with the measurement of negative efficiency and negative power (Figure 3.10(b) and Figure 4.5(b)). Furthermore, it can be seen that

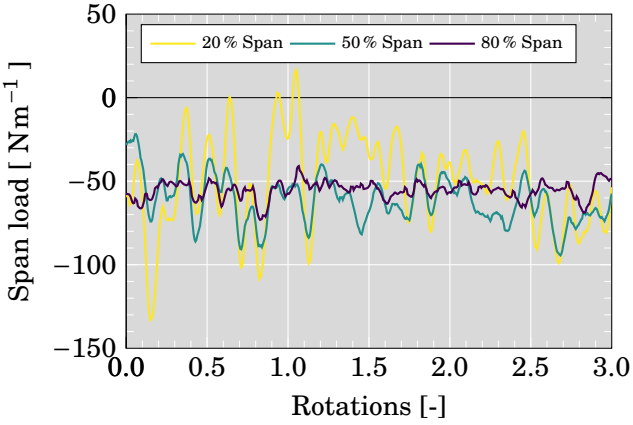

Figure 4.18: Spanwise loading for 80 % VGT opening; lowest simulated mass flow.

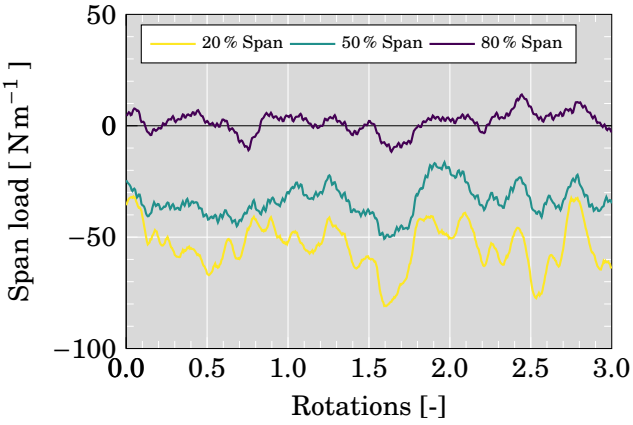

Figure 4.19: Spanwise loading for 30 % VGT opening; lowest simulated mass flow.

the flow at lower span (where reverse flow exists) initiates the main transient instability in the flow.

Since the validation has been executed at rather low reduced speed and very low mass flow, a further unsteady simulation at 6715 rpm/K$^{0.5}$ has been simulated (Figure 3.10(b) and Figure 4.5(b)). Here a back flow of 2 % from the net mass flow has been found in the trailing edge plain working with a rather high reduced mass flow of 0.61 kgK$^{0.5}$bar^{-1} and 1335 W power output.

4.5.1.3 Discussion

At low mass flow the flow exits the rotor with a naturally high tangential velocity component in the rotating direction of the rotor wheel. According to the approximated equation in Equation 4.1 this results in a radial static pressure gradient. Consequently the flow tends to flow to smaller radius and further following the pressure gradient resulting in a back-flow region that grows continuously from the hub surface when reducing the mass flow. Considering the observations of negative mass flow in turbines at pressure ratios higher than one done by [32, 33] this could lead to a transition from net positive mass flow towards net negative mass flow. It can be assumed that the back flow region grows from the hub up to the shroud, so that the net mass flow becomes negative. The initiating and fast growing of this phenomena explains the measured sudden drop of reduced mass flow when decreasing pressure ratio (Figure 3.10(b)). Furthermore, the observed change in the trend of ϕ in Figure 4.10 shows that the representation of ψ vs. ϕ is an efficient way to identify the arise of this phenomena at early stages.

As it has been demonstrated, reducing the pressure ratio can affect mass flow fluctuations with high frequencies. This could possibly be a critical factor for the turbine rotor stability comparable to compressor rotating stall for the compressor wheel.

On the one hand side, observed back-flow affects the energy transformation by the turbine, since the effective area of the exiting flow has been restricted towards higher radius. This way the full advantage of the radial machine cannot be used according to Euler's turbomachinery equation. On the other hand side, the reverse flow causes an local increase of mass flow and allows to extract energy from the flow again. In Figure 4.9 it can be seen that the reverse flow enters with a slightly lower $\Delta h_{\mathrm{t,RC}}$ as the flow that exits at mid chord. Hence, it can be assumed additional energy is extracted after the mixing of both contrarious flows. Thus, the energy extraction might be increased slightly while the pressure losses rise due to the mixing process.

Nevertheless, no noticeable sudden change in the efficiency curve in Figure 4.8 (or 3.10, 3.13, 3.15) or in the power curves in Figure 4.5 (b), (d), (f) can be identified. The lower slope of the stage loading coefficient in Figure 4.10

indicates that the reduction in specific total enthalpy drop per flow coefficient is less in off design condition. This could be caused by the aforementioned positive side effects on the power extraction. At the same time the mass flow and following the flow coefficient could be reduced due to rising pressure losses. This way both effects might be compensated so that changes in power output and efficiency are rather hidden. The almost vertical reduced mass flow curve at 30 % VGT opening and 3890 rpm/$K^{0.5}$ in Figure 4.5(a), where the reverse flow was observed most dominant could be affected by this effect. Also the observed drop of the reduced mass flow in subsection 3.3.3 also with 30 % VGT opening can be explained by this effect (Figure 3.11).

4.5.1.4 Conclusions

1. Increments in the reduction trend of load coefficient vs. flow coefficient can indicate the arise of reverse flow at the turbine rotor outlet and change less when rising the reduced speed significantly. For different speedlines and VGT positions the slope changes almost at the same coordinate.

2. When the turbine pressure ratio and thus, the mass flow decreases, the flow has a continuously growing swirl component. Hence, a radial static pressure gradient develops in the rotor outlet. This generates a back flow from the outer radius towards the hub and the flow rolls back into the turbine passage.

3. The reverse flow provokes instable flow conditions in the rotor passage resulting in time dependent mass flow fluctuations.

4. The back-flow characteristic has arisen at a moderate reduced speed of 3890 rpm/$K^{0.5}$ around efficiencies bigger than zero while the point of zero power production has become of interest for automotive industry. At higher speeds the reverse flow has been identified at moderate efficiency.

5. On the one hand side, the reverse flow restricts the passage area close to the hub so that it can not fully be taken advantage of the work extraction due to a reduction of the flow radius. On the other hand side, the reentering flow increases locally the mass flow and enthalpy can be extracted from the reverse flow. The flow mixing is expected to increase pressure losses. Hence, the impact on the efficiency might be of lower magnitude but the mass flow rate might be reduced.

6. The modeling of this effect is challenging since it only appears in extreme off-design conditions and is highly dependent on the radial pressure gradients downstream the turbine wheel. Hence, the fitting of a one-dimensional sub-model with typically available map data is not possible.

4.5.2 Rotor Tip Leakage Flow

First, further simulation results at different rotational speeds are presented and tip leakage flow has been analyzed in detail. Second, an commonly used methodology for the characterization of tip leakage flow has been assessed.

4.5.2.1 Tip Leakage Flow Analysis in Design & Off-Design

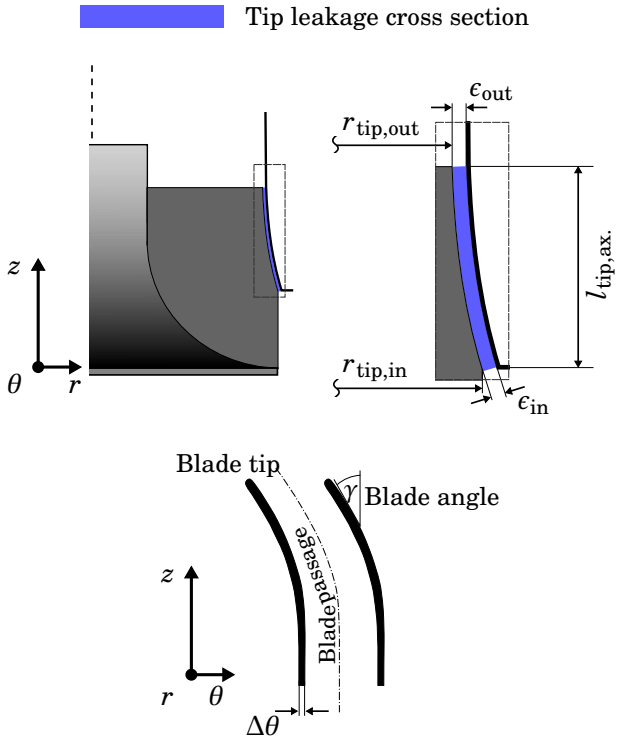

Figure 4.20: Tip geometry nomenclature.

The rotor is shown in Figure 4.1 and has the geometrical tip properties presented in Table 4.1. Tip clearance dimensions considered in Table 4.1 correspond to the *cold* geometry and the nomenclature definition in Figure 4.20. Modification of the tip profile due to the impeller thermal and centrifugal deformation (see [82]) is therefore neglected in this work.

To be able to analyze the tip leakage effect, which highly depends on the rotational speed, further simulations of the speedlines 1710 rpm/K$^{0.5}$ and 6715 rpm/K$^{0.5}$ have been executed with the VGT openings of three different VGT positions (30 %, 60 %, 80 %) and the same numerical setup as presented in section 4.2. Overall, results from 122 simulations of three different VGT

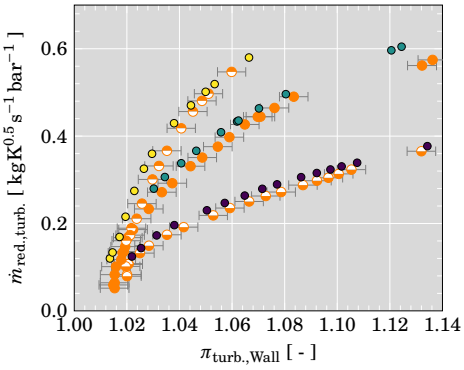

(a) $\dot{m}_{red.}$ at 1710 rpm/$K^{0.5}$.

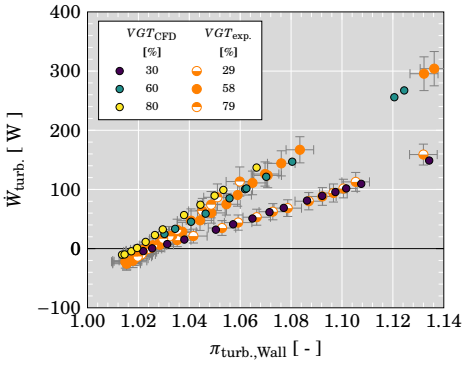

(b) $\dot{W}_{turb.}$ at 1710 rpm/$K^{0.5}$.

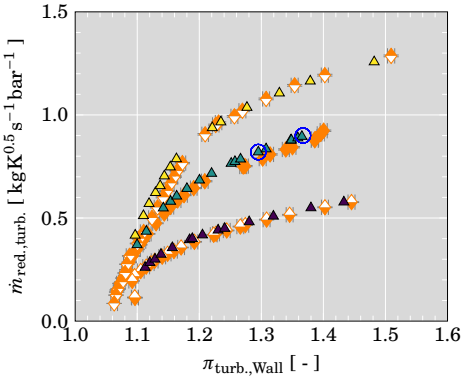

(c) $\dot{m}_{red.}$ at 3890 rpm/$K^{0.5}$.

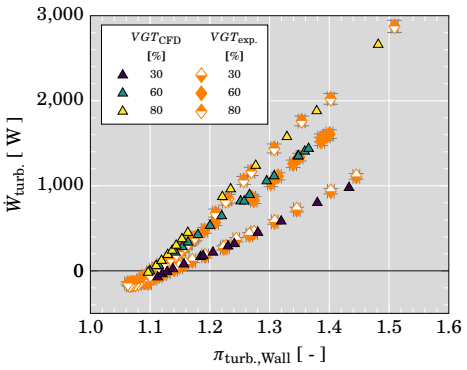

(d) $\dot{W}_{turb.}$ at 3890 rpm/$K^{0.5}$.

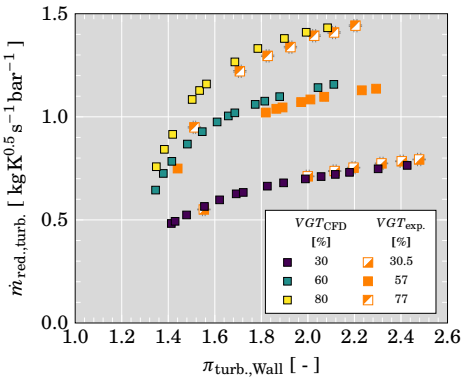

(e) $\dot{m}_{red.}$ at 6715 rpm/$K^{0.5}$.

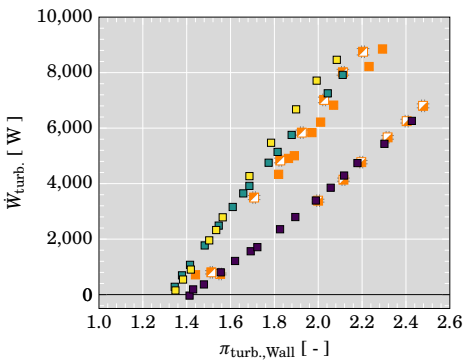

(f) $\dot{W}_{turb.}$ at 6715 rpm/$K^{0.5}$.

Figure 4.21: Reduced mass flow rate (left) and turbine power (right) for different reduced isospeeds.

positions and three different rotational speeds (1710 rpm/K$^{0.5}$, 3890 rpm/K$^{0.5}$, 6715 rpm/K$^{0.5}$) have been obtained. Thus, 9 speedlines, starting from design conditions down to even negative power output, have been employed as it can be seen in Figure 4.21.

The mesh convergence in the tip region was analyzed separately by doubling the mesh density without a considerable change in the tip leakage mass flow. In design conditions the negative leakage mass flow varies by 2.1% and the positive leakage mass flow by 1.3%. In off-design conditions variations are below 1%, when doubling the cells in the tip gap. The VGT opening was varied until the mass flow rate of the points at 3890 rpm/K$^{0.5}$ and with highest expansion ratio are obtained as explained in section 4.2. Therefore, numerical predictions for this speed show very good agreement with experimental results. The experimental measurements of other speeds were obtained during different measurement sessions, so that the experimental VGT position differs slightly for different speeds. The VGT position of the numerical model has not been further adjusted for the remaining speeds to allow a consistent CFD database. However, Figure 4.21 shows that the qualitative behavior of reduced mass flow and turbine power has been reproduced with an overall good quality for the highest and lowest simulated speeds.

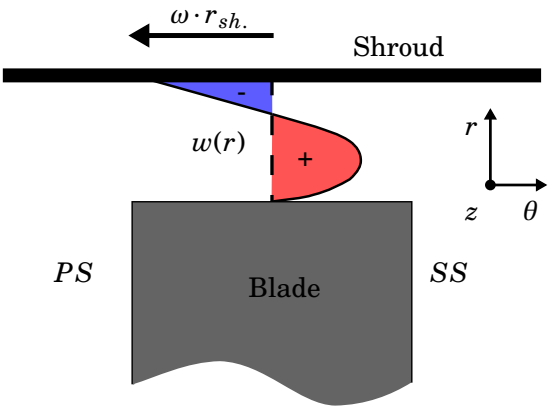

Figure 4.22: Tip leakage flow definition in rotating reference frame

In the following, the nomenclature for positive and negative tip leakage flow has been used according to Figure 4.22. Relative positive flow is directed towards the blade suction surface (SS) and relative negative flow towards the blade pressure surface (PS). Although positive and negative mass flows are provoked by different physical effects, both are considered as loss sources. Thus,

mass flow ratios into both directions are summed to highlight the overall impact of the existing tip gap.

$$\frac{\dot{m}_{\mathrm{tip},+}}{\dot{m}_{\mathrm{turb.}}} = \frac{\int \rho \cdot w_{\perp,\mathrm{tip},+}\,\mathrm{d}A_{+}}{\dot{m}_{\mathrm{turb.}}} \tag{4.5}$$

$$\frac{\dot{m}_{\mathrm{tip},-}}{\dot{m}_{\mathrm{turb.}}} = \frac{\left|\int \rho \cdot w_{\perp,\mathrm{tip},-}\,\mathrm{d}A_{-}\right|}{\dot{m}_{\mathrm{turb.}}} \tag{4.6}$$

$$\frac{\dot{m}_{\mathrm{tip}}}{\dot{m}_{\mathrm{turb.}}} = \frac{\dot{m}_{\mathrm{tip},+}}{\dot{m}_{\mathrm{turb.}}} + \frac{\dot{m}_{\mathrm{tip},-}}{\dot{m}_{\mathrm{turb.}}} \tag{4.7}$$

The integrals have been taken over the tip gap along the edge at the SS of the blade. Figure 4.23 shows the relative mass flow passing the tip gap with the definition of Equation 4.7 at all simulated running points. Apparently, the overall leakage flow ratio is higher at closer VGT openings. It can be seen that between 5 % and 9 % of the net mass flow passes the tip gap at higher simulated pressure ratios for different VGT openings at 1710 rpm/K$^{0.5}$. This variation diminishes with increasing speed. At the highest speed and high pressure ratios, the leakage flow ratio ranges between 6 % and 8 %. Reducing the pressure ratio, the leaking mass flow ratio decreases first for 1710 rpm/K$^{0.5}$ and 3890 rpm/K$^{0.5}$ while it rises slightly for 6715 rpm/K$^{0.5}$. Going to very low pressure ratios the tip leakage ratio shows a sharp increase. This confirms the importance of the tip leakage flow and losses at extreme off-design conditions.

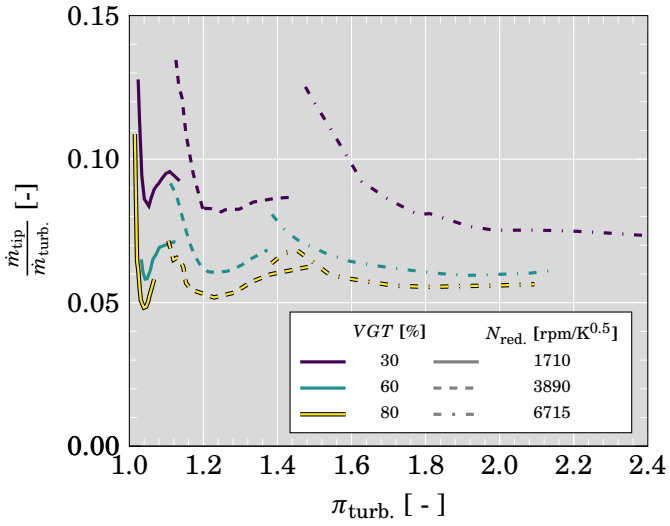

Figure 4.23: Overall relative mass flow fraction trough the rotor tip gap.

As mentioned before, the tip leakage flow of traditional radial turbines can be distinguished between certain zones of positive and negative (due to higher circumferential speed at the rotor inlet) mass flow over the tip gap along the chord length ([62]). Following, mass flows in both directions have been analyzed in detail for the observed radial turbine. In Figure 4.24 the relative tip leakage velocity $w_{\perp,tip}$ is shown at all three rotational speeds in the running points of highest and in Figure 4.25 of lowest simulated expansion ratio for 60 % VGT opening. It can be seen that the extension of regions with positive and negative

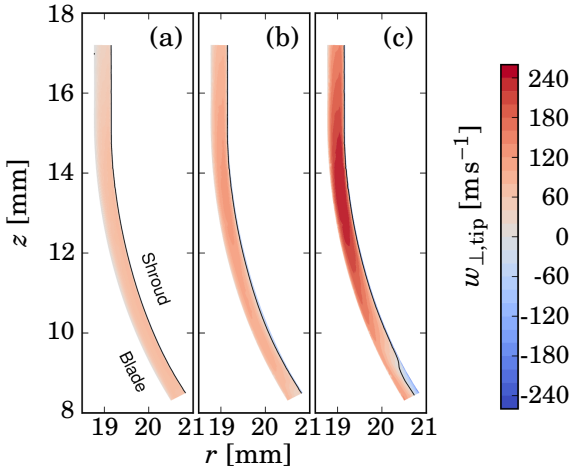

Figure 4.24: Tip leakage flow along the suction side edge at highest simulated $\pi_{\mathrm{turb.}}$: 1.12 in (a), 1.37 in (b), 2.11 in (c) with 60 % VGT opening; Solid black line corresponds to $w = 0$.

flow changes significantly from high pressure ratio points (Figure 4.24 (a), (b), (c)) to low pressure ratio points (Figure 4.25 (a), (b), (c)). The extension of the positive flow dominates clearly the one of the negative flow. The later, induced by shroud friction, is negligible at higher expansion ratios over the majority of the chord length. An increase of positive leakage flow over the tip leakage is visible when the rotational speed and thus the blade loading rises. At the same time, the positive tip leakage velocity diminishes in the inlet region of the rotor with increasing rotational speed. This might be affected by the higher negative incidence at faster wheel rotation as it can be seen in Figure 4.28. Nevertheless, Figure 4.26 shows that the negative incidence is not high enough to cause a swapping of the local pressure gradient at 6715 rpm/K$^{0.5}$ close to the tip. Another reason for increasing negative flow can be the high negative incidence inlet flow that owns high relative inlet swirl and inertia in contrariwise

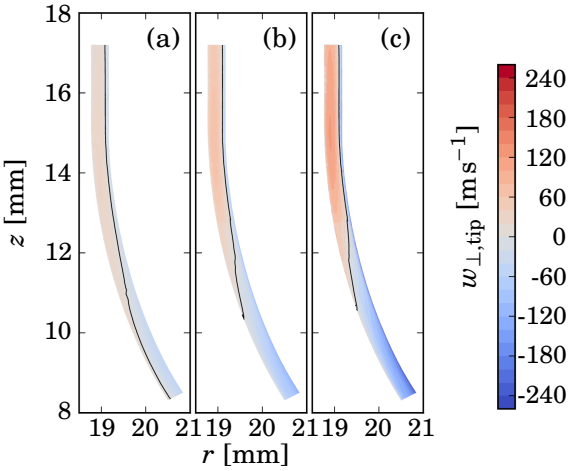

Figure 4.25: Tip leakage flow along the suction side edge at lowest simulated $\pi_{\mathrm{turb.}}$: 1.03 in (a), 1.10 in (b), 1.35 in (c) with 60 % VGT opening; Solid black line corresponds to $w = 0$.

direction. Also, the impact of shroud friction rises with increasing rotational speed and leads to more negative flow.

At reduced expansion ratio (Figure 4.25 (a), (b), (c)) the tip leakage flow behavior changes over the tip length. Two zones can be clearly distinguished. First, one zone at the outlet section, where the positive velocity flow still dominates. Although the shroud friction gains importance in this zone, the impact is rather low here. Second, one zone at the inlet section of the turbine wheel, where the negative leakage flow dominates. Although this characterization is similar to the one made by Dambach et al. [62], the origin of the negative flow in the inlet region is different. High negative incidence leads to flow separation at the leading edge and thus to a swap of the pressure potential between suction and pressure side as it can be seen in Figure 4.27. Furthermore, the negative incidence implies a high negative tangential velocity component w_θ as shown in Figure 4.28, which benefits the negative leakage mass flow.

For a more detailed view profiles of specific mass flow in blade normal direction through the tip gap are shown for two running points (marked blue in Figure 4.21(c) at 3890 rpm/K$^{0.5}$) in Figure 4.29 and in Figure 4.30. The first shows a running point close to design condition with low incidence. The later shows the flow at off-design condition and a high mean inflow incidence β of $-51°$. Since, the flow profile close to design conditions looks rather undisturbed the diminishing influence of wall friction can be observed towards higher chord length. The higher radius in the inducer of the radial turbine causes faster

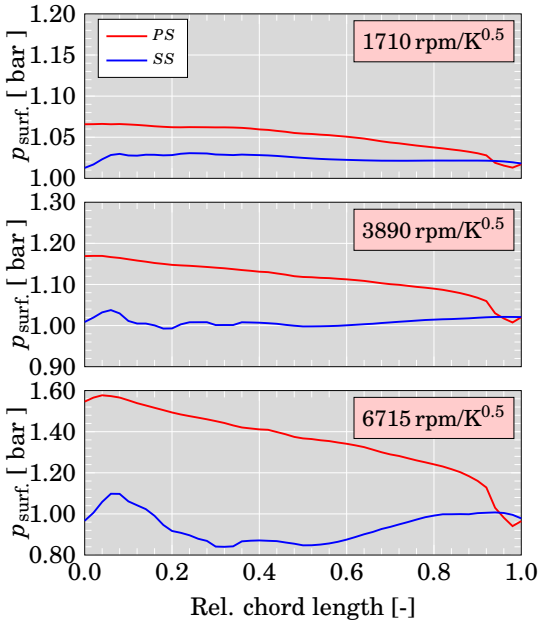

Figure 4.26: Surface pressure profiles at 95 % span at highest simulated $\pi_{\text{turb.}}$ for each speed with 60 % VGT opening ($\pi_{\text{turb.}}$:1.12 at 1710 rpm/K$^{0.5}$, 1.37 at 3890 rpm/K$^{0.5}$, 2.11 at 6715 rpm/K$^{0.5}$).

relative shroud velocity. This generates a stronger fluid dragging effect in the inducer. Hence, the maximum specific mass flow increases continuously up to a chord length of around 0.7. Looking at the profiles in Figure 4.30 a clear influence of the incidence flow can be seen. Maximums of positive specific mass flow seem to decrease by the contrariwise inflow momentum. On the one hand side, losses generated by positive tip flow might be reduced. On the other hand side, new losses are introduced by entropy increasing negative tip flow. Due to the pulsating flow in a turbocharger turbine, the turbine can operate in zones of extremely high incidences. This and the complexity of the tip leakage flow at design and off-design conditions highlights the importance of understanding the dynamic of this loss generating process.

The exclusive mass flow ratios of both contrariwise leakage streams according to Equation 4.5 and Equation 4.6 have been plotted in Figure 4.31. The positive mass flow ratio in Figure 4.31 (a) has an overall declining trend with decreasing pressure ratio $\pi_{\text{turb.}}$. However, at rather low pressure ratios some curves experience a rise for a short period. The reason for this sudden rise could be the restriction of the outlet cross section due to back flow into the rotor as

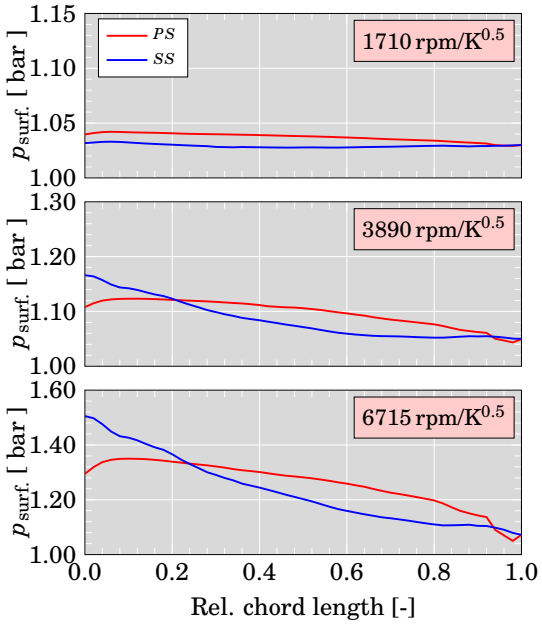

Figure 4.27: Surface pressure profiles at 95 % span at lowest simulated $\pi_{\text{turb.}}$ for each speed with 60 % VGT opening ($\pi_{\text{turb.}}$:1.03 at 1710 rpm/K$^{0.5}$, 1.10 at 3890 rpm/K$^{0.5}$, 1.35 at 6715 rpm/K$^{0.5}$).

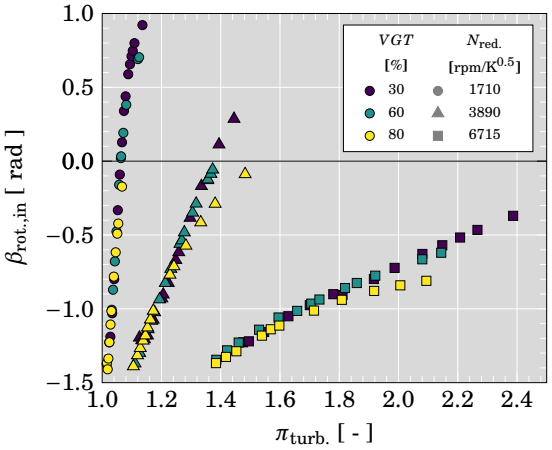

Figure 4.28: Rotor inlet angle in rotating reference frame.

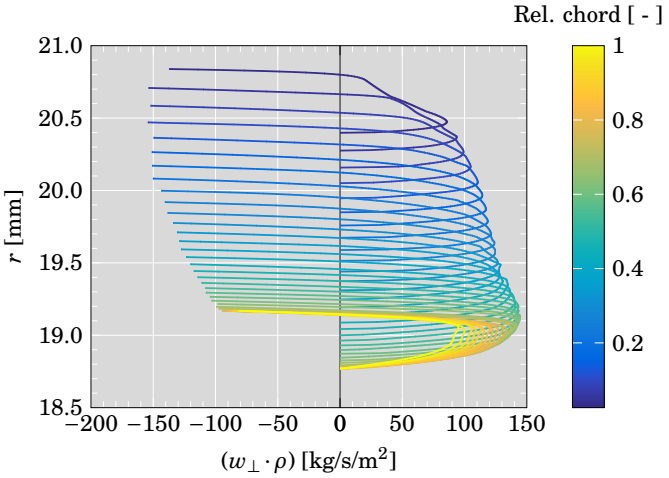

Figure 4.29: Tip leakage flow profiles of low negative incidence inlet flow over the tip gap at 3890 rpm/K$^{0.5}$ and a $\pi_{\text{turb.}}$ of 1.37.

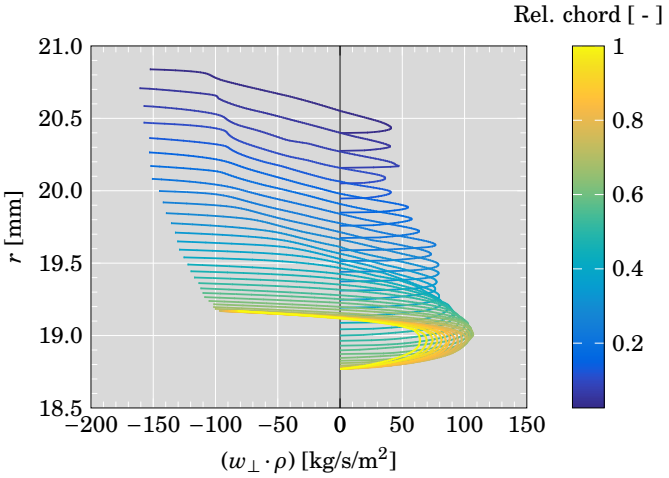

Figure 4.30: Tip leakage flow profiles of high negative incidence inlet flow over the tip gap at 3890 rpm/K$^{0.5}$ and a $\pi_{\text{turb.}}$ of 1.29.

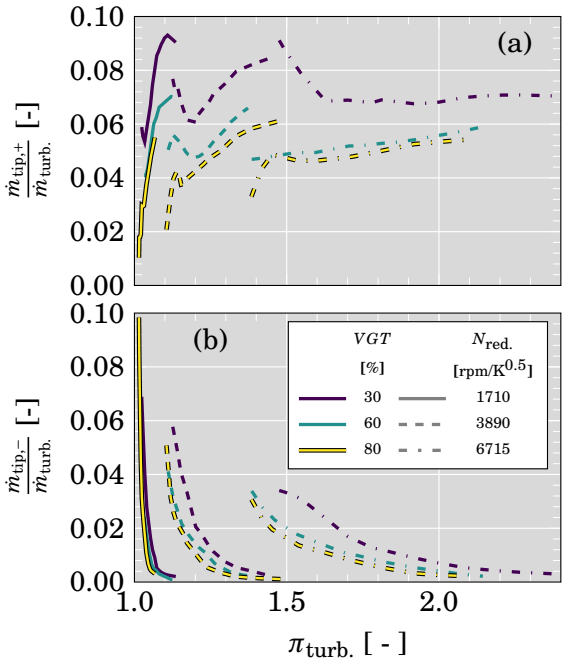

Figure 4.31: Relative tip leakage mass flow fraction: (a) flowing to blade SS; (b) flowing to blade PS.

it has been described in subsection 4.5.1. This way the positive passage flow consists of a higher mass flow than the net mass flow. At the same time the blade might become higher loaded at higher span due to the restricted flow area at the hub. The negative mass flow ratio in Figure 4.31 (b) is continuously rising for all speedlines by decreasing pressure ratio. While the negative mass flow is related to the rotational speed, the positive mass flow is rather related to the blade loading at the tip.

4.5.2.2 Geometrical Influence on Tip Leakage Flow Characteristics

As data basis for the following analysis CFD results of operating conditions in a wide range at 60 % VGT position have been used and further simulations have been executed to analyze the effect of changing tip gap height. Simulations have been executed at four different speedlines from a low reduced speed of 1710 rpm/K$^{0.5}$ up to a high reduced speed of 6715 rpm/K$^{0.5}$ while the VGT opening is set to 60 %. Each speedline has been simulated over a wide range to get a complete picture of flow conditions that can occur during transient driving conditions. The line of highest reduced speed has been further calculated with

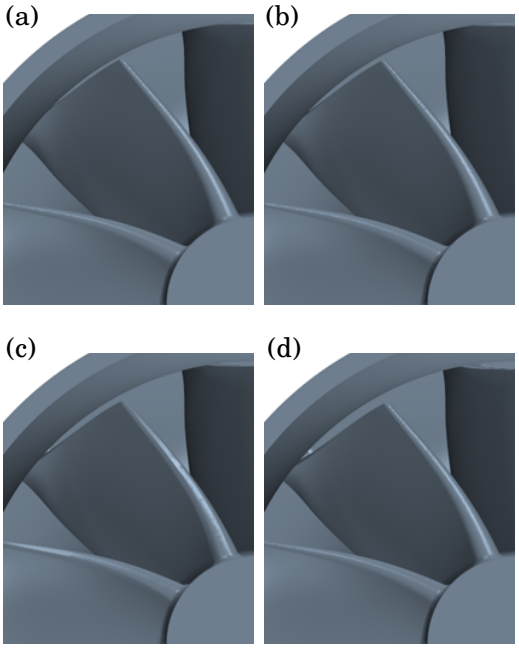

Figure 4.32: Tip gap geometry variation: (a) 50 % $\epsilon_{\text{ref.}}$; (b) 75 % $\epsilon_{\text{ref.}}$; (c) 100 % $\epsilon_{\text{ref.}}$; (d) 150 % $\epsilon_{\text{ref.}}$.

several tip gap geometries. The tip gap height has been decreased by 50 % and 25 % and increased by 50 % as it can be seen in Figure 4.32. The original shroud has been maintained and only the rotor blade has been adjusted for this modification.

Figure 4.33 and Figure 4.34 show the simulated turbine efficiency and reduced turbine mass flow of simulated cases in comparison with the experimentally obtained data. As described before, experimental variations in the VGT positioning are inherent to the VGT moving mechanism. Although this might cause small differences between experimental and CFD model VGT opening, the qualitative behavior of efficiency and mass flow curve have been well reproduced by CFD over the entire range of the 3 highest speeds with all tip gap configurations. At the lowest speed, efficiencies estimated by CFD are within the measurement errors, which are naturally high at points of low power output and small expansion ratios.

The comparison of CFD results with different tip gap heights in Figure 4.33 and in Figure 4.34 shows that this geometry change can influence significantly the turbine efficiency and rather less reduced mass flow. This has also been stated by Kammeyer et al. [63]. From the wide range data it can further be

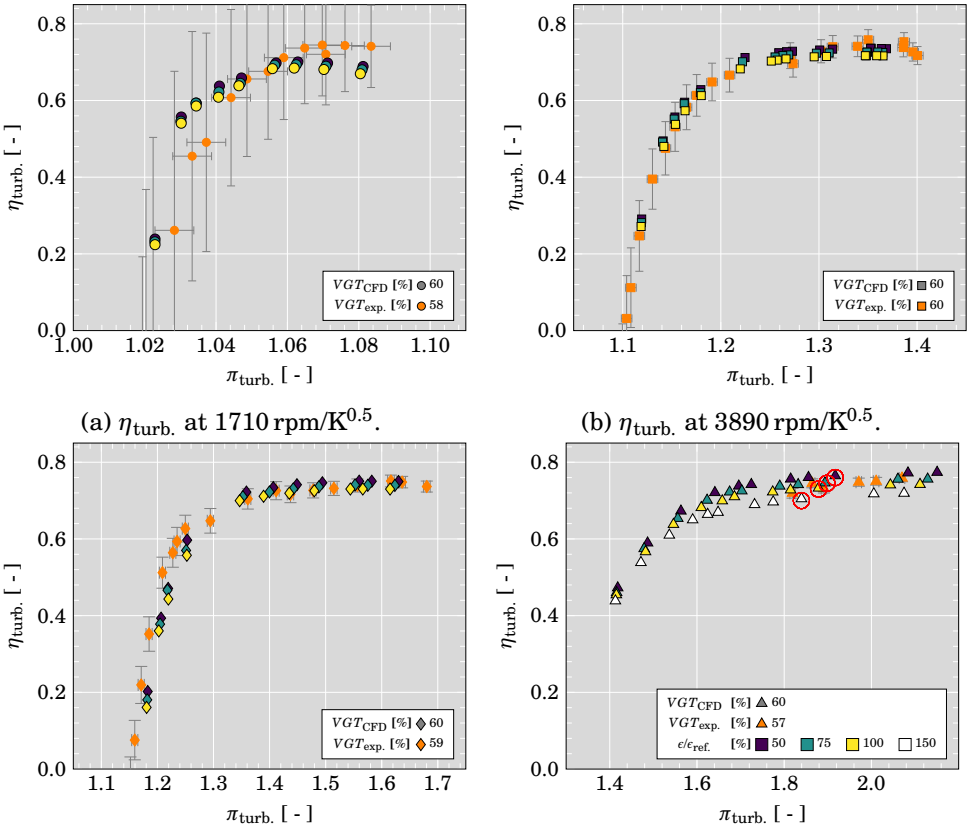

(a) $\eta_{\text{turb.}}$ at 1710 rpm/K$^{0.5}$.

(b) $\eta_{\text{turb.}}$ at 3890 rpm/K$^{0.5}$.

(c) $\eta_{\text{turb.}}$ at 4890 rpm/K$^{0.5}$.

(d) $\eta_{\text{turb.}}$ at 6715 rpm/K$^{0.5}$.

Figure 4.33: Efficiency of measured and simulated running points with different tip gap configurations.

seen that the difference in efficiency diminishes towards very low pressure ratios/high BSRs with varying tip gap height. The CFD results are consistent with the observation that tip leakage mass flow in positive direction decreases due to lower blade loading. Nevertheless, the relative part of negative tip mass flow $\frac{\dot{m}_{\text{tip,-}}}{\dot{m}_{\text{turb.}}}$ increases going towards operating conditions with low loads. Thus, increasing parts of the mass flow are not used for enthalpy extraction.

In Figure 4.35 pressure profiles for the red circles marked running points of Figure 4.33 (d) have been presented over the chord length. While the pressure profile changes rather less when the gap height is reduced, blade loading at the tip cannot be conserved in the same quality when the tip gap is 50 % increased.

Further, the simulated specific momentum trough the tip gap over a line at constant chord length has been processed from the CFD data according to

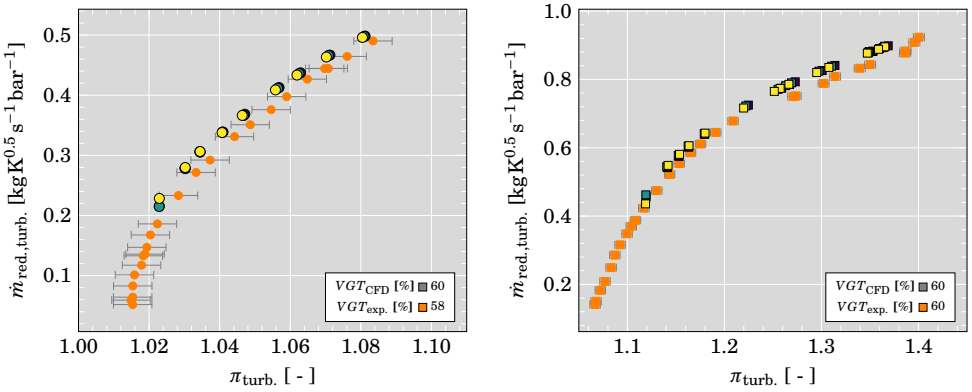

(a) $\dot{m}_{\text{red.,turb.}}$ at 1710 rpm/K$^{0.5}$.

(b) $\dot{m}_{\text{red.,turb.}}$ at 3890 rpm/K$^{0.5}$.

(c) $\dot{m}_{\text{red.,turb.}}$ at 4890 rpm/K$^{0.5}$.

(d) $\dot{m}_{\text{red.,turb.}}$ at 6715 rpm/K$^{0.5}$.

Figure 4.34: Reduced mass flow of measured and simulated running points with different tip gap configurations.

Equation 4.8 and Equation 4.9 in positive and negative direction.

$$M_{\text{tip,spec.,+}} = \int_{r_{\text{tip}}}^{r_{(w_{\perp,\text{tip}}=0)}} \rho \cdot w_{\perp,\text{tip}} \cdot w_{\perp,\text{tip}} \, \mathrm{d}r \,, \tag{4.8}$$

$$M_{\text{tip,spec.,-}} = \int_{r_{(w_{\perp,\text{tip}}=0)}}^{r_{\text{sh.}}} \rho \cdot w_{\perp,\text{tip}} \cdot w_{\perp,\text{tip}} \, \mathrm{d}r \,. \tag{4.9}$$

The simulated momentum ratio R_{CFD} has following been calculated by:

$$R_{\text{CFD}} = \frac{M_{\text{tip,spec.,+}}}{M_{\text{tip,spec.,-}}}. \tag{4.10}$$

In Figure 4.36 the ratio R from Equation 2.20 has been plotted over the chord

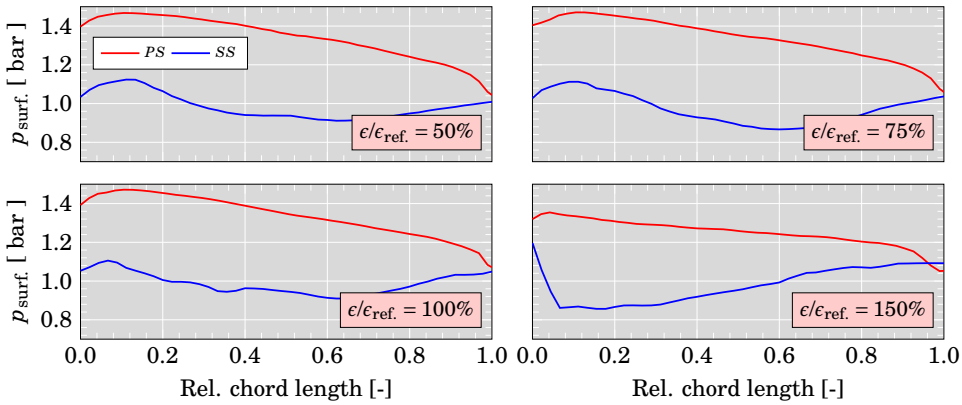

Figure 4.35: Surface pressure profiles at 95 % span for four different tip gap geometries at 6715 rpm/K$^{0.5}$ and 60 % VGT opening (red circle in Fig. 4.33 (d)).

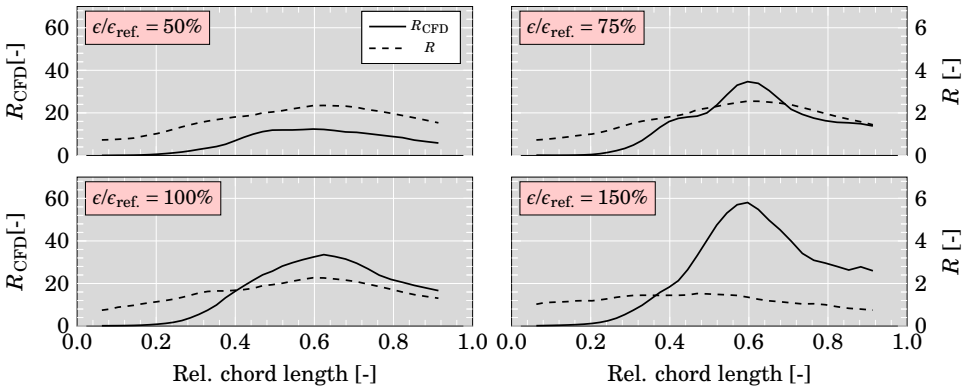

Figure 4.36: Momentum ratios R (Eqn. 2.20), R_{CFD} (Eqn. 4.10) for four different tip gap heights at 6715 rpm/K$^{0.5}$ and 60 % VGT opening (red circles in Figure 4.33 (d)).

length in comparison with R_{CFD} from Equation 4.10 for the running points with different tip gap configurations in red circles from Figure 4.33 (d) (with different y-axis for R_{CFD} and R). It can be seen that R misses the simulated momentum ratio R_{CFD} by one order of magnitude. However, the ratio R gives a rather good qualitative prediction of the maximum location of the simulated momentum ratio over the chord length for the first three tip gap setups from 50 % to 100 %. Since the pressure profile is the only input data from the fluid and no detailed tip geometry data is required for calculating R, it also fails to predict the momentum ratio growth with increasing tip gap height. With the tip gap configuration of Δr_{tip} = 150% the momentum ratio experiences an unexpected rise at around 0.6 chord length. At such a relatively high tip gap

height the flow seems to be less dominated by the pressure gradient and high values of R_{CFD} are reached by passing flow momentum from the blade passage that cannot be guided by the turbine blades. Furthermore, it can be seen in Figure 4.36 that all R_{CFD} profiles experience a sudden drop towards the turbine inlet. This drop has four main sources:

1. Higher shroud friction influence due to angle between blade and rotational axis (blade surface angle γ) in the inducer [62].
2. Slightly higher shroud radius and thus, increased shroud friction [62].
3. High impact of inflow momentum due to negative incidence.
4. Swapped pressure gradient due high negative incidence and flow separation at the leading edge.

The incidence flow through the tip gap causes an entropy increase and can be considered as additional loss. Furthermore, the determination of related mass flow and momentum is rather challenging since the aforementioned effects are mixed.

4.5.3 Conclusions

1. Steady state simulations at four different reduced speeds with three different tip gap variations (four tip gap variations at highest speed) have been executed in a wide range of operating conditions.
2. Incidence flow has been identified to influence the tip leakage specific mass flow and momentum. While it reduces the pressure induced specific mass flow in the tip gap at low chord length, the incidence inflow leads to an increase of inverse directed specific mass flow and momentum, which causes a further entropy rise.
3. Steady CFD simulations of a turbocharger radial turbine have shown that up to 14 % of the mass flow can pass through the rotor clearance at off-design conditions. Depending on the VGT position the mass flow ratio ranges from 5 % to almost 10 % at design condition.
4. Different causing effects are dominating at certain running conditions. While the leakage mass flow driven by the pressure gradient between suction and pressure surface dominates at design conditions, shroud friction and high incidence effects provoke contrariwise leakage mass flow at off-design conditions. The contrariwise leakage due to shroud friction can be neglected in design points but dominates the tip clearance in the rotor inlet section when operating in extreme off-design conditions.

5. Backflow close to the hub of the rotor can restrict the rotor effective area and increases the blade loading close to the rotor tip while the turbine pressure ratio becomes lower. This increases the pressure gradient driven mass flow after a decrease due to reducing blade loading.

6. The ratio of friction and pressure ratio driven momentum has been analyzed and it has been stated that available correlations are not capable of doing quantitative conclusions of tip leakage flow over the chord length and neither qualitative conclusions of tip gap geometry changes.

CHAPTER 5

1D Turbine Modeling

Contents

5.1 Introduction

Two main flow phenomena were analyzed in chapter 4. While it is assumed that the reverse flow phenomena shows no important influence on power or efficiency curves, the impact of the tip leakage loss is significant. Furthermore, changes of tip leakage flow characteristics with changing operation point or geometry must be modeled and included into an one-dimensional efficiency extrapolation model. Hence this section has been focused on the modeling and characterization of tip leakage losses and following on the development of an entire efficiency extrapolation model to achieve off-design performance data.

5.2 Tip Leakage Loss Model & Flow Characterization Method

Although much research has been done in the field of turbine tip leakage modeling yet, the need of fitting broad range data and later extrapolation towards extreme off-design condition requires a novel model which can estimate losses at different rotational speeds and loadings. Furthermore, turbocharger turbines are operating under very high rotational speeds and own different geometrical properties. No analysis of turbocharger turbine tip leakage flow in this wide range of data has been found in the literature. This thesis presents a tip leakage analysis based on the validated wide range CFD data presented in section 4.4 as well as a novel tip leakage loss and leakage mass flow model to allow consistent data fitting and to extrapolate the data reliably.

The objective of this chapter of the thesis is to find an aerodynamically based correlation that can predict the momentum ratio of friction and pressure induced flow for changed geometries and for a wide range of operating conditions, that can be used in one dimensional modeling and further analysis. Therefore, the simulated data base has been presented and shortly analyzed. Following, the new correlation for the tip momentum ratio has been derived. Finally, results and possible fields of application are shown.

5.2.1 Tip Leakage Loss & Mass Flow Model

To allow the modeling of wide range data, the new model has to consider effects which are dominant at low mass flows rates and effects of high dominance at higher mass flow rates. Especially for map extrapolation purposes, it is important to model both conditions as well as a transition phase in good quality. Here, data are usually fitted by means of measurements close to the optimum efficiency point and are extrapolated towards map regions of lower pressure ratio and mass flow. The portion of the total tip leakage mass flow (Equation 4.7)

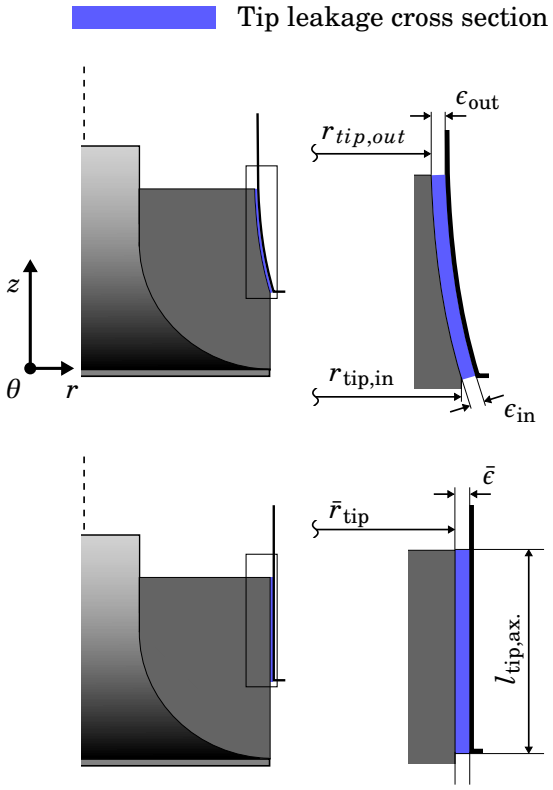

Figure 5.1: Geometry simplification of rotor tip gap.

rises towards very low turbine mass flow and contributes significantly to the loss system. Thus, the new model has been derived from the Navier Stokes Equation in a cylindric rotating reference frame relying on geometrical simplifications which are later fit by a geometrical coefficient. The main geometrical assumption which allows most of the following aerodynamic simplifications is shown in Figure 5.1.

Since most tip gaps in radial or mixed flow turbocharger turbines have a rather low variation in radial direction, the clearance has been simplified to a tip gap with constant radii. The values $\bar{r}_{\text{tip}}$ and $\bar{\epsilon}$ can be calculated as:

$$\bar{r}_{\text{tip}} = \frac{r_{\text{tip,out}} + r_{\text{tip,in}}}{2}, \tag{5.1}$$

$$\bar{\epsilon} = \frac{\epsilon_{\text{out}} + \epsilon_{\text{in}}}{2}, \tag{5.2}$$

$$\bar{r}_{\text{sh.}} = \bar{r}_{\text{tip}} + \bar{\epsilon}_{\text{tip}}. \tag{5.3}$$

It has been tested that the later model results change negligibly by changing $\bar{r}_{\mathrm{tip}}$. Changes in $\bar{\epsilon}$ influence the results severely but can be corrected by the proposed geometric coefficients.

5.2.1.1 Loss Correlation

First, the commonly used loss correlation for the tip leakage flow in Equation 5.4 has been modified to make it dependent of measured data.

$$\Delta h_{\mathrm{tip,loss}} = K \cdot \frac{\dot{m}_{\mathrm{tip}}}{\dot{m}_{\mathrm{turb.}}} \cdot \frac{w_{\mathrm{tip}}^2}{2} \cdot z \tag{5.4}$$

For simplicity the θ-component of the tip leakage velocity has been used in the following. Transforming the mass flow fraction of Equation 5.4 to an expression including the reduced mass flow leads to:

$$\frac{\dot{m}_{\mathrm{tip}}}{\dot{m}_{\mathrm{turb.}}} = \frac{A_{\mathrm{tip}}}{\dot{m}_{\mathrm{red.,turb.}}} \cdot \frac{w_{\mathrm{tip},\theta}}{\sqrt{T_{\mathrm{t},0}}} \cdot \frac{T_{\mathrm{t},0}}{T_{\mathrm{tip}}} \cdot \frac{p_{\mathrm{tip}}}{p_{\mathrm{t},0}} \cdot \frac{\sqrt{c_p}}{\sqrt{c_p}} \cdot \frac{1}{R}. \tag{5.5}$$

Instead of calculating the pressure p_{tip} at several chord lengths of the tip gap, the outlet condition has been taken. For high temperatures it can be assumed that $\frac{T_{\mathrm{t,tip}}}{T_{\mathrm{tip}}}$ is close to 1. Combining this assumption with the aspect of negligible work generation of the tip leakage flow, the ratio $\frac{T_{\mathrm{t},0}}{T_{\mathrm{tip}}}$ can be neglected leading to:

$$\frac{\dot{m}_{\mathrm{tip}}}{\dot{m}_{\mathrm{turb.}}} = \frac{A_{\mathrm{tip}}}{\dot{m}_{\mathrm{red.,turb.}}} \cdot \frac{1}{\pi_{\mathrm{turb.}}} \cdot \frac{w_{\mathrm{tip},\theta}}{\sqrt{c_p \cdot T_{\mathrm{t},0}}} \cdot \frac{\sqrt{c_p}}{R}. \tag{5.6}$$

Thus, Equation 5.6 can be calculated by means of measurable data and the unknown $w_{\mathrm{tip},\theta}$. The non-dimensional formulation of $\frac{w_{\mathrm{tip},\theta}}{\sqrt{c_p \cdot T_{\mathrm{t},0}}}$ can be substituted with a correlation including the Laval number:

$$\frac{w_{\mathrm{tip},\theta}}{\sqrt{c_p \cdot T_{\mathrm{t},0}}} = La_{\mathrm{tip}} \cdot \sqrt{2} \cdot \sqrt{\frac{\gamma - 1}{\gamma + 1}}. \tag{5.7}$$

5.2.1.2 Tip Leakage Velocity Modeling

The simplification of the tangential velocity as the mass flow relevant (area orthogonal) velocity implies a geometrical simplification towards a flat and straight blade close to the tip. This might neglect the centrifugal forces on a fluid particle streamline, when the rotor passage is bent. However, this reduction of complexity allows to use only the θ-component of the incompressible Navier

Stokes Equation in a rotating cylindrical coordinate frame to calculate the required velocity:

$$\begin{aligned}&\rho\left(\frac{\partial w_\theta}{\partial t}+w_r\frac{\partial w_\theta}{\partial r}+\frac{w_\theta}{r}\frac{\partial w_\theta}{\partial \theta}+\frac{w_r w_\theta}{r}+w_z\frac{\partial w_\theta}{\partial z}\right)\\ &=-\frac{1}{r}\frac{\partial p}{\partial \theta}+\rho g_\theta-2\rho\omega w_r+\\ &+\mu\left[\frac{1}{r}\frac{\partial}{\partial r}\left(r\frac{\partial w_\theta}{\partial r}\right)-\frac{w_\theta}{r^2}+\frac{1}{r^2}\frac{\partial^2 w_\theta}{\partial \theta^2}+\frac{2}{r^2}\frac{\partial w_r}{\partial \theta}+\frac{\partial^2 w_\theta}{\partial z^2}\right].\end{aligned} \tag{5.8}$$

This strategy matches the observation done by Yaras et al. [97], that the cord wise momentum in a tip gap is nearly conserved. Starting from Equation 5.8 the following assumptions can be made maintaining the idea of a flat and straight blade close to the tip:

$$\frac{\partial}{\partial t},\frac{\partial}{\partial \theta},\frac{\partial}{\partial z},w_r=0. \tag{5.9}$$

Here, a stationary profile is assumed, which remains constant over the tip gap in z direction. According to Dambach et al. [71] and the tip flow analysis in this thesis, inducer and exducer tip region have rather different leakage flow patterns. Thus, the aforementioned assumption might only be valid in different zones along the chord. However, the tip gap of radial or mixed flow turbocharger turbines feature rather radial gaps over the whole chord length. Hence, the Coriolis force has been neglected here. It has been assumed that the velocity profile does not change significantly in the tangential direction and does not own a radial component. Also the influence of gravity has been considered as negligible.

$$0=-\frac{1}{r}\frac{\partial p_{(\mathrm{PS,SS})}}{\partial \theta}+\mu\left[\frac{1}{r}\frac{\partial}{\partial r}\left(r\frac{\partial w_{\mathrm{tip},\theta}}{\partial r}\right)-\frac{w_{\mathrm{tip},\theta}}{r^2}\right] \tag{5.10}$$

$$\int\frac{1}{\mu}\frac{\partial p_{(\mathrm{PS,SS})}}{\partial \theta}\,\mathrm{d}r=r\frac{\partial w_{\mathrm{tip},\theta}}{\partial r}-\int\frac{w_{\mathrm{tip},\theta}}{r}\,\mathrm{d}r \tag{5.11}$$

To achieve an easily integrable function, the following substitutions are considered:

$$g=\frac{w_{\mathrm{tip},\theta}}{r}, \tag{5.12}$$

$$\frac{\partial g}{\partial r}=\frac{\partial w_{\mathrm{tip},\theta}}{\partial r}\frac{1}{r}-\frac{w_{\mathrm{tip},\theta}}{r^2}, \tag{5.13}$$

$$r\frac{\partial g}{\partial r}+g=\frac{\partial w_{\mathrm{tip},\theta}}{\partial r}. \tag{5.14}$$

By substituting Equation 5.12 and Equation 5.14 in Equation 5.11 the following equation has been obtained:

$$\int \frac{1}{\mu}\frac{\partial p_{(\mathrm{PS,SS})}}{\partial \theta}\,\mathrm{d}r = r^2\frac{\partial g}{\partial r} + rg - \int g\,\mathrm{d}r. \tag{5.15}$$

By further substituting Equation 5.16 in Equation 5.15 a homogeneous differential equation with non-constant coefficients appears, which can be solved easily.

$$g = \frac{\partial f}{\partial r} \tag{5.16}$$

$$\frac{1}{r^2}\int \frac{1}{\mu}\frac{\partial p_{(\mathrm{PS,SS})}}{\partial \theta}\,\mathrm{d}r = \frac{\partial^2 f}{\partial r^2} + \frac{1}{r}\frac{\partial f}{\partial r} - \frac{1}{r^2}f \tag{5.17}$$

After solving Equation 5.17 a simple function with two integration constants C_1 and C_2 has been obtained:

$$f = C_1 r + C_2\frac{1}{r} + \frac{r}{2}\frac{1}{\mu}\frac{\partial p_{(\mathrm{PS,SS})}}{\partial \theta}\ln(r) - \frac{r}{4}\frac{1}{\mu}\frac{\partial p_{(\mathrm{PS,SS})}}{\partial \theta}. \tag{5.18}$$

Undoing the substitutions from g to $w_{\mathrm{tip},\theta}$ and finding the integration constants by means of the known values $w_{\mathrm{tip},\theta}(\bar{r}_{\mathrm{tip}}) = 0$ and $w_{\mathrm{tip},\theta}(\bar{r}_{\mathrm{sh.}}) = \omega\cdot\bar{r}_{\mathrm{sh.}}$ an equation for the velocity profile has been found:

$$\begin{aligned} w_{\mathrm{tip},\theta}(r) = {} & \frac{\left(\frac{r}{\bar{r}_{\mathrm{tip}}^2} - \frac{1}{r}\right)}{\left(\frac{\bar{r}_{\mathrm{sh.}}}{\bar{r}_{\mathrm{tip}}^2} - \frac{1}{\bar{r}_{\mathrm{sh.}}}\right)}\cdot\left[\omega\cdot\bar{r}_{\mathrm{sh.}} - \frac{1}{2}\frac{1}{\mu}\frac{\partial p_{(\mathrm{PS,SS})}}{\partial \theta}\bar{r}_{\mathrm{sh.}}\ln\left(\frac{\bar{r}_{\mathrm{sh.}}}{\bar{r}_{\mathrm{tip}}}\right)\right] + \\ & + r\ln\left(\frac{r}{\bar{r}_{\mathrm{tip}}}\right)\cdot\frac{1}{2}\frac{1}{\mu}\frac{\partial p_{(\mathrm{PS,SS})}}{\partial \theta}. \end{aligned} \tag{5.19}$$

According to Equation 5.19, $w_{\mathrm{tip},\theta}$ depends on the pressure gradient in θ-direction as well as on the rotational speed. Here, the pressure gradient can be understood as the pressure difference between suction side and pressure side. For further modeling purposes Equation 5.19 has been integrated:

$$\begin{aligned} \int_{r_{\mathrm{tip}}}^{r_{\mathrm{sh.}}} w_{\mathrm{tip},\theta}(r)\,\mathrm{d}r = {} & \frac{\left[\frac{\bar{r}_{\mathrm{sh.}}^2 - \bar{r}_{\mathrm{tip}}^2}{2\cdot\bar{r}_{\mathrm{tip}}^2} + \ln\left(\frac{\bar{r}_{\mathrm{tip}}}{\bar{r}_{\mathrm{sh.}}}\right)\right]}{\left(\frac{\bar{r}_{\mathrm{sh.}}}{\bar{r}_{\mathrm{tip}}^2} - \frac{1}{\bar{r}_{\mathrm{sh.}}}\right)}\cdot\left[\omega\cdot\bar{r}_{\mathrm{sh.}} - \frac{1}{2}\frac{1}{\mu}\frac{\Delta p_{(\mathrm{PS,SS})}}{\Delta\theta}\bar{r}_{\mathrm{sh.}}\ln\left(\frac{\bar{r}_{\mathrm{sh.}}}{\bar{r}_{\mathrm{tip}}}\right)\right] + \\ & + \left[\frac{\bar{r}_{\mathrm{tip}}^2 - \bar{r}_{\mathrm{sh.}}^2}{4} + \frac{\bar{r}_{\mathrm{sh.}}^2}{2}\cdot\ln\left(\frac{\bar{r}_{\mathrm{sh.}}}{\bar{r}_{\mathrm{tip}}}\right)\right]\cdot\frac{1}{2}\frac{1}{\mu}\frac{\Delta p_{(\mathrm{PS,SS})}}{\Delta\theta}. \end{aligned} \tag{5.20}$$

The velocities for positive and negative Laval numbers have been modeled from the integral over the full tip clearance (Equation 5.20) divided by the tip gap height $\bar{\epsilon}$. The effects of wall friction and pressure gradient have been separated and assigned to negative and positive tip clearance velocity components as follows:

$$\bar{w}_{\mathrm{tip},\theta,+} = \left\{ \left[\frac{r_{\mathrm{tip}}^2 - r_{\mathrm{sh.}}^2}{4} + \frac{r_{\mathrm{sh.}}^2}{2} \cdot \ln\left(\frac{r_{\mathrm{sh.}}}{r_{\mathrm{tip}}}\right) \right] - \frac{\left[\frac{r_{\mathrm{sh.}}^2 - r_{\mathrm{tip}}^2}{2 \cdot r_{\mathrm{tip}}^2} + \ln\left(\frac{r_{\mathrm{tip}}}{r_{\mathrm{sh.}}}\right) \right]}{\left(\frac{r_{\mathrm{sh.}}}{r_{\mathrm{tip}}^2} - \frac{1}{r_{\mathrm{sh.}}} \right)} \cdot \left[r_{\mathrm{sh.}} \ln\left(\frac{r_{\mathrm{sh.}}}{r_{\mathrm{tip}}}\right) \right] \right\} \cdot \frac{1}{2} \frac{1}{\mu} \frac{\Delta p_{(\mathrm{PS,SS})}}{\Delta\theta\epsilon}, \tag{5.21}$$

$$\bar{w}_{\mathrm{tip},\theta,-} = \frac{\left[\frac{r_{\mathrm{sh.}}^2 - r_{\mathrm{tip}}^2}{2 \cdot r_{\mathrm{tip}}^2} + \ln\left(\frac{r_{\mathrm{tip}}}{r_{\mathrm{sh.}}}\right) \right]}{\left(\frac{r_{\mathrm{sh.}}}{r_{\mathrm{tip}}^2} - \frac{1}{r_{\mathrm{sh.}}} \right)} \cdot \frac{\omega \cdot r_{\mathrm{sh.}} \cdot \cos\gamma}{\epsilon}. \tag{5.22}$$

5.2.1.3 Pressure Gradient Modeling

According to Yaras et al. [67] the tip leakage flow pressure gradient depends mainly on the pressure difference between SS and PS in the main passage. Thus, a simple assumption can be made using two different power equations to achieve an estimation for a mean pressure loading from measured power, which lives up to the needs of one-dimensional modeling:

$$\dot{W} = \Delta p_{(\mathrm{PS,SS})} \cdot A_{\mathrm{bl.}} \cdot \omega \cdot \bar{r} = \frac{\Delta h_{\mathrm{t}} \cdot \dot{m}_{\mathrm{pas.}}}{z}. \tag{5.23}$$

On the basis of Equation 5.23, relevant map information is included:

$$\frac{\Delta p_{(\mathrm{PS,SS})}}{p_{\mathrm{t},0}} \cdot A_{\mathrm{bl.}} \cdot \omega \cdot \bar{r} = \frac{\Delta h_t}{h_{\mathrm{t},0}} \frac{\dot{m}_{\mathrm{pas.}}}{z} \frac{c_p \cdot T_{\mathrm{t},0}}{p_{\mathrm{t},0}}. \tag{5.24}$$

Finally, the following equation has been obtained to calculate the needed pressure difference of Equation 5.20 in θ direction:

$$\Delta p_{(\mathrm{PS,SS})} = \frac{\Delta h_t}{h_{\mathrm{t},0}} \frac{\dot{m}_{\mathrm{red.,turb.}} \cdot c_p \cdot \sqrt{T_{\mathrm{t},0}} \cdot \pi_{\mathrm{turb.}} \cdot p_{\mathrm{out}}}{z \cdot A_{\mathrm{bl.}} \cdot \omega \cdot \bar{r}}. \tag{5.25}$$

Here the inlet pressure $p_{\mathrm{t},0}$ has been substituted by $\pi_{\mathrm{turb.}} \cdot p_{\mathrm{out}}$ because p_{out} is a rather constant value than the turbine inlet pressure during typical turbine map measurements. This way atmospheric pressure can be assumed as p_{out} and

variations from this value can be recovered by the geometric fitting coefficient. Further, model results have been improved by using the square root of $\pi_{\text{turb.}}$:

$$\Delta p_{(\text{PS,SS})} = \frac{\Delta h_t}{h_{\text{t,0}}} \frac{\dot{m}_{\text{red.,turb.}} \cdot c_p \cdot \sqrt{T_{\text{t,0}}} \cdot \sqrt{\pi_{\text{turb.}}} \cdot p_{\text{out}}}{z \cdot A_{\text{bl.}} \cdot \omega \cdot \bar{r}}. \tag{5.26}$$

5.2.1.4 Modeling of Contrariwise Mass Flow Over the Tip

The possibly roughest simplification, that has been made, is to assume that no gradients in z-direction (axial direction) exist. As stated in subsection 4.5.2, even in radial turbocharger turbines with rather negligible axial tip gap, zones of dominating negative and dominating positive tip leakage flow exist. This leads to the simple modeling of two flows where either the effect of rotational speed or the effect of blade loading can be neglected in Equation 5.20. Following the velocity and mass flow of two zones can be calculated separately to formulate the tip leakage loss:

$$\frac{\dot{m}_{\text{tip,+}}}{\dot{m}_{\text{turb.}}} = \frac{A_{\text{tip}}}{\dot{m}_{\text{red.,turb.}}} \cdot \frac{La_{\text{tip,+}}}{\pi_{\text{turb.}}} \cdot \sqrt{\frac{\gamma-1}{\gamma+1}} \cdot \frac{\sqrt{2 \cdot c_p}}{R \cdot \cos\left(\beta_{\text{rot.,in}} - \beta_{\text{opt.,in}}\right)}, \tag{5.27}$$

$$\frac{\dot{m}_{\text{tip,-}}}{\dot{m}_{\text{turb.}}} = \frac{A_{\text{tip}}}{m_{\text{red.,turb.}}} \cdot \frac{La_{\text{tip,-}}}{\pi_{\text{turb.}}} \cdot \sqrt{\frac{\gamma-1}{\gamma+1}} \cdot \frac{\sqrt{2 \cdot c_p}}{R}. \tag{5.28}$$

Equation 5.27 for positive mass flow has been configured according to Yaras and Sjolander [67], who related the blade loading with $\cos\beta_{\text{rot,in}}$ and the tip leakage. Passing the tip leakage at the inlet zone of the rotor p_{tip} of Equation 5.5 is higher for the negative tip leakage flow. This has been taken into account by using the square root of the turbine expansion ratio $\pi_{\text{turb.}}$. If a full turbine one dimensional model supplies the pressure ratio of total inlet pressure $p_{\text{t,0}}$ to static rotor inlet pressure $p_{\text{rot,in}}$, this ratio can be used instead.

Since the most radical simplification has been assumed to simplify the Navier Stokes Equation and to obtain the velocity component $w_{\text{tip},\theta}$, two fitting coefficients K_+ and K_- have been introduced into the final velocity equations for positive and negative tip velocity (Equation 5.21, Equation 5.22). K_+ reduces the tip gap height to an effective section:

$$\begin{aligned} w_{\text{tip},\theta,+} = & \frac{\left[\frac{\bar{r}_{\text{sh.}}^2 - \bar{r}_{\text{tip}}^2}{2 \cdot \bar{r}_{\text{tip}}^2} + \ln\left(\frac{\bar{r}_{\text{tip}}}{\bar{r}_{\text{sh.}}}\right)\right]}{\left(\frac{\bar{r}_{\text{sh.}}}{\bar{r}_{\text{tip}}^2} - \frac{1}{\bar{r}_{\text{sh.}}}\right)} \cdot \left[-\frac{1}{2}\frac{1}{\mu}\frac{\Delta p_{(\text{PS,SS})}}{\Delta\theta\bar{\epsilon}} \bar{r}_{\text{sh.}} \ln\left(\frac{\bar{r}_{\text{sh.}}}{\bar{r}_{\text{tip}}}\right)\right] + \\ & + \left[\frac{\bar{r}_{\text{tip}}^2 - \bar{r}_{\text{sh.}}^2}{4} + \frac{\bar{r}_{\text{sh.}}^2}{2} \cdot \ln\left(\frac{\bar{r}_{\text{sh.}}}{\bar{r}_{\text{tip}}}\right)\right] \cdot \frac{1}{2}\frac{1}{\mu}\frac{\Delta p_{(\text{PS,SS})}}{\Delta\theta\bar{\epsilon}}, \\ & \text{with: } \bar{r}_{\text{sh.}} = \bar{r}_{\text{tip}} + K_+ \cdot \bar{\epsilon}. \end{aligned} \tag{5.29}$$

Thus, the initial loss coefficient K in Equation 5.4 is redundant and can be left out.

$$w_{\mathrm{tip},\theta,-} = K_- \cdot \frac{\left[\frac{\bar{r}_{\mathrm{sh.}}^2 - \bar{r}_{\mathrm{tip}}^2}{2 \cdot \bar{r}_{\mathrm{tip}}^2} + \ln\left(\frac{\bar{r}_{\mathrm{tip}}}{\bar{r}_{\mathrm{sh.}}}\right)\right]}{\left(\frac{\bar{r}_{\mathrm{sh.}}}{\bar{r}_{\mathrm{tip}}^2} - \frac{1}{\bar{r}_{\mathrm{sh.}}}\right)} \cdot \frac{\omega \cdot \bar{r}_{\mathrm{sh.}}}{\bar{\epsilon}} \tag{5.30}$$

Formulating Equation 5.4 as a loss relative to the inlet enthalpy, substituting Equation 5.6 and Equation 5.7 the overall relative tip loss can be calculated as:

$$\frac{\Delta h_{\mathrm{tip,loss}}}{h_{\mathrm{t},0}} = \frac{\dot{m}_{\mathrm{tip},+}}{\dot{m}_{\mathrm{turb.}}} \cdot \frac{\gamma - 1}{\gamma + 1} \cdot La_{\mathrm{tip},+}^2 \cdot z + \frac{\dot{m}_{\mathrm{tip},-}}{\dot{m}_{\mathrm{turb.}}} \cdot \frac{\gamma - 1}{\gamma + 1} \cdot La_{\mathrm{tip},-}^2 \cdot z \tag{5.31}$$

and its effect on the turbine efficiency as:

$$\eta_{\mathrm{ts}} = \frac{\Delta h_{\mathrm{t}}}{h_{\mathrm{t},0}} \cdot \left[1 - \left(\frac{1}{\pi_{\mathrm{turb.}}}\right)^{\frac{\gamma-1}{\gamma}}\right]^{-1} - \Delta\eta_{\mathrm{tip,loss}}, \tag{5.32}$$

and with $\Delta\eta_{\mathrm{tip,loss}}$ as:

$$\Delta\eta_{\mathrm{tip,loss}} = \frac{\Delta h_{\mathrm{tip,loss}}}{h_{\mathrm{t},0}} \cdot \left[1 - \left(\frac{1}{\pi_{\mathrm{turb.}}}\right)^{\frac{\gamma-1}{\gamma}}\right]^{-1}. \tag{5.33}$$

It can be seen that apart from map data, gas data, and geometrical data only the relative rotor inflow angle $\beta_{\mathrm{rot,in}}$ is needed. In common one dimensional models this angle is typically calculated. Hence, no additional effort has to be done to use the presented model.

5.2.1.5 Model Validation & Discussion

To prove the validity of the model the relative leakage mass flow as well as the tip leakage loss, according to Equation 5.4, have been validated by means of the CFD data.

First, the tip leakage efficiency model has been fitted with all available data from calculated simulations at the same time using the estimated loss according to Equation 5.33. Here, simulated data has been chosen as input to allow a consistent comparison between model and CFD results. As fitting coefficients 0.1824 and 0.4848 have been obtained for K_+ and K_- accordingly. The low magnitude of K_+ can be explained by the effective tip gap reduction due to flow separation, blocking, the dragging flow, mixing zones, and discharged flow [71]. Inherent in the coefficients K_+ and K_- is a correction of the chordwise extension of the flow into the related direction and radial simplification of the tip gap geometry. This also explains the magnitude of K_-.

The results in Figure 5.2 show the flexibility of the developed model to fit the whole data range of the results presented in subsubsection 4.5.2.1. It can be seen that the overall fitting quality is good. However, the efficiency loss fitting is rather bad for the points of highest $\pi_{\text{turb.}}$ with the speed of 1710 rpm/K$^{0.5}$. In this region the model under predicts the efficiency loss. At the speed of 6715 rpm/K$^{0.5}$ and with 60 % and 80 % VGT opening the model also under predicts the estimated efficiency loss at lower pressure ratios and slightly over predicts the loss at higher pressure ratios. Looking at the relative rotor inlet

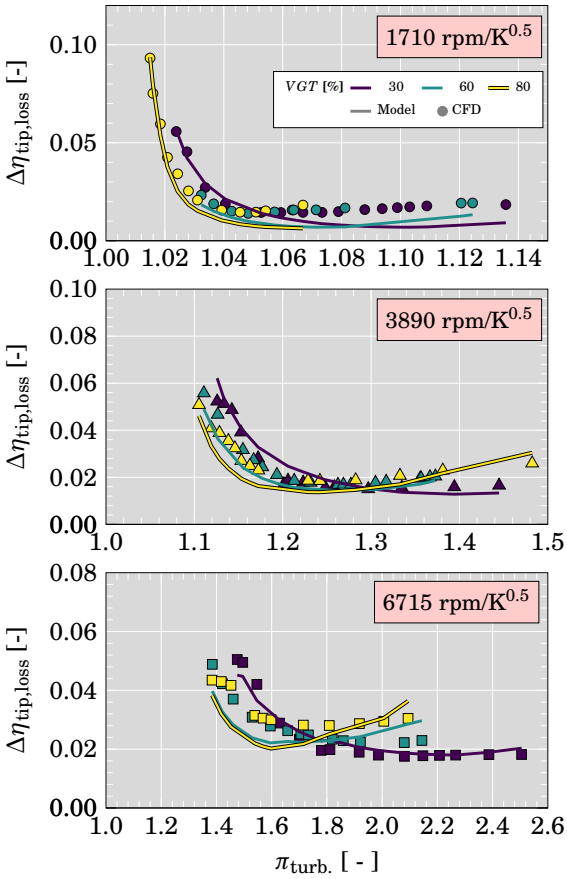

Figure 5.2: Efficiency model fitting for single speeds vs. $\pi_{\text{turb.}}$.

flow angle $\beta_{\text{rot,in}}$ of simulation results in Figure 4.28, it becomes clear that the tip leakage loss fitting is worse for points with a positive or close to zero inflow angle. During the development of the model significant modeling improvements have already been obtained for these points by using the aforementioned correlation with $\cos\beta_{\text{rot.,in}}$ (Equation 5.27). However the error in tip leakage efficiency

loss remains rather high in these points, the absolute error in turbine power loss is rather low compared with other impacting factors as heat transfer or measurement uncertainties especially at this speed where the power output is rather low as it can be seen in Figure 4.21. In general, a good fitting has been achieved for three VGT positions, three speeds spreading a wide range, and pressure ratios between 1.015 and 2.5 with only two fitting coefficients. Thus, the trends of all variable impact factors on the variable geometry turbine are correctly modeled.

Since the model is supposed to be used in a narrow map extrapolation model, its extrapolation capability has to be validated. In commonly available turbocharger turbine maps rather low number of measured points are available at only high expansion ratios.

Thus, for validating the functionality of the tip clearance model regarding its extrapolation capability five points (with highest expansion ratios) of every speedline and VGT opening have been used to fit the model with the same coefficients. As common K_+ and K_- have been fitted to 0.1803 and 0.4966. By following this strategy, the fitting coefficients and the model results in Figure 5.3 are almost identical to the case where all data have been used for the data fitting (Figure 5.2). Like in the whole data fitting, the fitting at design conditions at 1710 rpm/K$^{0.5}$ is of lower quality. The efficiency loss is extrapolated towards low pressure ratios in very high quality as it can be seen in Figure 5.3 and Figure 5.4. This highlights the high consistency and stability of the model. The fitting and extrapolating errors are lower than 1 percentage point for 94.3 % of the points as shown by Figure 5.4. The relative root mean square error (RMSE) is 16.3 %. Although highest relative errors have been obtained at 1710 rpm/K$^{0.5}$ around operating points that have been used for the model fitting, the extrapolation quality is not negatively affected.

Since the tip leakage mass flow can be a valuable information for one dimensional models, the tip leakage mass flow fraction calculated with the found coefficients of the tip leakage loss fitting is shown in Figure 5.5.

At 1710 rpm/K$^{0.5}$ and higher pressure ratios the model mass flow fraction shows rather poor agreement with the CFD data due to the aforementioned reasons. However, the tip leakage mass flow fraction at extremely low pressure ratios is well estimated by the model. For all points of 3890 rpm/K$^{0.5}$ and for the most points of 6715 rpm/K$^{0.5}$ a very good agreement has been achieved. The overall model trends are good estimated (as it can be seen in Figure 5.6), although a dedicated tuning of the fitting parameters on the basis of the mass flow fraction data has not been carried out. A relative RMSE of 11.7 % has been calculated.

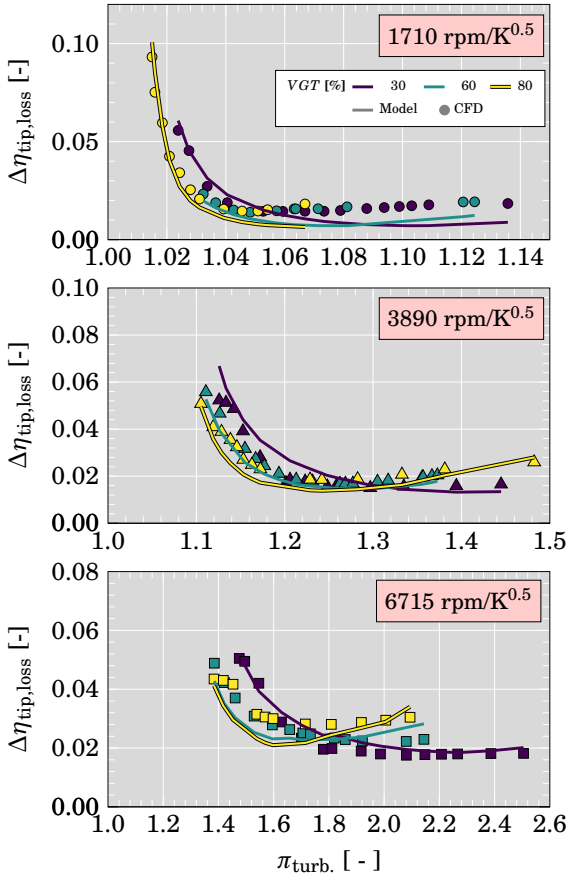

Figure 5.3: Model extrapolation of tip loss related efficiency vs. $\pi_{\text{turb.}}$ and after fitting K_+ and K_- coefficients with only five points at the highest $\pi_{\text{turb.}}$ for each speedline (independent of VGT opening).

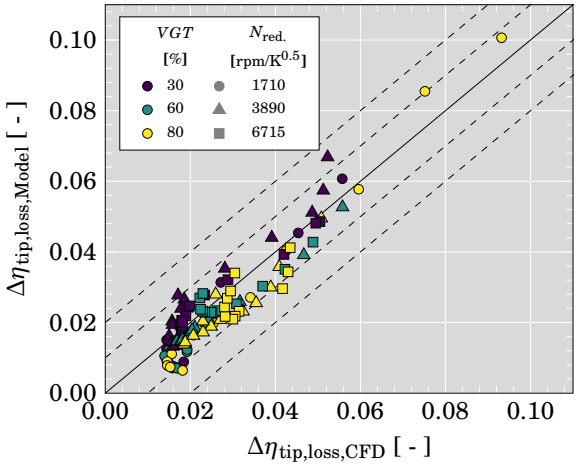

Figure 5.4: Model extrapolation of tip loss related efficiency vs. CFD results and after fitting K_+ and K_- coefficients with only five points at the highest $\pi_{turb.}$ for each speedline (independent of VGT opening).

5.2.1.6 Conclusions

1. The modeling of dragging and loading effects are important to realize good quality extrapolations based on design point data. The developed model is able to fit and extrapolate the CFD data in a wide range using mainly map data, gas data, and simple geometrical data. Fitting the tip leakage losses, also the mass flow fraction has been calculated in a good quality compared to CFD data.

2. Since the model has a strict physical basis, future analysis of further turbine geometries might make it possible to relate the two introduced fitting coefficients.

5.2.2 Method for Tip Leakage Flow Characterization

The physical model described in the previous chapter can model tip leakage mass flow and momentum, which has further been correlated to obtain tip leakage losses for one-dimensional extrapolation models. While this model also relies on general geometrical information, it uses fitting coefficients to model the complex composition of contrarious fluid flows though the tip gap over a wide range of speeds and pressure ratios. Thus, an estimation for changed geometries before building, measuring and applying the model is not possible yet.

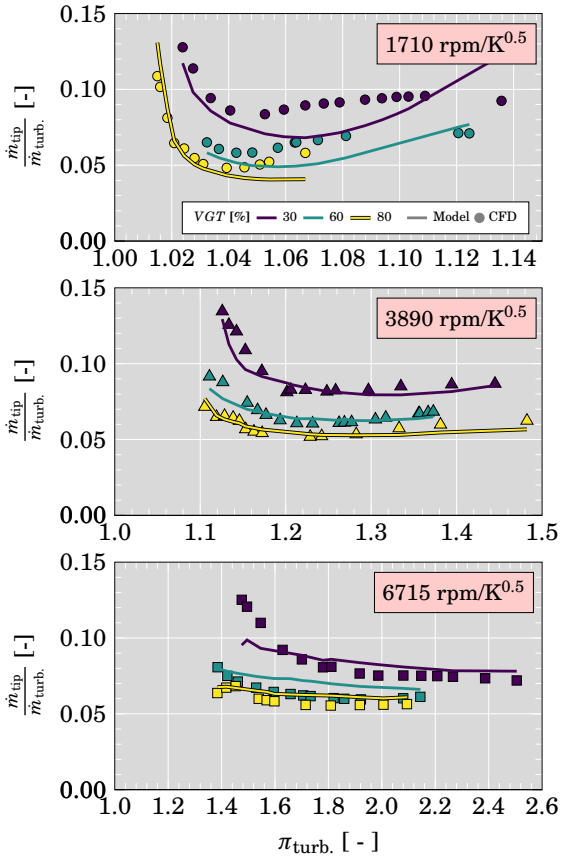

Figure 5.5: Model mass flow ratio extrapolation vs. $\pi_{\text{turb.}}$ and after fitting K_+ and K_- coefficients with only five points at the highest $\pi_{\text{turb.}}$ for each speedline (independent of VGT opening).

For one dimensional modeling and for design purposes it can be important to distinguish friction and pressure driven effects in the tip leakage flow from other effects as incidence flow or blow by. Thus, to be able to estimate the quantity of this loss generating flow phenomena dependent on geometrical details is of interest. The aforementioned momentum ratio correlates qualitatively well along the chord length with estimated loss productions but misses to predict the qualitative change in momentum ratio when the geometry is changed. Following, the correlation of both momentum flows has newly been derived.

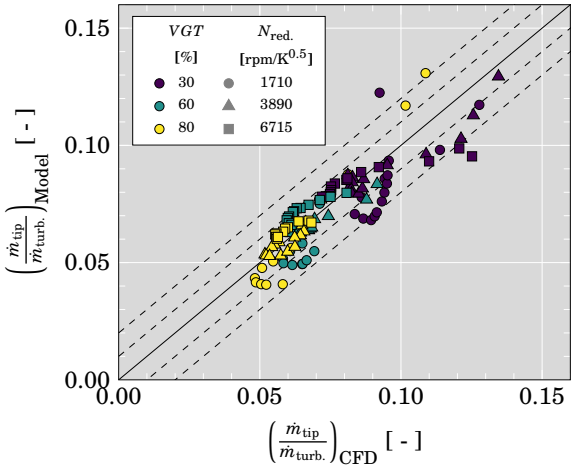

Figure 5.6: Model mass flow ratio extrapolation vs. CFD results and after fitting K_+ and K_- coefficients with only five points at the highest $\pi_{turb.}$ for each speedline (independent of VGT opening).

5.2.2.1 Novel Momentum Ratio

Based on the derived equation in subsubsection 5.2.1.4 for the contrarious tip leakage velocities the momentum ratio can be developed (Equation 5.21 and Equation 5.22). Here, the leading effects of wall friction and pressure difference between SS and PS have already been separated to model the mean relative velocity of the negative and positive tip leakage flow. In contrary to the overall tip leakage loss model derived in subsubsection 5.2.1.4 and its zonal approach, these effects have been modeled for each position along the chord. Furthermore, the geometrical terms (including $r_{sh.}$ and r_{tip}) have been concentrated into one factor. Next, the momentum ratio has been defined as:

$$R_{NS} = \frac{\rho_+}{\rho_-} \cdot \frac{\bar{w}^2_{tip,\theta,+}}{\bar{w}^2_{tip,\theta,-}}. \tag{5.34}$$

Substituting Equation 5.21 and Equation 5.22 in Equation 5.34 the novel momentum ratio can be described as:

$$R_{NS} = \frac{\rho_+}{\rho_-} \cdot \left\{ \frac{\left(\frac{r_{sh.}}{r^2_{tip}} - \frac{1}{r_{sh.}}\right)\left[\frac{r^2_{tip}-r^2_{sh.}}{4} + \frac{r^2_{sh.}}{2} \cdot \ln\left(\frac{r_{sh.}}{r_{tip}}\right)\right]}{\left[\frac{r^2_{sh.}-r^2_{tip}}{2 \cdot r^2_{tip}} + \ln\left(\frac{r_{tip}}{r_{sh.}}\right)\right] r_{sh.}} - \ln\left(\frac{r_{sh.}}{r_{tip}}\right) \right\}^2 \cdot \left\{ \frac{\frac{1}{2}\frac{1}{\mu}\frac{\Delta p_{(PS,SS)}}{\Delta\theta}}{\omega \cos\gamma} \right\}^2. \tag{5.35}$$

It can be seen that only the viscosity and the pressure on SS and PS are required from the flow to calculate the ratio. The viscosity has been assumed to be rather constant here. Simulation results have shown that the density ratio is close to 1. For the purpose of simplicity and for later analysis the following nomenclature has been chosen for the purely geometry dependent factor and the "fluid" factor:

$$R_{\text{geo.}} = \left\{ \frac{\left(\frac{r_{\text{sh.}}}{r_{\text{tip}}^2} - \frac{1}{r_{\text{sh.}}}\right)\left[\frac{r_{\text{tip}}^2 - r_{\text{sh.}}^2}{4} + \frac{r_{\text{sh.}}^2}{2} \cdot \ln\left(\frac{r_{\text{sh.}}}{r_{\text{tip}}}\right)\right]}{\left[\frac{r_{\text{sh.}}^2 - r_{\text{tip}}^2}{2 \cdot r_{\text{tip}}^2} + \ln\left(\frac{r_{\text{tip}}}{r_{\text{sh.}}}\right)\right] r_{\text{sh.}}} - \ln\left(\frac{r_{\text{sh.}}}{r_{\text{tip}}}\right) \right\}^2, \tag{5.36}$$

$$R_{\text{fl.}} = \left\{ \frac{\frac{1}{2}\frac{1}{\mu}\frac{\Delta p_{(\text{PS,SS})}}{\Delta\theta}}{\omega \cos\gamma} \right\}^2, \tag{5.37}$$

$$R_{\text{NS}} = \frac{\rho_+}{\rho_-} \cdot R_{\text{geom.}} \cdot R_{\text{fl.}}. \tag{5.38}$$

It is worth highlighting that $R_{\text{fl.}}$ would result in extremely high values, if $\Delta\theta$ would be defined by the small blade thickness. This might be the case because $\frac{\partial}{\partial\theta} = 0$ has been assumed deriving the final equations. This is an assumption for developed flow, which is apparently not the case after the short distance of a tip gap. However, this assumption overcomes estimating a flow profile at tip gap inlet to obtain a gap flow profile at the outlet and makes the solution of the Navier Stokes equation much easier, while maintaining the main trends. Thus, $\Delta\theta$ must be understood as an effective flow length $\Delta\theta_{\text{eff.}}$ and has been analyzed in more detail.

5.2.2.2 Effective Flow Length

The momentum ratio obtained from the CFD simulations has been used to calculate the effective flow length and the chordwise distributions of $\Delta p_{(\text{PS,SS})}$ values from the CFD results have been imposed:

$$\Delta\theta_{\text{eff.}} = \sqrt{\frac{\rho_+}{\rho_-} \cdot \frac{R_{\text{geom.}}}{R_{\text{CFD}}}} \cdot \frac{\frac{1}{2}\frac{1}{\mu}\Delta p_{(\text{PS,SS})}}{\omega \cos\gamma}. \tag{5.39}$$

$\Delta\theta_{\text{eff.}}$ is expected to behave as the discharge coefficient appearing in publications about flow characterization of flow through an orifice [98] and thus, can be characterized by means of the Reynolds numbers of both flow directions:

$$Re_+ = \frac{\rho_+ \cdot \bar{w}_{\text{tip},\theta,+} \cdot \epsilon}{\mu}, \tag{5.40}$$

$$Re_- = \frac{\rho_- \cdot \omega \cdot r_{\text{sh.}} \cdot \epsilon \cdot \cos\gamma}{\mu}. \tag{5.41}$$

It has been found out that plotting $\Delta\theta_{\text{eff.}}$ over the ratio $\frac{Re_-}{Re_+^{1/6}}$ gives a clear trend for all simulated points as Figure 5.7 shows. Here, average values from 0 to

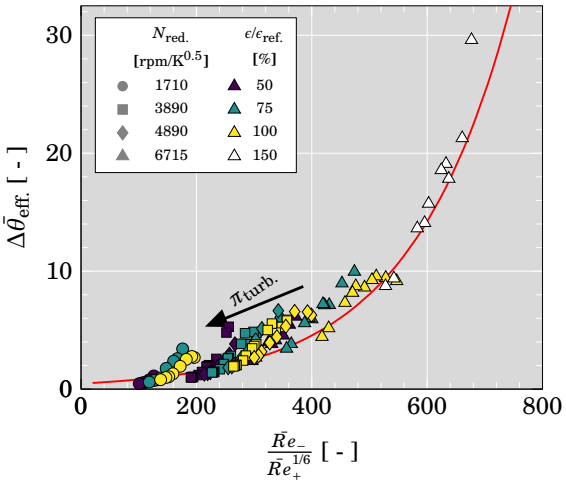

Figure 5.7: Fitting of $\Delta\bar{\theta}_{\text{eff.}}$ values

100 % chord length have been used to reduce complexity. Towards off-design condition the aforementioned influence of the incidence flow momentum on the momentum ratio causes higher values of the mean effective inflow length and explains the deviation from the overall trend for those points. The global trend is independent of the tip gap height ϵ, the rotational speed $N_{\text{red.}}$ and of the overall turbine pressure ratio $\pi_{\text{turb.}}$. It is worth highlighting, that the consistent line fitting can allow a correlation fit based on only a few data points of one single tip gap geometry. With this fitting results can be extrapolated towards different tip gap values.

Since friction and pressure driven effects have been decoupled to obtain the ratio R_{NS}, the relation in Figure 5.7 represents the coupling of both flows due to fluid friction. $\Delta\theta_{\text{eff.}}$ is increasing with rising rotational speed (increase of friction layer and reduction of effective area for pressure driven flow) and is decreasing when $\pi_{\text{turb.}}$ (and thus $\Delta p_{(\text{PS,SS})}$) is increasing. The working principle of $\Delta\theta_{\text{eff.}}$ is similar to the one of combined discharge coefficients of both tip leakage flows. However, in contrast to discharge coefficients, $\Delta\theta_{\text{eff.}}$ is not related to the tip gap height. This conserves the valuable trends inherent in $R_{\text{geom.}}$. Apparently, the relation of $\Delta\theta_{\text{eff.}}$ is dependent on itself, when Equation 5.40 is calculated with the proposed formula in Equation 5.21:

$$\Delta\theta_{\text{eff.}} = f\left(\frac{Re_-}{f(\Delta\theta_{\text{eff.}})}\right). \tag{5.42}$$

The data can directly be fitted with an exponential equation as it can be seen in Figure 5.7. However, this would only allow an iterative solution, what causes difficulties in the further analysis and conclusions. Since an analytical solution is aimed $\Delta\theta_{\text{eff.}}$ has been fitted with a simple parabolic function:

$$\Delta\theta_{\text{eff.}} = a \cdot \left(\frac{Re_-}{Re_+^{1/6}} \right)^b . \tag{5.43}$$

Following, the analytical solution of R_{NS} can be obtained by substituting Equation 5.43, Equation 5.40, Equation 5.41 in Equation 5.35 and considering $\Delta\theta$ as $\Delta\theta_{\text{eff.}}$:

$$\begin{aligned}
&R_{\text{NS}} = a^{\frac{12}{6-b}} \cdot \frac{\rho_+}{\rho_-} \cdot R_{\text{fl.,eff.}} \cdot R_{\text{mix,eff.}} \cdot R_{\text{geom.,eff.}} \\
&\text{with:} \\
&R_{\text{fl.,eff.}} = \left(\frac{1}{2} \frac{1}{\mu} \frac{\Delta p_{(\text{PS,SS})}}{\omega \cos\gamma} \right)^{\frac{12}{6-b}}, \\
&R_{\text{mix,eff.}} = \left(\frac{\rho_+}{\rho_-^6} \right)^{\frac{2\cdot b}{6-b}} \cdot \left\{ \frac{\mu^5}{\left(\cos\gamma \cdot \omega\right)^5} \right\}^{\frac{2\cdot b}{6-b}} \cdot \left(\frac{1}{\epsilon^5 \cdot r_{\text{sh.}}^5} \right)^{\frac{2\cdot b}{6-b}}, \\
&R_{\text{geom.,eff}} = R_{\text{geom.}}^{\frac{6}{6-b}} \cdot \left\{ \frac{\left[\frac{r_{\text{sh.}}^2 - r_{\text{tip}}^2}{2 \cdot r_{\text{tip}}^2} + \ln\left(\frac{r_{\text{tip}}}{r_{\text{sh.}}} \right) \right]}{\left(\frac{r_{\text{sh.}}}{r_{\text{tip}}^2} - \frac{1}{r_{\text{sh.}}} \right) \epsilon} \right\}^{\frac{2\cdot b}{6-b}} .
\end{aligned} \tag{5.44}$$

It can be seen that the factor $R_{\text{geom.}}$ has been extended and changes its exponent as well as $R_{\text{fl.}}$. Additionally, a third non-dimensional factor arises. This factor consists of geometry data and fluid information to model and is needed (together with aforementioned modifications of the equation) to model the interaction between wall friction flow and pressure driven flow.

5.2.2.3 Model Fitting

By means of a nonlinear fitting the MATLAB coded model has been fitted towards the chordwise R_{CFD} values of all simulated points including all tip gap configurations. Also here, the chordwise distribution of $\Delta p_{(\text{PS,SS})}$ from the CFD results have been utilized. The fitting coefficients have been obtained as $a = 1250$ and $b = 1.23$. The average fitting error in R_{NS} is relatively low with 3.19 and the RMSE has been determined to 6.36. Mean values of each tip gap and running point of R_{CFD} have been reproduced in good quality for the most of the analyzed points as it can be seen in Figure 5.8. The two outliers in Figure 5.8 are those of highest mass flow $\dot{m}_{\text{red.,turb.}}$ and biggest tip gap configuration. In

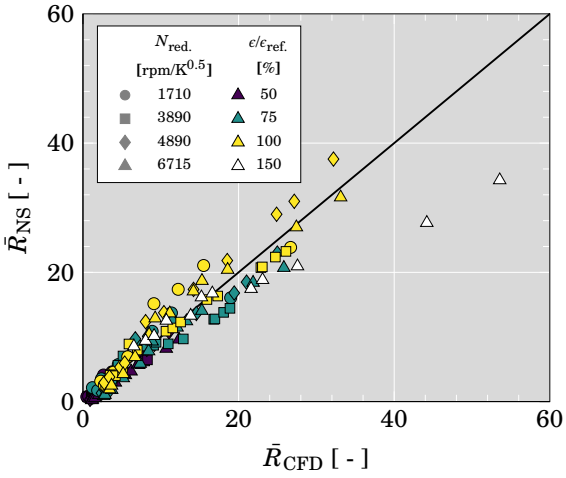

Figure 5.8: Mean values for momentum ratio R_{NS} with simple exponential function (Eqn. 5.43)

these conditions the proposed model underestimates the mean momentum ratio $\bar{R}_{NS}$. This could be caused by operating at high mass flow rates and following, higher simulated passage flow momentum passing through the tip gap.

Since the momentum through the tip gap can be related with the tip clearance losses and good fitting quality has been achieved for mean values of R_{NS}, the presented correlation might help to further reduce the number of fitting coefficients in one dimensional tip leakage models like the one described in subsection 5.2.1. Furthermore, the dependence on the geometry as blade angle γ, blade radius r_{tip}, and tip gap height ϵ allows to increase model sensibility for the analysis and prediction of the tip leakage flow and losses for a bigger range of unmeasured geometries.

$\epsilon/\epsilon_{ref.}$	50 %	75 %	100 %	150 %
MAE	1.07	2.33	3.16	14.80
RMSE	1.52	3.31	4.14	19.78

Table 5.1: Fitting quality for each tip gap configuration.

Apart from the capability to obtain good estimations for the mean value of R_{NS}, the fitted model can be applied to do further qualitative analysis. In Figure 5.9 it can be seen that the ratio R_{NS} is well predicted over the chord length for the 50 %, 75 %, and the 100 % tip gap configuration. R_{NS} is able to

catch the high momentum ratio reduction close to 0, at lower relative chord lengths, that R was not able to predict. Table 5.1 shows the fitting quality for each tip gap configuration. As it can be seen, the fitting quality is the best for the smallest tip gap and worsens continuously with opening the tip gap. The chordwise fitting becomes bad for 150 %. As mentioned before, the characteristic tip leakage flow with the biggest tip gap is affected by unguided passage flow momentum. This effect cannot be predicted by the model, since the model only considers blade loading and friction driven flow. Although this represents a limitation of the chordwise modeling, such values of the tip gap heights are technically less relevant.

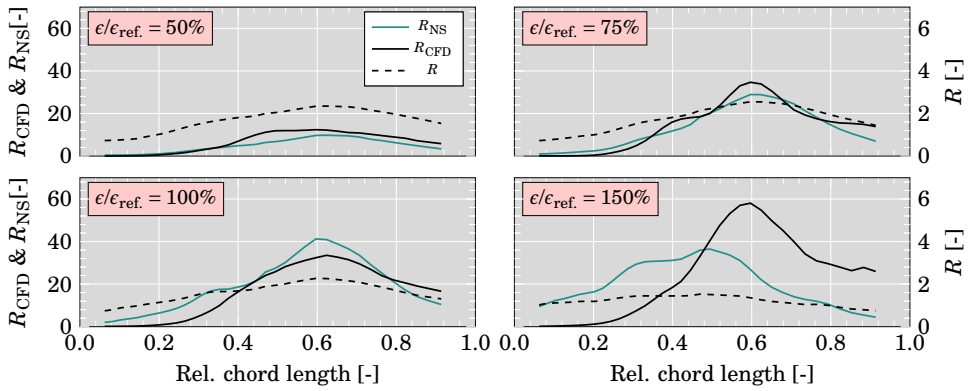

Figure 5.9: Momentum ratios R (Eqn. 2.20), R_{CFD} (Eqn. 4.10), and R_{NS} (Eqn. 5.44) for four different tip gap heights at 6715 rpm/K$^{0.5}$ and 60 % VGT opening (red circles in Fig. 4.33 (d))

Concluding, the modeled momentum ratio R_{NS} is able to reproduce the following trend: there are higher parts of pressure driven momentum flows through the tip gap, when the tip gap becomes bigger, even when the blade loading changes only slightly or decreases.

5.2.2.4 Momentum Ratio Analysis

While a non-dimensional analysis of the factor $R_{\text{fl.,eff.}}$ require further assumptions of the blade loading or rotational speed, the newly gained factors $R_{\text{geom.,eff.}}$ of Equation 5.44 can be analyzed only dependent on geometry variations. Surprisingly, the geometrical non-dimensional factor $R_{\text{geom.,eff.}}$ is quite independent from $\frac{\epsilon}{r_{\text{tip}}}$. This stands in line with loss models, where the aerodynamics were not considered yet. Models like Equation 2.13 are mainly dependent on $\frac{\epsilon}{r_{\text{tip}}}$. At the same time the ratio $R_{\text{geom.,eff.}}$ increases exponentially when the relative tip gap height $\frac{\epsilon}{r_{\text{tip}}}$ grows.

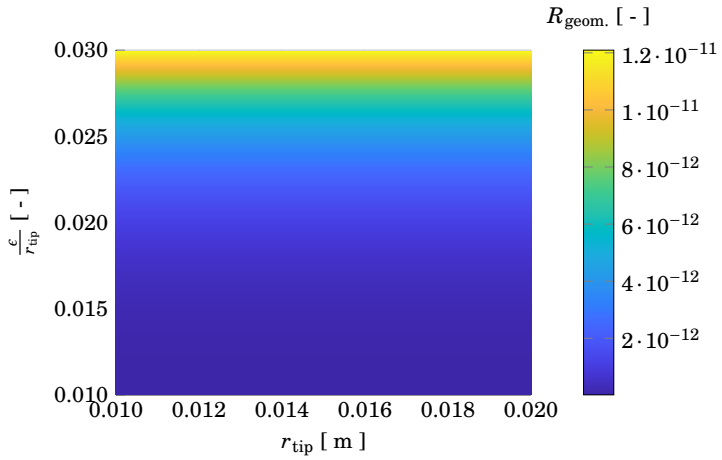

Figure 5.10: Geometry changes vs. geometrical factor $R_{\text{geom.,eff.}}$.

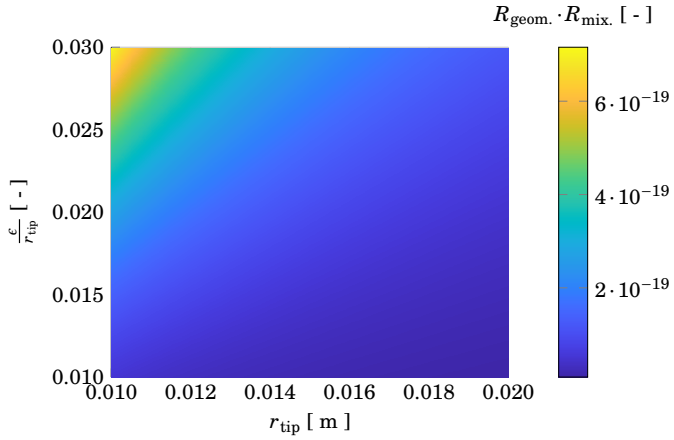

Figure 5.11: Geometry changes vs. geometrical factor $R_{\text{geom.,eff.}}$ times mixed factor $R_{\text{mix,eff.}}$

Since the mixed ratio $R_{\text{mix,eff.}}$ has further variables as: density ratio, blade angle correlations and radial velocity, assumptions and simplifications have had to be made for continuing the analysis. While the impact of the density and the blade angle have been neglected (= 1), a constant angle velocity of 14 347 rad/s ($U_{\text{in}} = 300 m/s$) has been assumed. For analyzing the overall impact of geometry changes on the momentum ratio, the newly gained ratio $R_{\text{mix,eff.}}$ with the aforementioned assumptions has been multiplied with $R_{\text{geom.,eff.}}$ as it can be seen in Figure 5.11. The factor $R_{\text{geom.,eff.}} \cdot R_{\text{mix,eff.}}$ increases exponentially with decreasing tip radius r_{tip} and increasing $\frac{\epsilon}{r_{\text{tip}}}$. This confirms independent from the factor $R_{\text{fl.,eff.}}$, which includes local blade loading and rotational speed, a tendency to higher positive leakage momentum and related losses at lower radius. Thus, front loaded blade designs are in favor of a minimization of tip leakage losses. Finally, Figure 5.12 shows the entire ratio of Equation 5.44

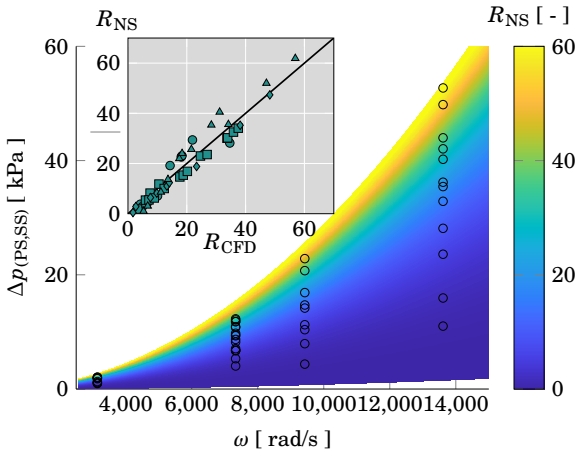

Figure 5.12: Model results and validation for the points of highest $\Delta p_{(\text{PS,SS})}$ per running point. Color: radial velocity and local blade loading vs. momentum ratio R_{NS}; Dots: simulated rotational velocity and maximum local blade loading in the exducer for each running point; Small: Momentum ratio R_{NS} vs. momentum ratio R_{CFD} at highest local blade loading close to the tip.

in dependence of the variables ω and $\Delta p_{(\text{PS,SS})}$, which are defining $R_{\text{fl.}}$. As geometry input for r_{tip}, $r_{\text{sh.}}$, and $cos\gamma$ constant values have been set. Here, the geometry of the chord length with highest blade loading that has been found for the most CFD solutions has been taken (with ϵ = 100 %). The highest blade loading occurs mostly close to 60 % chord length, in the exducer section. Also,

the highest found blade loading for each simulated running point has been shown against the radial velocity to highlight the simulated operating range and relevant values for R_{NS}. To evaluate the validity of the presented model results, a comparison of the momentum ratios $R_{\mathrm{CFD},\Delta\mathrm{pmax}}$ and $R_{\mathrm{NS},\Delta\mathrm{pmax}}$ at described location has been shown in Figure 5.12. The given trends are well reproduced by the found correlation.

In Figure 5.12 it can be seen that each simulated speed covers a similar range of R_{NS} from low values (1.7-5.3) up to values around 40 and higher. While the momentum ratio is changing rather less at off-design conditions with lower blade loading, a small increase in the local blade loading $\Delta p_{(\mathrm{PS,SS})}$ can cause a significant increase of the momentum ratio and thus, of the tip leakage losses when operating at high efficiencies and close to design condition. This inherent sensitivity of the tip leakage momentum ratio on $\Delta p_{(\mathrm{PS,SS})}$ highlights, why the model results at nearly design condition in Figure 5.9 can be considered as relatively good.

5.2.2.5 Tip Leakage Velocity Fitting

As in Equation 2.14 many tip leakage loss correlations are based on the positive tip leakage velocity. By using Equation 5.21 and correlating the effective inflow length with:

$$\Delta\theta_{\mathrm{eff.}} = c \cdot (Re_-)^b. \tag{5.45}$$

good fittings have been achieved with CFD data for modeled $\bar{w}_{\mathrm{tip},\theta,+}$ as it can be seen in Figure 5.13. Here, $\Delta\theta_{\mathrm{eff.}}$ does only depend on the the negative Reynolds number as it has been defined in Equation 5.41 and the same exponent ($b = 1.23$) that has been found for the momentum ratio can be applied. This way only one additional coefficient is necessary. The factor c has been fitted with 2332. Also here, $\Delta\theta_{\mathrm{eff.}}$ has a similar function as a discharge coefficient.

5.2.2.6 Incidence Flow Analysis

As highlighted before, incidence flow has significant influence on the momentum ratio in the rotor inlet and contributes to the tip leakage loss itself. Hence, the evaluation of this mixed flow effect can be of high importance. Taking advantage of the already found correlation for the momentum ratio and positive leakage velocity, the mean negative velocity and momentum driven by shroud friction can be found by Equation 5.46 and Equation 5.47 respectively.

$$\bar{w}_{\mathrm{tip},\theta,-,\mathrm{NS}} = \sqrt{\frac{\rho_+}{\rho_-}\frac{\bar{w}^2_{\mathrm{tip},\theta,+,\mathrm{NS}}}{R_{\mathrm{NS}}}} \tag{5.46}$$

$$\bar{M}_{\mathrm{tip},-,\mathrm{NS}} = \rho \bar{w}^2_{\mathrm{tip},\theta,-,\mathrm{NS}} \tag{5.47}$$

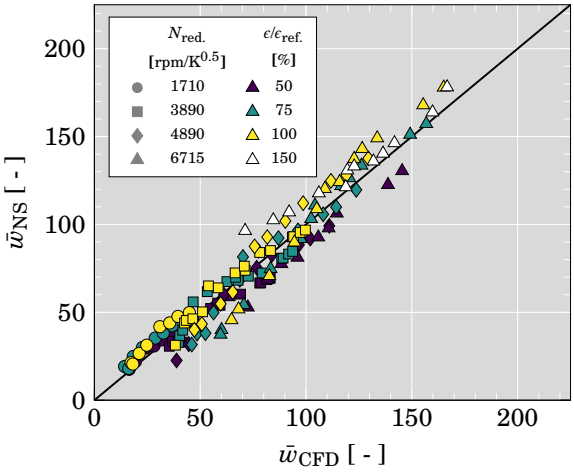

Figure 5.13: Fitting of $\bar{w}_{\mathrm{tip},\theta,+}$: model vs. CFD data

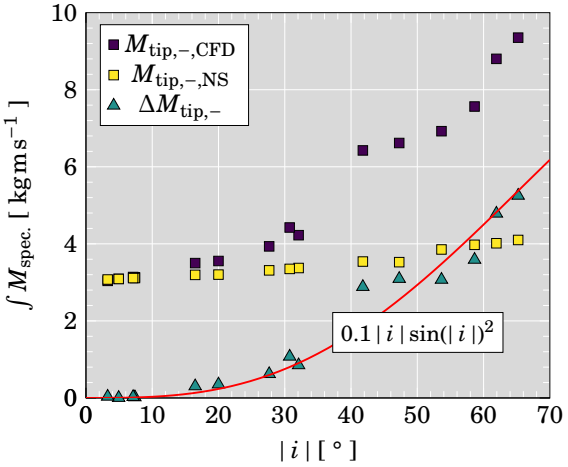

Figure 5.14: Chordwise integral of negative momentum and difference between CFD and model at 3890 rpm/K$^{0.5}$ and 100 % tip gap opening

In Figure 5.14 the chordwise integral of this momentum has been compared with the same value from the CFD results for the entire speedline of 3890 rpm/K$^{0.5}$, since this speed has running points from very low incidence to high negative incidence. Calculating the deviation between both shows clearly values close to zero when the inflow incidence is low and rising values towards higher negative incidence. This highlights again the validity of the before derived correlations for friction-driven and pressure-driven flow. Although the momentum ratio

R_{NS} is worse predicted at low cord length in Figure 5.9, the overall fitting is capable of characterizing both flow effects in this zone, where incidence is important. Hence, the found correlations can be used to separate these flow phenomena and to analyze the incidence flow. It is worth highlighting that the incidence-driven momentum reaches the same magnitude as the friction-driven momentum predicted by Equation 5.47 when the incidence becomes high. This again proofs the importance of incidence flow for the tip leakage flow.

The filtered incidence flow momentum can be fitted in good quality with $0.1 \mid i \mid \sin(\mid i \mid)^2$ as it has been demonstrated in Figure 5.14. Here $\sin(\mid i \mid)^2$ is clearly related with the tangential part of the inflow momentum. The factor $0.1 \mid i \mid$ is assumed to be related with geometric measures like the tip gap height and the distribution of γ in the passage inlet in combination with aerodynamic interactions with friction-driven and pressure-driven flow.

5.2.2.7 Possible Model Applications

Due to the origin of the model derivation nearly all flows, where a pressure driven flow and an opposing wall friction driven flow are mainly noticeable on different radial positions, can be characterized with the novel procedure presented in this section. Thus, e.g. parts of the flow in a floating bearing might be characterized based on the shown fitting of the effective inflow length $\Delta\theta_{\text{eff.}}$.

Certainly, the presented model validation allows the application within one-dimensional turbine tip leakage loss modeling, since trends and magnitudes of the simulated momentum ratio have been reproduced in a wide range of pressure ratios, rotational speeds and even with changed tip gap heights.

As the model consists of certain geometrical information as blade angle, local blade tip radius and shroud radius, it might find a application in turbine design processes. Hence, the impact of geometry changes or of blade loading profiles on the tip leakage flow can be analyzed.

The shown or similar procedures for data filtering of experimental and simulative results can be used to analyze mixed tip leakage flow driving effects.

5.2.2.8 Conclusions

The main conclusions of this chapter are highlighted as follows:

1. A new correlation to calculate the momentum ratio based on the Navier Stokes Equation has been derived. The equation inherent flow length, here interpreted as effective flow length, has been fitted dependent on the ratio of Reynolds numbers build for friction driven and pressure driven flow $\frac{Re_-}{Re_+^{1/6}}$ for all analyzed running conditions at design and off-design, from low to high rotational speed, and for varied geometry.

2. It has been demonstrated that the tip leakage flow reacts sensitive on small changes in the tip blade loading when operating close to design conditions. With slightly higher pressure between SS and PS the momentum ratio and related losses can increase significantly.

3. One additional correlation has been found to fit the pressure driven velocity, which allows to calculate the impact of friction momentum and to analyze the impact of the incidence flow momentum.

4. Found correlations can directly been used in efficiency extrapolation models that rely on tip leakage velocities, momentums, or momentum ratios.

5. As demonstrated the correlations can further been used to analyze mixed flow phenomena in the tip leakage flow as the incidence tip flow in the inlet. Also, found trends can be of interest for turbocharger turbine designer.

5.3 Efficiency Extrapolation Model

Mean line extrapolations towards lower, higher turbo rotational speeds, unmeasured VGT openings, and very high BSR at the same time have not been in the main focus of one-dimensional modeling yet.

This chapter of the thesis presents an adiabatic turbine efficiency model, which has the ability to extrapolate towards extremely high BSR as well as unmeasured VGT positions and shaft speeds. The physically based model relies on commonly used as well as novel loss correlations in rotor and stator. Its validity has been evaluated with a wide range of experimental data and several radial turbines.

First, the model and its working principle is presented. Second, the model extrapolation ability in shaft speed and VGT positioning is validated by means of various radial turbine maps. Further, the extrapolation in BSR is compared with maps of one turbocharger measured in a brought range of BSRs. High applicability for different turbos is shown. Third, results are discussed and concluded.

5.3.1 Turbine Model

The novel mean line model is designed for steady, nonreactive flow. In the extrapolated regions of the map towards high BSRs the Mach number is rather low. Although the flow in this condition can be seen as incompressible, extrapolation models are usually fitted with running points measured at high mass flows and Mach numbers. Thus, the gas compressibility has to be taken into account in most parts of the model. The developed extrapolation model has been designed

for turbocharger radial turbines with variable guide vanes. The used nomenclature for turbines equipped with stator blades can be seen in Figure 5.15. The model can also be used for vaneless turbines when the stator passage is taken out of the model. Thus, for vaneless turbines stations $2'$ and 2 are not considered and the outlet values of the volute define the inlet condition of the vaneless space.

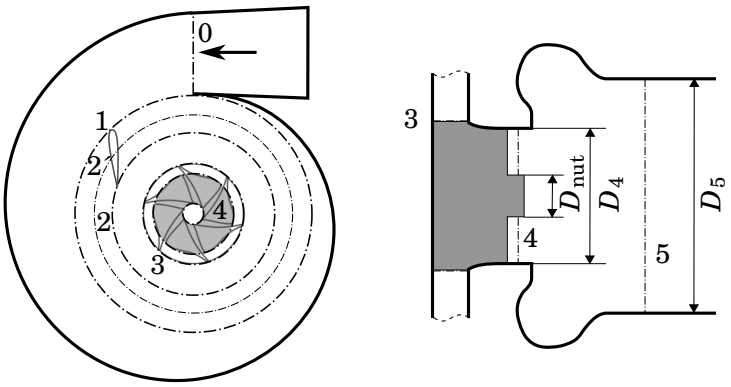

Figure 5.15: Turbine section nomenclature.

Dividing nominator and denominator of the total-to-static efficiency equation with the total inlet enthalpy $h_{\mathrm{t},0}$ the following equation has been obtained:

$$\eta_{\mathrm{ts}} = \frac{\frac{h_{\mathrm{t},3}}{h_{\mathrm{t},0}} - \frac{h_{\mathrm{t},4}}{h_{\mathrm{t},0}}}{\frac{h_{\mathrm{t},0}}{h_{\mathrm{t},0}} - \frac{h_{5,\mathrm{s}}}{h_{\mathrm{t},0}}}. \tag{5.48}$$

Here, non-dimensional numbers appear when the kinetic energy or the enthalpy losses are divided by the total inlet enthalpy. The relative enthalpy change along the turbine can be represented as in Figure 5.16 for stator and vaneless space and in Figure 5.17 for rotor and outlet. All losses have been modeled as relative enthalpy losses. The entire model has been developed with these non-dimensional numbers. This way no inlet temperature has to be assumed for the calculation of the efficiency based on reduced map numbers. Furthermore, the calculation of the density, which might require extra iterations in compressible models, can be omitted at all parts of the model. Additionally, the number of necessary iterations within the model can be reduced even more, since used loss models depend linearly on relative kinetic energies.

In common turbocharger test benches the total temperature is calculated with the static temperature and meridional velocity coming from mass flow measurements. Since the swirl is very high in the outlet duct when measuring in extreme off-design conditions, the kinetic energy of the tangential velocity

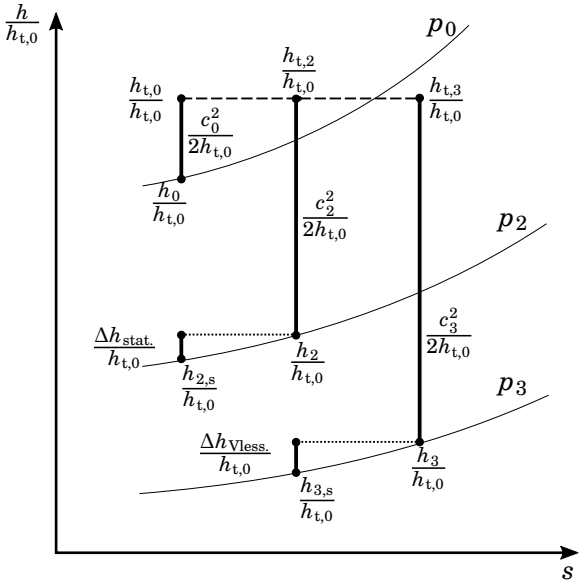

Figure 5.16: Stator and vaneless space enthalpy.

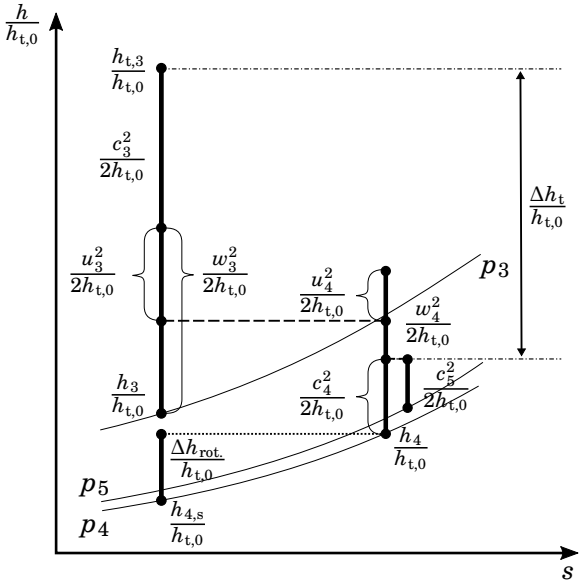

Figure 5.17: Rotor enthalpy.

component needs to be added. This way the experimentally measured efficiency can be modeled. (In a further step the efficiency considering the full kinetic energy in the turbine outlet can be calculated.) Thus, the efficiency can be deduced from Figure 5.17 as:

$$\eta_{\mathrm{ts}} = \frac{1 - \left(\frac{p_4}{p_{\mathrm{t},3}}\right)^{\frac{\gamma-1}{\gamma}} - \frac{c_{5,\mathrm{m}}^2}{2 \cdot h_{\mathrm{t},0}} - \frac{\Delta h_{\mathrm{loss,rot}}}{h_{\mathrm{t},0}} - \frac{\Delta h_{\mathrm{loss,rot,tip}}}{h_{\mathrm{t},0}}}{1 - \left(\frac{p_5}{p_{\mathrm{t},0}}\right)^{\frac{\gamma-1}{\gamma}}}. \tag{5.49}$$

Here, the pressure ratio $\frac{p_{\mathrm{t},0}}{p_5}$ is the overall pressure ratio ($\pi_{\mathrm{turb.}}$) that can be measured; $\frac{p_{\mathrm{t},3}}{p_4}$ is the rotor pressure ratio. The unknown rotor pressure ratio has been calculated from the stator pressure ratio, the pressure ratio over the vaneless space, the outlet pressure ratio and the overall pressure ratio:

$$\frac{p_{\mathrm{t},3}}{p_4} = \frac{\frac{p_{\mathrm{t},0}}{p_5}}{\frac{p_{\mathrm{t},0}}{p_{\mathrm{t},2}} \cdot \frac{p_{\mathrm{t},2}}{p_{\mathrm{t},3}} \cdot \frac{p_4}{p_5}}. \tag{5.50}$$

To calculate the unknown numbers in Equation 5.49 and Equation 5.50, the turbine zones have been solved partwise. The turbine has been split into volute (0-1), stator passage (1-2), vaneless space (2-3), rotor passage (3-4), and outlet region with diffuser (4-5). The modeling of each turbine section is shown in the following.

5.3.1.1 Volute

Due to the relatively low velocities the losses in the volute have been assumed as rather low in comparison the losses in stator, vaneless space, and rotor. Thus, the losses have been neglected first and the flow angle has been calculated easily from mass flow and momentum conservation:

$$\alpha_1 = atan\left(\frac{8 \cdot r_0 \cdot H_1}{D_0^2}\right). \tag{5.51}$$

Where D_0 is the diameter of the volute inlet (0); r_0 the radius from the rotor center to the middle point of the Volute inlet; H_1 the nozzle inlet height. The meridional velocity in the stator inlet (1) can be calculated from the reduced mass flow:

$$\frac{c_{1,\mathrm{m}}^2}{2 \cdot h_{\mathrm{t},0}} = \frac{R^2 \cdot \dot{m}_{\mathrm{red.}}^2}{A_1^2 \cdot c_{\mathrm{p}} \cdot 2}, \tag{5.52}$$

$$\frac{c_1^2}{2 \cdot h_{\mathrm{t},0}} = \frac{c_{1,\mathrm{m}}^2}{2 \cdot h_{\mathrm{t},0} \cdot cos(\alpha_1)}. \tag{5.53}$$

Thus, the stator inlet condition is fully defined.

5.3.1.2 Stator

To obtain a consistent set of fitting coefficients for all VGT positions at the same time, the moving mechanism of the stator vanes has to be modeled properly. First a linear correlation between vane opening percentage and stator blade angle has been assumed as it has been stated by Serrano et al. [52]. To calculate the stator throat length $l_{\text{thr.}}$ (blue dashed line in Figure 5.18) from the blade angle, the geometry can be resolved by means of the variables shown in Figure 5.18.

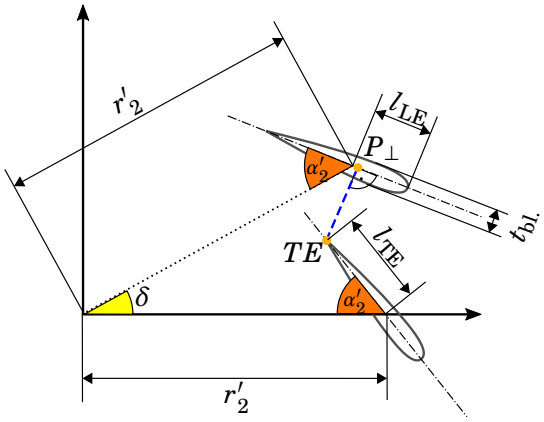

Figure 5.18: Stator throat (blue dashed line) calculation.

Using the known geometrical data a correlation between the stator vane angle and the throat area can be derived. This is done by calculating the position of the trailing edge of one vane (TE) and the closest point on the middle line of the next vane ($P_\perp$) in the indicated coordinate frame in Figure 5.18:

$$TE_x = r'_2 - l_{\text{TE}} \cdot \cos\left(\alpha'_2\right), \tag{5.54}$$

$$TE_y = \sin\left(\alpha'_2\right) \cdot l_{\text{TE}}, \tag{5.55}$$

$$P_{\perp,\mathrm{x}} = \frac{l_{\mathrm{TE}} \cdot \left(\sin(\delta) + \cos(\delta) \cdot \frac{-1}{\tan(\delta - \alpha_2')}\right)}{\frac{1+\tan^2(\delta-\alpha_2')}{\tan(\delta-\alpha_2')}} - \\ - \frac{r_2' \cdot \left(\sin(\delta) - \tan\left(-\alpha_2' - \delta\right) \cdot \cos(\delta) + \frac{-1}{\tan(\delta-\alpha_2')}\right)}{\frac{1+\tan^2(\delta-\alpha_2')}{\tan(\delta-\alpha_2')}}, \\ \text{with}: \delta = \frac{2 \cdot \pi}{z}, \tag{5.56}$$

$$P_{\perp,\mathrm{y}} = \tan\left(\delta - \alpha_2'\right) \cdot r_2' \cdot \left(P_{\perp,\mathrm{x}} \cdot \sin(\delta) - \cos(\delta)\right), \tag{5.57}$$

$$l_{\mathrm{thr.}} = \sqrt{\left(TE_x - P_{\perp,\mathrm{x}}\right)^2 + \left(TE_y - P_{\perp,\mathrm{y}}\right)^2} - \frac{t_{\mathrm{bl.}}}{2}. \tag{5.58}$$

Furthermore, changing stator inlet radius and outlet radius can be estimated as:

$$r_1 = \sqrt{\left(r_2' + l_{\mathrm{LE}} \cdot \cos\left(\alpha_2'\right)\right)^2 + \sin\left(\alpha_2'\right)^2 \cdot l_{\mathrm{LE}}^2}, \tag{5.59}$$

$$r_2 = \sqrt{\left(r_2' - l_{\mathrm{TE}} \cdot \cos\left(\alpha_2'\right)\right)^2 + \sin\left(\alpha_2'\right)^2 \cdot l_{\mathrm{TE}}^2}. \tag{5.60}$$

Loss models have been used to model the flow evolution in the stator. The same types of losses as they were recommended by Futral and Wasserbauer [57] for the rotor passage have been assumed for the stationary stator passage. Consequently, the stator takes incidence and passage losses into account:

$$\frac{\Delta h_{\mathrm{stat.}}}{h_{\mathrm{t},0}} = \frac{\Delta h_{\mathrm{stat.,inc.}}}{h_{\mathrm{t},0}} + \frac{\Delta h_{\mathrm{stat.,pas.}}}{h_{\mathrm{t},0}}. \tag{5.61}$$

In the non-dimensional formulation they can be formulated as:

$$\frac{\Delta h_{\mathrm{stat.,inc.}}}{h_{\mathrm{t},0}} = z_{\mathrm{stat.,inc.}} \cdot \sin^2 i_1 \cdot \frac{c_1^2}{2 \cdot h_{\mathrm{t},0}}, \tag{5.62}$$

$$\frac{\Delta h_{\mathrm{stat.,pas.}}}{h_{\mathrm{t},0}} = z_{\mathrm{stat.,pas.}} \cdot \left(\cos^2 i_1 \cdot \frac{c_1^2}{2 \cdot h_{\mathrm{t},0}} + \frac{c_2^2}{2 \cdot h_{\mathrm{t},0}}\right). \tag{5.63}$$

Here i_1 is the difference between the current inlet flow angle and the current stator vane angle. Following, the stator outlet velocity can be iteratively calculated with:

$$\dot{m}_{\mathrm{red.}} = \sqrt{\frac{c_2^2}{2 \cdot h_{\mathrm{t},0}} \cdot 2 \cdot c_{\mathrm{p}}} \cdot \frac{\cos \alpha_{2'} \cdot A_2 \cdot C_{\mathrm{d},2}}{R} \cdot \frac{p_{\mathrm{t},2}}{p_{\mathrm{t},0}}. \tag{5.64}$$

A discharge coefficient $C_{\mathrm{d},2}$ has been introduced to take into account that the real flow in a stator is not homogeneously distributed. Thus, the whole flow is assumed to flow though an effective area.

Finally, the stator total pressure ratio has been calculated by dividing the isentropic pressure ratio $\frac{p_{\mathrm{t},0}}{p_2}$ with the effective pressure ratio $\frac{p_{\mathrm{t},2}}{p_2}$:

$$\frac{p_{\mathrm{t},0}}{p_2} = \left(\frac{1}{1 - \frac{c_2^2}{2 \cdot h_{\mathrm{t},0}} - \frac{\Delta h_{\mathrm{stat.}}}{h_{\mathrm{t},0}}} \right)^{\frac{\gamma}{\gamma - 1}}, \tag{5.65}$$

$$\frac{p_{\mathrm{t},2}}{p_2} = \left(\frac{1}{1 - \frac{c_2^2}{2 \cdot h_{\mathrm{t},0}}} \right)^{\frac{\gamma}{\gamma - 1}}, \tag{5.66}$$

$$\frac{p_{\mathrm{t},0}}{p_{\mathrm{t},2}} = \left(\frac{1 - \frac{c_2^2}{2 \cdot h_{\mathrm{t},0}}}{1 - \frac{c_2^2}{2 \cdot h_{\mathrm{t},0}} - \frac{\Delta h_{\mathrm{stat.}}}{h_{\mathrm{t},0}}} \right)^{\frac{\gamma}{\gamma - 1}}. \tag{5.67}$$

5.3.1.3 Vaneless Space

It has been found out that the modeling of the vaneless space and its losses have a sensitive impact on the fitting of all VGT maps at the same time. Thus, the vane less space had to be modeled as an additional nozzle. The corresponding loss has been formulated depending on flow length and velocity as:

$$\frac{\Delta h_{\mathrm{Vless}}}{h_{\mathrm{t},0}} = z_{\mathrm{Vless}} \cdot L_{\mathrm{Vless}} \cdot \frac{c_3^2}{2 \cdot h_{\mathrm{t},0}}. \tag{5.68}$$

The flow length of each streamline through the vaneless space has been calculated as the curvature integral of a logarithmic spiral (a logarithmic spiral has a constant angle and thus, it is the analytic solution for the flow path in a radial nozzle with isentropic and incompressible flow):

$$L_{\mathrm{Vless}} = r_3 \cdot \tan(\alpha_3) \cdot \sqrt{\left[\left(\frac{1}{\tan(\alpha_3)} \right)^2 + 1 \right]} \cdot \left(\frac{r_2}{r_3} - 1 \right). \tag{5.69}$$

The differences between flow path lengths for different VGT positions can be significant due to the growing of vaneless space outer radius and increasing flow angle when the stator vales are closing (as it can be seen in Figure 5.19).

The stator outlet angle has been assumed according to [99] as:

$$\alpha_3 = \arctan\left(\frac{r_2 \cdot 2\pi \cdot b_1}{z_{2'} \cdot l_{\mathrm{thr.}} \cdot b_{2'}} \cdot \sin\left[\alpha_2' + \arctan\left(\frac{TE_{\mathrm{y}}}{TE_{\mathrm{x}}} \right) \right] \right). \tag{5.70}$$

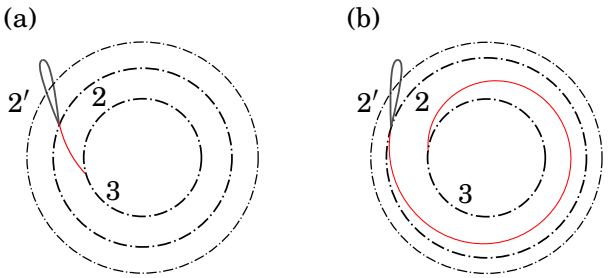

Figure 5.19: Vaneless space flow path with: (a) opened VGT; (b) closed VGT.

Here, it has been necessary to adjust the stator vane angle α_2' to obtain the middle line angle at the radius of the trailing edge.

The final nozzle outlet velocity has been iteratively calculated with modified Equation 5.64 and 5.67 for the vaneless region:

$$\dot{m}_{\text{red.}} = \sqrt{\frac{c_3^2}{2 \cdot h_{\text{t},0}} \cdot 2 \cdot c_{\text{p}} \cdot \frac{\cos\alpha_3 \cdot A_3 \cdot C_{\text{d},3}}{R} \cdot \frac{p_{\text{t},2}}{p_{\text{t},0}} \cdot \frac{p_{\text{t},3}}{p_{\text{t},2}}}, \tag{5.71}$$

$$\frac{p_{\text{t},2}}{p_{\text{t},3}} = \left(\frac{1 - \frac{c_3^2}{2 \cdot h_{\text{t},0}}}{1 - \frac{c_3^2}{2 \cdot h_{\text{t},0}} - \frac{\Delta h_{\text{Vless}}}{h_{\text{t},0}}} \right)^{\frac{\gamma}{\gamma - 1}}. \tag{5.72}$$

Finally, the total stator pressure ratio can be calculated by dividing the total to static pressure ratios of stator (0-2) and vaneless space (2-3):

$$\frac{p_{\text{t},0}}{p_{\text{t},3}} = \frac{p_{\text{t},0}}{p_{\text{t},2}} \cdot \frac{p_{\text{t},2}}{p_{\text{t},3}}. \tag{5.73}$$

Following, this pressure ratio can be used to calculate the rotor pressure ratio.

5.3.1.4 Rotor

To calculate the remaining terms of the efficiency equation the rotor flow has to get resolved. Therefore, the velocity triangle in the inlet of the turbine (Figure 5.20) can be solved by means of already known values:

$$\frac{c_{\text{m},3}^2}{2 \cdot h_{\text{t},0}} = \frac{c_3^2}{2 \cdot h_{\text{t},0}} \cdot \cos(\alpha_3)^2, \tag{5.74}$$

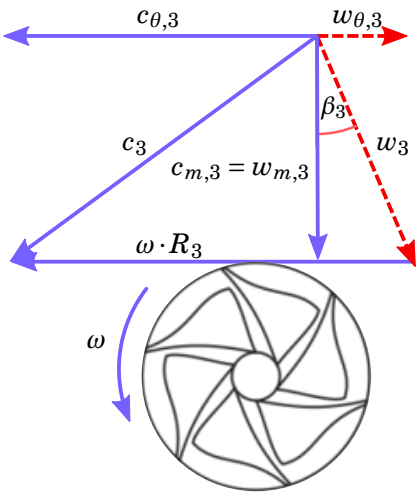

Figure 5.20: Rotor inlet velocity triangle.

$$\frac{c_{\theta,3}^2}{2 \cdot h_{\mathrm{t},0}} = \frac{c_3^2}{2 \cdot h_{\mathrm{t},0}} \cdot \sin(\alpha_3)^2, \tag{5.75}$$

$$\frac{w_3^2}{2 \cdot h_{\mathrm{t},0}} = \left(\sqrt{\frac{c_{\theta,3}^2}{2 \cdot h_{\mathrm{t},0}}} - \sqrt{\frac{u_3^2}{2 \cdot h_{\mathrm{t},0}}} \right)^2 + \frac{c_{\mathrm{m},3}^2}{2 \cdot h_{\mathrm{t},0}}, \tag{5.76}$$

$$\beta_3 = \arctan \left(\frac{\sqrt{\frac{c_{\theta,3}^2}{2 \cdot h_{\mathrm{t},0}}} - \sqrt{\frac{u_3^2}{2 \cdot h_{\mathrm{t},0}}}}{\sqrt{\frac{c_{\mathrm{m},3}^2}{2 \cdot h_{\mathrm{t},0}}}} \right). \tag{5.77}$$

Inlet rotational speed in non-dimensional form can be formulated as:

$$\frac{u_3^2}{2 \cdot h_{\mathrm{t},0}} = \frac{\left(\frac{N_{\mathrm{red.}}}{60} \cdot \pi \cdot D_3 \right)^2}{2 \cdot c_{\mathrm{p}}}. \tag{5.78}$$

For calculating turbine outlet gas conditions in the stationary frame the rotor outlet velocity triangle, shown in Figure 5.21, has been solved. Since the mass flow and performance extrapolation are executed in two different models as it was done by Serrano et al. [52], the mass flow is a known variable. Thus, the equations have one degree of freedom less and the velocity triangle in Figure 5.21 can be calculated without assuming one blade angle and related

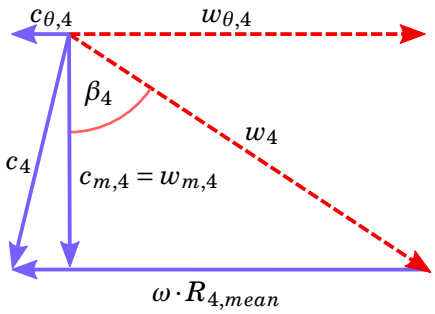

Figure 5.21: Rotor outlet velocity triangle.

deviation. This strategy has been chosen because current turbocharger turbines own varying trailing edge angles over the radius and thus various degrees of deviation. It is expected that the system of fitted loss models results in a good estimation of the mean velocity triangle. Thus, rothalpy conservation has been used to calculate the relative outlet velocity of the rotor as:

$$\begin{aligned}\frac{w_4^2}{2\cdot h_{t,0}} =& 1-\left(\frac{p_4}{p_{t,3}}\right)^{\frac{\gamma-1}{\gamma}} - \frac{c_3^2}{2\cdot h_{t,0}}\cdot\left[1-\left(\frac{\cos(\alpha_3)}{\cos(\beta_3)}\right)^2\right] - \\ & -\frac{\Delta h_{rot.}}{h_{t,0}} + \frac{u_4^2}{2\cdot h_{t,0}} - \frac{u_3^2}{2\cdot h_{t,0}}.\end{aligned} \tag{5.79}$$

The meridional velocity in the rotor outlet cross section has been calculated by means of the mass flow conservation:

$$\frac{c_{m,4}^2}{2\cdot h_{t,0}} = \left[\frac{R\cdot \dot{m}_{red.}}{A_4\cdot d_4\cdot\sqrt{2\cdot c_p}}\cdot\frac{h_4}{h_{t,0}}\cdot\frac{p_{t,0}}{p_5}\cdot\frac{p_5}{p_4}\right]^2. \tag{5.80}$$

While the relative static outlet enthalpy has been calculated with:

$$\frac{h_4}{h_{t,0}} = \left(\frac{p_4}{p_{t,3}}\right)^{\frac{\gamma-1}{\gamma}} + \frac{\Delta h_{rot.}}{h_{t,0}} \tag{5.81}$$

Outlet rotational speed has been calculated with:

$$\frac{u_4^2}{2\cdot h_{t,0}} = \frac{\left(\frac{N_{red.}}{60}\cdot\pi\cdot\bar{D}_4\cdot DC_4\right)^2}{2\cdot c_p}. \tag{5.82}$$

Also in the rotor outlet a discharge coefficient has been used. However, it has been adjusted on the needs of a rotating system with rather radially distributed

velocity field. Hence, the effective mean diameter $\bar{D}_4$ has been adjusted according to the discharged area as it can be seen in Figure 5.22. Due to the definition in Equation 5.83, the mean diameter separates always 50 % of the radially discharged area.

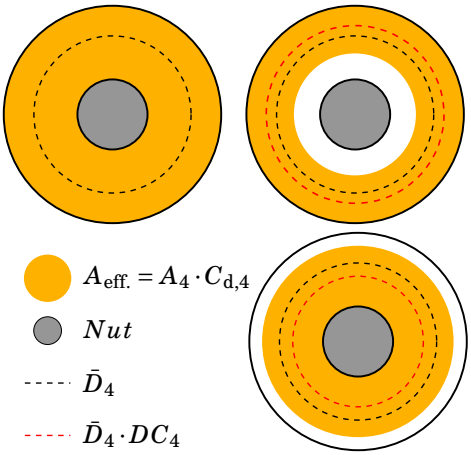

Figure 5.22: Rotor outlet discharge definition.

$$\begin{aligned} \text{for } DC_4 > 1\text{: } C_{\text{d},4} &= \frac{\left(D_{4,\text{out}}^2 - \bar{D}_4^2 \cdot {DC_4}^2\right) \cdot \pi}{2 \cdot A_4} \\ \text{for } DC_4 < 1\text{: } C_{\text{d},4} &= \frac{\left(\bar{D}_4^2 \cdot {DC_4}^2 - D_{4,\text{in}}^2\right) \cdot \pi}{2 \cdot A_4} \end{aligned} \tag{5.83}$$

The rotor losses are sub-divided into incidence losses, passage losses, and tip leakage losses. The models for the rotor incidence and rotor passage losses by Futral and Wasserbauer [57], which are well validated in the literature, are used for the rotor inside of the rotational reference frame.

$$\frac{\Delta h_{\text{rot.,inc}}}{h_{\text{t},0}} = \sin\left(\beta_3 - \beta_{3,\text{opt.}}\right)^2 \cdot \frac{w_3^2}{2 \cdot h_{\text{t},0}} \tag{5.84}$$

$$\frac{\Delta h_{\text{rot.,pas.}}}{h_{\text{t},0}} = z_{\text{rot.,pas.}} \cdot \left[\cos\left(\beta_3 - \beta_{3,\text{opt.}}\right)^2 \cdot \frac{w_3^2}{2 \cdot h_{\text{t},0}} + \frac{w_4^2}{2 \cdot h_{\text{t},0}}\right] \tag{5.85}$$

Here, the optimum inflow angle $\beta_{3,\text{opt.}}$ has been estimated by the slip-factor definition of Chen and Baines [100].

For the rotor tip leakage losses the model implemented in subsection 5.2.1, Equation 5.33 has been used. It has been proven to have good extrapolation

capability and requires only one set of coefficients for different VGT positions, speeds, and a wide range of pressure ratios.

All these sub-models own fitting coefficients, which have to be fitted by means of experimental data. Finally, the outlet velocity triangle has been solved with:

$$\frac{w_{\theta,4}^2}{2 \cdot h_{\mathrm{t},0}} = \frac{w_4^2}{2 \cdot h_{\mathrm{t},0}} - \frac{c_{\mathrm{m},4}^2}{2 \cdot h_{\mathrm{t},0}}, \tag{5.86}$$

$$\frac{c_{\theta,4}^2}{2 \cdot h_{\mathrm{t},0}} = \left(\sqrt{\frac{w_{\theta,4}^2}{2 \cdot h_{\mathrm{t},0}}} - \sqrt{\frac{u_4^2}{2 \cdot h_{\mathrm{t},0}}} \right)^2, \tag{5.87}$$

$$\frac{c_4^2}{2 \cdot h_{\mathrm{t},0}} = \frac{c_{\theta,4}^2}{2 \cdot h_{\mathrm{t},0}} + \frac{c_{\mathrm{m},4}^2}{2 \cdot h_{\mathrm{t},0}}. \tag{5.88}$$

5.3.1.5 Outlet

Finally, the pressure ratio between turbine rotor trailing edge up to the measurement duct has been calculated. Since the circulation in the turbine outlet is of high importance in off-design conditions towards high BSR as shown in subsection 4.5.1, all conservation equations have to be considered for modeling the transition of the static outlet pressure ratio. Thus, the following conservation equations are solved in non-dimensional form:

$$\frac{c_{\mathrm{t},5}^2}{2 \cdot h_{\mathrm{t},0}} = \frac{\bar{D}_4^2}{\bar{D}_5^2} \cdot \frac{c_{\mathrm{t},4}^2}{2 \cdot h_{\mathrm{t},0}}, \tag{5.89}$$

$$\frac{c_5^2}{2 \cdot h_{\mathrm{t},0}} = \frac{c_{\mathrm{t},5}^2}{2 \cdot h_{\mathrm{t},0}} + \frac{c_{\mathrm{m},5}^2}{2 \cdot h_{\mathrm{t},0}}, \tag{5.90}$$

$$\frac{h_5}{h_{\mathrm{t},0}} = \frac{h_4}{h_{\mathrm{t},0}} + \frac{c_4^2}{2 \cdot h_{\mathrm{t},0}} - \frac{c_5^2}{2 \cdot h_{\mathrm{t},0}}, \tag{5.91}$$

$$\frac{p_4}{p_5} = \frac{A_5 + \frac{c_{\mathrm{m},5}^2}{2 \cdot h_{\mathrm{t},0}} \cdot \frac{A_5 \cdot 2 \cdot c_\mathrm{p}}{R} \cdot \frac{h_{\mathrm{t},0}}{h_5}}{A_5 + \frac{c_{\mathrm{m},4}^2}{2 \cdot h_{\mathrm{t},0}} \cdot \frac{A_4 \cdot 2 \cdot c_\mathrm{p}}{R} \cdot \frac{h_{\mathrm{t},0}}{h_4}}, \tag{5.92}$$

$$\frac{c_{\mathrm{m},5}^2}{2 \cdot h_{\mathrm{t},0}} = \frac{c_{\mathrm{m},4}^2}{2 \cdot h_{\mathrm{t},0}} \cdot \left(\frac{A_4}{A_5} \right)^2 \cdot \left(\frac{p_4}{p_5} \right)^2 \cdot \left(\frac{h_5}{h_{\mathrm{t},0}} \right)^2 \cdot \left(\frac{h_{\mathrm{t},0}}{h_4} \right)^2. \tag{5.93}$$

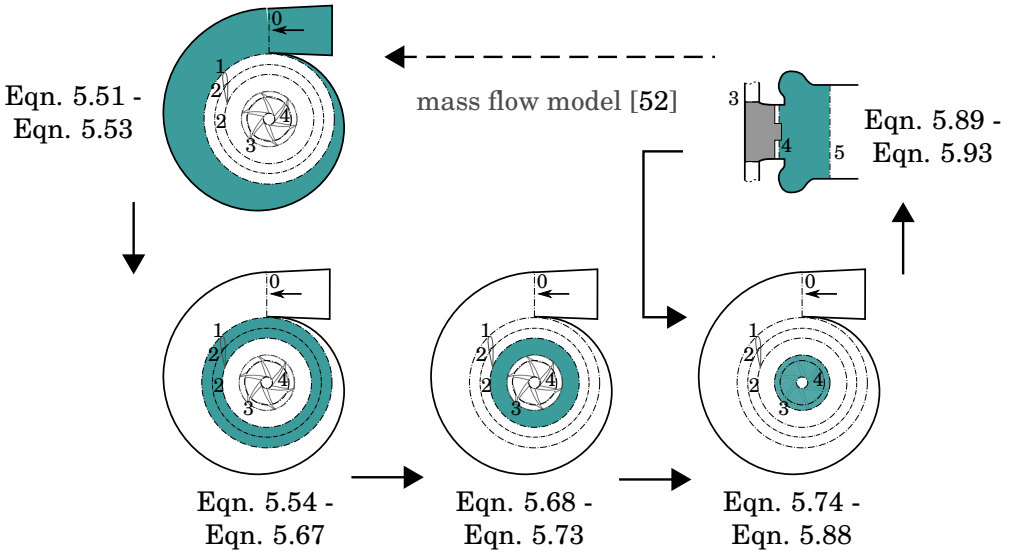

Figure 5.23: Solving flow chard.

5.3.1.6 Extrapolation Solving Scheme

The model has been programmed and run in MATLAB. Each turbine section has been resolved along the flow direction. However, a iteration between outlet section and turbine wheel is needed. Further, stator, vaneless space, rotor and outlet section have coupled equations and need to be solved in an internal iterative solution themselves.

By means of a nonlinear fitting the loss parameters and discharge coefficients have been found. Here, the Levenberg-Marquardt algorithm has been chosen. However, the model is robust enough to be fitted with other non-linear methods as well. During this fitting the experimental reduced mass flow has been used as data input. When the model extrapolates towards unmeasured regions of the map, mass flow and efficiency extrapolation models need to be coupled. For the following presented results the mass flow extrapolation model by Serrano et al. [52] has been used to obtain necessary mass flow data. Since this mass flow model requires an efficiency as input, iterations between efficiency model and mass flow model need to be executed as it is shown in Figure 5.23. The use of any other mass flow extrapolation model like the empirical model by Fang et al. [101] is also possible.

5.3.2 Results & Discussion

The model has been fitted by means of the data of 3 different turbochargers (T1, T2, and T3) equipped with variable stator vanes. Each turbine has been

measured at different VGT positions in quasi-adiabatic tests. While T1 was measured in a wide range in section 3.3, T2 and T3 were measured in a typical narrow range of operating conditions. Further, the adiabatic efficiency has been obtained by correcting residual internal turbocharger heat fluxes by means of the heat transfer model described in [39] and [46]. For the parameter fitting only data in a typically measurable range of operating conditions has been used. Thus, all data of turbines T2 and T3 and only the 7 measurements per speedline close to the highest measured efficiency of turbine T1 are used. Each turbine has been fitted individually. The determined fitting coefficients are listed in Table 5.2.

Parameter	T1	T2	T3
	Stator		
$Z_{\text{stat.,pass.}}$	0.27	0.31	0.74
$C_{\text{d,2}}$	1.00	1.00	0.60
	Vaneless Space		
Z_{Vless}	0.47	0.44	0.24
$C_{\text{d,3}}$	0.75	0.79	0.60
	Rotor		
$Z_{\text{rot.,pass.}}$	0.00	0.00	0.07
$K_{\text{rot.,tip,+}}$	0.04	0.04	0.05
$K_{\text{rot.,tip,−}}$	1.27	1.25	1.11
DC_4	0.88	0.91	1.00

Table 5.2: Found fitting coefficients by non-linear fitting for T1, T2, and T3.

	T1	T2	T3
MAE	0.0258	0.0142	0.0143
RMSE	0.0332	0.0186	0.0177

Table 5.3: Measures of overall fitting quality of T1, T2, and T3.

It can be seen that the found fitting parameters have similar magnitudes for all analyzed turbochargers. For any new turbocharger, the average of these values can be used as initial value of the parameter fitting. For T1 and T2 the new definition of the rotor outlet flow deformation has been fitted with a DC_4 value below 1. This represents a flow concentration towards the hub, which is consistent with the observation of higher $c_{4,\text{m}}$ in CFD results close to design conditions. At the same time the passage loss of Equation 5.85 has

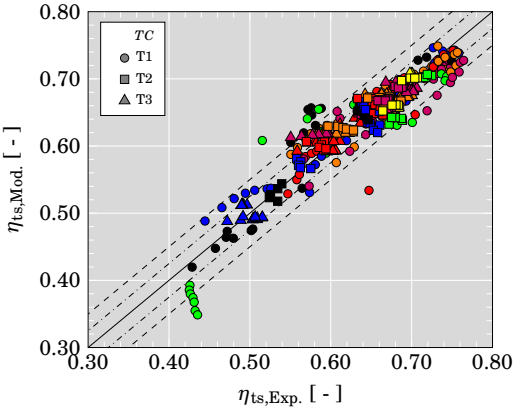

Figure 5.24: Overall fitting quality and extrapolation towards high BSR of T1, T2, and T3.

consistently been fit with 0. Although this loss is commonly used, Meitner and Glassman [102] showed the occurrence of high variations of this value dependent on the stator angle. Here, other loss models or the definition of the rotor outlet condition are able to compensate this loss for the desired fitting of all VGT positions. However, this might allow to reduce the model's number of fitting parameters by one.

The model is able to reproduce the turbine efficiencies in a good quality for all fitted turbines with different VGT positions and varying rotational speed, as it can be seen in Figure 5.24 and in Table 5.3. The majority of the running points are reproduced with less than 5 percentage points of error.

After finding the fitting parameters, the aforementioned solving scheme applying a separate mass flow extrapolation model has been used to extrapolate the efficiency data. In the following, the mass flow model described in [52] has been used. In Figure 5.25, Figure 5.26, and Figure 5.27 the extrapolation results are shown against the BSR. It can be seen that the model is capable of reproducing the trends with VGT opening and rotational speed at the same time for all tested turbocharger turbines. For all turbocharger turbines the following observations can be made:

1. From design condition towards off-design condition η_{ts} speedlines are further collapsing.

2. At closed VGTs: η_{ts} speedlines are wider spread; Towards opened VGTs: more and more overlapping and almost identical at very opened positions.

3. The x-axis is crossed at increasing BSR when opening the VGT.

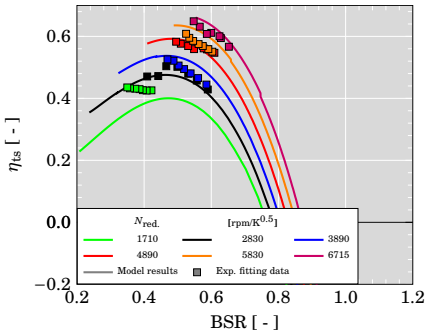

(a) Efficiency with 10 % VGT opening

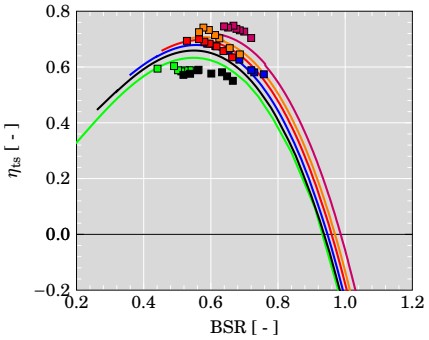

(b) Efficiency with 30 % VGT opening

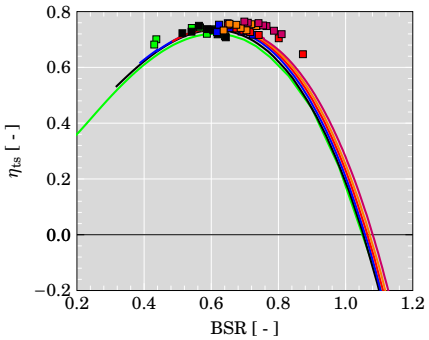

(c) Efficiency with 60 % VGT opening

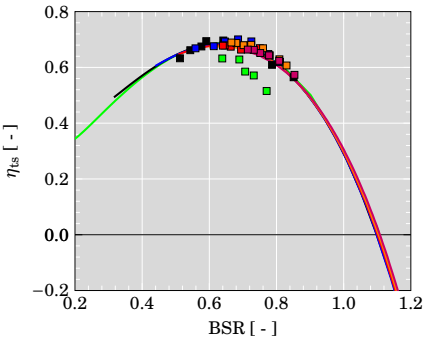

(d) Efficiency with 80 % VGT opening

Figure 5.25: Model fitting for turbocharger T1: η_{ts} vs. BSR.

Although all observations are qualitatively valid for the analyzed turbines, the development depends on each turbine. Comparing results for 40 % VGT opening of T2 and T3 shows different extension of the line spreading. Speedlines of T2 are spread over a much wider range of BSR than for T3 at zero efficiency. This highlights the model capability of fitting rather different turbocharger turbine behavior.

In comparison with the results of the semi-empirical model presented in [52] important differences can be highlighted. The collapsing characteristic of the data has been reproduced in more detail by the novel model. Also, the trend of stronger overlapping speedlines with the VGT opening is much better modeled in the new physical approach.

5.3.2.1 Extrapolation Towards Low Pressure Ratios

For the validation of the model extrapolation capability towards high BSR, the data has been compared against the experimental wide range data of turbine T1 obtained in section 3.3. As shown, the experimental measurements have

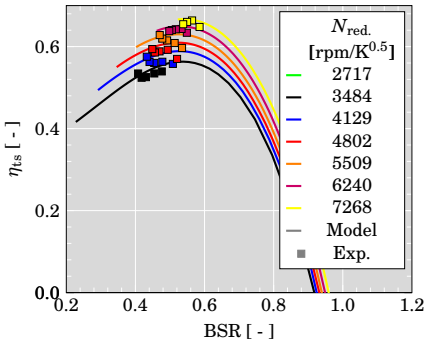

(a) Efficiency with 10 % VGT opening

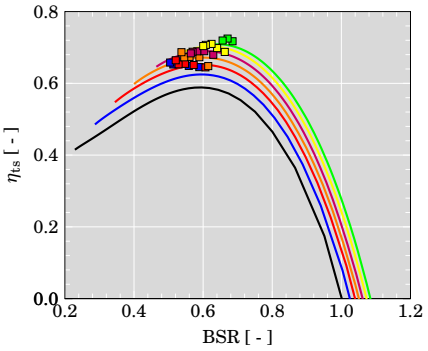

(b) Efficiency with 40 % VGT opening

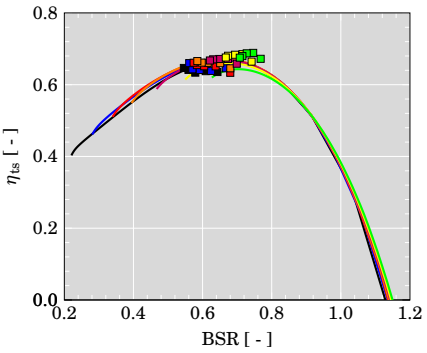

(c) Efficiency with 80 % VGT opening

Figure 5.26: Model fitting for turbocharger T2: η_{ts} vs. BSR.

very high inherent uncertainties in BSR in comparison to the turbine expansion ratio in the extrapolated zones. Hence, results are presented against the turbine expansion ratio $\pi_{turb.}$ in Figure 5.28.

The results show good extrapolation quality towards low pressure ratios by using only a limited number of experimental points at high turbine efficiency for the model fitting (Figure 5.28 shows a mean absolute error (MAE) of 0.0467 and a root mean square error (RMSE) of 0.0724). The efficiency is well reproduced up to very low and even negative values. However, turbine efficiency is rather under predicted in the highest efficiency region of 6715 rpm/K$^{0.5}$ measured turbo speed for the VGT openings of 30 % and 60 %. Also, the second lowest speed of 30 % VGT opening seems over predicted in design condition and 4890 rpm/K$^{0.5}$ of 60 % VGT opening seems under predicted in off-design. Nevertheless, high quality of surrounding results might indicate that inherent uncertainties in the VGT mechanism are responsible for highlighted mismatch.

Figure 5.29 shows the model results against the experimental results together with the experimental errors. A more detailed analysis of experimental

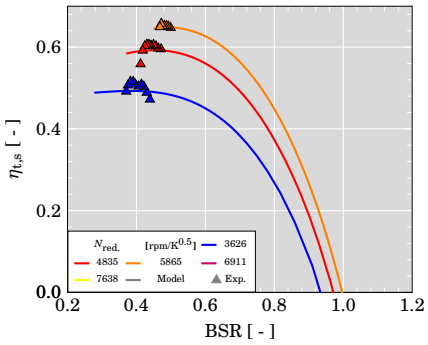

(a) Efficiency with 10 % VGT opening

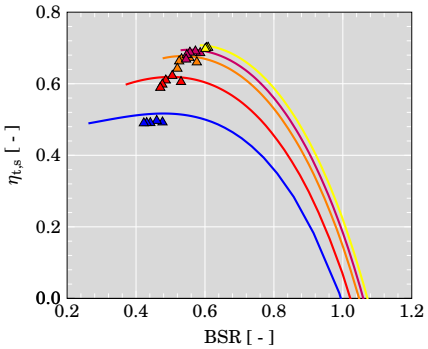

(b) Efficiency with 15 % VGT opening

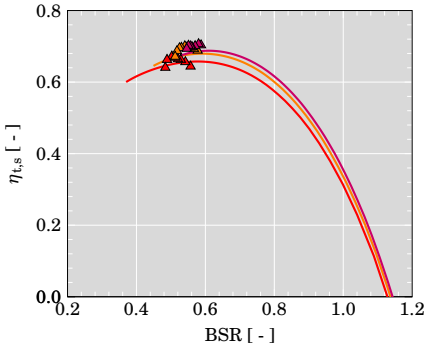

(c) Efficiency with 40 % VGT opening

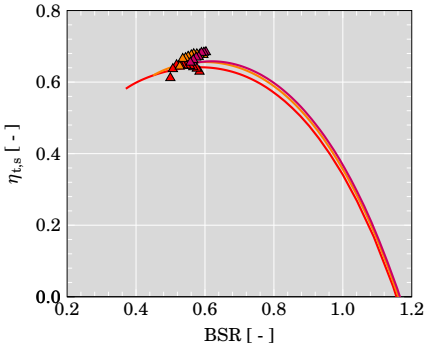

(d) Efficiency with 60 % VGT opening

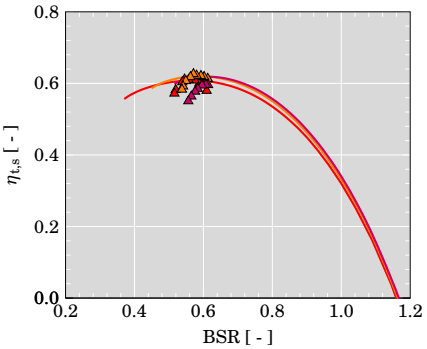

(e) Efficiency with 80 % VGT opening

Figure 5.27: Model fitting for turbocharger T3: η_{ts} vs. BSR.

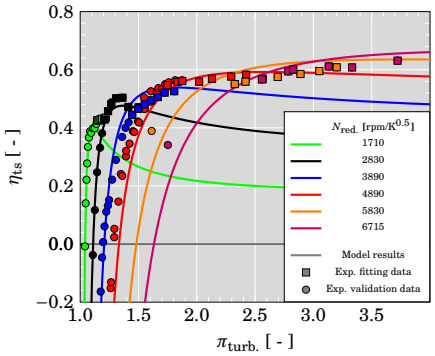

(a) Efficiency with 10 % VGT opening

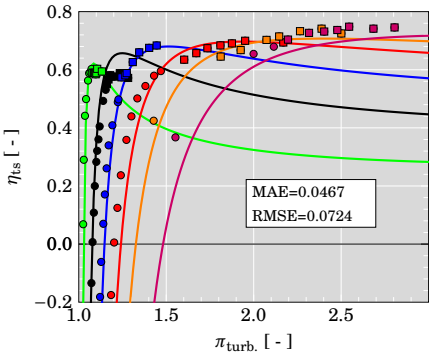

(b) Efficiency with 30 % VGT opening

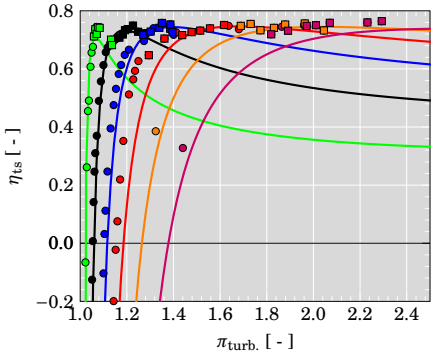

(c) Efficiency with 60 % VGT opening

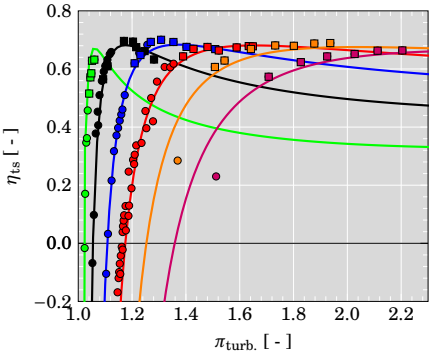

(d) Efficiency with 80 % VGT opening

Figure 5.28: Extrapolation towards low $\pi_{turb.}$ for turbocharger T1: η_{ts} vs. $\pi_{turb.}$.

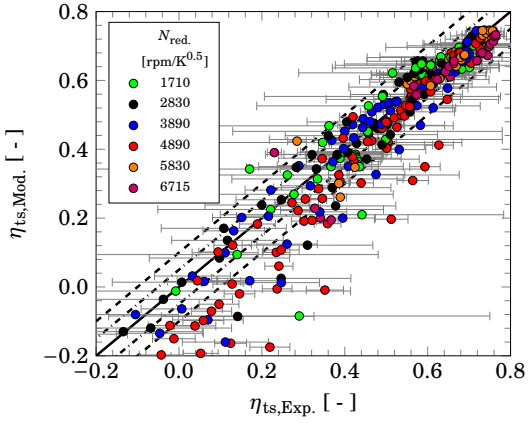

Figure 5.29: Overall fitting quality and extrapolation towards low $\pi_{turb.}$ with T1.

errors can be found in section 3.3. Clearly, measurement errors become very high when turbine power output is low especially in off-design conditions. This explains a certain degree of the final extrapolation error. Figure 5.29 also confirms that the efficiency of 4890 rpm/K$^{0.5}$ is rather under predicted. High absolute errors can occur easily due to the high slope of the curves at off-design. Hence, errors in the rotational speed can cause this kind of mismatch. All this shows the potential of this kind of models to monitor experimental measurements.

5.3.2.2 Extrapolation Towards Speed

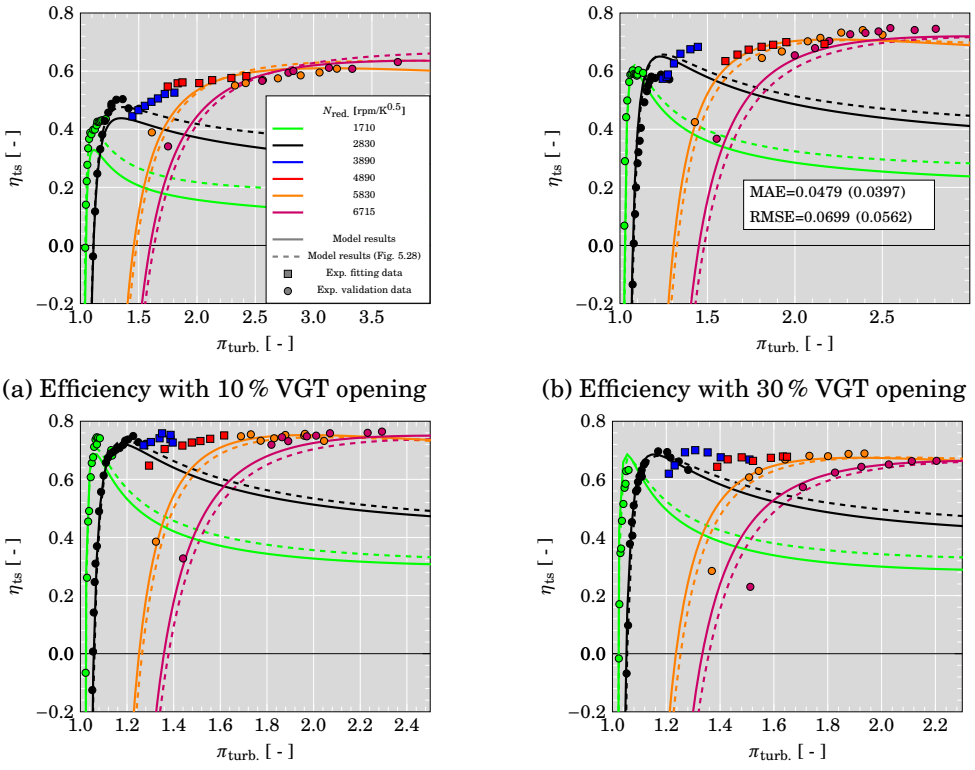

(a) Efficiency with 10 % VGT opening

(b) Efficiency with 30 % VGT opening

(c) Efficiency with 60 % VGT opening

(d) Efficiency with 80 % VGT opening

Figure 5.30: Extrapolation towards low $\pi_{turb.}$, lower, and higher speeds for turbocharger T1: η_{ts} vs. $\pi_{turb.}$.

For the extrapolation towards lower and higher speeds only the experimental data of 3890 rpm/K$^{0.5}$ and 4890 rpm/K$^{0.5}$ at design condition have been used as model fitting input. These speeds are not extrapolated here. Dashed lines in Figure 5.30 represent the extrapolation results of Figure 5.28 using close to design points of all measured speeds for comparison. In Figure 5.30 the

overall MAE of the two higher and two lower extrapolated speeds worsens from 0.0397 to 0.0479 in comparison to the fitting with all speeds (dashed lines or Figure 5.28). The RMSE worsens from 0.0562 to 0.0699 respectively. Figure 5.30 shows that the efficiency prediction for lower speeds has worsened slightly by under predicting the efficiency in close to design condition. However, the off-design prediction stays of the same quality. Extrapolations towards higher speeds show even a slightly better efficiency prediction for most of the points as when fitted with all speeds. Reason for this might be the fitting without the high uncertainty afflicted data of lower speedlines. In summary, fitting the model by means of only two different speeds allows to extrapolate towards higher and lower speed without loosing much quality.

5.3.2.3 Extrapolation in VGT Position

The model capability of fitting several VGT positions at the same time helps to fit the loss models over a wider range. At the same time it allows to extrapolate and interpolate towards unmeasured VGT positions. Thus, this extrapolation ability has been exercised. First, the model has been fitted by means of the measurements at high efficiency of the VGT opening of 30 %, 60 %, and 80 %. With the obtained coefficients model results for the VGT position of 10 %, that are shown in Figure 5.31, have been generated. In respect to the fitting with all available VGT positions (dashed line) and to the experimental results, extrapolations show under predicted efficiency. While high errors can be found at low speeds, higher speeds are still well predicted. In Figure 5.31 the extrapolated data worsens in respect to the extrapolation with all data close to design condition (Figure 5.28) its MAE from 0.0401 to 0.601 and its RMSE from 0.0543 to 0.0758. Due to the

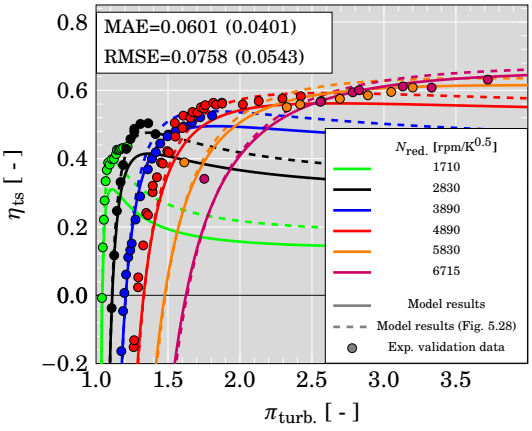

Figure 5.31: Extrapolation of 10 % VGT opening for turbocharger T1: η_{ts} vs. $\pi_{turb.}$.

high importance of $\frac{\Delta h_{\text{Vless}}}{h_{\text{t,0}}}$ for the fitting of all VGT maps especially at closed positions, the fitting of this loss plays a big role when extrapolating closed VGT positions. As Figure 5.32 shows, described losses are progressively increasing towards closed positions. Hence, missing information in this zone complicate a good prediction of this loss. This can be understood as main limitation of the model to extrapolate with high quality. Figure 5.33 shows the extrapolation

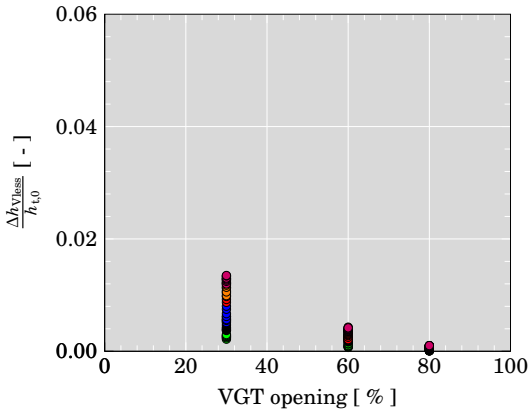

Figure 5.32: Modeled $\frac{\Delta h_{\text{Vless}}}{h_{\text{t,0}}}$ fitted in design condition of 30 %, 60 %, and 80 %

results of 80 % VGT efficiency map. Here, the model has been fitted by the data of 10 %, 30 %, and 60 % VGT opening. It can be seen that the model results have the same quality as with the fitting of the information of all VGT positions. In Figure 5.33 values of MAE and RMSE barely change in comparison to the extrapolation with all data close to design condition (Figure 5.28).

In Figure 5.34 the fitted loss $\frac{\Delta h_{\text{Vless}}}{h_{\text{t,0}}}$ with the three most closed VGT openings are shown. The high importance of very closed positions is clearly visible here. Since $\frac{\Delta h_{\text{Vless}}}{h_{\text{t,0}}}$ is becoming less important for opened VGT positions, it can be expected to reliably extrapolate towards opened VGT efficiency maps.

5.3.3 Conclusions

1. A one-dimensional adiabatic physically based efficiency model with novel loss correlations has been developed.

2. By using non-dimensional specific energies the model is independent of the turbine inlet temperature and reduced numbers can directly be used. Also, an iterative calculation of the density can be avoided in certain parts of the model.

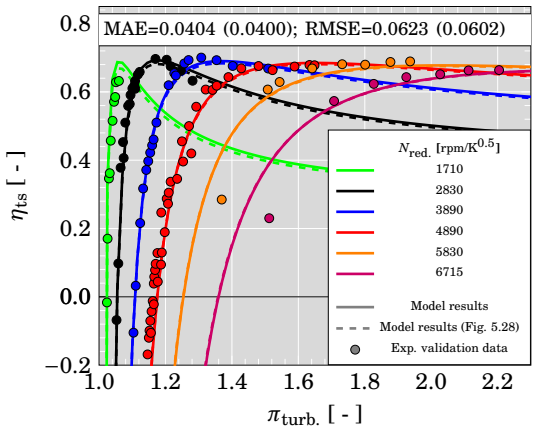

Figure 5.33: Extrapolation of 80 % VGT opening for turbocharger T1: η_{ts} vs. $\pi_{turb.}$.

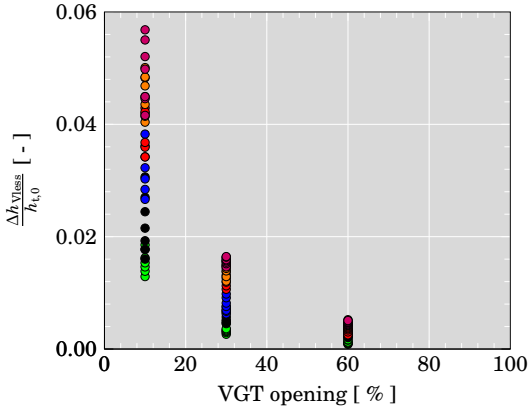

Figure 5.34: Modeled $\frac{\Delta h_{Vless}}{h_{t,0}}$ fitted in design condition of 10 %, 30 %, and 60 %.

3. The model owns a moderate number of fitting coefficients enhancing the stability for efficiency extrapolations.

4. Since the model uses the reduced mass flow as an input, equations have one degree of freedom less. Thus, for the presented model no mean blade outlet angle or outlet deviation has been estimated. The system of loss models is capable of solving the velocity triangle in the outlet of the turbine without this parameters, which might influence the result significantly.

5. A novel definition of the effective diameter in the rotor outlet has been given, taking the radial distribution of the flow into account, which can be important for the energy extraction of a radial turbine.

6. The model can fit data of different VGT positions at the same time. This increases the range of mass flow and pressure ratio and thus the information that makes the data fitting and extrapolation more reliable. Here, the loss model of the vaneless space plays an important role for the VGT fitting.

7. Good extrapolation quality towards low pressure ratios has been stated by means of wide range experimental data. Also, the extrapolation towards higher and lower speeds can be executed in good quality. Finally, the extrapolation towards unfitted opened VGT positions can be executed in high quality.

8. Due to the importance of the losses in the stationary frame for the fitting of closed VGT positions the extrapolation towards closed positions results in being challenging. Thus, it can be recommended to measure closed positions rather than extrapolating them.

9. The model can easily be modified to fit and extrapolate vaneless turbines, when the equations for calculating the stator outlet condition are skipped.

10. As the model is planned to be used in an one-dimensional entire engine simulation it needs to be solved fast. To increase the computational speed significantly the formulation of the velocities as relative kinetic energies has newly been introduced and can be used to solve the rotor by means of a system of linear equations. Further simplifications in the stator row and in the vaneless space (like assuming incompressible flow and loss calculation with isentropic velocities) can allow to solve these in a faster manner.

CHAPTER 6

Conclusions and Future Works

Contents

6.1 Conclusions

In the frame work of this thesis it was possible to contribute to different research sectors in radial turbomachinery. The conclusions that can be made are summarized in this section.

6.1.1 Contribution to Wide Range Turbine Map Measurement

A procedure for measuring extreme off-design conditions of radial turbocharger turbines without geometrical configurations on the turbocharger geometry was developed and industrialized. Conditions of extreme high blade to jet speed ratio and close to zero mass flow were made measurable by using the turbocharger compressor not only as braking device but also as power supplier for the turbine. Pressurizing the compressor inlet converts the the impeller into a centrifugal turbine with pressure ratios lower than one. Placing an IGV upstream of the compressor rotor adds swirl in the inlet, which enhances the power of the centrifugal turbine according to Euler's turbomachinery equation. This way the measurement of turbine efficiencies below zero and mass flows close to zero up to moderate speeds in quasi-adiabatic condition was achievable. In hot conditions these speeds are typical in engine running conditions. For achieving measurements at even higher speeds the compressor volute was milled to expand to the ambient and to avoid measurement restricting volute choking.

Analyzing variations of lubrication oil temperatures highlighted the importance of internal heat transfer under conditions of extremely low turbine power output. Based on this analysis a quick to use heat transfer correlation for governing internal heat transfer in the presented measurement environment was developed. This model requires only fluid temperature measurements in comparison to more complex heat transfer models which rely on several metal surface temperature measurements. Additionally, the procedure needs only a few measurements points (4 to 8) and is capable of delivering results of the same quality as more complex heat transfer models.

To omit bearing destruction due to compressor pushing, the friction losses must be monitored during the testing. It was shown that the friction loses can be estimated by means of adiabatized performance data from the compressor and turbine side. In the following compressor pushing can be avoided by also pressurizing the turbine inlet and throttling the turbine outlet. This stands also in line with the objective to measure low reduced speeds.

CFD simulations in off-design conditions have shown that the typical measurement of static pressure close to the wall can cause an overestimation of the real turbine efficiency, when the turbine is tested with low mass flow and high swirl in the outlet. Thus, it is recommended to measure at further radial locations and to calculate an area average.

6.1.2 Contribution to Off-Design CFD Simulation

For avoiding convergence problems with the extremely high swirled turbine outlet flow at close to zero mass flows the outlet duct has been extensively extended and a tapered duct was added to locally accelerate the flow at the outlet. This way operating points with pressure ratios close to 1.1 were simulated and convergent results were obtained. When the pressure ratio was reduced even more no stationary flow evolved in RANS simulations. A comparison of experimental data with RANS and URANS CFD simulations has shown very good agreement of reduced mass flow and turbine power prediction. Hence, the qualitative reliability of the flow analysis has been stated.

6.1.3 Contribution to Off-Design Passage Flow Characterization

CFD simulations of numerous running points with stationary boundary conditions in extreme off-design condition allowed the flow analysis in this region of the map. Due to the highly swirled rotor outflow and the radial pressure gradients caused by the radial equilibrium the rotor outlet flow tends to turn towards the rotation axis at off-design conditions. When the gradients are big enough a reverse flow is caused, which reenters the rotor passage close to the hub. The reverse flow was observed to cause significant flow instabilities as mass flow fluctuations in conditions of steady boundary conditions. The occurrence of the back flow was observed close to zero efficiency points at moderate speeds. However, due to rising outlet swirl with increasing rotational speeds the reverse flow was observed at moderate adiabatic turbine efficiencies.

On the one hand side, the reverse flow restricts the passage area close to the hub so that it can not fully be taken advantage of the work extraction due to a reduction of the flow radius. On the other hand side, the reentering flow increases locally the mass flow and enthalpy can be extracted from the reverse flow. The flow mixing is expected to increase pressure losses. Hence, the impact on the efficiency might be of lower magnitude.

The modeling of this effect is challenging since it only appears in extreme off-design conditions and is highly dependent on the radial pressure gradients downstream the turbine wheel. Hence, the fitting of a one-dimensional submodel with typically available map data in close to design condition is not possible.

6.1.4 Contribution to Rotor Tip Leakage Flow Analysis

By means of the detailed analysis of CFD data in the rotor tip gap a strong influence of incidence flow on the tip leakage specific mass flow and momentum in the inducer section was identified. While it reduces the pressure gradient

induced specific mass flow in the tip gap, the incidence inflow leads to an increase of inverse directed specific mass flow and momentum, which causes a further entropy rise when this flow mixes with the passage flow. The overall relative mass flow passing through the tip gap was observed to increase towards off-design conditions. Values of up to 14 % of the mass flow can pass through the tip gap. Depending on the VGT position the mass flow ratio ranges from 5 % to almost 10 % at design condition.

The contrariwise leakage due to shroud friction can be neglected in design points but dominates the tip clearance in the rotor inlet section when operating in extreme off-design conditions. Furthermore, the ratio of friction and pressure ratio driven momentum has been analyzed and it has been stated that available correlations are not capable of doing quantitative conclusions of tip leakage flow over the chord length and neither qualitative conclusions of tip gap geometry changes.

6.1.5 Contribution to Tip Leakage Loss Model & Flow Characterization

The modeling of dragging and loading effects are important to realize good quality extrapolations based on design point data. The developed model is able to fit and extrapolate the CFD data in a wide range using mainly map data, gas data, and simple geometrical data. Fitting the tip leakage losses, also the mass flow fraction has been calculated in a good quality compared to CFD data.

A new correlation to calculate the momentum ratio based on the Navier Stokes Equation has been derived. The equation inherent flow length, here interpreted as effective flow length, has been fitted dependent on the ratio of Reynolds numbers build for friction driven and pressure driven flow $\frac{Re_-}{Re_+^{1/6}}$ for all analyzed running conditions at design and off-design, from low to high rotational speed, and for varied geometry.

Furthermore, one additional correlation has been found to fit the pressure driven velocity, which allows to calculate the impact of friction momentum and to analyze the impact of the incidence flow momentum. As demonstrated the correlations can further been used to analyze mixed flow phenomena in the tip leakage flow as the incidence tip flow in the inlet.

6.1.6 Contribution to Efficiency Extrapolation Model

A novel physically based model for the extrapolation of adiabatic efficiencies was designed. The model takes advantage of a moderate number of loss models. Here, traditional and newly developed models like the described tip leakage model. Furthermore, the rotor outlet was modeled based on an effective flow diameter which affects the effective area. This way the radial distribution of the

flow and enthalpy extraction could be taken into account. For the realization of model fitting of the data of various VGT positions the loss model of the vaneless space played an important role. Here a simple loss correlation was used. Since the model is capable of fitting the data of several VGT positions at the same time, the physical information that can be passed to the model increases significantly and already extends the range of flow characterization and makes the extrapolation more reliable. Owning only a low number of fitting coefficients a good extrapolation stability was achieved for extrapolations towards high blade to jet speed ratio, lower and higher rotational speeds as well as to unknown stator vane openings.

The model is based on the calculation of kinetic energies and enthalpies in seperated turbine sections. Normalizing these energies by the inlet total enthalpy allows to directly use reduced numbers and to avoid the iterative calculation of densities in all stages. This gives the model the potential of fast programming and for further acceleration.

6.2 Future Works

In continuation of this thesis work can be advanced in different fields in order to measure, to model, or to avoid off-design conditions.

6.2.1 Measurement of Extended Turbine Maps

Apart from the presented three assemblies in section 3.3 remaining possibilities do exist to control and to increase the power output of the compressor in order to obtain turbine measurements at low mass flows for higher speeds. From Equation 3.2 and Equation 3.3 it is easily deduced that the inlet temperature has a high impact on the compressor work. Thus, increasing the inlet temperature results in significantly higher compressor power outputs according to the model results in figure Figure 6.1.

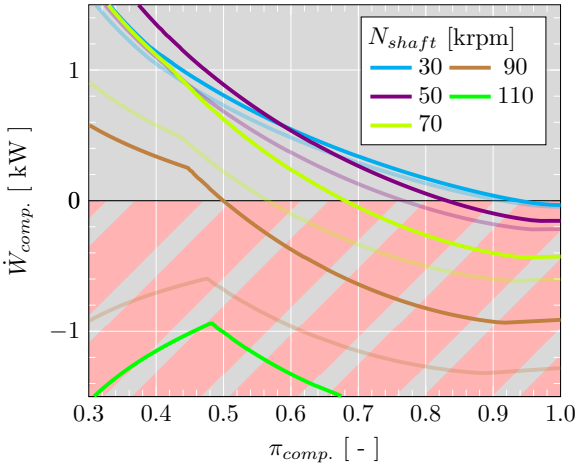

Figure 6.1: Compressor model results with 180 °C inlet temperature and imposed swirl component $c_{\theta,1}$ (α_1 = 50°); compared with results of Figure 3.7 (light color lines)

The inlet total temperature can be risen by means of a heater upstream the compressor or by increasing the power of the pressure supplying device in the inlet of the compressor. If a heater is utilized it has to be taken into account that the compressor might choke at lower mass flows so that a simultaneous increase of the inlet total pressure is desirable when the inlet total temperature is risen. Also it has to be taken care, that the quasi-adiabatic test condition keeps valid. Furthermore, the limitation of the second assembly due to lubrication film failure could be overcome by reducing the oil sump pressure below ambient (e.g. 0.7 to 0.6 bar) conditions by means of a vacuum pump. Thus, loss of the oil can be controlled.

To omit the problem of compressor pushing, the turbine pressure level could be increased, while throttling the turbine outlet for still operating at low turbine pressure ratios. This stands in line with the objective to measure at low reduced mass flows. As a testing guide during the measurements the relation of axial forces and friction forces as displayed in Figure 3.29 can be helpful. The adiabatic turbine and compressor power can be estimated with the newly presented method for fast internal heat transfer corrections. With these friction losses can be calculated during the test to adjust the required inlet pressures. This way, a conspicuous change in the calculated friction losses can indicate occurring metal-to-metal contact and an undesired axial shift.

6.2.2 Off-Design Aerodynamics in Pulsating Flow

Since it has been discovered that the reverse flow effect is self stabilizing, its effect of transient flow and performance characteristics should be investigated by means of further URANS simulations with relevant pulsating flow conditions. Results can be relevant for transient flow one-dimensional modeling and might help to translate stationary measured maps. Although it has already been stated that this effect is highly dependent on the geometry downstream of the rotor, the modeling of an additional volume for mass flow accumulation could help model this effect in transient models.

6.2.3 Modeling of One-Dimensional Off-Design Behavior

As described in subsection 4.5.1 the modeling of the reverse flow effect is challenging since it highly depends on the pressure gradients downstream the rotor. Hence, further geometries need to be analyzed to allow a reliable modeling which bets by without the use of too many fitting coefficients (because the effect occurs only in off-design and can not be fitted). This effect might be of importance for massflow extrapolations towards zero massflow and beyond.

The detailed characterization of the tip leakage flow by means of the momentum ratio R_{NS} bears the change to improve the modeling of tip leakage losses. Since geometric details are included in this correlation are of physical origin, global loss coefficients might be found that are valid for a wide variation of turbine geometries. Since the equations have their origin in the tangential momentum equation, also the tip leakage flow in axial turbines might be modeled with this correlations.

As the complete one-dimensional extrapolation model is planned to be used in an one-dimensional entire engine simulation it needs to be solved fast. To increase the computational speed significantly the formulation of the velocities as relative kinetic energies has newly been introduced and can be used to solve the rotor by means of a system of linear equations. Further simplifications in the stator row and in the vaneless space (like assuming incompressible flow and loss calculation with isentropic velocities) can allow to solve these in a faster manner without internal iterations.

6.2.4 Avoiding Off-Design Operation with New Technologies

In section 1.2 the importance and problematic of off-design performance for the final power output has been exhaustively illustrated. By means of a supersonic radial outflow turbine as it has been introduced by Inhestern et al. [9] this problem might be bypassed in a certain range. Since the designed geometry also works with subsonic inflow the application in the field of compact turbocharging might be possible. The inflow section and the passage act as a convergent

divergent nozzle itself. This avoids shocks in the passage inlet and allows a highly compact design due to high flow velocities in the passage.

When the flow enters with subsonic inflow a transition from subsonic flow to supersonic flow evolves close to the passage throat. Hence, the upstream Mach number is fixed by throat geometry and rotational speed. This means that pure pressure pulses barely change the operating point as the reduced massflow and efficiency maintains approximately constant when the reduced speed is kept constant. The upstream Mach number regulates itself. Indeed, fluctuations in the total and static temperature take additional influence on the reduced speed and Mach number and must be investigated in further detail. An IGV in the axial inflow duct might solve this issue. This type of technology might be promising to overcome the operation in off-design condition.

Bibliography

[1] **Serrano, J. R., Tiseira, A., García-Cuevas, L. M., Inhestern, L. B., and Tartoussi, H.**
"Radial turbine performance measurement under extreme off-design conditions"
in: *Energy* 125 (2017), pp. 72 –84. ISSN: 0360-5442. DOI: 10.1016/j.energy.2017.02.118 (cit. on pp. vii, viii)

[2] **Serrano, J. R., García-Cuevas, L. M., Inhestern, L. B., Mai, H., Rinaldi, A., and Miguel-Sanchez, A.**
"Methodology to evaluate turbocharger turbine performance at high blade to jet speed ratio under quasi adiabatic conditions"
in: *ASME Turbo Expo 2017: Turbomachinery Technical Conference and Exposition*. American Society of Mechanical Engineers 2017, V008T26A004. DOI: doi:10.1115/GT2017-63360 (cit. on pp. vii, viii)

[3] **Serrano, J. R., Gil, A., Navarro, R., and Inhestern, L. B.**
"Extremely Low Mass Flow at High Blade to Jet Speed Ratio in Variable Geometry Radial Turbines and its Influence on the Flow Pattern: A CFD Analysis"
in: *ASME Turbo Expo 2017: Turbomachinery Technical Conference and Exposition*. American Society of Mechanical Engineers 2017, V008T26A005–V008T26A005. DOI: doi:10.1115/GT2017-63368
(cit. on pp. vii, viii)

[4] **Serrano, J. R., Navarro, R., García-Cuevas, L. M., and Inhestern, L. B.**
"Turbocharger turbine rotor tip leakage loss and mass flow model valid up to extreme off-design conditions with high blade to jet speed ratio"
in: *Energy* 147 (2018), pp. 1299 –1310. ISSN: 0360-5442. DOI: https://doi.org/10.1016/j.energy.2018.01.083. URL: https://www.sciencedirect.com/science/article/pii/S0360544218301014
(cit. on pp. vii, viii)

[5] **Serrano, J. R., García-Cuevas, L. M., Inhestern, L. B., Guilain, S., and Tartoussi, H.**
"Analysis of Unsteady Energy Fluxes in a Turbocharger by Using a Holistic Model Extrapolating Standard Lookup Tables in Full Engine Operating Map"
in: *ASME Turbo Expo 2018: Turbomachinery Technical Conference and Exposition*. American Society of Mechanical Engineers 2018, V008T26A015–V008T26A015. DOI: doi:10.1115/GT2018-76470
(cit. on pp. vii, viii, 3)

[6] **Serrano, J. R., Navarro, R., García-Cuevas, L. M., and Inhestern, L. B.**
"Method for Non-Dimensional Tip Leakage Flow Characterization in Radial Turbines"
in: *ASME Turbo Expo 2018: Turbomachinery Technical Conference and Exposition*. American Society of Mechanical Engineers 2018, V008T26A016–V008T26A016. DOI: doi:10.1115/GT2018-76490
(cit. on pp. vii, viii)

[7] **Serrano, J. R., Martinez, F. J. A., García-Cuevas, L. M., and Inhestern, L. B.**
"An Innovative Losses Model for Efficiency Map Fitting of Vaneless and Variable Vaned Radial Turbines Extrapolating Towards Extreme Off-Design Conditions"
in: *Energy (under 2nd revision)* (2018) (cit. on pp. vii, viii)

[8] **Serrano, J. R., Navarro, R., García-Cuevas, L. M., and Inhestern, L. B.**
"Contribution to Tip Leakage Loss Modeling in Radial Turbines Based on 3D Flow Analysis and 1D Characterization"
in: *Heat and Fluid Flow (under 2nd revision)* (2018)
(cit. on pp. vii, viii)

[9] **Inhestern, L. B., Braun, J., Paniagua, G., and Serrano, J. R.**
"Design, Optimization and Analysis of Supersonic Radial Turbines"
in: *(Accepted for conference and journal publication)* (2019), GT2019–91756 (cit. on pp. vii, viii, 163)

[10] **Liu, Z., Inhestern, L. B., Braun, J., and Paniagua, G.**
"Unsteady Heat Transfer Assessment of Supersonic Turbines Downstream of a Rotating Detonation Combustor"
in: *(Accepted for conference publication)* (2019), GT2019–91460
(cit. on p. viii)

[11] **European Parliament, Council of the European Union**
"Regulation (EC) No 715/2007 of the European Parliament and of the Council of 20 June 2007 on type approval of motor vehicles with respect to emissions from light passenger and commercial vehicles (Euro 5 and Euro 6) and on access to vehicle repair and maintenance information (Text with EEA relevance) "
in: *Official Journal of the European Union* 50 (2007), pp. 1–16. ISSN: 1725-2555. URL: http://eur-lex.europa.eu/legal-content/EN/TXT/?uri=OJ:L:2007:171:TOC (cit. on p. 2)

[12] **Adhikary, B., Reitz, R., Ciatti, S., and Kolodziej, C.**
"Computational Investigation of Low Load Operation in a Light-Duty Gasoline Direct Injection Compression Ignition [GDICI] Engine Using Single-Injection Strategy"
in: *SAE Technical Paper 2014-01-1297* (2014). ISSN: 0148-7191. DOI: 10.4271/2014-01-1297 (cit. on p. 2)

[13] **Luján, J. M., Serrano, J. R., Piqueras, P., and García-Alfonso, O.**
"Experimental assessment of a pre-turbo aftertreatment configuration in a single stage turbocharged diesel engine. Part 2: Transient operation"
in: *Energy* 80 (Feb. 2015), pp. 614–627. DOI: 10.1016/j.energy.2014.12.017 (cit. on p. 2)

[14] **Serrano, J. R., Olmeda, P., Tiseira, A., García-Cuevas, L. M., and Lefebvre, A.**
"Theoretical and experimental study of mechanical losses in automotive turbochargers"
in: *Energy* 55.0 (2013), pp. 888 –898. ISSN: 0360-5442. DOI: 10.1016/j.energy.2013.04.042 (cit. on p. 2)

[15] **Galindo, J., Fajardo, P., Navarro, R., and García-Cuevas, L. M.**
"Characterization of a radial turbocharger turbine in pulsating flow by means of CFD and its application to engine modeling"
in: *Applied Energy* 103.0 (2013), pp. 116 –127. ISSN: 0306-2619. DOI: 10.1016/j.apenergy.2012.09.013 (cit. on pp. 2, 25)

[16] **Aymanns, R, Scharf, J, Uhlmann, T, and Lückmann, D**
"A revision of quasi steady modelling of turbocharger turbines in the simulation of pulse charged engines"
in: *16th Supercharging Conference* 2011 (cit. on pp. 2, 25)

[17] **Jensen, J.-P., Kristensen, A., Sorenson, S., Houbak, N., and Hendricks, E.**
"Mean Value Modeling of a Small Turbocharged Diesel Engine"
in: *International Congress and Exposition*. SAE International 1991.

DOI: https://doi.org/10.4271/910070. URL: https://doi.org/10.4271/910070 (cit. on p. 2)

[18] **Rajoo, S., Romagnoli, A., and Martínez-Botas, R. F.**
"Unsteady performance analysis of a twin-entry variable geometry turbocharger turbine"
in: *Energy* 38 (Feb. 2012), pp. 176–189. DOI: 10.1016/j.energy.2011.12.017 (cit. on p. 2)

[19] **Chiong, M. S., Rajoo, S., Martínez-Botas, R. F., and Costall, A.**
"Engine turbocharger performance prediction: One-dimensional modeling of a twin entry turbine"
in: *Energy Conversion and Management* 57 (May 2012), pp. 68–78. DOI: 10.1016/j.enconman.2011.12.001 (cit. on p. 2)

[20] **Galindo, J., Tiseira, A., Fajardo, P., and García-Cuevas, L. M.**
"Development and validation of a radial variable geometry turbine model for transient pulsating flow applications"
in: *Energy Conversion and Management* 85.0 (2014), pp. 190 –203. ISSN: 0196-8904. DOI: 10.1016/j.enconman.2014.05.072 (cit. on p. 2)

[21] **Simpson, A., Spence, S., and Watterson, J.**
"A comparison of the flow structures and losses within vaned and vaneless stators for radial turbines"
in: *Journal of turbomachinery* 131.3 (2009), p. 031010. DOI: doi:10.1115/1.2988493 (cit. on pp. 13, 24, 25, 70)

[22] **Marsan, A and Moreau, S**
"Analysis of the Flow Structure in a Radial Turbine"
in: *11th European Conference on Turbomachinery Fluid dynamics & Thermodynamics* 2015 (cit. on p. 13)

[23] **Baines, N. C.**
"Flow development in radial turbine rotors"
in: *ASME 1996 International Gas Turbine and Aeroengine Congress and Exhibition*. American Society of Mechanical Engineers 1996, V001T01A021–V001T01A021. DOI: doi:10.1115/96-GT-065 (cit. on p. 13)

[24] **Murugan, D., Tabakoff, W, and Hamed, A**
"Flow measurements and flow analysis in the exit region of a radial turbine"
in: *International Journal of Rotating Machinery* 3.2 (1997), pp. 93–105. DOI: http://dx.doi.org/10.1155/S1023621X97000109 (cit. on pp. 13, 78, 79)

[25] **Walkingshaw, J., Spence, S., Ehrhard, J., and Thornhill, D.**
"A numerical study of the flow fields in a highly off-design variable geometry turbine"
in: *ASME Turbo Expo 2010: Power for Land, Sea, and Air*. American Society of Mechanical Engineers 2010, pp. 1951–1960. DOI: doi:10.1115/GT2010-22669 (cit. on p. 14)

[26] **Sauret, E. and Gu, Y.**
"Three-dimensional off-design numerical analysis of an organic Rankine cycle radial-inflow turbine"
in: *Applied Energy* 135 (2014), pp. 202 –211. ISSN: 0306-2619. DOI: http://dx.doi.org/10.1016/j.apenergy.2014.08.076. URL: http://www.sciencedirect.com/science/article/pii/S0306261914008873 (cit. on p. 14)

[27] **SAE**
"Turbocharger gas stand test code SAE J1826"
in: *Society of Automotive Engineers* (1995) (cit. on p. 14)

[28] **Romagnoli, A. and Martinez-Botas, R.**
"Performance prediction of a nozzled and nozzleless mixed-flow turbine in steady conditions"
in: *International Journal of Mechanical Sciences* 53.8 (2011), pp. 557 –574. ISSN: 0020-7403. DOI: 10.1016/j.ijmecsci.2011.05.003 (cit. on pp. 14, 19)

[29] **Bellis, V. D., Bozza, F., Schernus, C., and Uhlmann, T.**
"Advanced Numerical and Experimental Technique for the Extension of Turbine Mapping"
in: *SAE int. J. Engines* 3.6 (2013), pp. 1771–1785. DOI: 10.4271/2013-24-0119 (cit. on pp. 14, 19)

[30] **Smiljanovski, V., Schorn, N., Scharf, J., Funken, B., and Pischinger, S.**
"Messung des Turbinenwirkungsgrades bei niedrigen Turboladerdrehzahlen"
in: *13. Aufladetechnische Konferenz (25-26 September 2008, Dresden)* (2008) (cit. on pp. 14, 42)

[31] **Deligant, M., Podevin, P., and Descombes, G.**
"Experimental Identification of Turbocharger Mechanical Friction Losses"
in: *Energy* 39.1 (Mar. 2012), pp. 388–394. DOI: 10.1016/j.energy.2011.12.049 (cit. on p. 15)

[32] **Terdich, N.**
"Impact of electrically assisted turbocharging on the transient response of an off-highway diesel engine"
PhD thesis. Imperial College London 2015 (cit. on pp. 15, 42, 43, 89)

[33] **Salameh, G., Chesse, P., and Chalet, D.**
"Different Measurement Techniques for Wider Small Radial Performance Maps"
in: *Experimental Techniques* 40.6 (Dec. 2016), pp. 1511–1525. DOI: 10.1007/s40799-016-0107-8 (cit. on pp. 15, 43, 89)

[34] **Pucher, A.**
"Overall Engine Process Simulation - an Important Tool for the Development of Supercharged Engines"
in: *International Conference on Turbochargers and Turbocharging* C602.045 (2002), pp. 155–166 (cit. on p. 16)

[35] **Leufén, O. and Eriksson, L.**
"Measurements, Analysis and Modeling of Centrifugal Compressor Flow for Low Pressure Ratios"
in: *International Journal of Engine Research* (2013). DOI: 10.1177/1468087414562456 (cit. on p. 16)

[36] **Wallace, F. J., Whitfield, A., and Atley, R. C.**
"Experimental and Theoretical Performance of Radial Flow Turbocharger Compressor with Inlet Prewhirl"
in: *Proceedings of the Institution of Mechanical Engineering* 189.43/75 (1975), pp. 177–186. DOI: 10.1243/PIME_PROC_1975_189_024_02 (cit. on pp. 16, 38)

[37] **Najjar, Y. S. H. and Akeel, S. A.M. S.**
"Effect of Prewhirl on Performance of Centrifugal Compressors"
in: *International Journal of Rotating Machinery* 8.6 (2002), pp. 397–401. DOI: 10.1080/10236210214326 (cit. on pp. 16, 38)

[38] **Müller, M., Sumser, S., P.Fledersbacher, Rößler, K., Fieweger, K., and Bauer, H.-J.**
"Using the Centrifugal Compressor as a Cold Air Turbine"
in: *8th International Conference on Turbochargers and Turbocharging*. Ed. by editor, T. Vol. 8. Institution of Mechanical Engineers Combustion Engines and Fuels Group. Woodhead Publishing in Mechanical Engineering May 2006, pp. 55–67 (cit. on p. 16)

[39] **Serrano, J. R., Olmeda, P., Arnau, F. J., Dombrovsky, A., and Smith, L.**
"Analysis and Methodology to Characterize Heat Transfer Phenomena in Automotive Turbochargers"
in: *Journal of Engineering for Gas Turbines and Power* 137 (Feb. 2015), pp. 021901–1 –021901–11. DOI: 10.1115/1.4028261 (cit. on pp. 16, 17, 47, 51, 146)

[40] **Serrano, J. R., Olmeda, P., Arnau, F. J., Dombrovsky, A., and Smith, L.**
"Turbocharger heat transfer and mechanical losses influence in predicting engines performance by using one-dimensional simulation codes"
in: *Energy* 86 (June 2015), 204–218. DOI: 10.1016/j.energy.2015.03.130 (cit. on p. 16)

[41] **Schinnerl, M., Seume, J., Ehrhard, J., and Bogner, M.**
"Heat Transfer Correction Methods for Turbocharger Performance Measurements"
in: *Turbine Technical Conference and Exposition*. ASME Turbo Expo June 2016. DOI: 10.1115/1.4034234 (cit. on p. 16)

[42] **Serrano, J. R., Olmeda, P., Arnau, F. J., Reyes-Belmonte, M. A., and Tartoussi, H.**
"A study on the internal convection in small turbochargers. Proposal of heat transfer convective coefficients"
in: *Applied Thermal Engineering* 89 (2015), pp. 587 –599. DOI: 10.1016/j.applthermaleng.2015.06.053 (cit. on p. 17)

[43] **Sirakov, B. and Casey, M.**
"Evaluation of Heat Transfer Effects on Turbocharger Performance"
in: *Journal of Turbomachinery* 135.2 (2012). DOI: 10.1115/1.4006608 (cit. on p. 17)

[44] **Zimmermann, R., Baar, R., and Biet, C.**
"Determine the isentropic turbine efficiency due to adiabatic measurements, and the validation of the conditions via a new criterion"
in: *12th International Conference on Turbochargers and Turbocharging (17-18 May 2016, London)* 2016 (cit. on pp. 17, 52)

[45] **Serrano, J. R., Olmeda, P., Arnau, F. J., and Dombrovsky, A.**
"General Procedure for the Determination of Heat Transfer Properties in Small Automotive Turbochargers"
in: *SAE Int. J. Engines* 8.1 (2014). DOI: 10.4271/2014-01-2857 (cit. on pp. 17, 68, 72)

[46] **Serrano, J. R., Olmeda, P., Páez, A., and Vidal, F.**
"An experimental procedure to determine heat transfer properties of turbochargers"
in: *Measurement Science and Technology* 21.3 (2010), p. 035109. DOI: 10.1088/0957-0233/21/3/035109 (cit. on pp. 17, 51, 146)

[47] **Watson, N.**
"Transient Performance Simulation and Analysis of Turbocharged Diesel Engines"

in: *SAE Transactions* 90 (1981), pp. 1391–1409. ISSN: 0096736X, 25771531. DOI: https://doi.org/10.4271/810338. URL: http://www.jstor.org/stable/44632711 (cit. on p. 18)

[48] **Eriksson, L., Nielsen, L., Brugård, J., Bergström, J., Pettersson, F., and Andersson, P.**
"Modeling of a Turbo Charged SI Engine"
in: *IFAC Proceedings Volumes* 34.1 (2001). 3rd IFAC Workshop on Advances in Automotive Control 2001, Karlsruhe, Germany, 28-30 March 2001, pp. 369 –377. ISSN: 1474-6670. DOI: https://doi.org/10.1016/S1474-6670(17)34425-7. URL: http://www.sciencedirect.com/science/article/pii/S1474667017344257 (cit. on p. 18)

[49] **Orkisz, M. and Stawarz, S.**
"Modeling of Turbine Engine Axial-Flow Compressor and Turbine Characteristics"
in: *Journal of Propulsion and Power* 16 (2000). DOI: https://doi.org/10.2514/2.5574 (cit. on p. 18)

[50] **Fang, X. and Xu, Y.**
"Development of an empirical model of turbine efficiency using the Taylor expansion and regression analysis"
in: *Energy* 36.5 (2011), pp. 2937 –2942. ISSN: 0360-5442. DOI: https://doi.org/10.1016/j.energy.2011.02.036. URL: http://www.sciencedirect.com/science/article/pii/S0360544211001149 (cit. on p. 18)

[51] **Martins, G., Mendoza, O. S. H., and Tumialan, J. A.**
"Semi-Empirical Modeling of Small Size Radial Turbines for Refrigeration Purpose"
in: *International Compressor Engineering Conference* (2006) (cit. on p. 19)

[52] **Serrano, J. R., Arnau, F. J., García-Cuevas, L. M., Dombrovsky, A., and Tartousi, H.**
"Development and Validation of a Radial Turbine Efficiency Model at Extreme Off-Design Conditions"
in: *Energy Conversion and Management* (2016). DOI: 10.1016/j.enconman.2016.09.032 (cit. on pp. 19, 40, 54, 74, 137, 141, 145, 147, 148)

[53] **Baines, N.**
"A meanline prediction method for radial turbine efficiency"
in: *IMECHE conference transactions*. Vol. 11. Mechanical Engineering Publications 1998, pp. 45–56 (cit. on pp. 19, 22)

[54] **Zhu, S., Deng, K., and Liu, S.**
"Modeling and extrapolating mass flow characteristics of a radial turbocharger turbine"
in: *Energy* 87 (July 2015), pp. 628–637. DOI: 10.1016/j.energy.2015.05.032 (cit. on p. 19)

[55] **Song, K., Upadhyay, D., Zeng, T., and Sun, H.**
"A physics-based control-oriented model for the turbine power of a variable-geometry turbo-charger"
in: *ASME 2016 Dynamic Systems and Control Conference*. American Society of Mechanical Engineers 2016, V002T19A005–V002T19A005 (cit. on p. 19)

[56] **Serrano, J. R., Pla, B., Gozalbo, R., and Ospina, D.**
"Estimation of the Extended Turbine Maps for a Radial Inflow Turbine"
in: *SAE 2010 World Congress and Exhibition*. SAE International 2010. DOI: https://doi.org/10.4271/2010-01-1234. URL: https://doi.org/10.4271/2010-01-1234 (cit. on p. 20)

[57] **Futral, S. and Wasserbauer, C.**
Off-design performance prediction with experimental verification for a radial-inflow turbine
tech. rep. NASA TN D-2621. NASA 1965. URL: http://books.google.es/books?id=N1kzLAHfK-IC (cit. on pp. 19, 31, 138, 143)

[58] **Suhrmann, J. F., Peitsch, D., Gugau, M., Heuer, T., and Tomm, U.**
"Validation and development of loss models for small size radial turbines"
in: *ASME Turbo Expo 2010: Power for Land, Sea, and Air*. American Society of Mechanical Engineers 2010, pp. 1937–1949. DOI: doi:10.1115/GT2010-22666 (cit. on p. 19)

[59] **Meroni, A., Robertson, M., Martinez-Botas, R., and Haglind, F.**
"A methodology for the preliminary design and performance prediction of high-pressure ratio radial-inflow turbines"
in: *Energy* 164 (2018), pp. 1062 –1078. ISSN: 0360-5442. DOI: https://doi.org/10.1016/j.energy.2018.09.045. URL: http://www.sciencedirect.com/science/article/pii/S036054421831805X (cit. on p. 19)

[60] **Bunker, R. S.**
"Axial Turbine Blade Tips: Function, Design, and Durability"
in: *Journal of Propulsion and Power* 22 (2006). DOI: https://doi.org/10.2514/1.11818 (cit. on p. 21)

[61] **Wallace, F.**
"Theoretical assessment of the performance characteristics of inward radial flow turbines"
in: *Proceedings of The Institution of Mechanical Engineers* 172.1 (1958), pp. 931–952 (cit. on pp. 21, 22)

[62] **Dambach, R, Hodson, H., and Huntsman, I**
"An experimental study of tip clearance flow in a radial inflow turbine"
in: *ASME. Turbo Expo: Power for Land, Sea, and Air, Volume 1: Turbomachinery ():V001T01A110.* American Society of Mechanical Engineers 1998 (cit. on pp. 21–23, 95, 96, 105)

[63] **Kammeyer, J., Natkaniec, C., and Seume, J. R.**
"Tip Leakage in Small Radial Turbines: Optimum Tip-Gap and Efficiency Loss Correlations"
in: *ASME Turbo Expo 2010: Power for Land, Sea, and Air*. American Society of Mechanical Engineers 2010, pp. 391–401
(cit. on pp. 21, 23, 101)

[64] **Krylov, E. and Spunde, Y. A.**
About the influence of the clearance between the working blades and housing of a radial turbine on its exponent
tech. rep. FOREIGN TECHNOLOGY DIV WRIGHT-PATTERSON AFB OHIO 1967 (cit. on p. 21)

[65] **Rohlik, H. E.**
Analytical determination of radial inflow turbine design geometry for maximum efficiency
tech. rep. Lewis Research Center; National Aeronautics and Space Administration; Cleveland, Ohio 1968. URL: https://ntrs.nasa.gov/archive/nasa/casi.ntrs.nasa.gov/19680006474.pdf
(cit. on p. 21)

[66] **Glassman, A. J.**
Computer program for design analysis of radial-inflow turbines
tech. rep. Lewis Research Center; National Aeronautics and Space Administration; Cleveland, Ohio 1976. URL: https://ntrs.nasa.gov/archive/nasa/casi.ntrs.nasa.gov/19760010058.pdf
(cit. on p. 21)

[67] **Yaras, M. and Sjolander, S.**
"Prediction of tip-leakage losses in axial turbines"
in: V001T01A050. ISBN: 978-0-7918-7904-7. DOI: doi:10.1115/90-GT-154 (cit. on pp. 21, 114, 115)

[68] **Spraker, W. A.**
"Contour clearance losses in radial inflow turbines for turbochargers"
in: *ASME Paper* 87-ICE-52 (1987) (cit. on p. 22)

[69] **Baines, N.**
"RADIAL TURBINE DESIGN"
in: *Axial and Radial Turbines*. Concepts NREC 2006 (cit. on p. 22)

[70] **Kammeyer, J., Natkaniec, C., and Seume, J. R.**
"Influence of tip-gap losses on the stage efficiency of downsizing turbocharger turbines"
in: *9th International Conference on Turbochargers and Turbocharging,19-20 May, London* 2010 (cit. on p. 23)

[71] **Dambach, R. and Hodson, H.**
"Tip leakage flow in a radial inflow turbine with varying gap height"
in: *Journal of Propulsion and Power* 17.3 (2001), pp. 644–650. DOI: https://doi.org/10.2514/2.5791 (cit. on pp. 23, 112, 116)

[72] **Dambach, R, Hodson, H., and Huntsman, I**
"Tip-leakage flow: a comparison between axial and radial turbines"
in: *Micro-Turbine Generators* (2002), p. 97 (cit. on p. 23)

[73] **Deng, Q. H., Niu, J. F., and Feng, Z. P.**
"Study on leakage flow characteristics of radial inflow turbines at rotor tip clearance"
in: *Science in China Series E: Technological Sciences* 51.8 (2008), pp. 1125–1136. ISSN: 1862-281X. DOI: 10.1007/s11431-008-0164-z. URL: http://dx.doi.org/10.1007/s11431-008-0164-z (cit. on p. 23)

[74] **Mendonça, F, Clement, J, Palfreyman, D, and Peck, A**
"Validation of unstructured CFD modelling applied to the conjugate heat transfer in turbine blade cooling"
in: *ETC_8-198, European Turbomachinery Conference, Graz* 2008 (cit. on pp. 23, 70)

[75] **Deardorff, J. W.**
"A numerical study of three-dimensional turbulent channel flow at large Reynolds numbers"
in: *Journal of Fluid Mechanics* 41.2 (1970), pp. 453–480. DOI: https://doi.org/10.1017/S0022112070000691 (cit. on p. 24)

[76] **Launder, B. and Spalding, D.**
"The numerical computation of turbulent flows"
in: *Computer Methods in Applied Mechanics and Engineering* 3.2 (1974), pp. 269 –289. ISSN: 0045-7825. DOI: https://doi.org/10.1016/0045-

7825(74)90029-2. URL: http://www.sciencedirect.com/science/article/pii/0045782574900292 (cit. on p. 24)

[77] **Wilcox, D. C.**
Turbulence Modeling for CFD
DCW Industries 1998. ISBN: 0963605100 (cit. on p. 24)

[78] **Wilcox, D. C.**
"Formulation of the k-w Turbulence Model Revisited"
in: *AIAA Journal* 46.11 (2008), pp. 2823–2838. DOI: https://doi.org/10.2514/1.36541 (cit. on p. 24)

[79] **Menter, F. R.**
"Two-equation eddy-viscosity turbulence models for engineering applications"
in: *AIAA journal* 32.8 (1994), pp. 1598–1605 (cit. on p. 24)

[80] **Menter, F. R., Langtry, R., and Hansen, T.**
"CFD simulation of turbomachinery flows verification, validation and modeling"
in: *European Congress on Computational Methods in Applied Sciences and Engineering, ECCOMAS* 2004 (cit. on p. 24)

[81] **Lim, S., Dahlkild, A., and Mihaescu, M.**
"Aerothermodynamics and Exergy Analysis in Radial Turbine With Heat Transfer"
in: *Journal of Turbomachinery* 140 (2018). DOI: doi:10.1115/1.4040852 (cit. on p. 24)

[82] **Galindo, J., Tiseira, A., Navarro, R., and López, M.**
"Influence of tip clearance on flow behavior and noise generation of centrifugal compressors in near-surge conditions"
in: *International Journal of Heat and Fluid Flow* 52 (2015), pp. 129–139. DOI: 10.1016/j.ijheatfluidflow.2014.12.004 (cit. on pp. 24, 91)

[83] **Menter, F., Kuntz, M., and Langtry, R.**
"Ten years of Industrial experience with the SST model."
in: *Turbulence, Heat and Mass Transfer 4*. Ed. by Hanjalić, K., Nagano, Y., and Tummers, M. 2003 (cit. on p. 24)

[84] **Palfreyman, D. and Martinez-Botas, R.**
"The pulsating flow field in a mixed flow turbocharger turbine: An experimental and computational study"
in: *Journal of Turbomachinery* 127 (2005). DOI: doi:10.1115/1.1812322 (cit. on p. 25)

[85] **Lam, J., Roberts, Q., and McDonell, G.**
"Flow modelling of a turbocharger turbine under pulsating flow"
in: *Seventh International Conference Turbochargers and Turbocharging* (2002) (cit. on p. 25)

[86] **Galindo, J., Serrano, J. R., Guardiola, C., and Cervelló, C.**
"Surge Limit Definition in a Specific Test Bench for the Characterization of Automotive Turbochargers"
in: *Experimental Thermal and Fluid Science* 30.5 (May 2006). DOI: 10.1016/j.expthermflusci.2005.06.002 (cit. on p. 29)

[87] **Inc., M.**
Field Experiences with V–Cone Technology
tech. rep. McCrometer Inc. Hemet, CA., pp. 1–12 (cit. on p. 34)

[88] **Jacobs, E. N., Ward, K. E., and Pinkerton, R. M.**
The Characteristics of 78 Related Airfoils Sections From Tests in the Variable-Density Wind Tunnel
tech. rep. National Advisory Committee for Aeronautics 1933 (cit. on p. 38)

[89] **Payri, F., Serrano, J. R., Fajardo, P., Reyes-Belmonte, M. A., and Gozalbo-Belles, R.**
"A physically based methodology to extrapolate performance maps of radial turbines"
in: *Energy Conversion and Management* 55.0 (2012), pp. 149 –163. ISSN: 0196-8904. DOI: 10.1016/j.enconman.2011.11.003 (cit. on pp. 40, 45)

[90] *Evaluation of measurement data – Guide to the expression of uncertainty in measurement*
100:2008. JCGM 2008. URL: http://www.bipm.org/utils/common/documents/jcgm/JCGM_100_2008_E.pdf (cit. on p. 47)

[91] **Baar, R., Biet, C., Boxberger, V., Mai, H., and Zimmermann, R.**
"New Evaluation of Turbocharger Components Based on Turbine Outlet Temperature Measurements in Adiabatic Conditions"
in: *International Symposium on Transport Phenomena and Dynamics of Rotating Machinery* 15 (2014) (cit. on p. 47)

[92] *STAR-CCM+. Release version 10.02.012.*
URL: http://www.cd-adapco.com (cit. on p. 69)

[93] **Dixon, S. L. and Hall, C.**
Fluid mechanics and thermodynamics of turbomachinery
Butterworth-Heinemann 2010 (cit. on p. 74)

[94] **Fajardo, P.**
"Methodology for the Numerical Characterization of a Radial Turbine under Steady and Pulsating Flow"
PhD thesis. Universidad Politecnica de Valencia 2012 (cit. on p. 76)

[95] **Chen, H, Abidat, M, Baines, N., and Firth, M.**
"The effects of blade loading in radial and mixed flow turbines"
in: *ASME 1992 International Gas Turbine and Aeroengine Congress and Exposition*. American Society of Mechanical Engineers 1992, V001T01A049–V001T01A049. DOI: doi:10.1115/92-GT-092 (cit. on p. 80)

[96] **Drela, M. and Youngren, H.**
A User's Guide to MISES 2.63
tech. rep. MIT Aerospace Computational Design Laboratory 2008 (cit. on p. 82)

[97] **Yaras, M, Zhu, Y., and Sjolander, S.**
"Flow field in the tip gap of a planar cascade of turbine blades"
in: *Journal of Turbomachinery* 111.3 (1989), pp. 276–283. DOI: doi:10.1115/1.3262266 (cit. on p. 112)

[98] **Borutzky, W., Barnard, B, and Thoma, J**
"An orifice flow model for laminar and turbulent conditions"
in: *Simulation Modelling Practice and Theory* 10.3 (2002), pp. 141–152 (cit. on p. 123)

[99] **Watson, N. and Janota, M. S.**
Turbocharging the internal combustion engine
1982. DOI: https://doi.org/10.1007/978-1-349-04024-7 (cit. on p. 139)

[100] **Chen, H and Baines, N.**
"The aerodynamic loading of radial and mixed-flow turbines"
in: *International journal of mechanical sciences* 36.1 (1994), pp. 63–79. DOI: https://doi.org/10.1016/0020-7403(94)90007-8 (cit. on p. 143)

[101] **Fang, X., Dai, Q., Yin, Y., and Xu, Y.**
"A compact and accurate empirical model for turbine mass flow characteristics"
in: *Energy* 35.12 (2010). The 3rd International Conference on Sustainable Energy and Environmental Protection, SEEP 2009, pp. 4819 –4823. ISSN: 0360-5442. DOI: https://doi.org/10.1016/j.energy.2010.09.006. URL: http://www.sciencedirect.com/science/article/pii/S0360544210004858 (cit. on p. 145)

[102] **Meitner, P. and Glassman, A.**
Off-design performance loss model for radial turbines with pivoting, variable-area stators
tech. rep. NASA TP 1708 1980. URL: https://ntrs.nasa.gov/archive/nasa/casi.ntrs.nasa.gov/19810002530.pdf (cit. on p. 147)